


Winter 2001

Mathematical modeling for fabricating a microstructure with a pre-specified geometry using laser -induced chemical vapor deposition

Chaoyang Zhang
Louisiana Tech University

Follow this and additional works at: <https://digitalcommons.latech.edu/dissertations>

 Part of the [Chemical Engineering Commons](#), [Materials Science and Engineering Commons](#), and the [Mechanical Engineering Commons](#)

Recommended Citation

Zhang, Chaoyang, "" (2001). *Dissertation*. 135.
<https://digitalcommons.latech.edu/dissertations/135>

This Dissertation is brought to you for free and open access by the Graduate School at Louisiana Tech Digital Commons. It has been accepted for inclusion in Doctoral Dissertations by an authorized administrator of Louisiana Tech Digital Commons. For more information, please contact digitalcommons@latech.edu.

INFORMATION TO USERS

This manuscript has been reproduced from the microfilm master. UMI films the text directly from the original or copy submitted. Thus, some thesis and dissertation copies are in typewriter face, while others may be from any type of computer printer.

The quality of this reproduction is dependent upon the quality of the copy submitted. Broken or indistinct print, colored or poor quality illustrations and photographs, print bleedthrough, substandard margins, and improper alignment can adversely affect reproduction.

In the unlikely event that the author did not send UMI a complete manuscript and there are missing pages, these will be noted. Also, if unauthorized copyright material had to be removed, a note will indicate the deletion.

Oversize materials (e.g., maps, drawings, charts) are reproduced by sectioning the original, beginning at the upper left-hand corner and continuing from left to right in equal sections with small overlaps.

Photographs included in the original manuscript have been reproduced xerographically in this copy. Higher quality 6" x 9" black and white photographic prints are available for any photographs or illustrations appearing in this copy for an additional charge. Contact UMI directly to order.

**Bell & Howell Information and Learning
300 North Zeeb Road, Ann Arbor, MI 48106-1346 USA
800-521-0600**

UMI[®]

.

**MATHEMATICAL MODELING FOR FABRICATING
A MICROSTRUCTURE WITH A PRE-SPECIFIED
GEOMETRY USING LASER-INDUCED
CHEMICAL VAPOR DEPOSITION**

by

Chaoyang Zhang, M.S.

**A Dissertation Presented in Partial Fulfillment
of the Requirements for the Degree
Doctor of Philosophy**

**COLLEGE OF ENGINEERING AND SCIENCE
LOUISIANA TECH UNIVERSITY**

February 2001

UMI Number: 9994472

UMI[®]

UMI Microform 9994472

Copyright 2001 by Bell & Howell Information and Learning Company.

All rights reserved. This microform edition is protected against
unauthorized copying under Title 17, United States Code.

Bell & Howell Information and Learning Company
300 North Zeeb Road
P.O. Box 1346
Ann Arbor, MI 48106-1346

LOUISIANA TECH UNIVERSITY

THE GRADUATE SCHOOL

January 26, 2001

Date

We hereby recommend that the dissertation prepared under our supervision by Chaoyang Zhang

entitled Mathematical Modeling for Fabricating a Microstructure with a Pre-specified Geometry Using Laser-Induced Chemical Vapor Deposition

be accepted in partial fulfillment of the requirements for the Degree of Doctor of Philosophy in Computational Analysis and Modeling

Wei Zhou Dai

Supervisor of Dissertation Research

Raja Nassar

Head of Department

Department

Recommendation concurred in:

Wei Zhou Dai

Raja Nassar

[Signature] 010129

[Signature]

Advisory Committee

Approved:

[Signature]

Director of Graduate Studies

Approved:

[Signature]

Director of the Graduate School

[Signature]

Dean of the College

APPROVAL FOR SCHOLARLY DISSEMINATION

The author grants to the Prescott Memorial Library of Louisiana Tech University the right to reproduce, by appropriate methods, upon request, any or all portions of this Dissertation. It is understood that "proper request" consists of the agreement, on the part of the requesting party, that said reproduction is for his personal use and that subsequent reproduction will not occur without written approval of the author of this Dissertation. Further, any portions of the Dissertation used in books, papers, and other works must be appropriately referenced to this Dissertation.

Finally, the author of this Dissertation reserves the right to publish freely, in the literature, at any time, any or all portions of this Dissertation.

Author Chaoyang Zhang

Date January 26, 2001

ABSTRACT

Laser-induced chemical vapor deposition (LCVD) is an emerging new technique with many practical applications. To optimize the system for fabricating a microstructure with a pre-specified geometry in pyrolytic LCVD, a three-dimensional mathematical model is developed for predicting temperature distributions and laser dwell times across the substrate scanned by the laser beam. A microstructure is fabricated layer by layer, and for each layer the laser beam moves from one pixel to the next. The complicated correlations among temperature distribution, deposit growth rate, and laser dwell time are investigated. A purely heterogeneous reaction is assumed and any gas-phase transport is ignored.

A finite difference scheme and an iterative numerical algorithm were developed for solving the model. The numerical computation is stable and convergent. The normal growth at each pixel is computed from the geometry of the deposit and the temperature distribution is obtained when the laser beam is focused at different pixels. From the temperature and normal growth, the dwell time for every pixel of each deposit layer is predicted.

The processes for fabricating a convex and a concave microlens with a pre-specified geometry in pyrolytic LCVD with a Gaussian laser beam were simulated. Nickel and graphite were selected as materials for deposit and substrate, respectively. Factors such as intensity of the laser beam and geometry of the microstructure are

discussed. The temperature distributions when the laser beam is focused at different pixels on the surface of deposit were obtained and analyzed for each layer. The dwell time distribution, which determines the laser scanning pattern, is predicted. The process for fabricating a microlens is quite different from that of a rod. The maximum temperature on the surface of the deposit decreases with an increase in the deposit thickness. This result indicates that when the temperature reaches a certain threshold, growth will stop unless the laser intensity is increased.

TABLE OF CONTENTS

ABSTRACT	iv
LIST OF TABLES	viii
LIST OF FIGURES	ix
NOMENCLATURE	xiv
ACKNOWLEDGMENTS	xx
CHAPTER 1 INTRODUCTION	
1.1 General Overview.....	1
1.2 Research Objectives.....	3
1.3 Organization of the Dissertation.....	4
CHAPTER 2 HISTORICAL REVIEW OF LCVD	
2.1 Technical Background.....	6
2.1.1 LCVD Mechanisms.....	6
2.1.2 Deposition Rates.....	9
2.1.3 LCVD Process Parameters.....	11
2.2 Theoretical Solution.....	12
2.3 Numerical Simulation.....	16
2.4 Conclusion	17
CHAPTER 3 A THREE-DIMENSIONAL LCVD MATHEMATICAL MODEL	
3.1 Physical Description.....	19
3.1.1 Laser Beam	21
3.1.2 Natural Convection.....	24
3.1.3 Radiation.....	26
3.1.4 Discussion.....	26
3.2 Governing Equations and Boundary Conditions.....	28
3.2.1 Deposit Temperature.....	29
3.2.2 Substrate.....	30
3.2.3 Growth Rates.....	32
3.3 Mathematical Model for a Parabolic Microstructure	33
3.3.1 Problem Description.....	34
3.3.2 Predicting the Temperature Distribution.....	35
3.3.3 Predicting Dwell Times.....	38

CHAPTER 4 NUMERICAL METHOD	
4.1 Deposit Growth.....	42
4.2 Discretization.....	46
4.3 Solving the Linear System.....	50
4.4 Algorithms.....	52
CHAPTER 5 SIMULATION OF A CONVEX MICROLENS	
5.1 Description of the Simulation.....	55
5.2 Physical Parameters.....	58
5.3 Temperature Distribution.....	60
5.4 Dwell Time vs. Deposit Growth	63
CHAPTER 6 SIMULATION OF A CONCAVE MICROLENS	
6.1 Description of the Simulation.....	110
6.2 Physical Parameters.....	112
6.3 Temperature Distribution.....	113
6.4 Dwell Time vs. Deposit Growth	114
CHAPTER 7 DISCUSSION AND CONCLUSION	141
APPENDIX SOURCE CODE OF THE 3D-LCVD	
MATHEMATICAL MODEL.....	146
REFERENCES	162

LIST OF TABLES

TABLE	DESCRIPTION	PAGE
5.1	Conductivities of nickel and graphite.....	59
5.2	Physical parameters.....	60

LIST OF FIGURES

FIGURE	DESCRIPTION	PAGE
1.1	LCVD schematic.....	2
2.1	Pyrolytic Deposition.....	7
2.2	Deposition rate limit regimes.....	9
2.3	Schematic picture of a two-dimensional model for the description of pyrolytic LCVD.....	16
3.1	Conductive, Radiative and Convective Heat Losses.....	20
3.2	Cartesian coordinate system for the substrate.....	28
3.3	A parabolic microstructure on the surface of the substrate.....	34
3.4	A cross-section of two consecutive layers of a parabolic surface.....	39
3.5	A schematic diagram of a region with subelements.....	40
4.1	Coordinate system for deposit.....	42
4.2	Domain decomposition of substrate and deposit.....	46
5.1	A convex microlens with a parabolic surface.....	55
5.2	Mesh and deposit zone on the surface of the substrate.....	65
5.3	Convex microlens resulting from 5 layers of the deposit.....	66
5.4	Convex microlens resulting from 10 layers of the deposit.....	67
5.5	Convex microlens resulting from 15 layers of the deposit.....	68
5.6	Convex microlens resulting from 20 layers of the deposit.....	69

5.7	Heat flow mechanisms.....	61
5.8	Temperature contour on the surface of the substrate ($P_0 = 0.08W$, Layer = 0, Position = A)	70
5.9	Temperature contour on the vertical cross-section of the substrate ($P_0 = 0.08W$, Layer = 0, Position = A).....	71
5.10	Temperature contour on the surface of the deposit ($P_0 = 0.08W$, Layer = 5, Position = A).....	72
5.11	Temperature contour on the surface of the deposit ($P_0 = 0.08W$, Layer = 10, Position = A).....	73
5.12	Temperature contour on the surface of the deposit ($P_0 = 0.08W$, Layer = 150, Position = A).....	74
5.13	Temperature contour on the surface of the deposit ($P_0 = 0.08W$, Layer = 20, Position = A).....	75
5.14	Temperature contour on the vertical cross-section of the substrate ($P_0 = 0.08W$, Layer = 5, Position = A).....	76
5.15	Temperature contour on the vertical cross-section of the substrate ($P_0 = 0.08W$, Layer = 10, Position = A).....	77
5.16	Temperature contour on the vertical cross-section of the substrate ($P_0 = 0.08W$, Layer = 15, Position = A).....	78
5.17	Temperature contour on the vertical cross-section of the substrate ($P_0 = 0.08W$, Layer = 20, Position = A).....	79
5.18	Maximum temperature vs. layers of deposit on the surface of the microlens ($P_0 = 0.08W$, Position = A, B, C, D, E).....	80
5.19	Temperature contour on the surface of the substrate ($P_0 = 0.08W$, Layer = 0, Position = E).....	81
5.20	Temperature contour on the surface of the deposit ($P_0 = 0.08W$, Layer = 5, Position = E).....	82
5.21	Temperature contour on the surface of the deposit ($P_0 = 0.08W$, Layer = 10, Position = E).....	83
5.22	Temperature contour on the surface of the deposit	

	($P_0 = 0.08W$, Layer = 15, Position = E).....	84
5.23	Temperature contour on the surface of the deposit ($P_0 = 0.08W$, Layer = 20, Position = E).....	85
5.24	Temperature contour on the vertical cross-section of the substrate ($P_0 = 0.08W$, Layer = 0, Position = E).....	86
5.25	Temperature contour on the vertical cross-section of the substrate ($P_0 = 0.08W$, Layer = 5, Position = E).....	87
5.26	Temperature contour on the vertical cross-section of the substrate ($P_0 = 0.08W$, Layer = 10, Position = E).....	88
5.27	Temperature contour on the vertical cross-section of the substrate ($P_0 = 0.08W$, Layer = 15, Position = E).....	89
5.28	Temperature contour on the vertical cross-section of the substrate ($P_0 = 0.08W$, Layer = 20, Position = E).....	90
5.29	Temperature contour on the surface of the substrate ($P_0 = 0.05W$, Layer = 0, Position = A).....	91
5.30	Temperature contour on the surface of the deposit ($P_0 = 0.05W$, Layer = 5, Position = A).....	92
5.31	Temperature contour on the surface of the deposit ($P_0 = 0.05W$, Layer = 10, Position = A).....	93
5.32	Temperature contour on the surface of the deposit ($P_0 = 0.05W$, Layer = 15, Position = A).....	94
5.33	Temperature contour on the surface of the deposit ($P_0 = 0.05W$, Layer = 20, Position = A).....	95
5.34	Temperature contour on the vertical cross-section of the substrate ($P_0 = 0.05W$, Layer = 0, Position = A).....	96
5.35	Temperature contour on the vertical cross-section of the substrate ($P_0 = 0.05W$, Layer = 5, Position = A).....	97
5.36	Temperature contour on the vertical cross-section of the substrate ($P_0 = 0.05W$, Layer = 10, Position = A).....	98
5.37	Temperature contour on the vertical cross-section of the substrate	

	($P_0 = 0.05W$, Layer = 15, Position = A)	99
5.38	Temperature contour on the vertical cross-section of the substrate ($P_0 = 0.05W$, Layer = 20, Position = A).....	100
5.39	Highest temperature vs. layers of deposit on the surface of the microlens ($P_0 = 0.05W$, Position = A, B, C, D, E)	101
5.40	Sum of dwell times at each pixel for all layers 1-20 ($P_0 = 0.08W$).....	102
5.41	Sum of dwell times at each pixel for layers 6-10 ($P_0 = 0.08W$).....	103
5.42	Sum of dwell times at each pixel for layers 11-16 ($P_0 = 0.08W$).....	104
5.43	Sum of dwell times at each pixel for layers 16-20 ($P_0 = 0.08W$).....	105
5.44	Sum of dwell times at each pixel for all layers 1-20 ($P_0 = 0.05W$).....	106
5.45	Sum of dwell times at each pixel for layers 6-10 ($P_0 = 0.05W$).....	107
5.46	Sum of dwell times at each pixel for layers 11-15 ($P_0 = 0.05W$).....	108
5.47	Sum of dwell times at each pixel for layers 16-20 ($P_0 = 0.05W$).....	109
6.1	A concave microlens with a parabolic surface.....	111
6.2	Mesh and deposit zone on the surface of the substrate.....	117
6.3	Concave microlens resulting from 20 layers of deposit.....	118
6.4	Temperature contour on the surface of the substrate ($P_0 = 0.08W$, Layer = 0, Position = A).....	119
6.5	Temperature contour on the surface of the deposit ($P_0 = 0.08W$, Layer = 5, Position = A).....	120
6.6	Temperature contour on the surface of the deposit ($P_0 = 0.08W$, Layer = 10, Position = A).....	121
6.7	Temperature contour on the surface of the deposit ($P_0 = 0.08W$, Layer = 15, Position = A).....	122
6.8	Temperature contour on the surface of the deposit ($P_0 = 0.08W$, Layer = 20, Position = A).....	123

6.9	Temperature contour on the vertical cross-section of the substrate ($P_0 = 0.08W$, Layer = 0, Position = A).....	124
6.10	Temperature contour on the vertical cross-section of the substrate ($P_0 = 0.08W$, Layer = 5, Position = A).....	125
6.11	Temperature contour on the vertical cross-section of the substrate ($P_0 = 0.08W$, Layer = 10, Position = A).....	126
6.12	Temperature contour on the vertical cross-section of the substrate ($P_0 = 0.08W$, Layer = 15, Position = A).....	127
6.13	Temperature contour on the vertical cross-section of the substrate ($P_0 = 0.08W$, Layer = 20, Position = A).....	128
6.14	Highest temperature vs. layers of deposit on the surface of the concave microlens ($P_0 = 0.08W$, Position = A, B, C, D, E).....	129
6.15	Sum of dwell times at each pixel for all layers 1-20 ($P_0 = 0.08W$).....	130
6.16	Sum of dwell times at each pixel for layers 16-20 ($P_0 = 0.08W$).....	131
6.17	Sum of dwell times at each pixel for layers 11-15 ($P_0 = 0.08W$).....	132
6.18	Contour of the sum of dwell times for all layers 1-20 ($P_0 = 0.08W$).....	133
6.19	Contour of the sum of dwell times for layers 5-10 ($P_0 = 0.08W$).....	134
6.20	Contour of the sum of dwell times for layers 11-15 ($P_0 = 0.08W$).....	135
6.21	Contour of the sum of dwell times for layers 16-20 ($P_0 = 0.08W$).....	136
6.22	Contour of the sum of dwell times for all layers 1-20 ($P_0 = 0.05W$).....	137
6.23	Contour of the sum of dwell times for layers 5-10 ($P_0 = 0.05W$).....	138
6.24	Contour of the sum of dwell times for layers 11-15 ($P_0 = 0.05W$).....	139
6.25	Contour of the sum of dwell times for layers 16-20 ($P_0 = 0.05W$).....	140

NOMENCLATURE

English Symbols

a	coefficient of a polynomial
A	absorptivity, or coefficient matrix of a linear system
A_s	surface area
b	coefficient of a polynomial
\bar{b}	right hand side vector of a linear system
c	speed of light, or coefficient of a polynomial
c_D	heat capacity of deposit
c_S	heat capacity of substrate
d	diameter of a hemisphere, or coefficient of a polynomial
D	gas diffusivity
e	coefficient of a polynomial
E_a	activation energy
f	coefficient of a polynomial
G_r	Grashoff number
h	maximum height corresponding to a deposit layer
$h_0(x,y)$	function of a deposit layer
$h_i(x,y)$	function of the i th deposit layer
h_1, h_2	heights of deposit layer or heat transfer coefficients

h_3, h_4, h_5, h_6	heat transfer coefficients
h_{conv}	convective heat transfer coefficient
H	maximum height of a convex microlens
H_1	maximum height of a concave microlens
H_2	minimum height of a concave microlens
H_S	height of substrate
I_0	laser power density
J_{loss}	energy loss to the gas phase
K_0	growth rate constant
k_d	thermal conductivity of deposit material
$k_D(T^D)$	temperature-dependent conductivity of deposit
k_{gas}	thermal conductivity of gas species
$k_S(T^S)$	temperature-dependent conductivity of substrate
$k_{S,\parallel}$	in-plane (i.e. parallel) thermal conductivity of substrate material
$k_{S,\perp}$	z-axis (i.e. perpendicular) thermal conductivity of substrate material
k^*	ratio of the conductivities of deposit and substrate
L	length (or diameter) of deposit
L_S	length of substrate
M	carrier gas or number of elements in the x-direction
M_0	total number of elements within the reaction zone in the x-y plane
n	precursor concentration
$\hat{n}(x)$	unit normal vector
n_i	index of reflection

N	number of elements in the y-direction
N_u	Nusselt number
N_1, N_2, N_3	the number of elements in the x, y, z direction, respectively
p	precursor partial pressure
P_0	average laser power
P_r	Prandtl number
Q_{cond}	heat loss rate due to conduction [J/s]
Q_{conv}	heat loss rate due to convection [J/s]
Q_{in}	heat input rate from light absorption [J/s]
Q_{rad}	heat loss rate due to radiation [J/s]
Q''_{in}	heat flux due to the distributed heat source [J/m ² s]
Q''_{loss}	heat flux due to the distributed heat sink [J/m ² s]
Q'''_{in}	distributed heat source [J/m ³ s]
Q'''_{loss}	distributed heat sink [J/m ³ s]
r	radius
r_d	radius of a hemisphere
r_s	steady state radius
r_w	reaction zone radius
R	universal gas constant
R_n	normal deposition rate
R_0	axial deposition rate
R_v	volumetric deposition rate
t	time

T	temperature
T_s	surface temperature
T^D	temperature of deposit
T^S	temperature of substrate
T_{th}	threshold temperature
T_∞	ambient temperature
U	wave function
W_s	width of substrate
x	axial coordinate from rod base to rod tip or planar coordinate
x_0	x coordinate of a selected point
x_i	coordinate at the i th element
\bar{x}	unknown vector in a linear system
y	planar coordinate
y_0	y coordinate of a selected point
y_i	coordinate at the i th element
z	paraxial position along beam focus, depth, coordinate
z_0	Reyleigh range of focused beam or z coordinate of a selected point

Greek and Other Symbols

Υ	deposit volume per unit surface area
$\Gamma(z)$	wavefront radius of curvature
δT_{th}	width of threshold temperature
$\Delta \bar{Z}(x, y)$	local normal deposit growth

Δ_i	the i th subelement
Δt	time interval
$\Delta t_{i,j}$	deposition dwell time at element (i,j)
ε_s	surface emissivity
$\varepsilon_1, \varepsilon_2$	given tolerances
θ	convergence angle
Θ	Temperature excess
λ	wavelength of light
Λ	angular spectral absorbance
ρ	a parameter for length
ρ_D	density of deposit
ρ_S	density of substrate
σ	Stephan-Boltzman constant
σ_1	standard deviation of the intensity distribution of the laser beam
ϕ	incident angle from the surface normal vector
ω	beam waist radius or over-relaxation factor
ω_0	beam waist radius at focus
\mathfrak{R}	angular spectral reflectance
∇^2	Laplace operator
∇_3^2	three dimensional Laplace operator
∇	del operator
φ	a parameter

Superscript

- * non-dimensional variable
- n, k iteration step
- D deposit material
- S substrate material

Subscript

- ∞ ambient condition, or infinity norm
- i index of grid in the x-direction
- j index of grid in the y-direction
- k index of grid in the z-direction

ACKNOWLEDGMENTS

I would like to express my gratitude and sincere appreciation to my advisor Dr. Weizhong Dai and co-advisor Dr. Raja Nassar for their continuous guidance and excellent advice. Their numerous office hours, patience, and effort make this dissertation a reality. Many thanks go to Dr. Mats Boman and Dr. James Maxwell for their useful suggestions in developing the mathematical model, and to Dr. Ben Choi for his advice in computer science and service on my advisory committee. Also thanks to Dr. Piglmayer Klaus of JKUL, Austria, for his useful information and technical input.

I would also like to thank Dr. Richard Greechie for his kindness and financial support which provided me the opportunity to study at Louisiana Tech University.

Finally, I would like to thank my family and friends who support me throughout this massive undertaking. I dedicate this dissertation especially to my supportive wife, Hong Lan, for her persistent support and encouragement, and also to my lovely son, Benny.

CHAPTER 1

INTRODUCTION

1.1 General Overview

Microtechnology is a critical technology with an enormous potential for new products and product enhancement. Current micromanufacturing techniques have some drawbacks in that the microstructures produced are planar, somewhat fragile, and not suitable for building robust three-dimensional structures. For further development of the technology, it is necessary to develop new processes suitable for the manufacture of high aspect ratio microstructures that improve the rigidity of microparts and allow coupling to them, thus enabling the manufacture of complex mechanisms.

Laser-induced chemical vapor deposition (LCVD) is an important technique in freeform fabrication of high aspect ratio microstructures. The LCVD process is rapid, flexible, and relatively inexpensive to operate. To develop a working micro-scale freeform fabrication process, a laser beam is used as a physically measurable energy source to induce precipitation of a solid material from a surrounding medium.

The application of LCVD in micro-patterning requires proper selection of precursor molecules. Precursors for freeform fabrication must be chemicals which can be modified, dissociated, or decomposed in such a way that at least some portion of the precursor molecule solidifies, precipitates, or adsorbs onto an evolving part surface when the induction factor is applied, thereby forming the part. The decomposition of precursor

molecules in LCVD can be activated thermally or non-thermally or by a combination of both. The type of process activation can be verified from the morphology of the deposit and from measurements of the deposition rate as a function of laser power, wavelength, substrate materials, etc. While much progress has been made in recent years to fabricate microstructures, there remain fundamental constraints in the manufacture of microelectromechanical system (MEMS) via conventional means. Current processes are limited both in the part shapes that can be manufactured, as well as in the materials that can be exploited.

An LCVD experimental system usually consists of a laser, vacuum chamber, and movable stage, as shown in Figure 1.1.

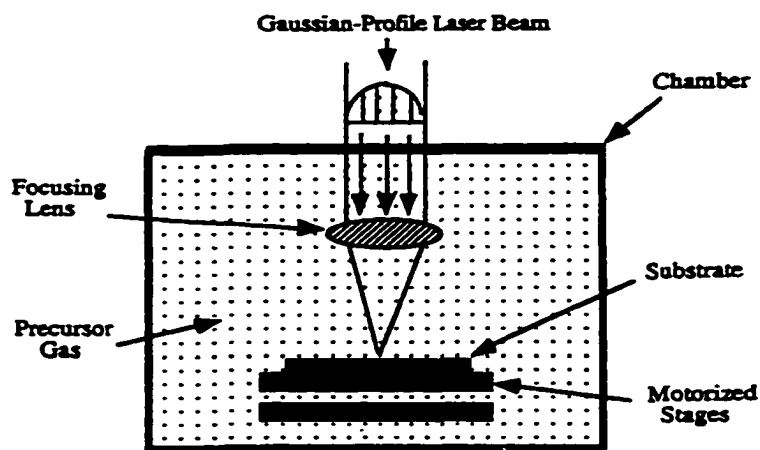


Figure 1.1 LCVD schematic

The laser beam is focused onto a substrate target. The reactive gas is introduced into the chamber, and it reacts at (or near) the focal spot on the substrate, leaving behind any solid-phase reaction products. Precursors are chosen so that the by-products of the reaction are volatile and return to the surrounding gas mixture. If the focal spot is scanned

across the substrates, a trace of material is left behind, in a manner similar to other rapid prototyping system, and microstructures with different specific shapes can be manufactured.

For some simple cases, analytic solutions can be obtained under some assumptions [Brugger 1972] [El-Adawi 1986][Bäuerle 1990]. However, it is impossible to develop a general three-dimensional mathematical model to completely describe the correlation between temperature and deposit growth and derive its exact solution. Usually, for each specific physical problem one should develop a simplified mathematical model and solve it using a numerical method. Several studies in the literature are related to numerical simulations related to deposit spot, direct writing of a line, and rod growth [Arnold 1993] [Maxwell 1996] [Dai 1999], in which case the laser beam is focused on one fixed point or is moving in one direction. However, for one to produce a microstructure conforming to a desired geometry with high resolution, the laser beam must scan all the pixels on the surface of deposit or substrate according to a specified pattern. To achieve a process with a high resolution, accurate predictive models must be developed for process control and optimization.

1.2 Research Objectives

The goal of this dissertation is to develop a mathematical model to simulate the transport and thermal phenomena which underlie the LCVD process, so that the deposition dwell time for given process conditions and material properties can be predicted in order to fabricate a microstructure with a specified geometry.

In fact, three-dimensional LCVD (3D-LCVD) is a very complex process. The temperature at each point on a deposit surface determines the growth rate. This growth, in turn, changes both the shape of the deposit and the concentration of the precursor gases adjacent to the reaction zone. The surface temperature distribution is then cyclically affected by the shape of the deposit.

The 3D-LCVD mathematical model in this dissertation will describe the heat transport in both deposit and substrate, as well as the heat exchange on their interface. The model should establish a relationship among heat transfer, growth rate and dwell time.

To solve the coupling equations numerically in the developed 3D-LCVD mathematical model, an effective numerical method is introduced for iterative calculation. The computation should be stable and convergent.

After the 3D-LCVD mathematical model and the corresponding numerical method have been developed, several examples are selected to verify the capability of the model. Finally, we use this model to predict the temperature distribution and dwell time for fabricating convex and concave microlenses, with nickel as the deposit and graphite as the substrate.

1.3 Organization of the Dissertation

This dissertation is about mathematical modeling of 3D-LCVD. Before developing a mathematical model, one should not only know the various physical phenomena but also understand the physical principles and mechanisms underlying these phenomena. No mathematical model can completely describe all these physical

phenomena, so some assumptions should be made to simplify the model. A refined model for simulating certain kind of problems can be developed by ignoring the negligible factors. A model may correspond to a numerical method. This numerical method should be stable and convergent to the unique solution. After the model and the relevant numerical method have been developed and verified, they are applied to the simulation of numerical examples or specific physical problems. This dissertation follows the above general concept of mathematical modeling, and it is structured as follow bellow.

Chapter 2 provides the necessary technical background for the remainder of the document. A historical review of LCVD modeling is given. Chapter 3 presents details of the three-dimensional LCVD mathematical model for simulating the process of fabricating a microstructure with a pre-specified geometry. In chapter 4, the numerical methods--including the numerical scheme, iteration algorithm, and various computational details--are discussed. In chapters 5 and 6, we apply the mathematical model and corresponding numerical method to simulate the process for fabricating a convex microlens and a concave microlens. The computational results are described. In chapter 7, the discussion and conclusion are provided.

CHAPTER 2

HISTORICAL REVIEW OF LCVD

2.1 Technical Background

2.1.1 LCVD Mechanisms

LCVD is carried out through two possible mechanisms: photolytic or pyrolytic dissociation of the precursor, or a combination of both processes.

Photolytic LCVD Photolytic LCVD is based on selective excitations of precursor molecules. Both single and multi-phase excitations may be required to drive photolytic dissociation reactions, depending on the precursor employed. Photolytic LCVD occurs when the precursor compounds are dissociated directly by light, the incident phase breaking the molecules bonds of the compound through their absorption. The product species diffuse and condense, in part, on the substrate surface.

Photolysis of a precursor gas is generally done in either a parallel or direct-write orientations of the beam relative to the substrate. In parallel configuration, the beam is parallel to the substrate. The parallel configuration is employed to grow blanket deposit across a wafer, and is often denoted photo-assisted CVD. In direct-write photolysis, the beam is incident to the substrate. Direct-write photolysis is essentially the same as photo-assisted CVD, and the deposition occurs only near the focus of the beam where dissociated radicals diffuse to the deposit surface from the gas-phase and/or adsorbed precursor molecules are dissociated on the substrate surface [Maxwell 1996]. Photolytic

normal deposit rates of organometallic compounds usually are several orders of magnitude smaller than pyrolytic deposition rates. Photolytic LCVD can therefore be employed for thin-film formation at relatively low temperature. Although the comparatively small volumetric deposition rates do not justify its use for MEMS manufacture, direct-write photolysis qualifies as a freeform fabrication process.

Pyrolytic LCVD Pyrolytic LCVD operates through adsorption of a precursor onto a substrate surface and subsequent thermal dissociation of the compound through heating of the substrate (or deposit) surface. In such experiments, the substrate is immersed in a reactive gaseous ambient and is perpendicularly irradiated by a focused laser beam. The setup typically employed is shown in Figure 1.1. In this case, the substrate is chosen to be absorptive of the light, and the precursor is chosen to be transparent to the incident radiation. The mechanism of pyrolytic LCVD is represented in Figure 2.1, where an impinging laser reaction zone of radius, w_0 , is focused at the substrate, and a heated reaction zone of radius, r_w , is generated.

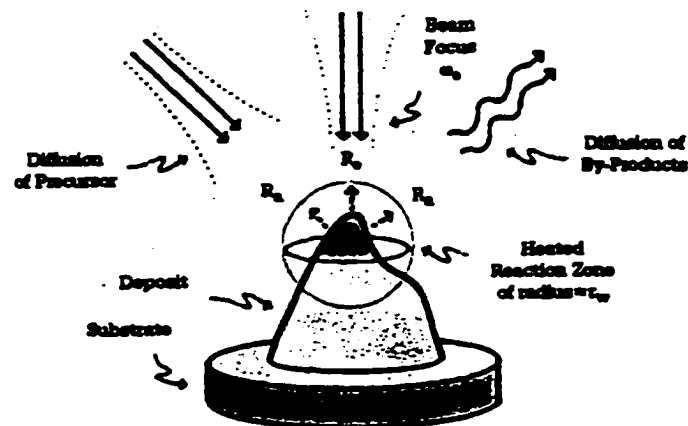


Figure 2.1 Pyrolytic Deposition

The pyrolytic reaction occurs at the surface only within this reaction zone, and the surface temperature outside of this region is assumed to be below the threshold temperature T_{th} for deposition. The local deposition rate at each surface point is determined by the temperature at the surface, the activation energy and the ability of the precursor reactants, and by-products to transport to and from the surface. When a reactive gas reacts at the reaction zone, it leaves behind any solid-phase reaction product, which leads to the growth of deposit. At the same time, precursor by-products desorb from the growth surface and diffuse into the ambient.

We now analyze the kinetics of precursor reaction in the reaction zone. Consider, for example, the common reaction of the deposition of silicon from silane



Here, as each SiH_4 molecule decomposes, two molecules of H_2 are produced. H_2 Diffuses away from the reaction zone, i.e. in the opposite direction of SiH_4 . This counter-diffusion of reaction products influences the transport properties within the ambient medium, and thereby the overall reaction rate within the reaction zone.

In most case, precursors used in LCVD are of the form, $P = AB_\mu$. Hereafter, we consider a reaction of the type



where AB_μ is the reactant, M is a carrier gas and A is a metal or element to be deposited, and B_μ are μ ligands which are loosely bound to A . The reaction of gas-phase molecules AB_μ shall be heterogeneous, i.e. it shall occur exclusively on the surface r_s . Here, the species A condense on the surface r_s and either forms the deposit or it reacts further, while atoms/molecules B immediately desorb from this surface.

For more details about the reaction kinetics in laser-induced pyrolytic chemical processing, see the reference [Bäuerle 1986] [Bäuerle 1990].

2.1.2 Deposition Rates

A pyrolytic process may be influenced by several factors and the actual deposition rate is determined by several constraints for a given set of process parameters. While the deposition rate of a heterogeneous reaction is driven by surface temperature, the rate obtained depends on the reaction activation energy and the ability of the precursor reactants and by-product to transport to and from the surface.

When the reaction rate is limited by the activation energy and temperature the process is termed kinetically limited. Similarly, when the precursor and by-product diffusion control the rate, the reaction is termed mass transport limited. For exothermic reaction at high temperatures, it is the thermodynamically-limited case. The three deposition rate limit regimes are shown in Figure 2.2.

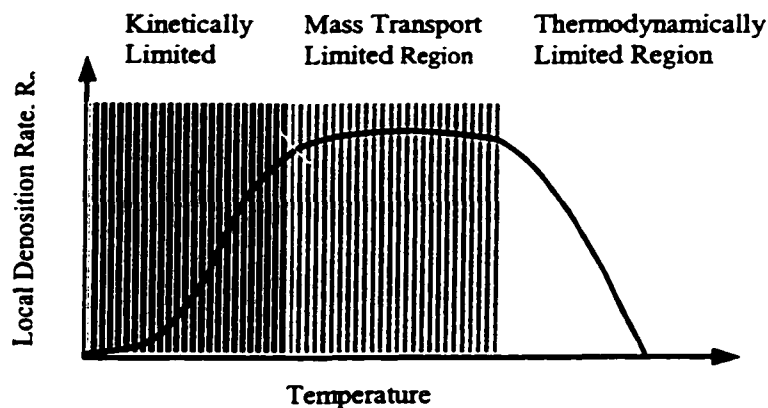


Figure 2.2 Deposition rate limit regimes

Kinetically Limited Rates From Figure 2.2, the local rate, R_n , rises exponentially at first, according to the Arrhenius relation given below [Bäuerle 1990],

$$R_n = K_0(p, T)e^{-E_a/(RT)} \quad (2.3)$$

where K_0 is a concentration-dependent growth rate constant, p is the pressure, and E_a and R are the activation energy and the universal gas constant, respectively.

The local deposit rate, R_n , is strictly defined as the magnitude of the rate at any given point on the growth surface, and R_n is known as the normal deposit rate, where the vector \bar{R}_n lies along the normal to the surface. Usually, there are two kinds of deposition rate measures: the volumetric deposition rate, R_v , and the axial deposition rate, R_0 . R_v takes into account the overall three-dimensional volumetric growth of the deposit and R_0 is only a measure of the maximum growth rate at the center of the laser beam.

Diffusion Limited Rates When the temperature increases, the process passes into the diffusion-limited regime, and with the increasing temperature, the reaction proceeds rapidly enough and the relative conversion of reactants becomes large. The ability of the precursor to arrive at the surface of the reaction zone is insufficient to support the continued exponential increase with temperature, and hence the deposit rate levels off [Maxwell 1996].

In the mass transportation regime, the deposition rate does not depend on Equation (2.3), but on the precursor concentration, n , which is given by the diffusion equation:

$$D\nabla^2 n - \frac{\partial n}{\partial t} = 0 \quad (2.4)$$

where D is the diffusivity.

With the complex geometry of the deposit, the solution of the partial differential equation can be solved numerically.

Thermodynamically-Limited Rates For exothermic reaction at high temperatures, the free energy becomes less negative with temperature, thereby slowing the deposition rate. There is little advantage to increasing the temperature into this regime for exothermic reaction, as the rate has already peaked.

A process can be thermodynamically limited for several reasons. Often it is caused by an increase in the apparent activation energy due to the greater desorption of the precursor (or its intermediates) with temperature; i.e., the precursor desorbs before it can react. In this case the reaction rate can be modeled by the Langmuir-Hinshelwood equation:

$$R_n = \left(K_0 p^2 e^{-\frac{\Delta H_a}{RT}} \right) / \left(K_{des} e^{-\frac{\Delta H_{des}}{RT}} + p \right) \quad (2.5)$$

Here, K_{des} and ΔH_{des} are the rate constant and the enthalpies of the deposition, respectively. If the pressure is very high, or the temperature moderate, the Langmuir-Hinshelwood rate reduces to an Arrhenius Reaction as presented in Equation (2.3).

2.1.3 LCVD Process Parameters

LCVD deposition rate is a function of many variables, such as laser fluence, vapor pressure, local temperature, and thermal conductivity of the substrate and deposit. The LCVD process is determined by thermal physics and continuum mechanics. In the kinetically limited regime, the local deposition rate rises exponentially according to the Arrhenius law. The heat transfer in the deposit and substrate depends on the laser beam

conditions, surface properties, and fluid conditions. Beam conditions include laser power, laser intensity profile, wavelength, spot/line geometry. Surface properties include optical absorption, reflectivity and emissivity, refraction index, material thermal conductivity, surface geometry and roughness. Fluid conditions include Nusselt Number, Reynolds Number, Grashoff Number, Prantle Number and thermal conductivity of the fluid. These fluid parameters determine the thermal physics and continuum mechanics of the gas phase in the reaction zone.

More details about these parameters will be given in the next chapter.

2.2 Theoretical Solution

A brief description of the microscopic mechanisms involved in LCVD and the reaction rate has been given in the previous section. In this section, an overview of the theoretical solutions for pyrolytic LCVD will be given. LCVD is not only a physical process but also a chemical process that contains heat transfer, mass transfer, and chemical reaction. We first introduce some theoretical results on the kinetics of the laser chemical process and then introduce some analytic solutions of the temperature profile on the substrate and deposit as well as of the growth rate of the deposit.

While the relation among the laser-induced temperature, reaction rate, and geometry of the deposit is quite complex, we can simplify this problem with some assumptions. For example, we consider laser direct writing of a stripe onto a semi-infinite substrate and quasi-stationary conditions with the coordinate system fixed with the laser beam. Thus, in this system, the geometry of the stripe remains unchanged. A one-dimensional approach can obtain the analytic solution for this problem, and self-

consistent model calculations on pyrolytic laser direct writing are presented [Arnold 1993]. In this approach, however, any gas-phase transport is ignored and a purely heterogeneous reaction is assumed. A case is considered where the ratio of thermal conductivity of deposit and substrate are much large than 1. This approach applies to laser direct writing of thermally well-conducting strips onto insulating substrates. The geometry of the deposit is determined from a self-consistent calculation. The equation is solved simultaneously with the laser-induced temperature distribution which in turn is approximated by an analytic equation. Results of these calculations are compared with experimental data on the direct writing of W lines.

For the axisymmetric rod, the 3D LCVD problem can be reduced to a 2D problem. To solve for the shape of any axisymmetric deposit, the temperature profile along the deposit length must be known. Several simplifications can be made. First, time-dependence of the heat flow can be neglected so that the heat flux into and out of the deposit is assumed to be in equilibrium and a steady temperature distribution exists over the deposit. A second simplification can be made by assuming that conductivities of deposit and substrate are constant. Under these assumptions, the diffusion equation may be expressed as follows [Maxwell 1996]:

$$k_d \nabla^2 \Theta + Q_{in}^-(x, r, t) - Q_{loss}^-(x, r, t) = 0 \quad (2.6)$$

where Q_{in}^- and Q_{loss}^- are distributed heat sources and sinks at or within the deposit boundaries, such as absorption of the laser light, or convective/radiative losses at the deposit surface.

In the instance of an axisymmetric deposit of arbitrary profile, $r(x)$, where the length of the deposit is typically much greater than its width, one can assume that the

temperature gradient is largely one-dimensional along the axial x-coordinate. For a Gaussian beam absorbed completely at a rod tip, and simultaneous convection and radiation from the rod surface, the temperature may be derived numerically from:

$$\frac{d^2\Theta}{dx^2} + \frac{2}{r(x)} \frac{dr(x)}{dx} \frac{d\Theta}{dx} = \left(\frac{2}{k_d r(x)}\right) Q_{loss}^-(x, r, t) - \left(\frac{2}{k_d r(x)}\right) Q_{in}^-(x, r, t) \quad (2.7)$$

where Q_{in}^- and Q_{loss}^- are the heat fluxes, $Q^- = Q^- / \gamma$.

If one ignores the spatial distribution and time variance of the laser input at the tip of a rod, and neglects radiation as a source of heat loss, the temperature along the length of the deposit, $T(x, t)$ can be solved analytically.

Based on the temperature approximation in Equation (2.7), a simple rod growth simulation can be obtained which qualitatively describes the form of the rods deposited from various precursor chemistries [Maxwell 1996]. Beginning with a set of seed points which describe the initial deposit surface, the model calculates the unit normal to a curve passing through all points in the set, and then each point is successively translated according to the Arrhenius relation given in Equation (2.3). A simulation of graphite rod growth is presented, showing different stages in the evolution of a rod. This result is compared with experimental results from ethylene pyrolysis. In all cases, the simulation closely approximates the actual growth profiles, with the exception that the actual rods are somewhat broader and flattened near the tip. These deviations from the predicted kinetic shape may be explained by the mass transport limitation at the rod tip.

A mathematical model for heat transfer in the substrate during LCVD is presented, in which the three-dimensional and transient heat conduction equation is solved for a slab having finite dimension and moving at a constant velocity [Kar 1988].

The temperature-dependent thermophysical properties of the material of the slabs are considered, and both convective and radiative losses of energy from the slab to the surrounding medium are taken into account. The laser beam is considered to be Gaussian in shape. The three-dimensional nonlinear governing equation is linearized by using the Kirchoff's transformation and then solved by successively applying the Fourier-transformation in the x , y , and z directions. Based on these considerations and techniques, an analytic expression for the three-dimensional and transient temperature field is obtained. Thermal analysis can provide information on the variation of film width with laser power and scanning speed, and the upper and lower limits of the operating scanning speed for LCVD processes. For a given laser power, the peak temperature varies linearly with the operating scanning speed of the laser beam on the log-log scale. Also, the peak temperature varies linearly with the laser power on the linear scale for a given scanning speed of the laser beam. Unfortunately, in some case the deposit growth may greatly influence the temperature distribution of the substrate. This paper studied only the three-dimensional transient heat transfer in the substrate and did not include the deposit.

Generally, analytic solution can be obtained only for some simple physical problems with simple boundary conditions [Brugger 1972] [El-Adawi 1986] [Bäuerle 1990]. For a more complicated problem, numerical methods are needed for obtaining its solution.

2.3 Numerical Simulation

Now we consider a spot of deposit as seen in Figure 2.3. The deposit is placed on a semi-infinite substrate. The origin of the coordinate system is fixed with the laser beam and is indicated by the dot.

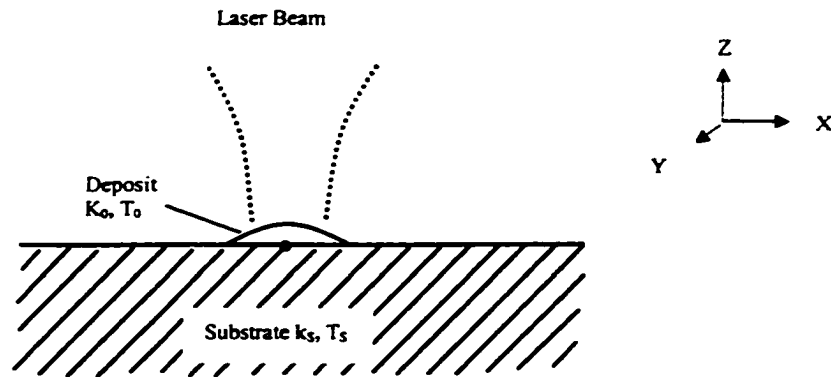


Figure 2.3 Schematic picture of a two-dimensional model for the description of pyrolytic LCVD

In the model [Arnold 1993], the heat equation and corresponding boundary conditions that describe the heat transfer and temperature distribution are given. The equation of heat transfer for the deposit is integrated along the z direction, which reduces the original 3-D problem to a 2-D problem. Some further simplifying assumptions are made for the above physical problem: (1) growth shall be quasi-stationary; (2) heat losses to the gas phase shall be ignored; and (3) the laser light is totally absorbed within the deposit. With these assumptions, the boundary-value problem of heat transfer, together with the corresponding equations for the substrate, and the equation of growth can directly be solved numerically. The heat transfer in the substrate is given by the Laplace equation from which the temperature distribution of the substrate can be calculated using

Green's function. The temperature of the deposit and substrate are related at their interface. After the temperature of the substrate has been obtained, the real temperature of the deposit can be obtained from the inverse of the Kirchhoff's transformation. The numerical computation was performed by employing an iteration procedure.

The above model calculations can be applied to the deposition of spots and to the direct writing of lines by pyrolytic LCVD. The contour lines and isotherms were obtained for various stages of direct writing of W lines deposited from WCl_6+H_2 . The shapes of deposits calculated for different systems are in semi-quantitative agreement with those observed experimentally. Note that in this case, the deposit should be flat and with a stationary shape.

Maxwell presented a mathematical model based on a stationary laser focal spot to predict the transport and thermal phenomena that underlie the three-dimensional LCVD process [Maxwell 1996]. Based on his study, a numerical model for simulating an axisymmetric rod growth was presented and good results were obtained [Dai 1999].

2.4 Conclusion

The availability of high-power lasers and the economical advantage of using lasers as a tool for material processing have led to many interesting applications of laser technology. The process of heat transfer in the substrate and deposit plays an important role in laser processing of materials and in microfabrication. In the literature, much work has been done to simulate such manufacturing processes. These mathematical models allow us to examine the effect of various parameters on the performance of these processes. These studies consider either constant thermophysical properties for the

substrate material or a finite or semi-infinite geometry, and thus they can be applied only to relatively simple and specific manufacturing cases because of various assumptions and approximations.

With the rapid progress in the application of LCVD in microfabrication, it is necessary to develop a model that can predict the laser beam dwell time across the substrate in order to obtain solid deposit with pre-specified geometry. The process of LCVD is very complex, and no mathematical model can completely simulate all its physical and chemical properties. However, mathematical modeling may provide some useful information for experimental control and application by simulating the LCVD processes and predicting the influence of various parameters and different conditions on its performance.

Some research work has been done in mathematical modeling of LCVD, in which the process cannot be controlled to produce deposits of a desired shape. However, in applications of LCVD, one may want to fabricate a microstructure with pre-specified geometry. To obtain such a deposit with a pre-specified shape, we should know the laser power, laser beam distribution, and laser dwell time, or scanning speed in order to control the process. We may use mathematical modeling to predict the values of these physical parameters necessary for depositing such a solid with a pre-specified geometry. To my knowledge, little research work has been done to simulate such a problem. Based on these considerations, a mathematical model and a corresponding numerical method will be presented to predict the laser beam dwell time across the substrate for growing a desired three-dimensional microstructure.

CHAPTER 3

A THREE-DIMENSIONAL LCVD MATHEMATICAL MODEL

In this chapter, the kinetics of three-dimensional laser-induced chemical vapor deposition (3D-LCVD) will be explored, and a mathematical model will be presented which describes the heat transfer in the deposit and substrate, and predicts the growth of deposit and the dwell times for fabricating a deposit with a pre-specified geometry. As pyrolytic 3D-LCVD is a thermally-driven process, we do not consider the kinetics in the gas phase and the mass transfer limitation, but emphasize the analysis of the kinetically limited growth rates in this study. In an LCVD process a strong correlation exists between the geometry of the deposit and the laser-induced temperature distribution. The temperature field has to be obtained to determine the chemical reaction zone and the growth rate on the surface of the substrate.

3.1 Physical Description

One of the basic quantities in laser processing is the temperature rise induced by the absorbed laser radiation on a material surface or within its bulk. The knowledge of the temperature distribution is a prerequisite for both fundamental investigations and technique application. When the laser beam (usually of Gaussian profile) is focused in a chamber onto a substrate target, the balance of heat flow into and out of a deposit

determines the surface temperature and hence the growth rate. The laser power absorbed at the deposit surface drives the reaction, whereas heat losses such as radiation, convection, and conduction to the substrate, determine how the surface temperature will change over time. The three primary mechanisms that contribute to heat loss in 3D-LCVD are shown schematically in Figure 3.1.

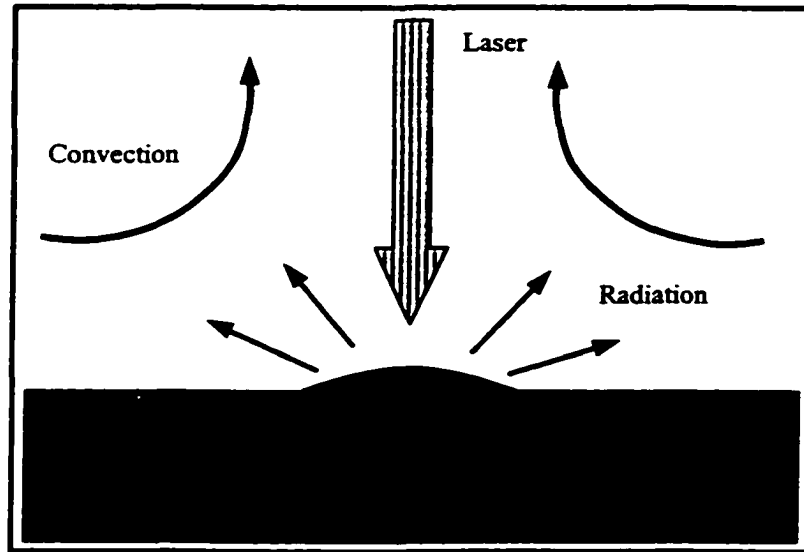


Figure 3.1 Conductive, Radiative and Convective Heat Losses

The balance of the heat flow through the deposit boundaries can be described by the simple continuity expression:

$$Q_{in} = Q_{cond} - Q_{conv} - Q_{rad} \quad (3.1)$$

where Q_{in} represents the heat transfer rate from the absorbed laser fluence, Q_{conv} the heat loss rate due to convection, Q_{rad} the loss rate from radiation, and Q_{cond} the heat conduction rate. These four terms will be discussed in turn.

3.1.1 Laser Beam

The power delivered to the surface determines the local surface temperature, and hence the growth rate and deposit shape. If U is a wave function and c the speed of light, then the wave equation for the propagation of the electromagnetic waves is as follows:

$$\frac{\partial^2 U}{\partial t^2} = c^2 \nabla^2 U \quad (3.2)$$

Substituting the time-varying solution, $U(r, t) = U(r) \cdot e^{i\omega t}$, one can obtain the Helmholtz equation for the propagation of paraxial waves:

$$\nabla^2 U(r)_{x,y} - 2i \frac{\omega^2}{c^2} \frac{\partial}{\partial z} U(r) = 0 \quad (3.3)$$

Among the most important beam shapes employed in laser processing is the Gaussian beam. Equation (3.3) has several solutions, however, in most cases, the solution for the laser beam has the following Gaussian form:

$$U(r) = U_0 \frac{\omega_0}{\omega(z)} \left[e^{-\frac{r^2}{\omega^2(z)}} \right] \left[e^{-\frac{i\omega^2(z)}{2c^2\Gamma(z)}} \right] e^{-i\frac{\omega^2(z)z}{c^2}} e^{i\arctan\left(\frac{z}{z_0}\right)} \quad (3.4)$$

where $\omega(z)$ is the $1/e^2$ beam waist radius at any axial position z , ω_0 is the $1/e^2$ spot radius at the focus, z_0 is the Reyleigh range, and $\Gamma(z)$ is the wavefront radius of the curvature, defined by [Maxwell 1996]:

$$\omega_0 \approx \frac{\lambda}{\pi\theta} \quad (3.5)$$

$$z_0 = \frac{\pi\omega_0^2}{\lambda} \quad (3.6)$$

$$\omega(z) = \omega_0 \left[1 + \left(\frac{z}{z_0} \right)^2 \right] \quad (3.7)$$

and

$$\Gamma(z) = z \left[1 + \left(\frac{z}{z_0} \right)^2 \right] \quad (3.8)$$

In Equation (3.5), θ is the convergence angle of the focused beam, and λ is the laser wavelength. Taking the time average of the $U(r)$, i.e. $|U(r)|^2$, one arrives at the spatially-dependent intensity of a laser beam, defined as

$$I(r, z) = I_0 \left[\frac{\omega_0}{\omega(z)} \right]^2 \left[e^{-\frac{2r^2}{\omega^2(z)}} \right] \quad (3.9)$$

where $I_0 = |U_0|^2$. Defining the peak beam intensity (i.e., the power density), I_0 , in terms of the average laser power, P_0 , the peak intensity becomes

$$I_0 = \frac{2P_0}{\pi\omega_0^2} \quad (3.10)$$

The spatially-dependent intensity at the focal plane may be written as

$$I(r, 0) = \frac{2P_0}{\pi\omega_0^2} \left[e^{-\frac{2r^2}{\omega_0^2}} \right] \quad (3.11)$$

Integrating over r , the power delivered to a surface at the focal plane within a circle of radius, r , is

$$P(r, z) = P_0 \left[1 - e^{-\frac{2r^2}{\omega^2(z)}} \right] \quad (3.12)$$

If r is equal to $\omega(z)$ in Equation (3.12), $P(r, z) = 0.86P_0$, which means the total power delivered to a surface within a $1/e^2$ spot size is $0.86 P_0$.

As an incident beam passes into the surface of a solid, the radiation is attenuated, some of it is reflected, and the rest is eventually absorbed or completely transmitted. The optical absorption and attenuation coefficients of the deposit and substrate materials may be critical in determining the absorbed heat flux. In this dissertation, it will be assumed that the laser light not reflected at a gas-solid boundary is transmitted into the solid and eventually completely absorbed within the solid. Let \mathcal{J} be the spectral reflectance at the gas-solid boundary, and n_i the deposit index of the reflection. Then the angular spectral absorption coefficient, Λ , is given by:

$$\Lambda = 1 - \mathcal{J}(\phi) \quad (3.13)$$

where ϕ is the local incidence angle, and $\mathcal{J}(\phi)$ is the angular spectral reflectance defined by [Seigel 1992]:

$$\mathcal{J}(\phi) = \frac{1}{2} \left\{ \left[\frac{\cos \phi - \sqrt{n_i^2 - \sin^2 \phi}}{\cos \phi + \sqrt{n_i^2 - \sin^2 \phi}} \right]^2 + \frac{n_i^2 \cos \phi - \sqrt{n_i^2 - \sin^2 \phi}}{n_i^2 \cos \phi + \sqrt{n_i^2 - \sin^2 \phi}} \right\} \quad (3.14)$$

The deposit index of refraction n_i , can be obtained from Snell's law. This expression is valid only for a randomly polarized beam, and a given wavelength, λ .

The heat transfer rate, Q_{in} , at the surface of deposit or substrate can be specified as a function of the radial distance from the centerline, r , and the angle of incidence, $\phi(r)$, to the unit surface normal vector, $\hat{n}(x, r, t)$. Assuming a Gaussian incident beam and absorption over a surface, from Equations (3.11) and (3.13), we can obtain an approximate expression for the heat flux Q_{in}'' :

$$Q_{in}''(r) = 2P_0 \frac{\Lambda[\phi(r)]}{\pi\omega^2(z)} e^{-\frac{2r^2}{\omega^2(z)}} (\hat{z}, \hat{n}(x)) \quad (3.15)$$

To obtain the heat transfer rate, Q_{in} , in Equation (3.1), the expression in Equation (3.15) should be integrated over the absorption surface, s . From Equations (3.13) to (3.15), one can calculate the heat transfer rate, Q_{in} . Note that the shape of deposit will influence the heat transfer rate. In the case where the deposit shape is changing over time, the exact solution to Equation (3.15) must be obtained iteratively with the equation of growth over time since the reflectance depends on the shape, and the induced temperature depends on the reflectivity.

3.1.2 Natural Convection

The rate at which heat is convected from a solid body into a surrounding medium can be described by:

$$Q_{conv} = A_s h_{conv} (T_s - T_\infty) \quad (3.16)$$

where A_s is the surface area of a heated body, h_{conv} is the heat transfer coefficient, and T_s is the body surface temperature.

If k_{gas} is the thermal conductivity of the dominant gas species, the heat transfer coefficient, h_{conv} , can be determined from the dimensionless Nusselt number, N_u , using the following relation:

$$h_{conv} = N_u \frac{k_{gas}}{2r_s} \quad (3.17)$$

The Nusselt number, which represents the ratio of convection to the conduction losses is an empirical expression that depends on the dimensionless Grashoff and Prandtl number, G_r and P_r . The Grashoff number is a measure of the ratio of buoyancy to viscous forces in the precursor gas. The Prandtl number is the ratio of the kinematic viscosity to

the thermal diffusivity. In general, for a given body geometry, the Nusselt number in Equation (3.17) is of the form:

$$N_u = C + f(G_r + P_r) \quad (3.18)$$

where C is a constant which depends on the body geometry.

The heat loss rate depends on the geometry and size of the body. For example, the heat loss from a rod during 3D-LCVD depends on the rod's radius and length. An empirical formulation has been widely accepted for the laminar Nusselt number over a sphere:

$$N_u = 2 + 0.43(G_r + P_r)^{1/4} . \quad (3.19)$$

For a rod less than $1000\mu\text{m}$ in diameter, the Nusselt number can be approximated to an accuracy of 15% by the non-zero value:

$$N_{u_{sphere}} \approx 2 . \quad (3.20)$$

When natural convection occurs over a solid horizontal cylinder of uniform temperature, the Nusselt number will be of the form:

$$N_u = 0.36 + f(G_r + P_r) . \quad (3.21)$$

For small Grashoff number,

$$N_{u_{cylinder}} \approx 0.36 . \quad (3.22)$$

This formula is a crude approximation to the actual situation where the shape may be parabolic or even dimpled; however, it is sufficient for the purpose of this dissertation.

3.1.3 Radiation

Radiation from a blackbody surface into a medium of refractive index, n_i , can be described by Planck's distribution, which gives the spectral emission vs. wavelength, λ , and surface temperature, T_s :

$$Q_{rad}^{\cdot}(\lambda, T_s) = \frac{2\pi n_i^2 hc}{\lambda^5 (e^{(hc)/(\lambda T_s)} - 1)} \quad (3.23)$$

here, h is Planck's constant, and c is the speed of light in a vacuum. Assuming a deposit of emissivity ε_s , and integrating Equation (3.23) over all wavelength, one arrives at the Stephan – Boltzman equation for hemispherical total emissive power (where σ is the Stephan – Boltzman constant):

$$Q_{rad}^{\cdot}(T_s) = \varepsilon_s n_i^2 \sigma T_s^4 . \quad (3.24)$$

For the hemispherical geometry of a rod tip, the heat loss rate, Q_{rad} due to radiation into an infinite region filled with a precursor gas of refractive index, can be estimated from [Maxwell 1996]:

$$Q_{rad}(T_s) = \left(\frac{4}{3}\right) \pi r_s^2 \varepsilon_s n_i^2 \sigma (T_s^4 - T_{\infty}^4) . \quad (3.25)$$

For a deposit with arbitrary geometry, one can obtain the heat loss due to radiation from Equation (3.24) and the surface area.

3.1.4 Discussion

Heat conduction in the deposit and substrate depends on their geometry and thermal properties. There are several stages to the growth of the deposit on the substrate. During the initial stage, the deposit surface area is generally small and thus inhibits radiation and convection, so heat conduction to the substrate is the dominant mode of

heat transfer. Once a deposit forms, the laser beam will hit the surface of the deposit and the temperature then depends on the optical and thermal properties of both deposit and substrate. During the transient growth regime, conduction to the substrate diminishes. As a result, the properties of the substrate become less important, and eventually it can be assumed that conduction in the rod is one-dimensional or linear. For an insulating deposit on a highly conductive substrate, a large linear gradient over the rod will result. However, for a conductive deposit on an insulating substrate, the base temperature will be high and little gradient will occur over the rod. If the conductivity k_d of the deposit is much larger than the conductivity k_s of the substrate, it is difficult to grow a relatively long rod, since the entire rod would grow outward and broaden the rod.

In the instances of graphite, nickel, and iron, the thermal conductivity drops with temperature; Beginning at about 20 ~ 200K, it falls continuously until the Curie point (just below the melting point). This process further isolates the heated zone and increases the peak temperature, which in turn further lowers the conductivity. As a result, the growth terminates at some height from the substrate where the peak temperature exceeds the melting point [Maxwell 1996].

If the deposit is not a rod (cylinder), but a paraboloid, the conduction in the deposit and substrate will be more complicated. We will use the governing differential equations and the corresponding boundary conditions to describe the heat transfer in the deposit and substrate and discuss this case in the next section in details.

3.2 Governing Equations and Boundary Conditions

We consider a rectangular stationary substrate with the laser beam hitting one point or moving from one point to the next on the surface of the substrate. The deposit region and the substrate in a Cartesian coordinate system are shown in Figure 3.2.

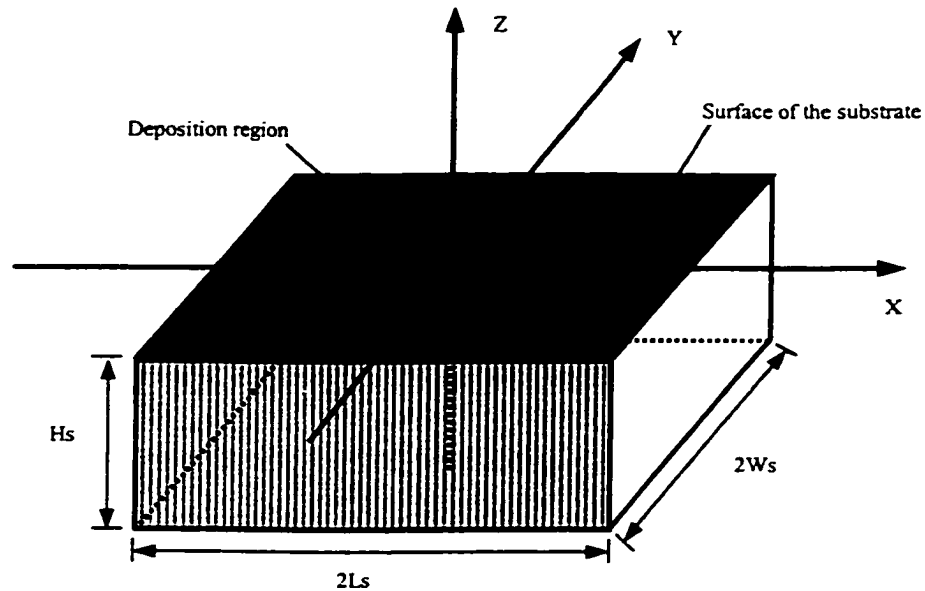


Figure 3.2 Cartesian coordinate system for the substrate

A three-dimensional heat transfer equation is used to describe the LCVD process. If the conductivity of the substrate is much smaller than that of the deposit, we can assume that the substrate is isolated and the heat transfer on the interface of the deposit and substrate can be ignored. This assumption simplifies our calculation but limits the application range of the model developed in this dissertation. Our model contains both the heat transfers in the deposit and substrate as well as that on their interface, so it can be used to study the temperature profile for different deposit and substrate materials.

3.2.1 Deposit Temperature

Temperature distributions induced by the absorption of laser radiation within the solids can be calculated on the basis of the heat equation. In most cases, the temperature is a function of both the spatial coordinates and time. With fixed laser parameters, the temperature distribution depends on the optical absorption within the irradiated zone, on the transport of heat out of this zone and, if relevant, on the transformation enthalpies for crystallization, melting, vaporization, and on chemical reaction enthalpies (exothermal or endothermal), etc. In this study, we ignore the transformation and chemical reaction enthalpies. In a coordinate system fixed with the deposit, the heat equation that describes the heat flow through the deposit can be written as:

$$c_D(T^D)\rho_D(T^D)\frac{\partial T^D}{\partial t} - \nabla[k_D(T^D)\nabla T^D] = Q_{in} \quad (3.26)$$

where $T^D \equiv T^D(x, y, z, t)$ is the temperature of the deposit at any point (x, y, z) , in the Cartesian coordinate system, and any time t . The parameters $\rho_D(T^D)$, $c_D(T^D)$ and $k_D(T^D)$ denote the temperature-dependent density, heat capacity and thermal conductivity of the deposit, respectively. ∇ is the three-dimensional del operator. Q_{in} is the heat source at or within the deposit boundaries due to the absorption of the laser beam light.

The boundary condition on the interface $z = 0$ between the deposit and the substrate is

$$T^D = T^S \quad (3.27a)$$

$$k_D(T^D)\frac{\partial T^D}{\partial z} = k_S(T^S)\frac{\partial T^S}{\partial z} \quad (3.27b)$$

On the surface of the deposit

$$-k_D(T^D)\frac{\partial T^D}{\partial z} = J_{loss} \quad (3.28)$$

where J_{loss} describes the energy loss to the gas phase on the surface of the deposit.

The diffusion of the precursor concentration, n , over a hemispherical reaction zone of the radius, r_w , can be expressed as

$$D\nabla^2 n - \frac{\partial n}{\partial t} = 0 \quad (3.29)$$

where D is the diffusivity of the precursor gas and ∇^2 is the Laplace operator. The boundary conditions are

$$\begin{aligned} \frac{\partial n}{\partial r} &= r_0^{-1}u, \quad r = r_w \\ n(r) &= cons, \quad r > r_w \\ \frac{\partial n}{\partial z} &= 0, \quad z = 0, \quad r = r_w \end{aligned} \quad (3.30)$$

where r_0 is a length scale

3.2.2 Substrate

The solid is deposited on the surface of the substrate, and the heat in the deposit will be transferred to the substrate through their interface. When the ratio of the thermal conductivities of deposit and substrate is not too large, the heat transfer to the interface cannot be ignored since it will influence the temperature distribution of the deposit and hence the growth rates and the shape of the deposit. The energy transfer equation that describes the heat flow through the substrate is given by

$$c_s(T^S)\rho_s(T^S)\frac{\partial T^S}{\partial t} = \nabla[k_s(T^S)\nabla T^S] \quad (3.31)$$

where $T^S \equiv T^S(x, y, z, t)$ is the temperature of the substrate at any point (x, y, z) , in the Cartesian coordinate system, and at any time t . $\rho_s(T^S)$, $C_s(T^S)$ and $k_s(T^S)$ denote the temperature-dependent density, heat capacity and thermal conductivity of the substrate, respectively, and ∇ is the three dimensional del operator.

The initial condition ($t = 0$) is

$$T^S = T_i^S \quad (3.32)$$

where T_i^S is the initial temperature of the substrate.

For a rectangular stationary substrate, boundary conditions need to be specified on six planes.

$$-k_s(T^S)\frac{\partial T^S}{\partial x} = h_1(T^S - T_\infty) + \sigma\varepsilon[(T^S)^4 - T_\infty^4] \quad \text{at } x = 0 \quad (3.33a)$$

$$k_s(T^S)\frac{\partial T^S}{\partial x} = h_2(T^S - T_\infty) + \sigma\varepsilon[(T^S)^4 - T_\infty^4] \quad \text{at } x = -L_s \quad (3.33b)$$

$$-k_s(T^S)\frac{\partial T^S}{\partial y} = h_3(T^S - T_\infty) + \sigma\varepsilon[(T^S)^4 - T_\infty^4] \quad \text{at } y = 0 \quad (3.33c)$$

$$k_s(T^S)\frac{\partial T^S}{\partial y} = h_4(T^S - T_\infty) + \sigma\varepsilon[(T^S)^4 - T_\infty^4] \quad \text{at } y = -W_s \quad (3.33d)$$

$$k_s(T^S)\frac{\partial T^S}{\partial z} = h_5(T^S - T_\infty) + \sigma\varepsilon[(T^S)^4 - T_\infty^4] \quad \text{at } z = -H_s \quad (3.33e)$$

$$-k_s(T^S)\frac{\partial T^S}{\partial z} = h_6(T^S - T_\infty) + \sigma\varepsilon[(T^S)^4 - T_\infty^4] \quad \text{at } z = 0 \quad (3.33f)$$

where T_∞ is the ambient temperature. $h_1, h_2, h_3, h_4, h_5, h_6$ denote the heat transfer coefficients on the surface $x = 0, x = -L_s, y = 0, y = -W_s, z = -H_s,$ and $z = 0$ of the substrate, respectively, where L_s, W_s, H_s are, respectively, the length, width and height of the substrate. The parameter σ is the Stefan-Boltzmann constant and ε is the thermal emissivity.

Note that there are two kinds of boundary conditions at the surface $z = 0$ of the substrate. The boundary condition beyond the reaction zone at the surface $z = 0$ of the substrate is given by Equation (3.33f). The boundary condition in the reaction zone at the surface $z = 0$ of the substrate is given by Equation (3.27).

3.2.3 Growth Rates

A complete 3D-LCVD model should include both growth kinetics and diffusive transport of the precursors. In this section, the emphasis is on the thermalphysics occurring during the 3D-LCVD process, but diffusive transport of the precursors has been ignored. The governing equations for heat flow through the deposit and the substrate can be used to predict the temperature distribution. Based on the temperature distribution on the surface of the deposit, one can predict the deposit growth rate from the Arrhenius law, Equation (2.3). In the actual LCVD process, the geometry of the deposit will affect the growth. From a macroscopic viewpoint, one may assume that growth during 3D-LCVD occurs along the instantaneously normal vector at each point on the surface of an evolving deposit. While the temperature may affect the magnitude of growth at each point, the direction of deposition remains normal to the surface due to the nature of the diffusion, adsorption, nucleation, and coalescence processes that produce polycrystalline

or amorphous deposits. The exception to this rule is the deposition of single crystals, where growth may indeed be anisotropic due to lattice activation. For the following analysis, this normal-growth rule is assumed, so the growth is a normal vector that can be expressed as follows:

$$\Delta\bar{z}_n(x, y) = K_0 e^{\frac{E_a}{RT^D}} \left[1 + e^{\frac{T_{th}-T^D}{\delta T_{th}}} \right]^{-1} \hat{n}(x, y) \Delta t \quad (3.34)$$

where $\Delta\bar{z}_n(x, y)$ is the local deposit growth at a point on the surface of the deposit, K_0 is a concentration-dependent rate constant that can be determined empirically, E_a and R are the activation energy and universal gas constant, respectively. T_{th} is the threshold temperature, δT_{th} is the width of this threshold, which describes the drop in deposition rate near T_{th} . Δt is the time increment to obtain a deposit growth $\Delta\bar{z}_n(x, y)$. Here $\hat{n}(x, y)$ is the unit outward normal vector on the instantaneous surface of deposition.

Equation (3.34) can account for the threshold behavior of the deposition process, i.e. for the fact that deposition becomes significant only if the surface temperature T^D exceeds the threshold temperature.

3.3 Mathematical Model for a Parabolic Microstructure

The governing equations and corresponding boundary conditions are described in the previous section. The governing equations take into account many factors that may affect the temperature distribution and the growth rate. So these equations can be used for simulating the 3D-LCVD processes in different situations, such as a spot, rod, direct writing, and so on. However, the complex interrelation among the heat flow between the deposit and substrate, the temperature field, and the deposit growth, makes it hard to get a

satisfactory solution. The advantage of a general and complete mathematical model may be counteracted by the possible error caused by a very complicated numerical method. Thus, for different kinds of physical problems, we should simplify the above governing equations as much as possible. Our goal is to develop an effective mathematical model to predict the dwell times across the substrate for the fabrication of a microstructure with a pre-specified geometry so that the model can describe the main aspects of the original physical problem and can be easily and accurately solved.

3.3.1 Problem Description

Much research work has been done on simulating a spot growth, direct writing, and a rod. Here, we consider a parabolic microstructure, as shown in Figure 3.3.

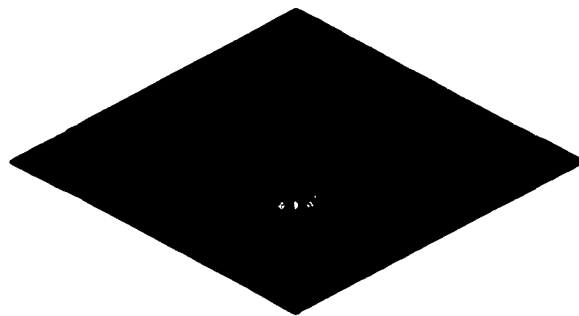


Figure 3.3 A parabolic microstructure on the surface of the substrate

Usually, it is difficult to fabricate such a microstructure in a single step. The process depends on many aspects such as the parameters of laser beam, and the thermalphysical properties of the deposit and substrate. Given these parameters and the dwell times of the laser beam, one can fabricate a microstructure. However, if the geometry of the microstructure is pre-specified, it is interesting to consider how to

specify the experimental conditions and how to control the processes to obtain such a microstructure. This reverse problem is much more difficult than the original problem, and we can not directly use Equation (3.34) to predict the dwell times, even if we can calculate the temperature distribution from the heat transfer equations and the corresponding boundary conditions. So in the ongoing section, we will establish a mathematical model for simulating the temperature profile and dwell times.

3.3.2 Predicting the Temperature Distribution

Since the geometry of deposit may be arbitrary and the heat transfer equations are coupled with the deposit growth equation, it is impossible to obtain the analytic solution for the governing equations in the foregoing section. A numerical method should be considered to simulate the complex process of 3D-LCVD and hence to predict the dwell times for fabricating a solid with a pre-specified geometry. However, it is still difficult to numerically solve the governing equations described in the previous section. First, the governing equations contain both heat transfers in the deposit and substrate. Since the shape of the deposit is usually complicated, this factor may cause many difficulties in grid partitioning, whether the finite difference method (FAM) or the finite element method (FEM) is used. Second, the heat equations are coupled with the deposit growth rate, which requires that the governing equations should be solved iteratively. The numerical method will be discussed in details in Chapter 4. For these reasons, the coupled equations that describe heat flow, gas diffusion and deposit growth must be simplified for different kinds of problems.

In this research, a mathematical model that describes the heat transfer in the deposit and the dwell times for fabricating a microlens will be established. To this end, we assume that the pre-specified shape of the deposit can be described by an arbitrary function

$$z = h_0(x, y) \quad (3.35)$$

Integrating Equation (3.26) within the region $0 \leq z \leq h_0$ gives

$$\int_0^{h_0} c_D(T^D) \rho_D(T^D) \frac{\partial T^D}{\partial t} dz = \int_0^{h_0} \frac{\partial}{\partial z} (k_D(T^D) \frac{\partial T^D}{\partial z}) dz + \int_0^{h_0} \nabla_2 [k_D(T^D) \nabla_2 T^D] dz + \int_0^{h_0} Q_{in} dz \quad (3.36)$$

We now make the following assumptions: 1) the deposit should be flat so that

$$\frac{\partial h_0}{\partial x} \ll 1. \quad 2) \quad T^D \equiv T^D(x, y, z, t) \approx T^D(x, y, 0, t), \quad \text{which holds if } \frac{h_0}{r_D k^*} \ll 1, \quad \text{where}$$

$k^* = \frac{k_D}{k_S}$, and r_D is the radius of the base of the deposit. With these approximations, we

can obtain the energy balance equation for a volume element of the deposit with base area $dxdy$ and height $h_0(x, y)$.

$$c_D(T) \rho_D(T) h \frac{\partial T^D}{\partial t} = \nabla_2 [h k_D(T) \nabla_2 T^D] + \int_0^h Q_{in} - J_{loss}(z=h) - J_{loss}(z=0) \quad (3.37)$$

We then make some further assumptions:

The growth shall be quasi-stationary. Thus, the time to reach thermal equilibrium

is $\tau_T \ll \left[\frac{\partial(\ln h)}{\partial t} \right]^{-1}$. For the same reason, we ignore any changes in the temperature

distribution during any time interval when the laser beam is focused on a point on the surface of the deposit.

Heat losses to the gas phase may be ignored, i.e. $J_{loss}(z = h_0) = 0$. At the interface $z = 0$, we set

$$J_{loss}(z = 0) = k_s(T^S) \frac{\partial T^S}{\partial z} \Big|_{z=0} \quad (3.38)$$

The laser light is absorbed at (x, y) within the deposit according to the following formula

$$\int_0^{h_0} Q_{in} dz = AI_{i,j}(x, y) = \frac{AP_0}{\sqrt{2\pi}\sigma_1} e^{-\frac{(x-x_i)^2 + (y-y_j)^2}{2\sigma_1^2}} (\hat{z}, \hat{n})_{(x,y)} \quad (3.39)$$

where A is the absorptivity, P_0 is the laser intensity, and σ_1 is the standard deviation of the intensity distribution of the laser beam. Here we consider a Gaussian distribution for the laser beam intensity. Due to the Gaussian beam distribution, it is seen from Equation (3.39) that the laser beam when focused in the subelement $\Delta_{i,j}$ (the center point is (x_i, y_j)) contributes to the heat source at point (x, y) . Then from Equation (3.37) at the interface we obtain

$$k_s(T^S) \frac{\partial T^S}{\partial z} = AI_{i,j}(x, y) + \frac{\partial}{\partial x} [h_0 k_D(T^D) \frac{\partial T^D}{\partial x}] + \frac{\partial}{\partial y} [h_0 k_D(T^D) \frac{\partial T^D}{\partial y}] \quad (3.40)$$

The second term on the right side of Equation (3.40) originates from the ‘‘lateral spread’’ of the surface temperature due to the deposit. Equation (3.40) can be considered as a modified boundary condition for calculating the temperature distribution in the reaction zone at the surface of the substrate.

From Equation (3.31), the equation for steady state heat conduction in the substrate is given by the Laplace equation:

$$\nabla_3^2 T^s = 0 \quad (3.41)$$

The initial and boundary conditions for the substrate are given in Equation (3.33). From Equations (3.40) and (3.41), we may be able to obtain the temperature distribution for the deposit and substrate.

3.3.3 Predicting Dwell Times

Now we consider how to use Equation (3.34) to predict the deposit dwell time. In the process of obtaining a deposit with a pre-specified geometry, the temperature and deposit shape change with time and with the position of the laser beam. So we should divide this process into a number of steps. At each step, the time needed for the temperature to reach its steady state can be ignored and the dwell times can be obtained from Equation (3.34). Because the total dwell time is unknown, we cannot divide it into a number of time intervals and perform calculation in each time step. However, we can divide the microstructure such as a microlens into a number of layers. For each layer of deposit we can compute its steady state temperature distribution and then predict the dwell times needed for the fabrication of that layer. Hence, the sum of these dwell times at each point for different deposit layers is equal to the total dwell time. In fact, the number of layers can be large enough so that the assumption, that the growth should be quasi-stationary, can be always satisfied. Given the laser power, properties of the substrate and deposit, and the dwell time at each point in a layer, can control the process of 3D-LCVD to fabricate a microlens with a pre-specified geometry.

To this end, we first consider two consecutive layers of the deposit described by the functions $z = h_0(x, y)$ and $z = h_1(x, y)$, respectively, as shown in Figure 3.4.

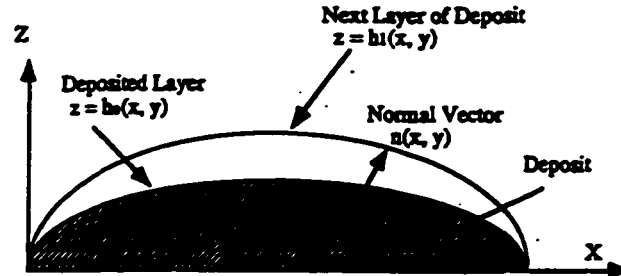


Figure 3.4 A cross-section of two consecutive layers of a parabolic surface

We want to determine the laser beam dwell time at each point on the surface $z = h_0(x, y)$ in order to obtain the next surface $z = h_1(x, y)$. Consider a point (x_0, y_0, z_0) on the surface $z = h_0(x, y)$. To calculate the growth $\Delta\vec{z}_n(x_0, y_0)$ in Equation (3.34) between this point and the next surface $z = h_1(x, y)$, we need to find the normal straight line at (x_0, y_0, z_0) and the intersect point on the surface $z = h_1(x, y)$. This normal line can be described using the following equation in parameter form:

$$x = x_0 - \frac{\partial h_0}{\partial x} \rho, \quad y = y_0 - \frac{\partial h_0}{\partial y} \rho, \quad z = z_0 + \rho \quad (3.42)$$

where ρ is a parameter. Substituting Equation (3.42) into $z = h_1(x, y)$, one can obtain an equation for the unknown ρ . Solving for ρ one can find the intersect point (x_1, y_1, z_1) on the surface of $z = h_1(x, y)$. Hence, the growth $\Delta\vec{z}_n(x_0, y_0)$ can be expressed as follows:

$$|\Delta\vec{z}_n(x_0, y_0)| = \sqrt{(x_1 - x_0)^2 + (y_1 - y_0)^2 + (z_1 - z_0)^2} = \varphi\rho \quad (3.43)$$

$$\text{where } \varphi = \sqrt{1 + \left(\frac{\partial h_0}{\partial x}\right)^2 + \left(\frac{\partial h_0}{\partial y}\right)^2} .$$

In order to obtain the surface $z = h_1(x, y)$, the laser beam must scan the surface $z = h_0(x, y)$, by moving from one point to the next point. We first decompose the total deposition region into a number of small subelements, $\Delta_{i,j}$, $i = 1, \dots, M$ and $j = 1, \dots, N$, as shown in Figure 3.5.

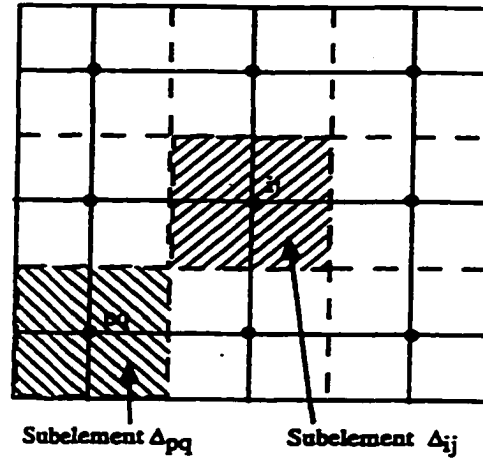


Figure 3.5 A schematic diagram of a region with subelements

Let $T_{i,j}^D(x_p, y_q, h_0(x_p, y_q))$ be the temperature in subelement $\Delta_{p,q}$ when the laser beam is focused in $\Delta_{i,j}$. We assume that the temperature is the same everywhere in each subelement. The temperatures in other subelements also contribute to the deposit growth in $\Delta_{p,q}$. We let $[\Delta \bar{z}_n(x_p, y_q)]_{i,j}$ denote the growth of the deposit in $\Delta_{p,q}$ due to the temperature $T_{i,j}^D(x_p, y_q, h_0(x_p, y_q))$ when the laser beam is focused in $\Delta_{i,j}$. Thus, the sum of the growth $[\Delta \bar{z}_n(x_p, y_q)]_{i,j}$, $i = 1, \dots, M$, $j = 1, \dots, N$ is the total growth in subelement

$\Delta_{p,q}$ after the laser beam scans all the subelements in the chemical reaction zone on the surface $z = h_0(x, y)$. As such, one obtain

$$\sum_{i=1}^M \sum_{j=1}^N |\Delta \bar{z}_n(x_p, y_q)|_{i,j} = |\Delta \bar{z}_n(x_p, y_q)| \quad (3.44)$$

Form Equation (3.34), we have

$$[\Delta \bar{z}_n(x_p, y_q)]_{i,j} = K_0 e^{\frac{E_a}{RT_{i,j}^D(x_p, y_q, h_0(x_p, y_q))}} \left[1 + e^{\frac{T_{ih} - T_{i,j}^D(x_p, y_q, h_0(x_p, y_q))}{\delta T_{ih}}} \right]^{-1} \hat{n}(x_p, y_q) \Delta t_{i,j} \quad (3.45)$$

where $\Delta t_{i,j}$ is the dwell time when the laser beam is focused on the subelement $\Delta_{i,j}$. Substituting Equation (3.45) into Equation (3.44), we obtain an equation that describes the relations among the temperature, dwell time and growth of the deposit. Applying the same idea to all other subelements, we obtain the following linear system that can be solved for the dwell time at each subelement $\Delta_{p,q}$ in the chemical reaction zone on the surface $z = h_0(x, y)$.

$$\sum_{i=1}^M \sum_{j=1}^N K_0 e^{\frac{E_a}{RT_{i,j}^D(x_p, y_q, h_0(x_p, y_q))}} \left[1 + e^{\frac{T_{ih} - T_{i,j}^D(x_p, y_q, h_0(x_p, y_q))}{\delta T_{ih}}} \right]^{-1} \Delta t_{i,j} = |\Delta \bar{z}_n(x_p, y_q)| \quad (3.46)$$

$p = 1, \dots, M, \quad q = 1, \dots, N$

Here, the chemical reaction zone is defined as the region on the surface of the substrate in which the temperature is higher than or equal to the chemical reaction temperature necessary for growth to occur.

CHAPTER 4

NUMERICAL METHOD

4.1 Deposit Growth

The surface of the deposit is assumed to be described by a general second-degree polynomial as follows:

$$z(x, y) = ax^2 + bxy + cy^2 + dx + ey + f \quad (4.1)$$

For convenience, we assume that the original point of the local Cartesian coordinate system is fixed at the center of the microlens, and the x-y plane is on the surface of the substrate, as shown in Figure 4.1.

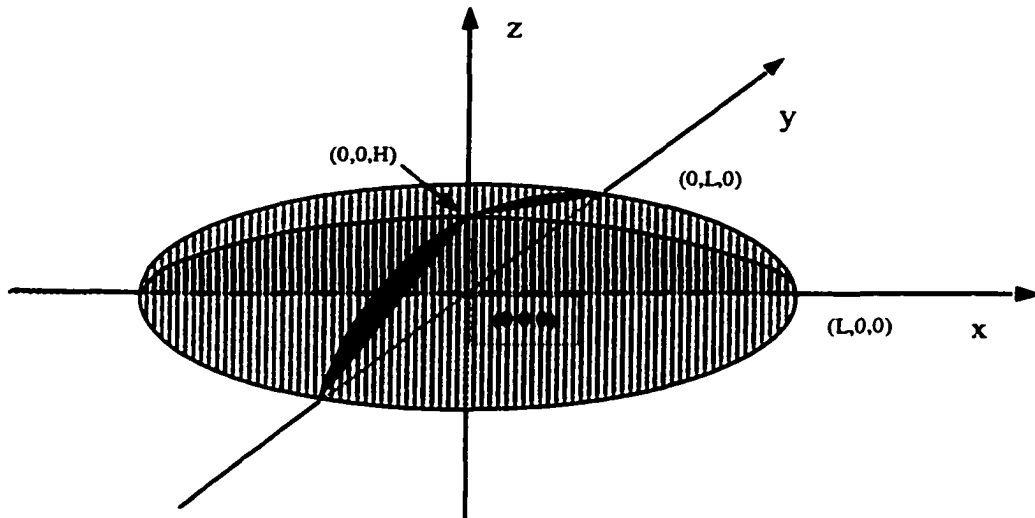


Figure 4.1 Coordinate system for deposit

If the microstructure is a microlens with a parabolic surface, the above function can be simplified. Let H and L denote the maximum height and radius of the microlens, then Equation (4.1) will satisfy the following condition:

$$\begin{aligned}
 z(-L,0) &= 0 \\
 z(L,0) &= 0 \\
 z(0,-L) &= 0 \\
 z(0,L) &= 0 \\
 z(0,0) &= H \\
 z(x,y) &= z(x,-y)
 \end{aligned} \tag{4.2}$$

From the above conditions, the coefficients in Equation (4.1) can be easily determined. Hence, the equation that describes the parabolic surface of the microlens can be written as follows:

$$z(x,y) = -\frac{H}{L^2}(x^2 + y^2) + H \tag{4.3}$$

As described in the previous section, the microlens is obtained by depositing layer by layer. We assume that the microlens is divided into n layers along the z axis and that the maximum thickness h of each layer is the same, $h = \frac{H}{n}$. Then, the equation that describes the parabolic surface in the kh layer of the microlens is

$$z = h_k(x,y) = -\frac{kh}{L^2}(x^2 + y^2) + kh \tag{4.4}$$

Consider a point (x_k, y_k, z_k) on the surface of $z = h_k(x,y)$. To obtain the growth $\Delta \bar{z}_n(x_k, y_k)$ between the point (x_k, y_k, z_k) and the next surface of $z = h_{k+1}(x,y)$, we need to find the normal straight line at the point (x_k, y_k, z_k) and the intersect point on the surface of $z = h_{k+1}(x,y)$. From Equation (3.42), the equation of this normal line in parameter form is

$$x = x_k - \left(\frac{\partial h_k}{\partial x}\right)\rho, \quad y = y_k - \left(\frac{\partial h_k}{\partial y}\right)\rho, \quad z = z_k + \rho \quad (4.5)$$

where ρ is a parameter. Substituting Equation (4.5) into $z = h_{k+1}(x, y)$, one obtains a quadratic equation in the unknown ρ . Solving for ρ from the quadratic formula, one can find the intersect point $(x_{k+1}, y_{k+1}, z_{k+1})$ and then calculate the growth, $\Delta \bar{z}_n(x_k, y_k)$.

From $z = h_{k+1}(x, y)$, we have

$$\frac{\partial h_k}{\partial x} = -\frac{2kx}{L^2}, \quad \frac{\partial h_k}{\partial y} = -\frac{2ky}{L^2} \quad (4.6)$$

From Equations (4.5) and (4.6), we obtain

$$x_{k+1} = \left(1 + \frac{2kh\rho}{L^2}\right)x_k, \quad y_{k+1} = \left(1 + \frac{2kh\rho}{L^2}\right)y_k \quad (4.7)$$

Substituting Equation (4.7) into Equation (4.4), we have

$$z_{k+1} = -\frac{(k+1)h}{L^2} \left(1 + \frac{2kh\rho}{L^2}\right)^2 (x_k^2 + y_k^2) + (k+1)h \quad (4.8)$$

From Equation (4.5), we have

$$\rho = z_{k+1} - z_k \quad (4.9)$$

Substituting Equation (4.8) into Equation (4.9), we can obtain the following equation in

ρ :

$$\frac{4k^2h^3(k+1)}{L^6} (x_k^2 + y_k^2)\rho^2 + \left[\frac{4k(k+1)h^2}{h^4} (x_k^2 + y_k^2) + 1\right]\rho + \left(\frac{x_k^2 + y_k^2}{L^2}\right)h = 0 \quad (4.10)$$

The positive value of ρ is obtained from Equation (4.10) as follows:

$$\rho = \frac{-b + \sqrt{b^2 - 4ac}}{2a} \quad (4.11)$$

where

$$\begin{aligned}
a &= 4k^2(k+1)h^3(x_k^2 + y_k^2) \\
b &= L^6 + 4k(K+1)h^2L^2(x_k^2 + y_k^2) \\
c &= -hL^6 + hL^4(x_k^2 + y_k^2)
\end{aligned}$$

Because the magnitude of $4ac$ can be very small, the numerator in Equation (4.11) is calculated by subtracting two close values, which may lead to a truncation error. To avoid this problem, we use the following equation, instead of Equation (4.11), to calculate ρ .

$$\rho = \frac{-2c}{b + \sqrt{b^2 - 4ac}} \quad (4.12)$$

As such, from Equation (4.5), the growth, $\Delta\bar{z}_n(x_k, y_k)$, can be expressed as follows:

$$|\Delta\bar{z}_n(x_k, y_k)| = \sqrt{(x_{k+1} - x_k)^2 + (y_{k+1} - y_k)^2 + (z_{k+1} - z_k)^2} = \varphi|\rho| \quad (4.13)$$

where

$$\varphi = \sqrt{1 + \left(\frac{\partial h_k}{\partial x}\right)^2 + \left(\frac{\partial h_k}{\partial y}\right)^2} = \frac{1}{L^2} \sqrt{L^4 + 4n^2 h^2 (x_k^2 + y_k^2)}$$

Thus, the growth, $\Delta\bar{z}_n(x_k, y_k)$, at point (x_k, y_k, z_k) on the surface of $z = h_k(x, y)$ in the k th layer of deposit can be obtained from Equations (4.12) and (4.13).

Further, the angle between the unit outward normal vector $\hat{n}(x, y)$ and the z-direction \bar{z} at point (x_k, y_k, z_k) can be calculated from

$$\cos(\hat{n}, \bar{z}) = \frac{1}{\varphi} \quad (4.14)$$

4.2 Discretization

We now apply a finite difference scheme to discretize the Laplace equation (Equation (3.38)). First, we assume the substrate is a rectangle with size $L_s \times W_s \times H_s$ (μm^3), where L_s , W_s and H_s are the length, width and height of the substrate, respectively. We divide L_s , W_s , H_s evenly into N_1 , N_2 , N_3 subintervals, respectively, so that the domain is decomposed into a number of subelements. The size of each subelement is $\Delta x \times \Delta y \times \Delta z$, as shown in Figure 4.2, where

$$\Delta x = \frac{L_s}{N_1}, \quad \Delta y = \frac{W_s}{N_2}, \quad \Delta z = \frac{H_s}{N_3} \quad (4.15)$$

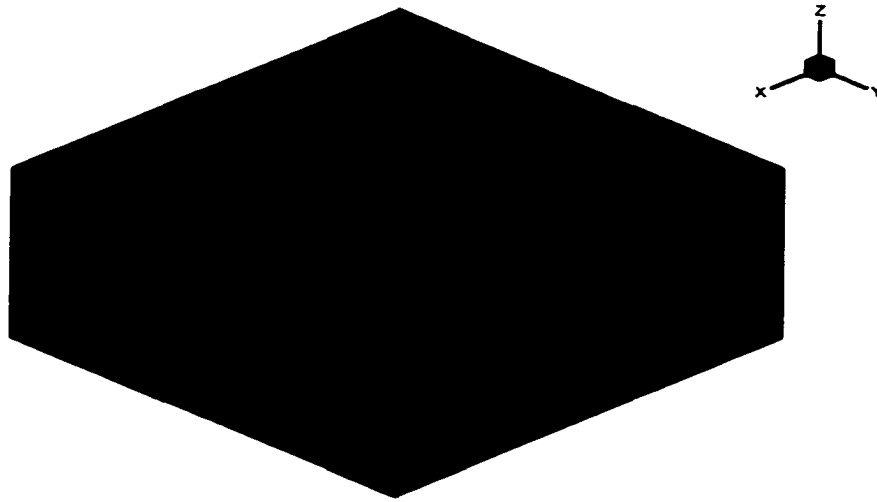


Figure 4.2 Domain decomposition of substrate and deposit

Let $T_{i,j,k}^s$ denote the temperature at the subelement (i, j, k) . The standard central difference derived from the Taylor series is employed to approximate the second derivative in the Laplace equation.

As such,

$$\frac{\partial^2 T^S}{\partial x^2} + \frac{\partial^2 T^S}{\partial y^2} + \frac{\partial^2 T^S}{\partial z^2} = 0 \quad (4.16)$$

can be written as follows:

$$\begin{aligned} \left(\frac{\partial^2 T^S}{\partial x^2}\right)_{i,j,k} &= \frac{1}{\Delta x^2} (T_{i-1,j,k}^S - 2T_{i,j,k}^S + T_{i+1,j,k}^S) \\ \left(\frac{\partial^2 T^S}{\partial y^2}\right)_{i,j,k} &= \frac{1}{\Delta y^2} (T_{i,j-1,k}^S - 2T_{i,j,k}^S + T_{i,j+1,k}^S) \\ \left(\frac{\partial^2 T^S}{\partial z^2}\right)_{i,j,k} &= \frac{1}{\Delta z^2} (T_{i,j,k-1}^S - 2T_{i,j,k}^S + T_{i,j,k+1}^S) \end{aligned} \quad (4.17)$$

Substituting Equation (4.17) into Equation (4.16) and solving for $T_{i,j,k}^S$ gives

$$\begin{aligned} T_{i,j,k}^S &= \frac{1}{\frac{2}{\Delta x^2} + \frac{2}{\Delta y^2} + \frac{2}{\Delta z^2}} \left[\frac{1}{\Delta x^2} (T_{i-1,j,k}^S + T_{i+1,j,k}^S) + \frac{1}{\Delta y^2} (T_{i,j-1,k}^S + T_{i,j+1,k}^S) \right. \\ &\quad \left. + \frac{1}{\Delta z^2} (T_{i,j,k-1}^S + T_{i,j,k+1}^S) \right] \end{aligned} \quad (4.18)$$

Since the above scheme is implicit, we use the Jacobi's iteration to obtain the steady-state temperature:

$$\begin{aligned} (T^S)^{(n+1)}_{i,j,k} &= \frac{1}{\frac{2}{\Delta x^2} + \frac{2}{\Delta y^2} + \frac{2}{\Delta z^2}} \left[\frac{1}{\Delta x^2} ((T^S)^{(n)}_{i-1,j,k} + (T^S)^{(n)}_{i+1,j,k}) + \frac{1}{\Delta y^2} ((T^S)^{(n)}_{i,j-1,k} + (T^S)^{(n)}_{i,j+1,k}) \right. \\ &\quad \left. + \frac{1}{\Delta z^2} ((T^S)^{(n)}_{i,j,k-1} + (T^S)^{(n)}_{i,j,k+1}) \right] \end{aligned} \quad (4.19)$$

where $(T^S)^{(n)}_{i,j,k}$ denotes the temperature at the subelement (i, j, k) at the n th iteration.

The Jacobi method is very slow to converge. Since the newest values of $(T^S)^{(n+1)}_{i-1,j,k}$, $(T^S)^{(n+1)}_{i,j-1,k}$, $(T^S)^{(n+1)}_{i,j,k-1}$ have already been obtained when we calculate the

temperature $(T^S)^{(n)}_{i,j,k}$, we may use these updated temperature values in the Equation (4.19) and then employ the Gauss-Seidel iterative technique:

$$\begin{aligned} (T^S)^{(n+1)}_{i,j,k} &= \frac{1}{\frac{2}{\Delta x^2} + \frac{2}{\Delta y^2} + \frac{2}{\Delta z^2}} \left[\frac{1}{\Delta x^2} ((T^S)^{(n+1)}_{i-1,j,k} + (T^S)^{(n)}_{i+1,j,k}) \right. \\ &+ \frac{1}{\Delta y^2} ((T^S)^{(n+1)}_{i,j-1,k} + (T^S)^{(n)}_{i,j+1,k}) + \left. \frac{1}{\Delta z^2} ((T^S)^{(n+1)}_{i,j,k-1} + (T^S)^{(n)}_{i,j,k+1}) \right] \end{aligned} \quad (4.20)$$

The Gauss-Seidel method converges faster than Jacobi's method. However, the fastest method is the Successive Over-Relaxation (SOR) method which is particularly useful for solving linear systems that occur in the numerical solution of certain partial-difference equations. Here, the SOR method can be expressed as

$$\begin{aligned} (T^S)^*_{i,j,k} &= \frac{1}{\frac{2}{\Delta x^2} + \frac{2}{\Delta y^2} + \frac{2}{\Delta z^2}} \left[\frac{1}{\Delta x^2} ((T^S)^{(n+1)}_{i-1,j,k} + (T^S)^{(n)}_{i+1,j,k}) \right. \\ &+ \frac{1}{\Delta y^2} ((T^S)^{(n+1)}_{i,j-1,k} + (T^S)^{(n)}_{i,j+1,k}) + \left. \frac{1}{\Delta z^2} ((T^S)^{(n+1)}_{i,j,k-1} + (T^S)^{(n)}_{i,j,k+1}) \right] \end{aligned} \quad (4.21a)$$

$$(T^S)^{(n+1)}_{i,j,k} = (T^S)^{(n)}_{i,j,k} + \omega [(T^S)^*_{i,j,k} - (T^S)^{(n)}_{i,j,k}] \quad (4.21b)$$

where ω is an over-relaxation factor used to accelerate the convergence.

The boundary conditions in Equation (3.33) for predicting the temperature distribution of the substrate can be discretized as follows:

$$(T^S)^{(n+1)}_{1,j,k} = (T^S)^{(n)}_{2,j,k} \frac{\Delta x}{k_S (T^S)^n_{1,j,k}} \{ h_2 [(T^S)^{(n)}_{1,j,k} - T_\infty] + \sigma \varepsilon [((T^S)^{(n)}_{1,j,k})^4 - T_\infty^4] \} \quad (4.22)$$

Similarly, we can obtain the discrete difference formulas for the other boundary conditions in Equation (3.33). Noting that Equation (3.40) is the boundary condition for the chemical reaction zone on the surface of the substrate, we use the following formulas to approximate the first and second derivatives in Equation (3.40):

$$\left(\frac{\partial T^S}{\partial z}\right)_{i,j,1} = \frac{1}{\Delta z} (T_{i,j,1}^S - T_{i,j,2}^S) \quad (4.23a)$$

$$\begin{aligned} \left[\frac{\partial}{\partial x} (hk_D(T^D) \frac{\partial T^D}{\partial x})\right]_{i,j,1} &= \frac{1}{\Delta x} \{h_{i-\frac{1}{2},j,1} k_D(T_{i,j,1}^D) T_{i-1,j,1}^D - [(h_{i-\frac{1}{2},j,1} k_D(T_{i-\frac{1}{2},j,1}^D) + \\ &\quad (h_{i+\frac{1}{2},j,1} k_D(T_{i+\frac{1}{2},j,1}^D))] T_{i,j,1}^D + h_{i+\frac{1}{2},j,1} k_D(T_{i+\frac{1}{2},j,1}^D) T_{i+1,j,1}^D \} \end{aligned} \quad (4.23b)$$

Similarly, we can derive the discrete formula for term $\left[\frac{\partial}{\partial x} (hk_D(T^D) \frac{\partial T^D}{\partial x})\right]_{i,j,1}$.

Substituting these formulas into Equation (3.40) and noting that $T_{i,j,1}^D = T_{i,j,1}^S$, we can obtain the following formula for solving $T_{i,j,1}^D$,

$$C_{yz} T_{i,j,1}^D = A I_{i,j} + C_z T_{i,j,2}^S + C_{x_1} T_{i-1,j,1}^D + C_{x_2} T_{i+1,j,1}^D + C_{y_1} T_{i,j-1,1}^D + C_{y_2} T_{i,j+1,1}^D \quad (4.24)$$

where

$$\begin{aligned} C_{x_1} &= \frac{1}{2} [k_D(T_{i-1,j,1}^D) h_{i-1,j} + k_D(T_{i,j,1}^D) h_{i,j}] \\ C_{x_2} &= \frac{1}{2} [k_D(T_{i,j,1}^D) h_{i,j} + k_D(T_{i+1,j,1}^D) h_{i+1,j}] \\ C_{y_1} &= \frac{1}{2} [k_D(T_{i,j-1,1}^D) h_{i,j-1} + k_D(T_{i,j,1}^D) h_{i,j}] \\ C_{y_2} &= \frac{1}{2} [k_D(T_{i,j,1}^D) h_{i,j} + k_D(T_{i,j+1,1}^D) h_{i,j+1}] \\ C_z &= \frac{k_S}{\Delta z} \\ C_{yz} &= C_z + C_{x_1} + C_{x_2} + C_{y_1} + C_{y_2} \end{aligned}$$

From Equation (4.24) coupled with the boundary conditions, we can obtain the steady-state temperature distribution when the laser beam is focused on one point on the surface of deposit. The steady-state temperature distribution is obtained when the maximum norm of the difference between $(T^S)^{(n+1)}$ and $(T^S)^{(n)}$ satisfies the convergence condition:

$$\left\| \frac{(T^s)^{(n+1)} - (T^s)^{(n)}}{(T^s)^{(n)}} \right\|_{\infty} \leq \varepsilon_1 \quad (4.25)$$

where ε_1 is a given tolerance.

4.3 Solving the Linear System

For a microlens, the chemical reaction zone is a circle. The laser beam scans this zone from one point to the next on a grid. Since Equation (3.46) cannot be directly used to calculate the dwell times, we change the two-dimensional notation in Equation (3.46) into a one-dimensional notation and then assume that there are a total of M_0 subelements in the chemical reaction zone. Hence, Equation (3.46) can be rewritten as follows:

$$\sum_{i=1}^{M_0} K_0 e^{\frac{E_a}{RT_i^D(x_j, y_j, h_0(x_j, y_j))}} \left[1 + e^{\frac{T_{in} - T_i^D(x_j, y_j, h_0(x_j, y_j))}{\delta T_{in}}} \right]^{-1} \Delta t_i = \left| \Delta \bar{z}_n(x_j, y_j) \right| \quad (4.26)$$

where $T_i^D(x_j, y_j, h_0(x_j, y_j))$ is the temperature of the deposit in subelement Δ_j , when the laser beam is focused in the subelement Δ_i . $\Delta \bar{z}_n(x_j, y_j)$ and Δt_i are deposit growth and dwell time, respectively.

We rewrite Equation (4.26) in matrix form

$$A\bar{x} = \bar{b} \quad (4.27)$$

where

$$A = (a_{ij})_{M_0 \times M_0},$$

$$a_{ij} = K_0 e^{\frac{E_a}{RT_i^D(x_j, y_j, h_0(x_j, y_j))}} \left[1 + e^{\frac{T_{in} - T_i^D(x_j, y_j, h_0(x_j, y_j))}{\delta T_{in}}} \right]^{-1} \quad (4.28)$$

$$\bar{x} = (\Delta t_1, \Delta t_2, \dots, \Delta t_{M_0})^T$$

$$\bar{b} = (b_1, b_2, \dots, b_{M_0})^T$$

$$b_j = |\Delta \bar{z}_n(x_j, y_j)|$$

Thus, the deposit dwell time at each subelement for each layer can be obtained by solving the linear system in Equation (4.27). It should be noted that sometimes we may obtain an unreasonable negative dwell time, or cannot obtain the convergent dwell time at all. We should discuss this linear system in order to obtain accurate and reasonable solution. If A is strictly diagonally dominant, then both the Jacobi method and the Gauss-Seidel (or SOR) method give a sequence $\{x^{(k)}\}_{k=0}^{\infty}$ that converges to a unique solution of $A\bar{x} = \bar{b}$. We note that the temperature distribution determines whether matrix A is strictly diagonally dominant. When the laser beam is focused on a subelement on the surface of the deposit, a temperature distribution can be obtained. In different subelements, the heights and their corresponding temperature distributions are different, so it is difficult to determine whether matrix A is strictly diagonally dominant. However, we can analyze some general relations between them, which is helpful for us to determine the size of the subelements and the intensity of the laser beam. For instance, from Equation (3.39) we know that if the standard deviation σ_1 of the intensity of the laser beam is large, the corresponding temperature distribution is flat and will then lead to a coefficient matrix that is not strictly diagonally dominant. On the other hand, for certain intensity distributions of the laser beam, the size of the subelement will affect the property of matrix A . For the same temperature distribution, if the size of the subelement is too small, we have $\sum_{\substack{j=1 \\ j \neq i}}^{M_0} |a_{i,j}| > |a_{ii}|$, and then A is not strictly diagonally dominant. From

the above analysis, we should choose an appropriate size of the subelement for different intensity distributions of the laser beam.

The SOR iterative technique can be used for solving the linear system $A\bar{x} = \bar{b}$ and is expressed as

$$x_i^* = \frac{1}{a_{ii}} \left[-\sum_{j=1}^{i-1} a_{ij} x_j^{(k)} - \sum_{j=i+1}^{M_0} a_{ij} x_j^{(k-1)} + b_i \right]$$

$$x_i^{(k)} = x_i^{(k-1)} + \omega(x_i^* - x_i^{(k-1)}) \quad (4.29)$$

where $a_{ii} \neq 0$, which is unconditionally satisfied in our model and ω is an over-relaxation factor used to accelerate the convergence, where $1 < \omega < 2$. A convergent solution for the linear system is obtained when the maximum norm of the difference between $x^{(k)}$ and $x^{(k-1)}$ is less than a given tolerance ε_2 , as expressed in Equation (4.30):

$$\left\| \frac{x^{(k+1)} - x^{(k)}}{x^{(k)}} \right\|_{\infty} \leq \varepsilon_2 \quad (4.30)$$

4.4 Algorithms

The three algorithms are used in this model. The source code can be seen in the appendix.

Algorithm 1. Main structure

Step 1. Input all constants and coefficients.

Step 2. Call a function to calculate the deposit growth at each subelement for each layer.

Step 3. Begin the loop for calculating the deposit dwell times for each layer.

Step 4. When the laser beam is focused in a subelement, call a function to calculate the steady state temperature distribution.

Step 5. Calculate the coefficient matrix A in the linear system.

Step 6. Call a function for solving the linear system and for obtaining the dwell time distribution in each layer.

Step 7. End the loop for calculating the deposit dwell times.

Step 8. Output the results.

Algorithm 2. Temperature calculation

Step 1. Input the over-relaxation factor ω , tolerance ε_1 , maximum number of iterations, and other coefficients.

Step 2. Calculate the intensity distribution of the laser beam.

Step 3. Begin the loop for calculating the temperature distribution.

Step 4. Use Equation (4.21) to calculate the temperature inside the substrate.

Step 5. Use Equation (4.22) to calculate the temperature on the surface of the substrate.

Step 6. Use Equation (4.24) to calculate the temperature on the interface between the deposit and substrate.

Step 7. Exit the loop if the norm of the difference between the temperature of two successive iterations is less than a given tolerance ε_1 , or the number of iterations exceeds the maximum number of iterations.

Algorithm 3. Solving the linear system to obtain the deposit dwell times

Step 1. Input the matrix A , deposit growth, tolerance ε_2 and maximum number of iteration.

Step 2. Give the initial approximation $\bar{x}^{(0)}$.

Step 3. Begin the iteration loop to calculate the dwell times.

Step 4. Use Equation (4.29) to calculate the dwell times for each layer.

Step 5. Calculate the norm of the difference between $\bar{x}^{(k)}$ and $\bar{x}^{(k-1)}$.

Step 6. End the iteration loop if the convergence criteria in Equation (4.30) is satisfied or the number of iterations exceeds the maximum number of iterations.

CHAPTER 5

SIMULATION OF A CONVEX MICROLENS

In this chapter we use the mathematical model and the corresponding numerical method described in the previous chapter to simulate the process of fabricating a convex microlens. We choose nickel as the deposit and graphite as the substrate. The temperature distributions in the different layers of deposit will be calculated and hence used to determine the dwell times needed to fabricate the convex microlens.

5.1 Description of the Simulation

It is assumed that the microlens parabolic in shape. Hence, the geometry of the deposit is pre-specified, as shown in Figure 5.1. The mathematical model of the deposit has been described in section 4.1.

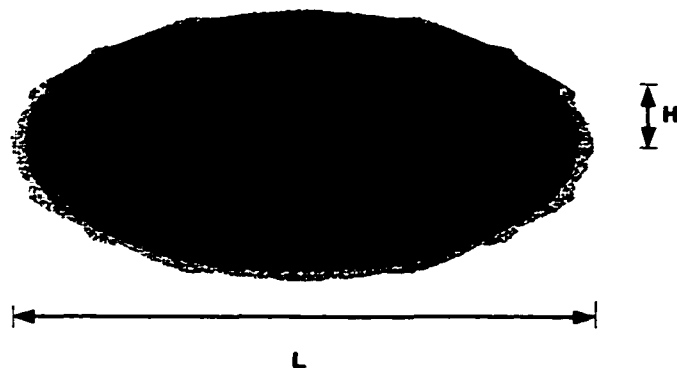


Figure 5.1 A convex microlens with a parabolic surface

The diameter L and maximum height H are assumed to be $20 \mu\text{m}$ and $2\mu\text{m}$, respectively. The substrate is rectangular with dimensions $40 \times 40 \times 10 (\mu\text{m}^3)$. The calculation domain for the substrate is chosen to be much larger than the deposit size so that the boundary conditions can hold. If the conductivity of the substrate is small, compared with the conductivity of the deposit, we may assume that the temperature on the boundary of the substrate is close to the ambient temperature. In our calculation, the ratio of conductivity of deposit (nickel) and substrate (graphite) is about 40. Thus, the domain of the substrate is appropriate for our calculation.

It is impossible to obtain the deposit with the pre-specified geometry in a single step because of the complicated correlation between the temperature distribution and growth rate. Given the laser beam intensity and its distribution (Gaussian distribution), one might obtain a deposit with a specific shape; however, the reverse process is extremely hard to control. From the discussion of the mathematical model in chapter 3, we need to simulate the fabrication process layer by layer. To simulate the fabrication process, the laser beam should scan each pixel on the surface of the deposit. We need to determine how long the laser beam should be focused on each local pixel of each layer.

The multilayer scanning approach to simulate the whole process for fabricating a microlens with a pre-specified geometry has been described in chapter 3. Given a microlens with a parabolic surface, as shown in Figure 5.1, there are many ways to divide the microlens into multiple layers. A convenient way is to specify the number of layers n and then evenly divide the whole maximum height H of the microlens into a number of subintervals, each with height h . If $H = 2\mu\text{m}$, we may choose $n = 20$, and $h = 0.1\mu\text{m}$.

After specifying the geometry properties of each layer, we need to decompose the substrate and deposit in horizontal plane. Note that the domain decomposition is important in our calculation and the size of each sub-element is determined by the physical properties of the laser beam and deposit conductivity.

In the numerical example the size of each element (pixel) is chosen to be $1\mu m \times 1\mu m$. The mesh of deposit zone on the substrate surface is shown in Figure 5.2. The five points A, B, C, D, E in the figure are selected pixels for analyzing the temperature change corresponding to each layer. The substrate is involved in the three dimensional calculation, where each element is chosen to be $1\mu m \times 1\mu m \times 0.5\mu m$. The convex microlens shapes resulting from 5, 10, 15 and 20 layers of deposit are given in Figures 5.3 to 5.6, respectively.

The computation includes the three algorithms described in section 4.4. Algorithm 2 and Algorithm 3 are nested in Algorithm 1. When the laser beam is focused on certain element, Algorithm 2 is used to calculate the quasi-steady state temperature distribution, which will be used to calculate the coefficient matrix in the linear system. The convergence of Algorithm 2 should be controlled carefully. In our example, the tolerance of the temperature calculation is chosen to be $\varepsilon_l = 1.0 \times 10^{-2}$. Algorithm 3 is used to predict the dwell time at each element for each layer. If the size of the element is chosen appropriately, the linear system is diagonally dominant and the calculation for the SOR method is stable and convergent. In addition, for each layer we only need solve the linear system one time to obtain the dwell times for the whole layer. Algorithm 3 takes less CPU time than Algorithm 2 in our model. After balancing CPU time and high accuracy, a

smaller tolerance value can be chosen for Algorithm 3, with $\varepsilon_l = 1.0 \times 10^{-4}$. Of course the consistency in accuracy should be maintained for the whole computation.

Equations (4.12) and (4.13) are used to calculate the growth for each element on each layer, given a microlens with a pre-specified geometry. Part of the calculation is only related to the geometry and is independent from the temperature and dwell time calculation. Hence, it can be performed using an independent procedure. The data of ΔZ forms the right hand side of the linear system in Equation (4.26) and the linear system is then solved using Algorithm 3. The program (Appendix B) for predicting the dwell times is written in the Fortran language and is run on a SGI Origin 2000.

5.2 Physical Parameters

Several key parameters determine the outcome of the LCVD process. The LCVD deposition rate is a function of many variables, such as laser power, laser scan rate, vapor pressure of the precursors, and thermal conductivity of the substrate. The parameters that ultimately limit and control the process lie within the realm of thermal physics and continuum mechanics. In this chapter, emphasis has been placed on the kinetics of growth, rather than on the diffusive transport of the precursor in the gas phase. Without considering convection, the primary mode of heat transfer is conduction to the substrate. Besides the precursor partial pressure, the laser power is the process parameter that most influences growth. The laser intensity and its distribution can be calculated from Equations (3.10) and (3.11).

A common LCVD precursor, tetracarbonyl nickel, $Ni(CO)_4$, was employed which has a vapor pressure of 1000mbar at 316 K. $Ni(CO)_4$ dissociate according to the reaction:



with an activation energy, E_a , of 94000 J/mol [Maxwell 1996]. The compound also decomposes at a relatively low temperature, having a threshold temperature, T_{th} , of 423K.

Nickel has a moderate thermoconductivity for a metal, $k_d = 65.6 W/m \cdot K$ at 600K, and nickel's thermocunductivity is representative of many transition and refractory metals. Most important, the conductivity of Ni is relatively constant over the 400-1500K interval, and Ni melts at 1728K. The conductivities of nickel and graphite [Incropera 1985] are listed in Table 5.1, in which $k_{s,\parallel}$ and $k_{s,\perp}$ are in-plane (i.e. parallel) and z-axis (i.e. perpendicular) thermal conductivity of substrate material, respectively. k_d is thermal conductivity of deposit material. The melting point of graphite is 2273K, much higher than nickel.

Table 5.1 Conductivities of nickel and graphite

Composition	Conductivity $k(W/m \cdot K)$								
	200K	300K	400K	600K	800K	1000K	1200K	1500K	2000K
Nickel k_d	107	90.7	80.2	65.6	67.6	71.8	76.2	82.6	
Graphite $k_{s,\parallel}$ to layers	3230	1950	1390	892	667	534	448	357	262
Graphite $k_{s,\perp}$ to layers	9.23	5.70	4.09	2.68	2.01	1.60	1.34	1.08	0.81

K_0 , R , T_{th} are the rate constant, universal gas constant and the threshold temperature in the Arrhenius Equation (3.31), respectively. The threshold temperature is an important factor determining the laser power required to initiate growth.

The physical parameters used in the numerical example are listed in Table 5.2 [Nassar 2000], where n_i and σ are the deposit index of refraction and the Stephan-Boltzman constant, respectively.

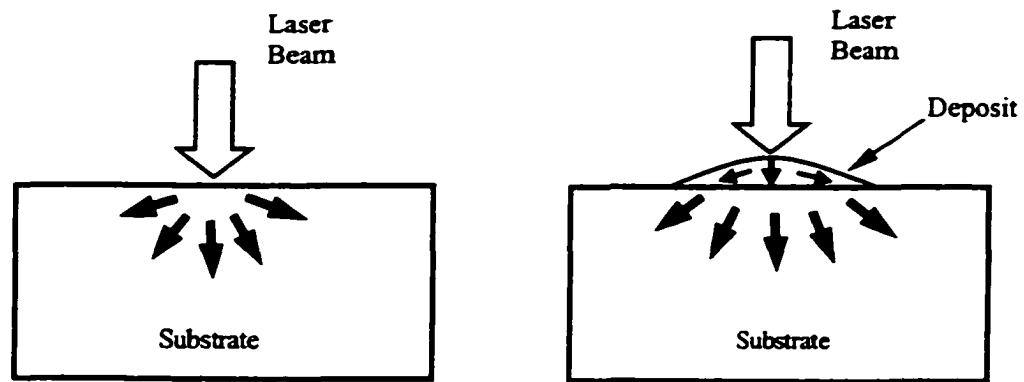
Table 5.2 Physical parameters

Parameters	Values
E_a	$9.4 \times 10^4 (J/mol)$
R	$8.314 (J/mol \cdot K)$
K_o	$1.37 \times 10^4 (mm/sec)$
T_a	$475 (K)$
P_o	$0.10 (W)$
σ	$0.0005 (mm)$
n_i	3.95

5.3 Temperature Distribution

The temperature distribution determines the growth rate and dwell time. For a deposit with a pre-specified flat shape the area of the interface between the deposit and substrate is relatively large, so the primary mode of heat transfer is conduction to the substrate (initially). As a deposit begins to form, the temperature distribution is largely determined by conduction in the deposit. The heat flow at the initial stage and after the deposit has been formed can be illustrated as shown in Figure 5.7.

At the initial stage, the heat directly conducts to the substrate. When the laser beam is focused at the center of the deposition zone, the temperature distributions on the surface and on the central vertical cross-section of the substrate are given in Figures 5.8 and 5.9. Here, the central vertical cross-section is defined as the x-z plane that bisects the substrate.



a. Initial stage (without deposit)

b. After deposit has been formed

Figure 5.7 Heat flow mechanism

As the deposit has been formed, both temperature distributions of deposit and substrate can be predicted. Temperature contours on the surface of the substrate, when the laser beam is focused at the center, are given in Figures 5.10 to 5.13 for to the layers 5, 10, 15 and 20. Similarly, temperature contours on the central vertical intersection of the substrate when the laser beam is focused at the center element are given in Figures 5.14 to 5.17, corresponding to the selected layers (Layer 5, 10, 15, 20).

When the laser beam is focused at one pixel, the corresponding temperature distribution can be obtained, in which the maximum temperature occurs at the pixel in question. As the layer number becomes larger, the height of deposit becomes larger and the maximum temperature decreases. The change in trend of the maximum temperature with increase in the number of layers is illustrated in Figure 5.18, in which the five lines correspond to the five pixels A, B, C, D and E where the laser beam is focused (see

Figure 5.2). As the layer number becomes large, the maximum temperature decreases slowly.

It is seen from the Figure 5.18 that the maximum temperature decreases as one moves from the periphery of the surface (pixel E) to the center (pixel A) because the deposit height near the center is larger than at the periphery, and there is enough cross-section area to transfer the heat to the surrounding area. This result also can be explained from Equation (3.37) that describes the heat flow in the deposit. The diffusion term in Equation (3.37) contains the parameter h . Thus if h is large, the effect of diffusion will increase. As a result, the temperature distribution becomes flatter and the peak temperature lower.

To examine the effect of the boundary condition and deposit height on the temperature distribution, we present temperature results when the laser beam is focused at the pixel E. The temperature contours on the surface of the substrate for layers 0, 5, 10, 15 and 20 are given in Figures 5.19 to 5.23, respectively. The temperature contours on the central vertical cross-section of the substrate corresponding to deposit layers 0, 5, 10, 15 and 20 are given in Figures 5.24 to 5.28, respectively. Here, the central vertical cross-section of the substrate is the x - z plane that bisects the substrate and passes through A and E. When the laser beam is focused at a pixel near the boundary, such as pixel E, the temperature distribution is not symmetric. On the contrary, the temperature distribution is symmetric when the laser beam is focused at the central pixel of the deposit such as pixel A. Near the boundary, the small deposit height constraints the heat transport, thus giving rise to a high temperature.

With the laser intensity $P_0 = 0.05W$, the heat source term in Equation (3.36) is small and the maximum temperature is smaller than that for $P_0 = 0.08W$. The temperature contours on the surface of the substrate with $P_0 = 0.05W$ for layers 0, 5, 10, 15 and 20 are given in Figures 5.29 to 5.33, respectively. The temperature contours on the central vertical intersection of the substrate with $P_0 = 0.05W$ corresponding to deposit layers 0, 5, 10, 15 and 20 are given in Figures 5.34 to 5.38, respectively. Comparing Figures 5.29 ($P_0 = 0.05W$) with Figures 5.8 ($P_0 = 0.08W$), one can see that the surface temperature distribution contours are similar but the maximum temperature decreases when the laser intensity is lower.

The maximum temperature for $P_0 = 0.05W$ decreases also with an increase in the layer number, as shown in Figure 5.39. The change in trend of the maximum temperature in Figure 5.39 is similar to that shown in Figure 5.18 ($P_0 = 0.08W$), but the value is smaller, since there is less heat source from laser beam to be transferred to deposit and substrate.

5.4 Dwell Time vs. Deposit Growth

After the temperature distribution of the deposit has been obtained, one can simulate the deposit growth and hence the geometry of the deposit at a certain time step, since the temperature determines the growth rate. In our case, the geometry of the deposit is pre-specified so we can predict the dwell time that the laser beam has to stay in each element for each layer in order to obtain the pre-specified deposit geometry.

Using the physical parameter values in Table 5.1, the dwell time at each pixel of each layer of the microlens can be predicted when $P_0 = 0.08W$. For the first several

layers, the height of deposit is still low so that it limits heat transport to the surrounding area, so less time is needed to fabricate these layers. Figure 5.40 shows the total dwell time at each pixel needed to fabricate the whole microlens with 20 layers. Figures 5.41 to 5.43 give the sum of dwell time at each pixel for fabricating layers 6-10, 11-15, 16-20, respectively. It is seen from these figures that when the height of deposit increases, the surface temperature decreases and, as expected, the dwell time needed to deposit another layer increases.

When $P_0 = 0.05W$ the dwell time at each pixel for layers 1-20, 6-10, 11-15 and 16-20 are given in Figures 5.44 to 5.47, respectively. It is seen that when the laser intensity is smaller, the temperature is lower, and a larger dwell time is needed to fabricate the same microlens.

From the above results, one can see that more time is needed to grow the deposit near the center than near the edge. This result is attributed to the fact that the temperature is lower at the center than near the edge.

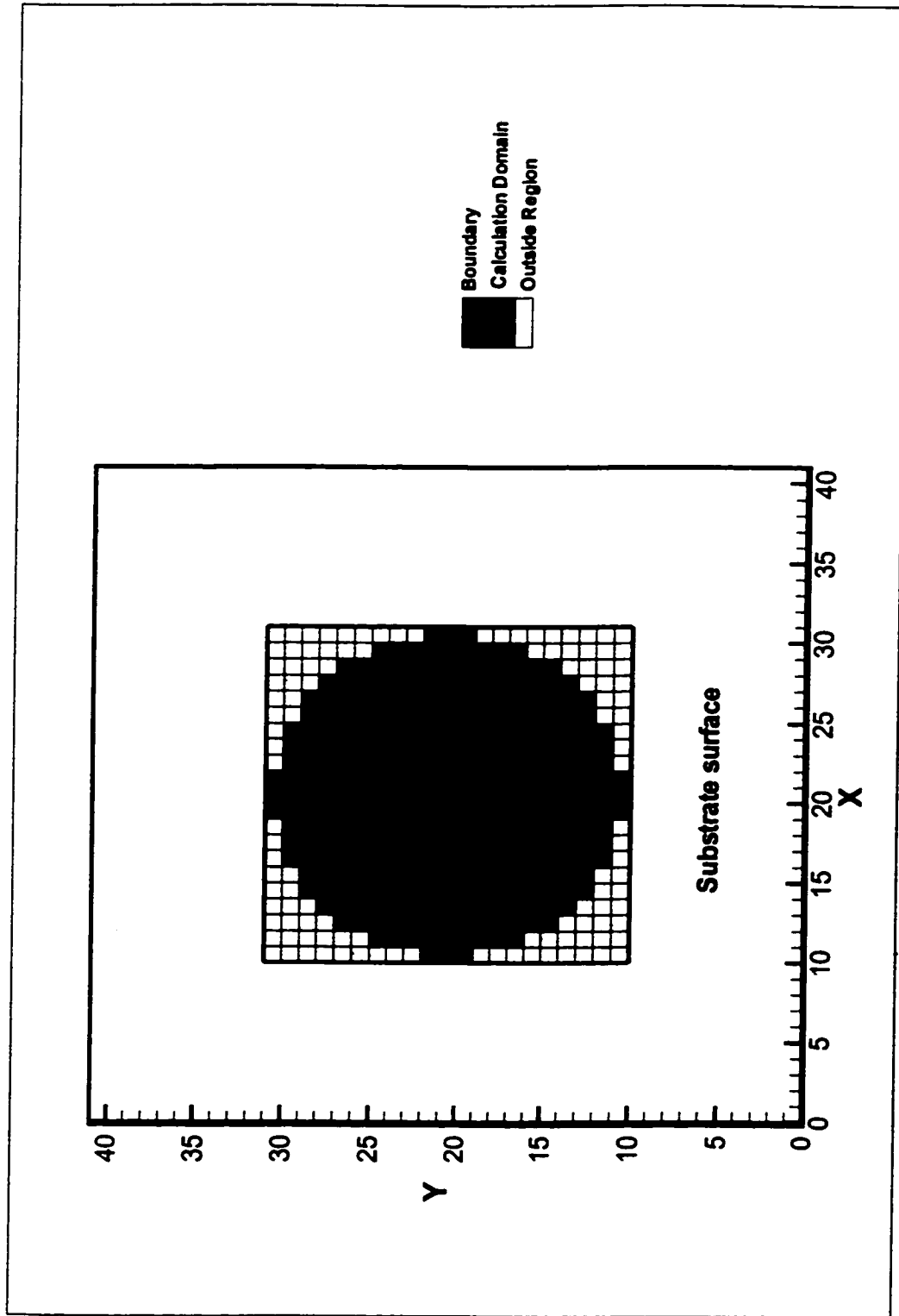


Figure 5.2 Mesh and deposit zone on the surface of the substrate

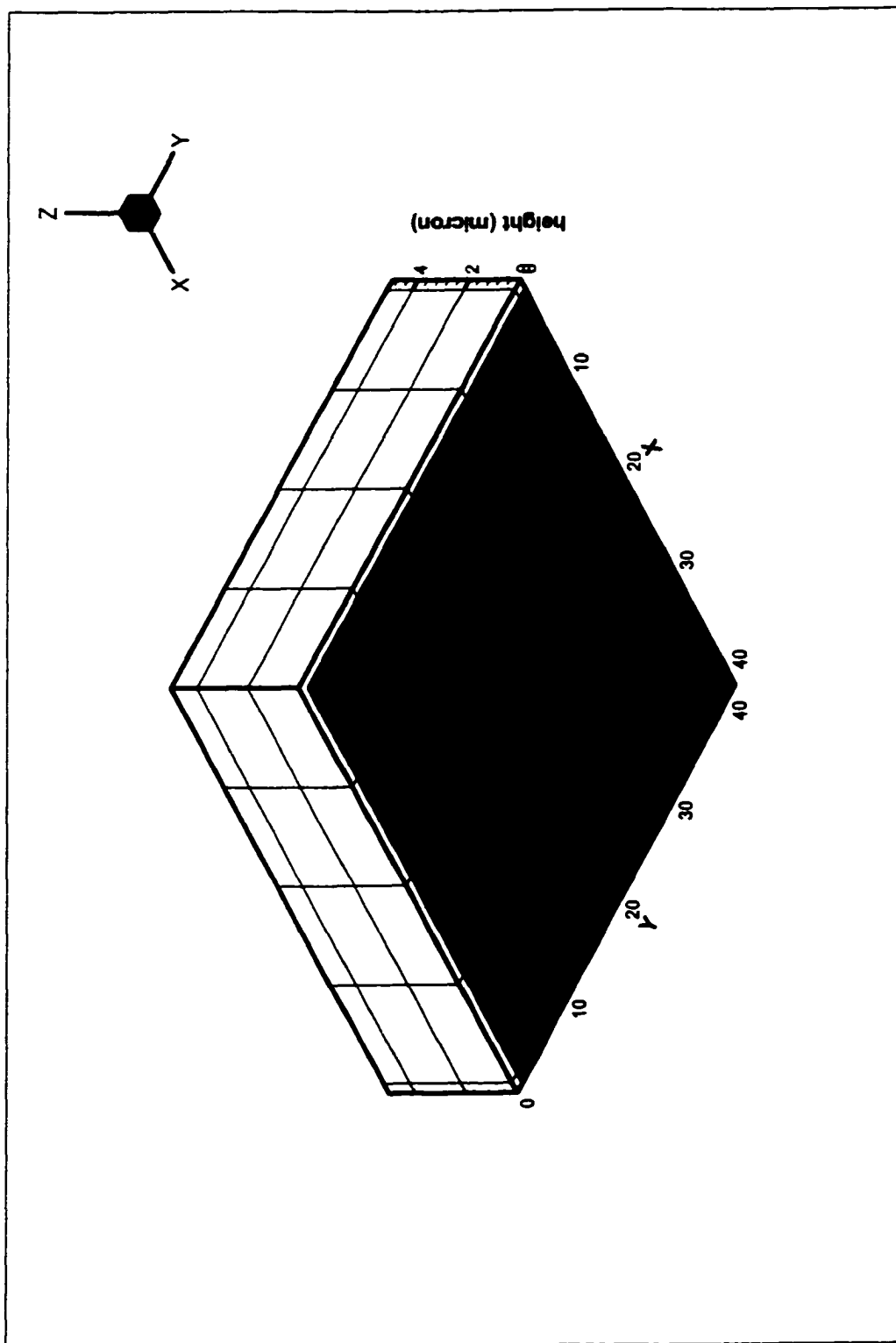


Figure 5.3 Convex microlens resulting from 5 layers of the deposit

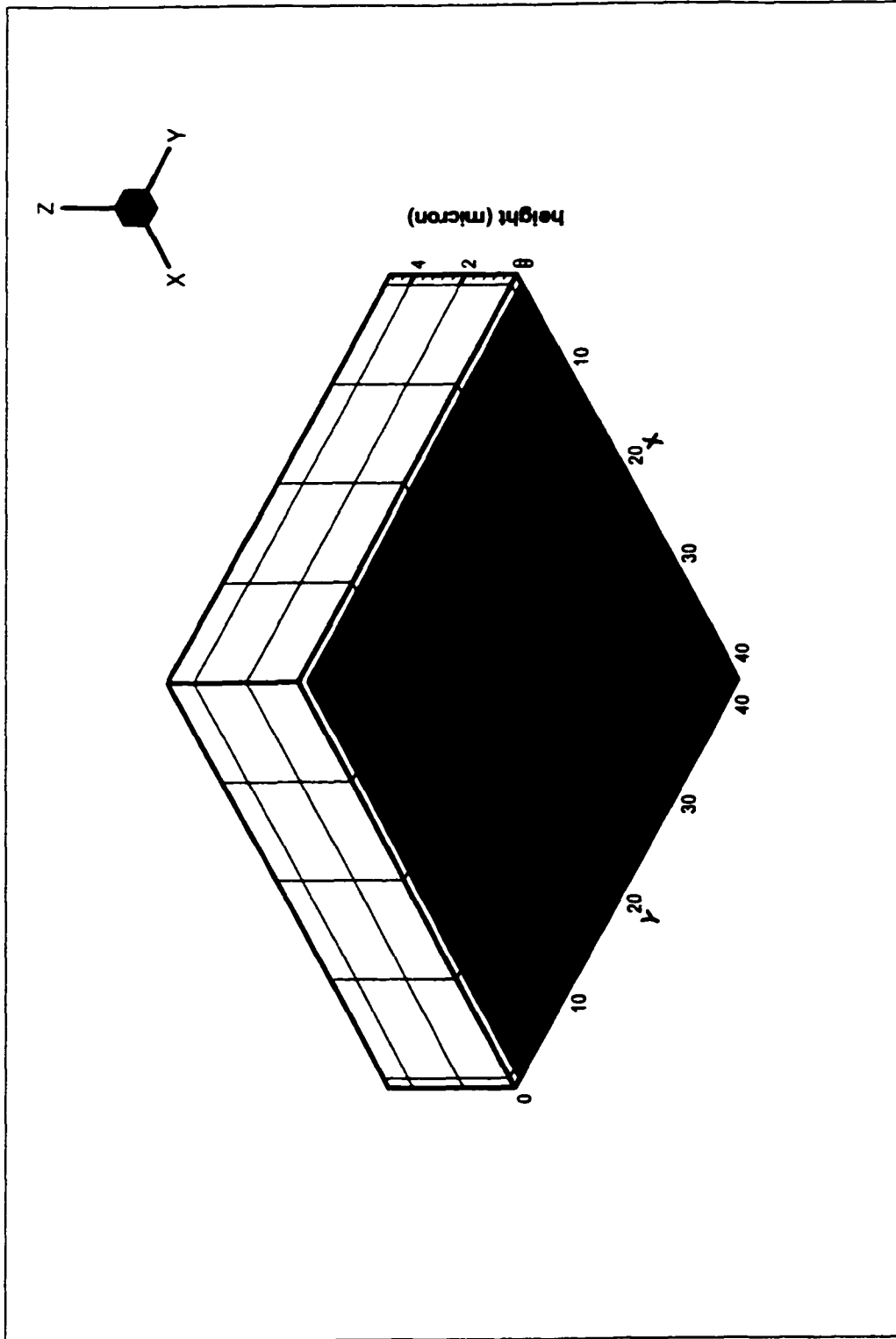


Figure 5.4 Convex microlens resulting from 10 layers of the deposit

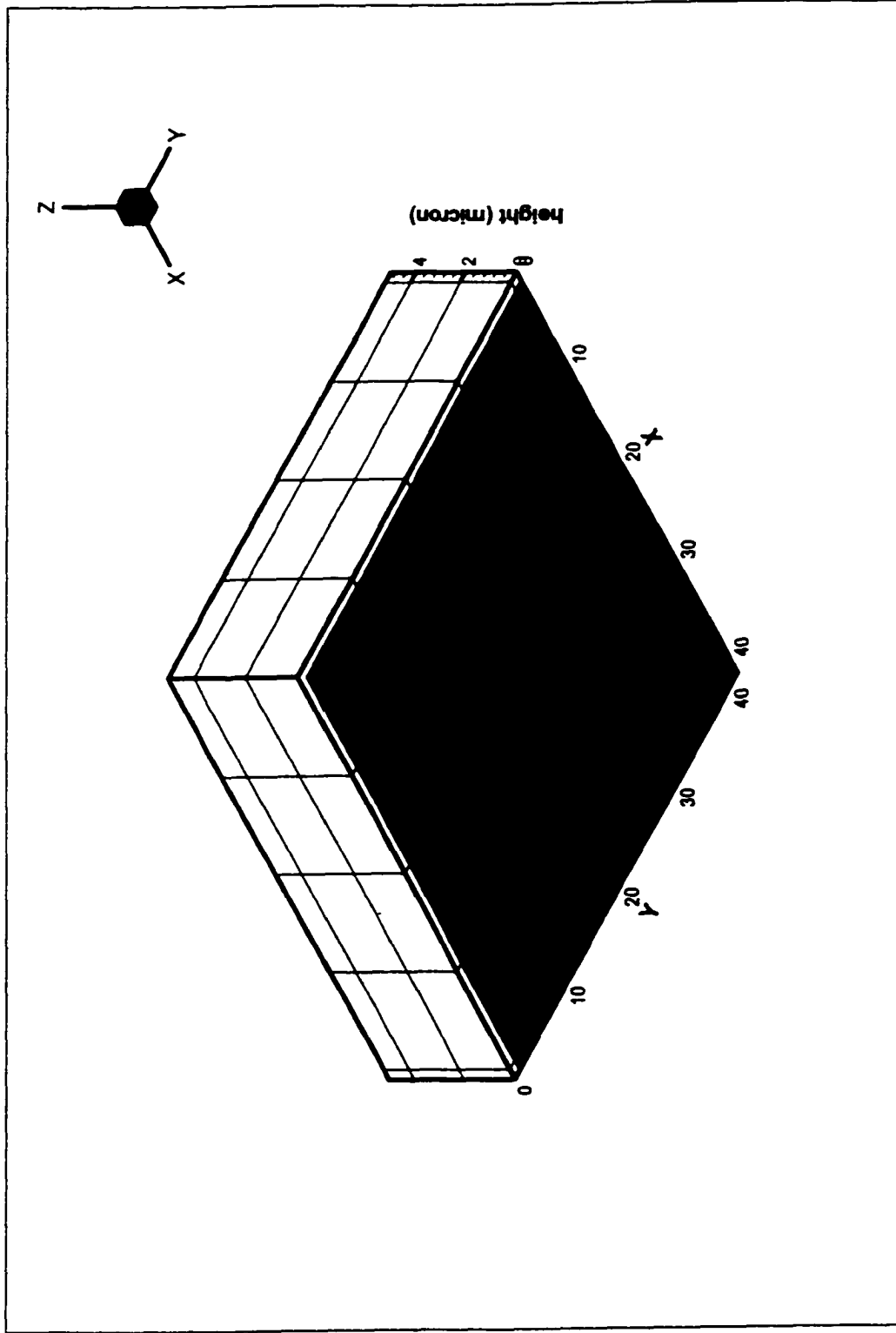


Figure 5.5 Convex microlens resulting from 15 layers of the deposit

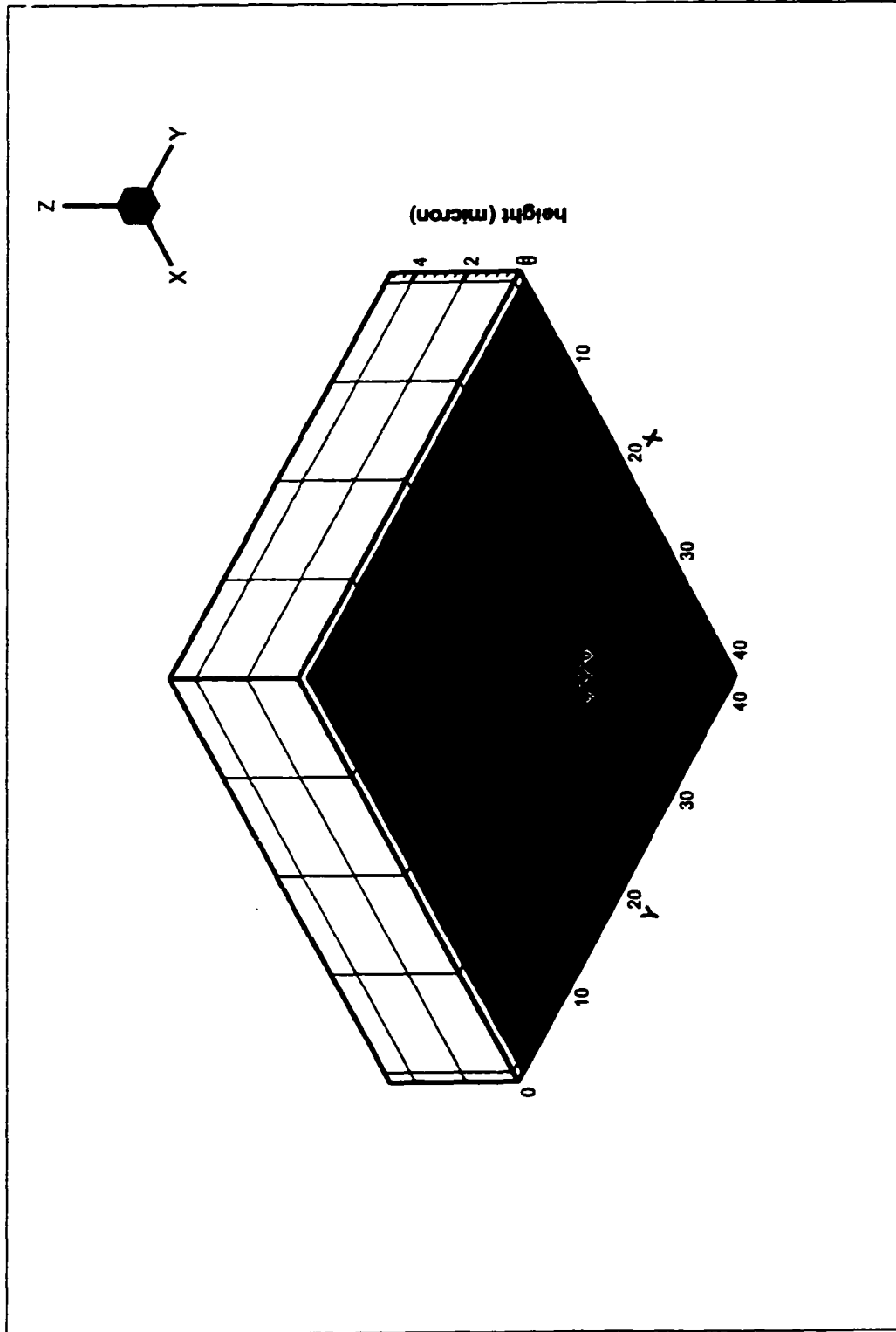


Figure 5.6 Convex microlens resulting from 20 layers of the deposit

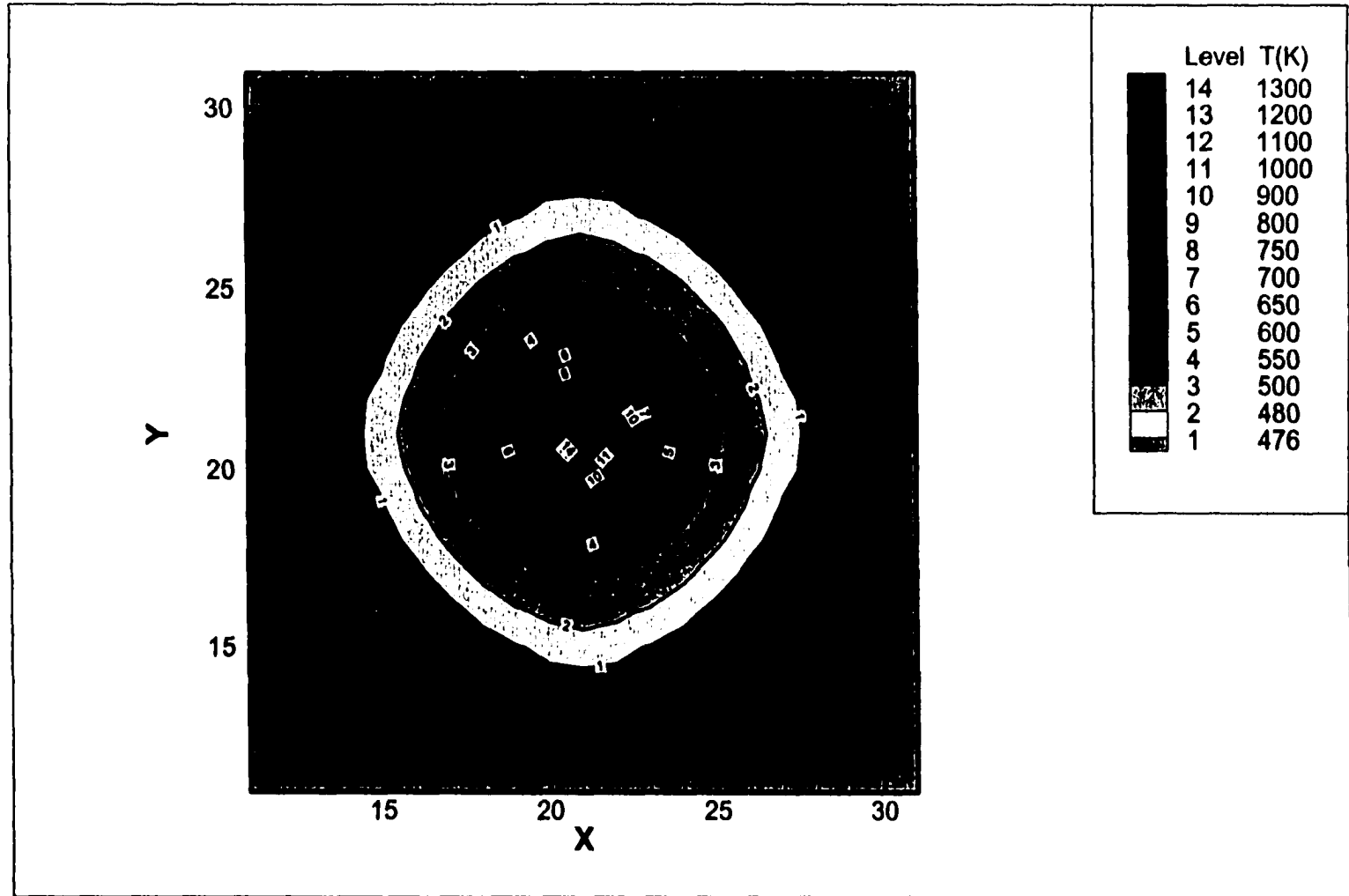


Figure 5.8 Temperature contour on the surface of the substrate ($P_0 = 0.08W$, Layer = 0, Position = A)

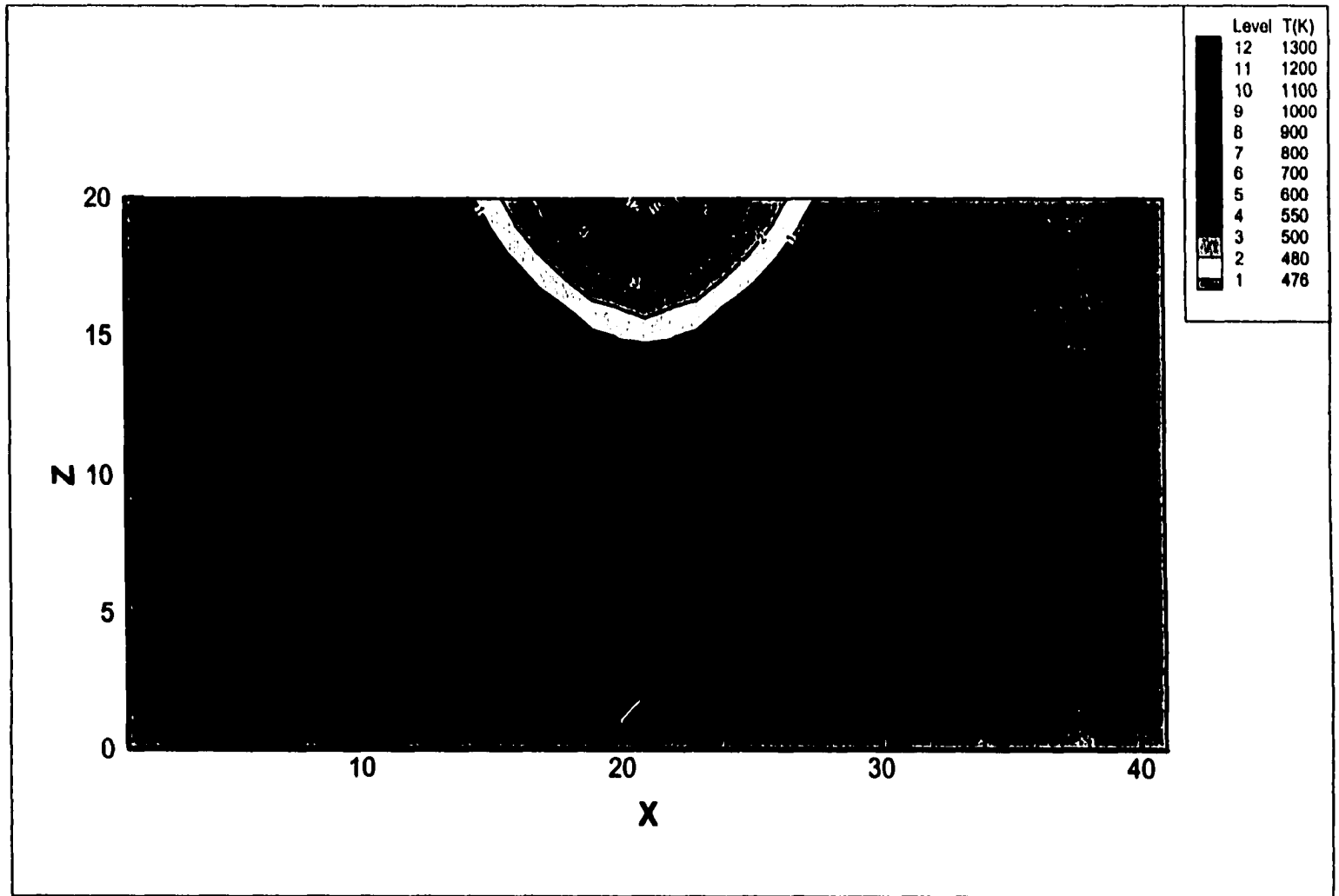


Figure 5.9 Temperature contour on the vertical cross-section of the substrate ($P_0 = 0.08W$, Layer = 0, Position = A)

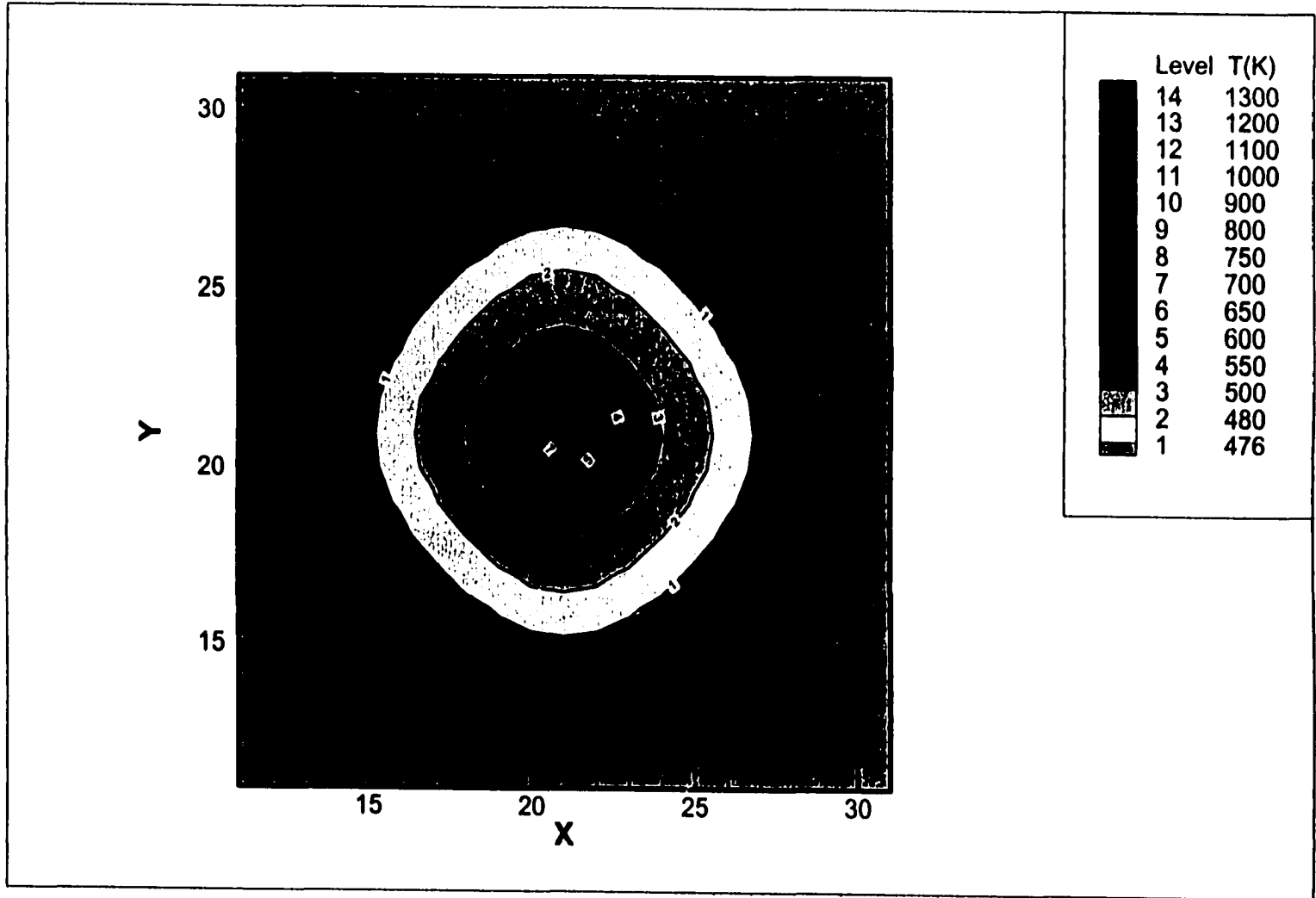


Figure 5.10 Temperature contour on the surface of the deposit ($P_0 = 0.08W$, Layer = 5, Position = A)

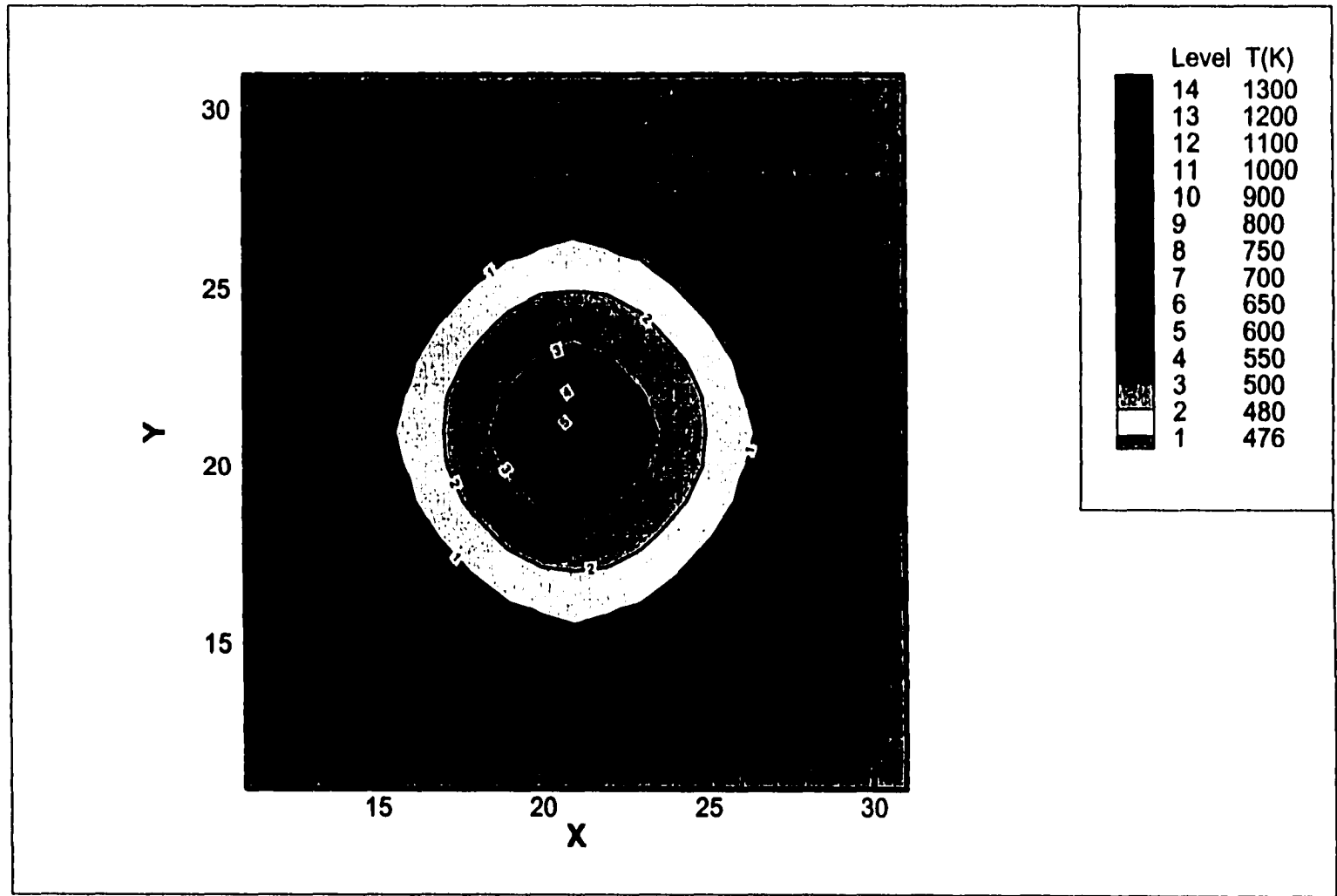


Figure 5.11 Temperature contour on the surface of the deposit ($P_0 = 0.08W$, Layer = 10, Position = A)

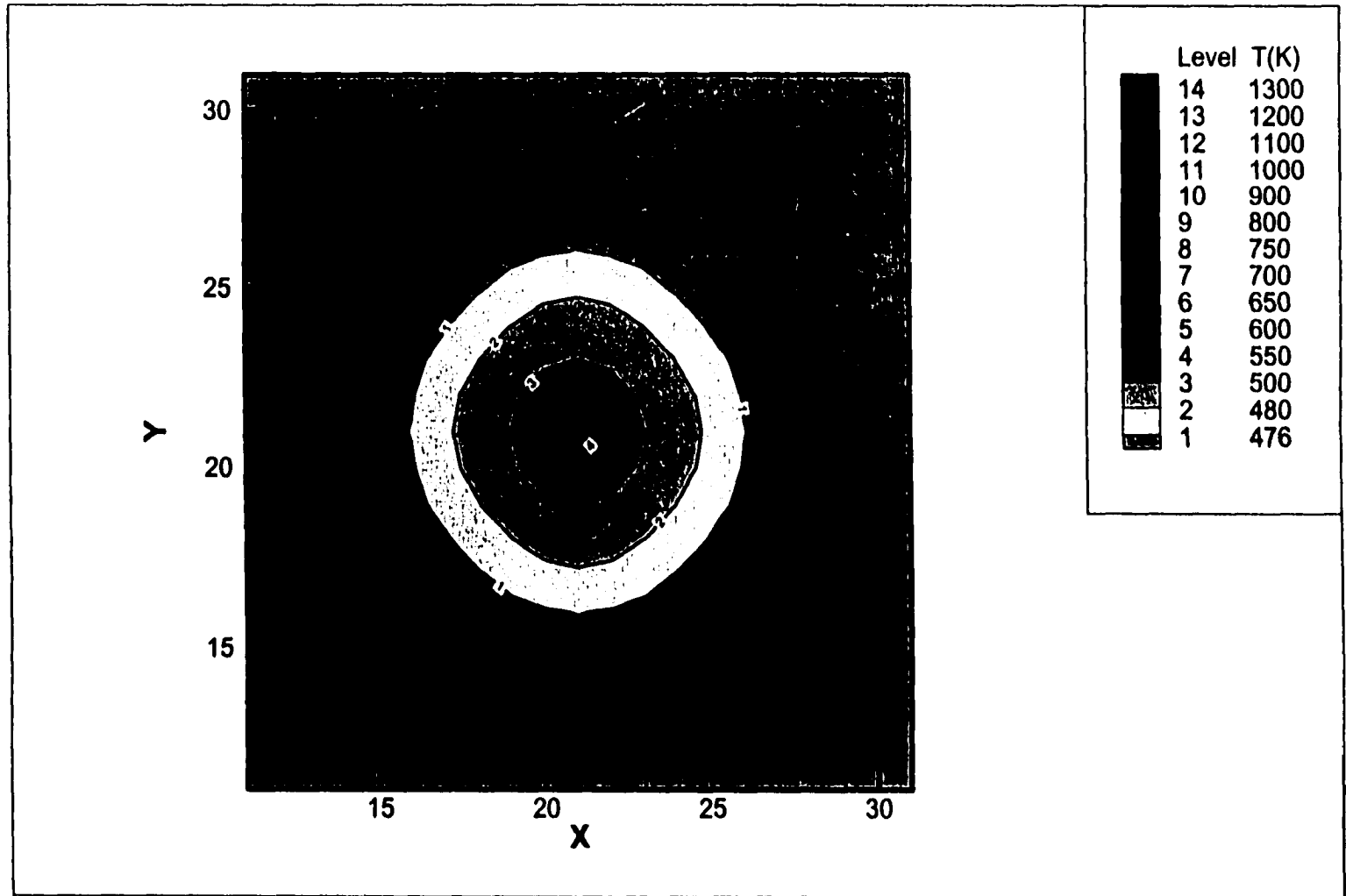


Figure 5.12 Temperature contour on the surface of the deposit ($P_0 = 0.08W$, Layer = 15, Position = A)

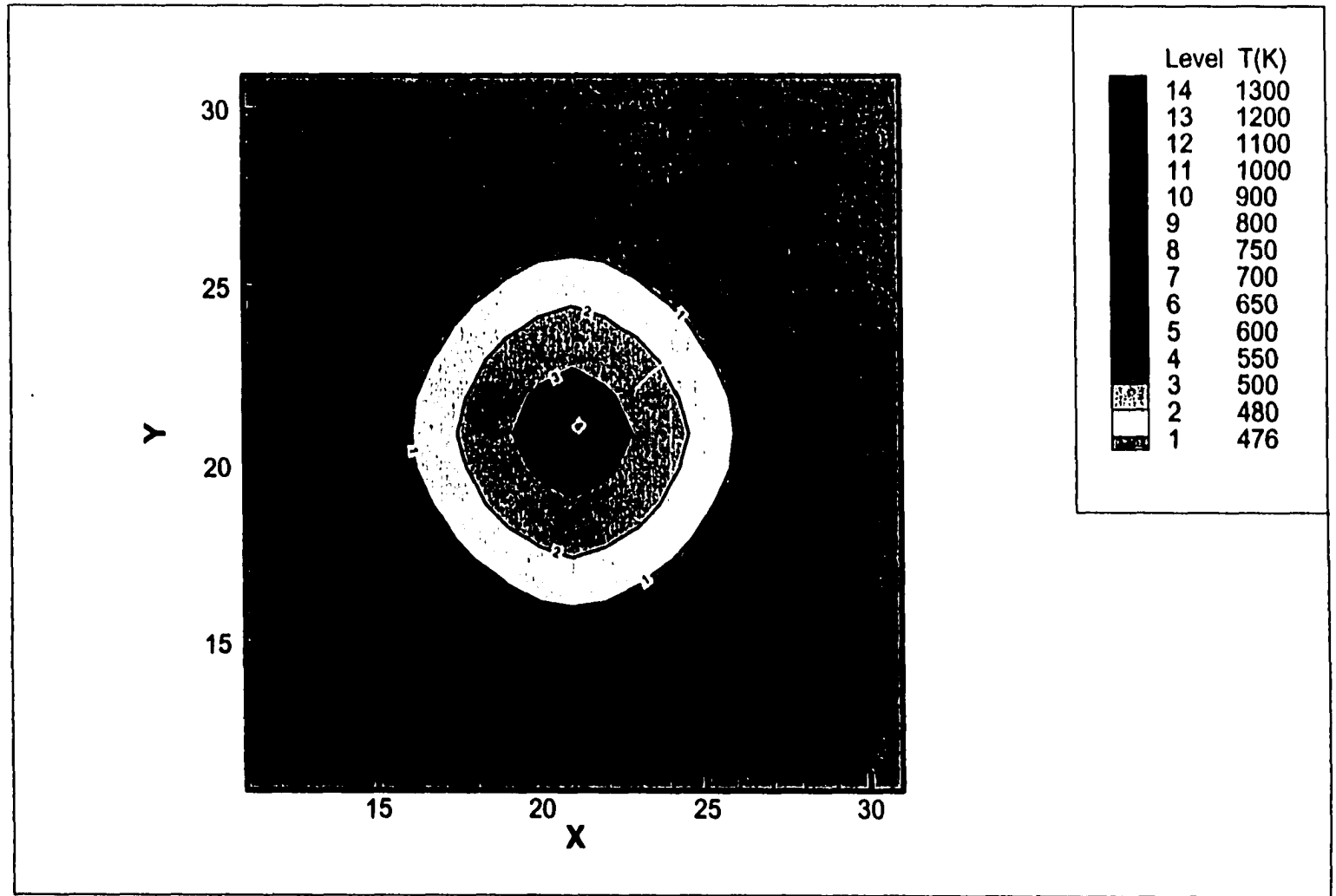


Figure 5.13 Temperature contour on the surface of the deposit ($P_0 = 0.08W$, Layer = 20, Position = A)

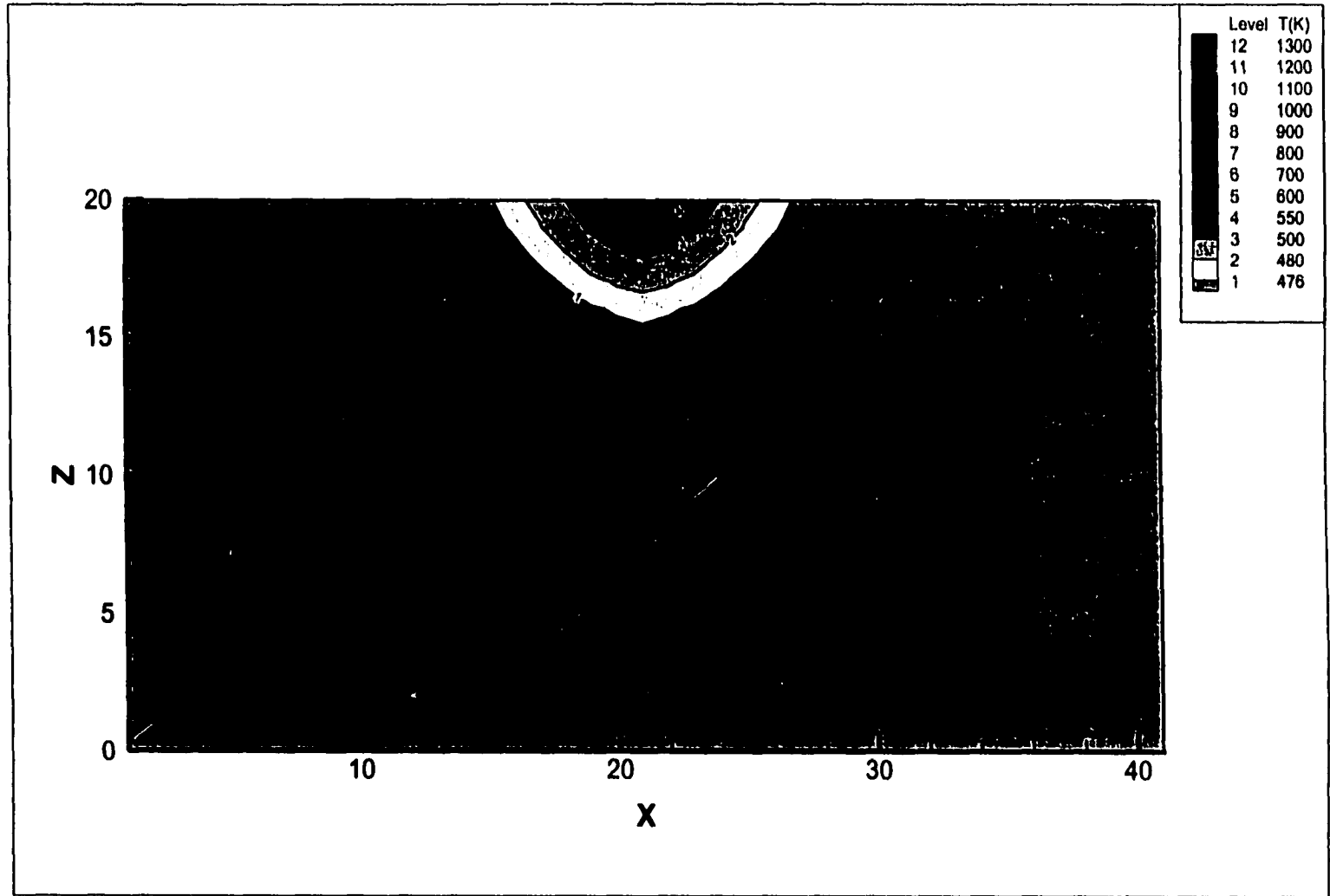


Figure 5.14 Temperature contour on the vertical cross-section of the substrate ($P_0 = 0.08W$, Layer = 5, Position = A)

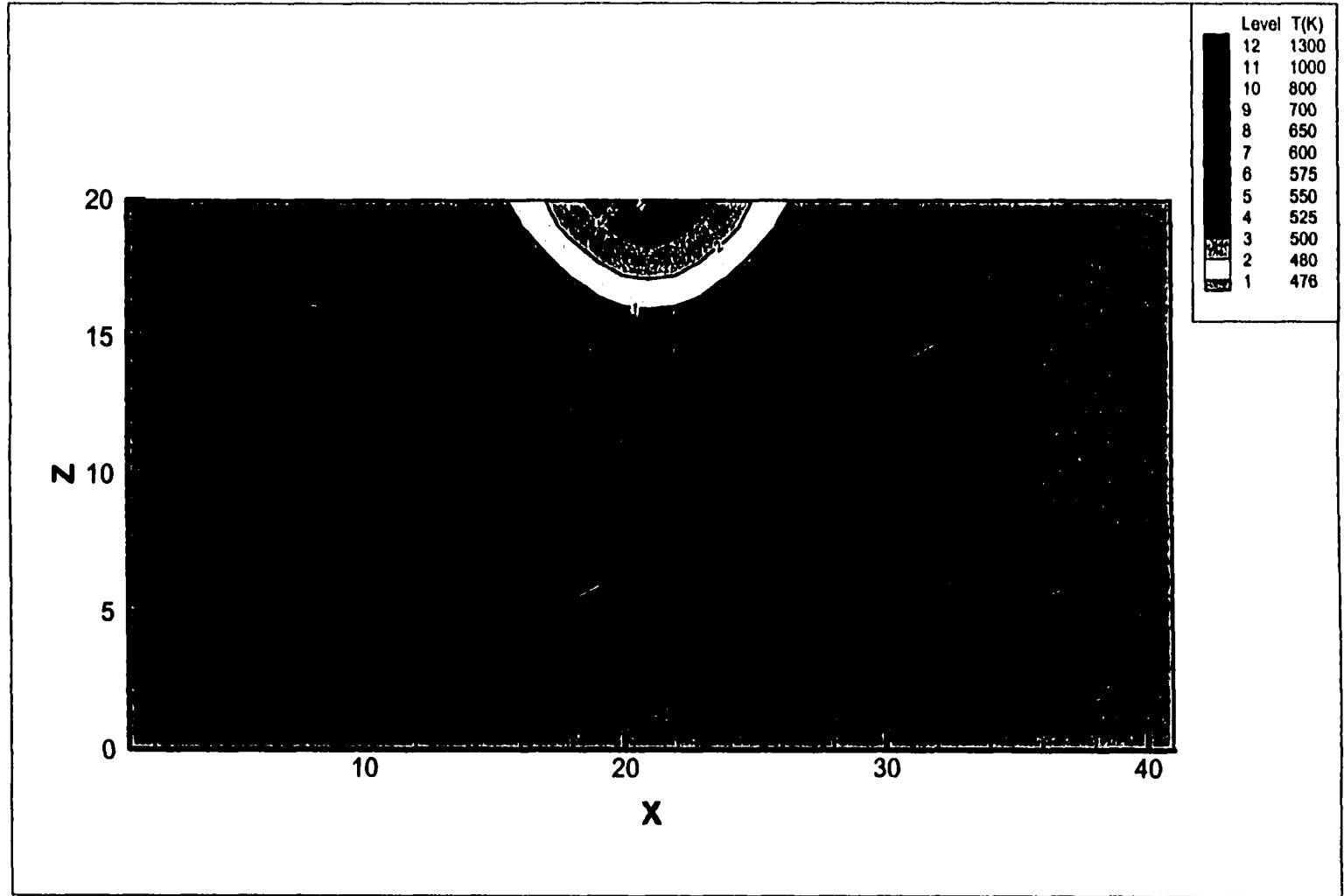


Figure 5.15 Temperature contour on the vertical cross-section of the substrate ($P_0 = 0.08W$, Layer = 10, Position = A)

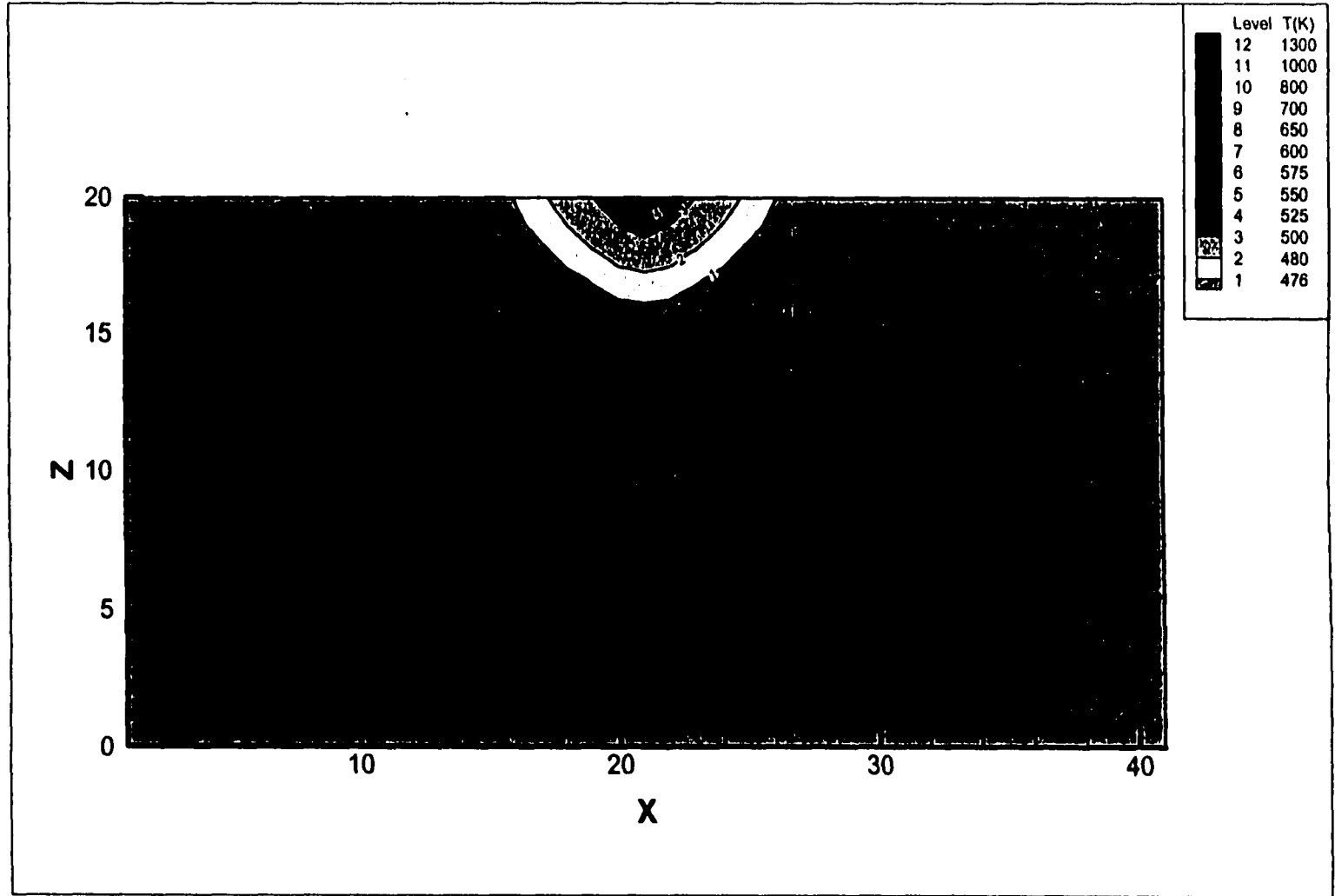


Figure 5.16 Temperature contour on the vertical cross-section of the substrate ($P_0 = 0.08W$, Layer = 15, Position = A)

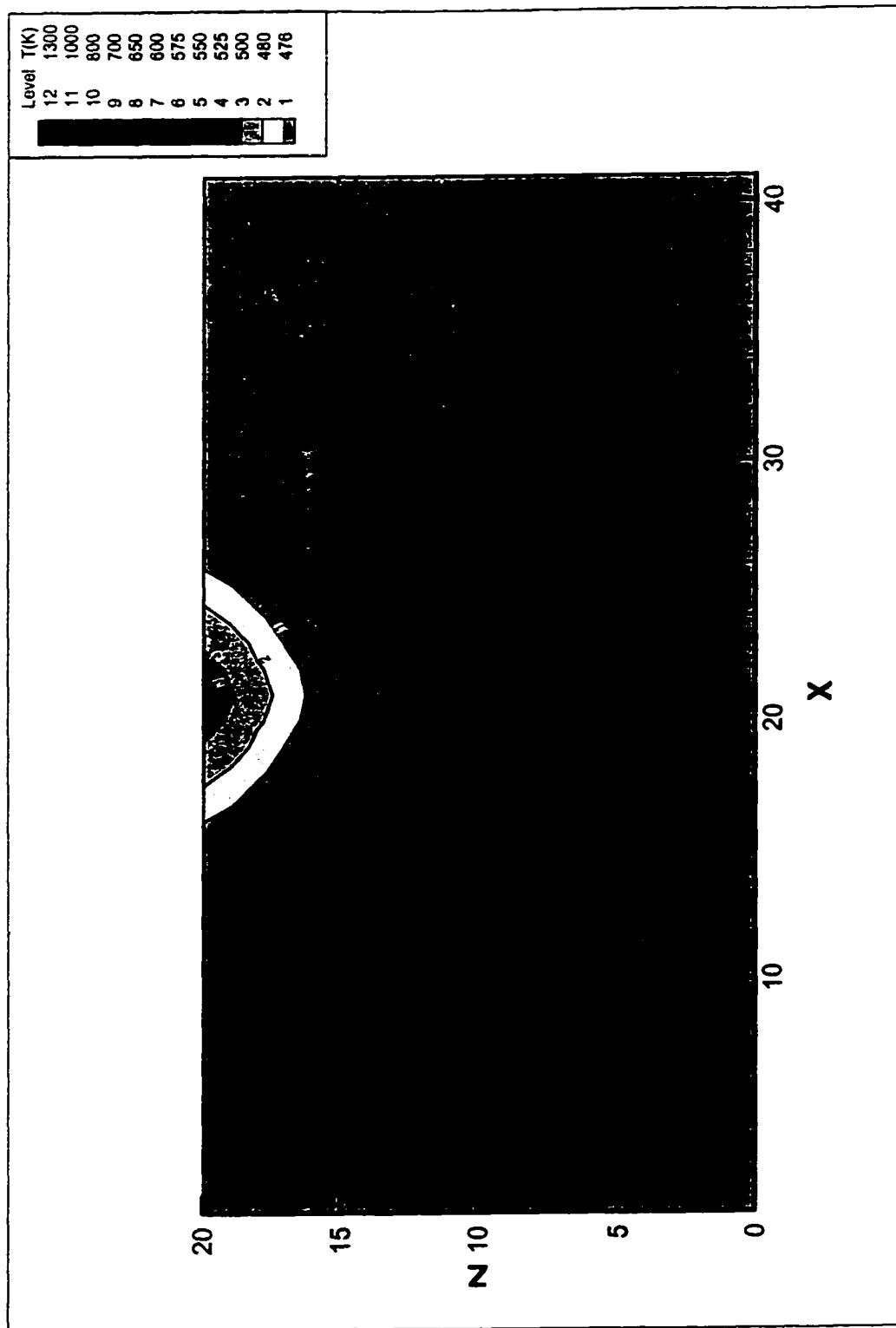


Figure 5.17 Temperature contour on the vertical cross-section of the substrate ($P_0 = 0.08W$, Layer = 20, Position = A)

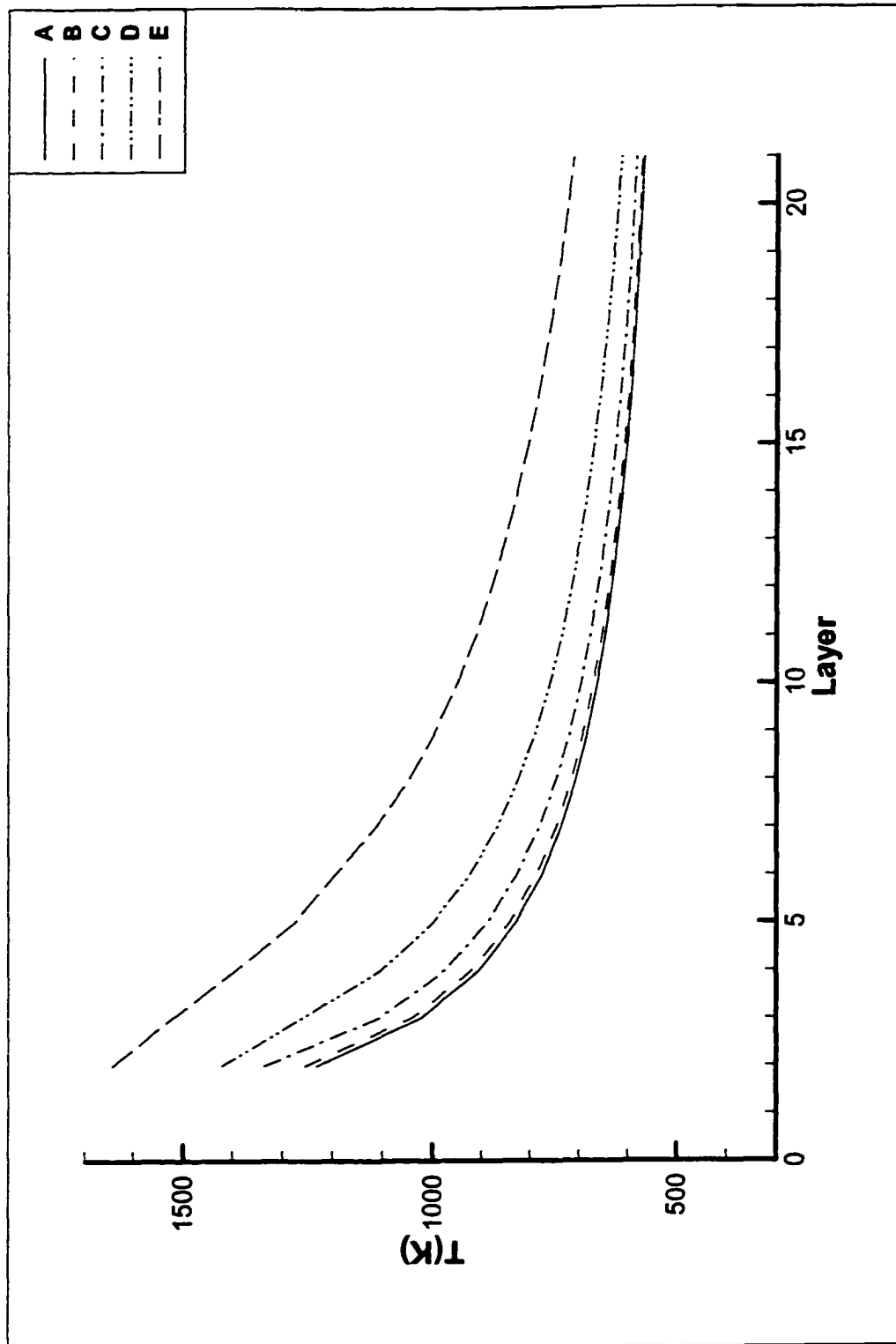


Figure 5.18 Maximum temperature vs. layers of deposit on the surface of the microlens
($P_0 = 0.08W$, Position = A, B, C, D, E)

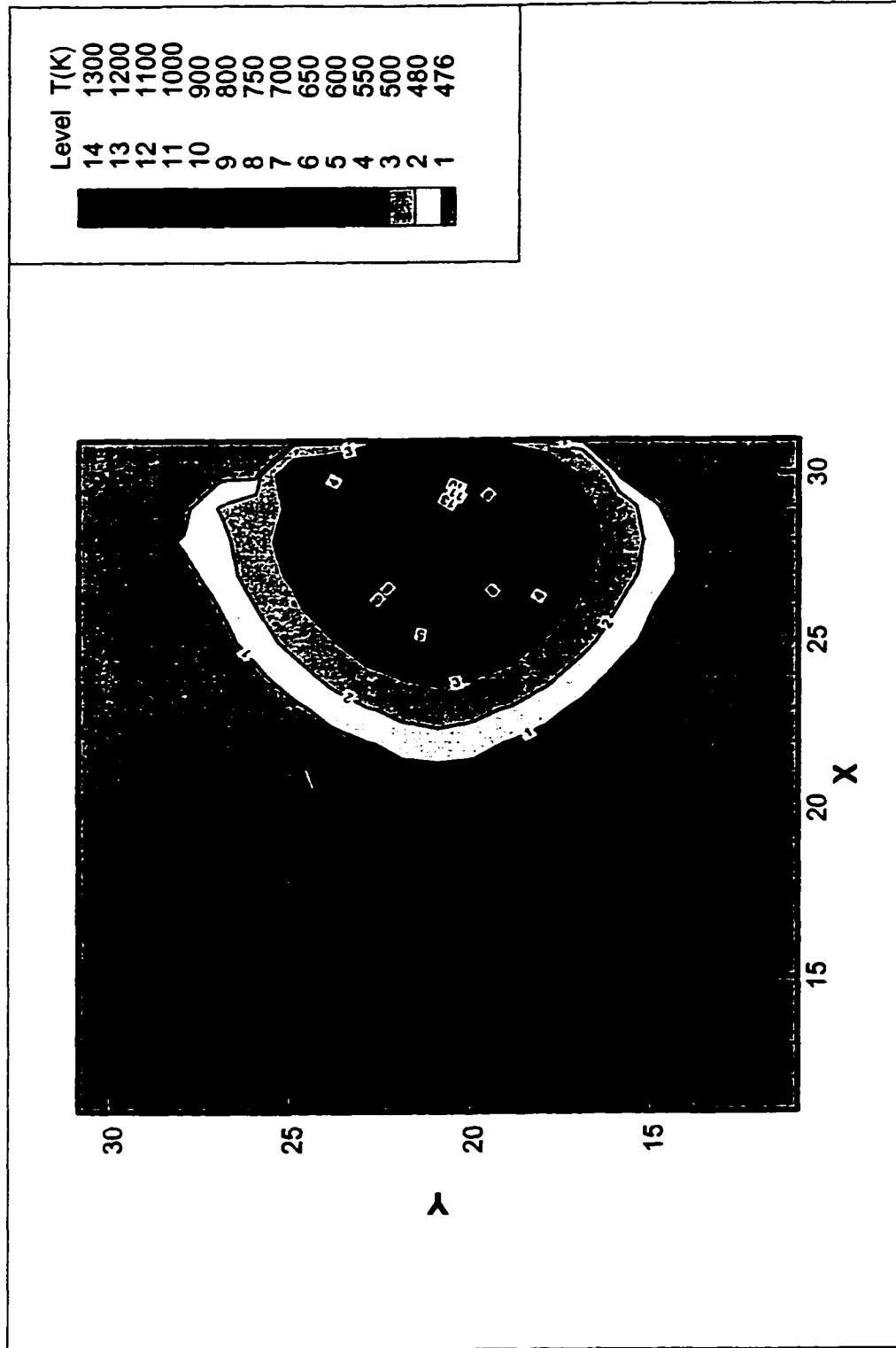


Figure 5.19 Temperature contour on the surface of the substrate ($P_0 = 0.08W$, Layer = 0, Position = E)

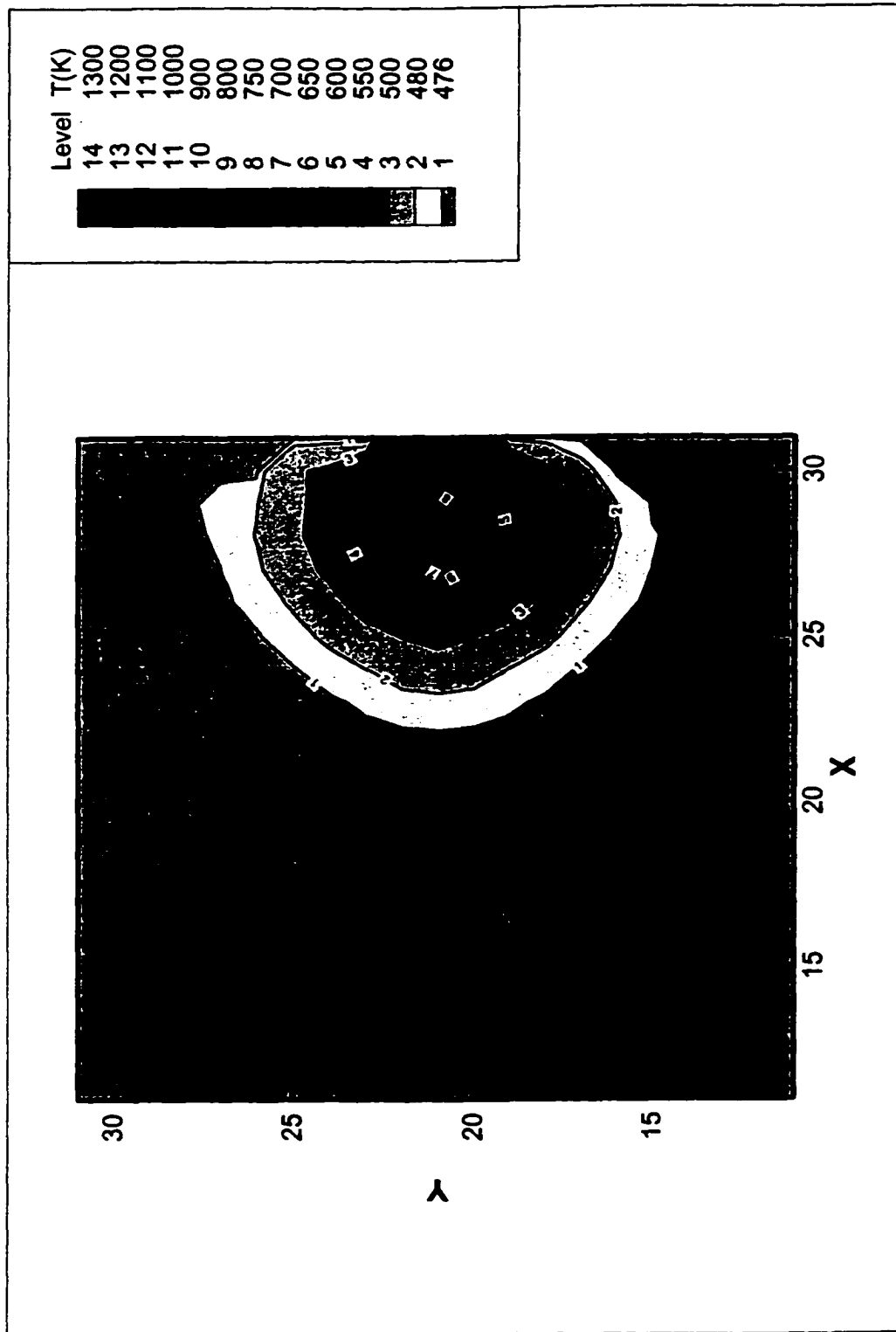


Figure 5.20 Temperature contour on the surface of the deposit ($P_0 = 0.08W$, Layer = 5, Position = E)

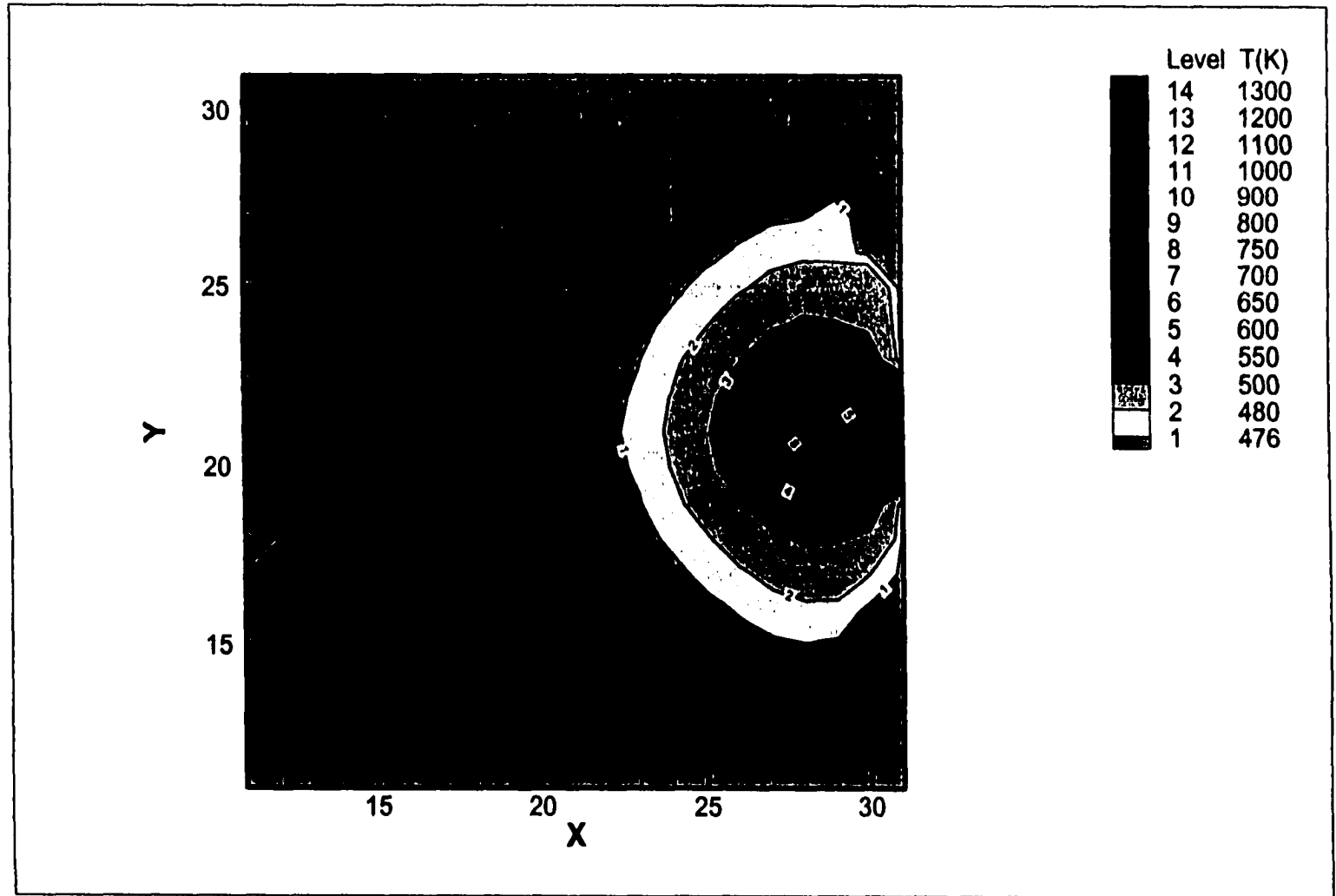


Figure 5.21 Temperature contour on the surface of the deposit ($P_0 = 0.08W$, Layer = 10, Position = E)

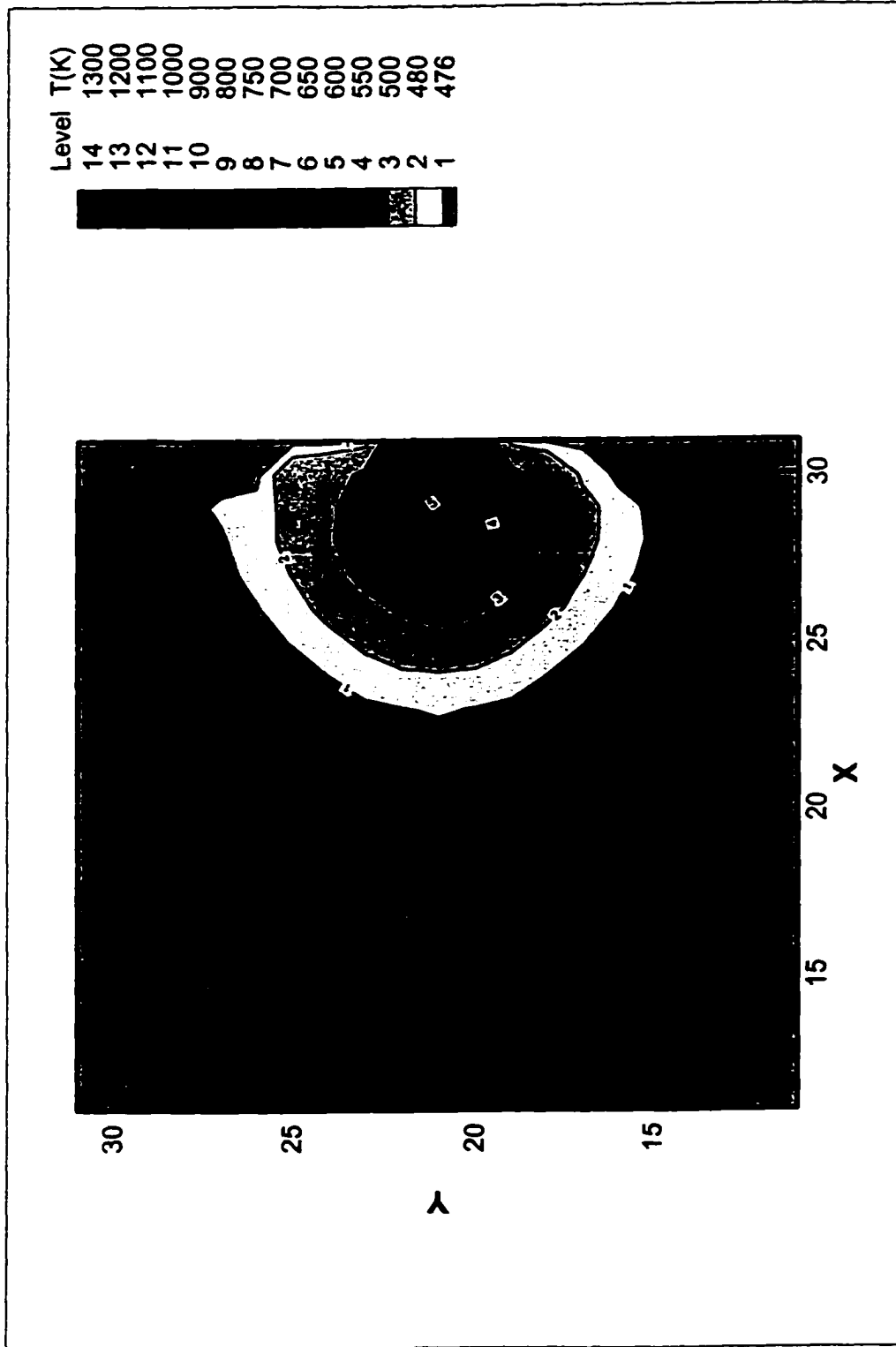


Figure 5.22 Temperature contour on the surface of the deposit ($P_0 = 0.08W$, Layer = 15, Position = E)

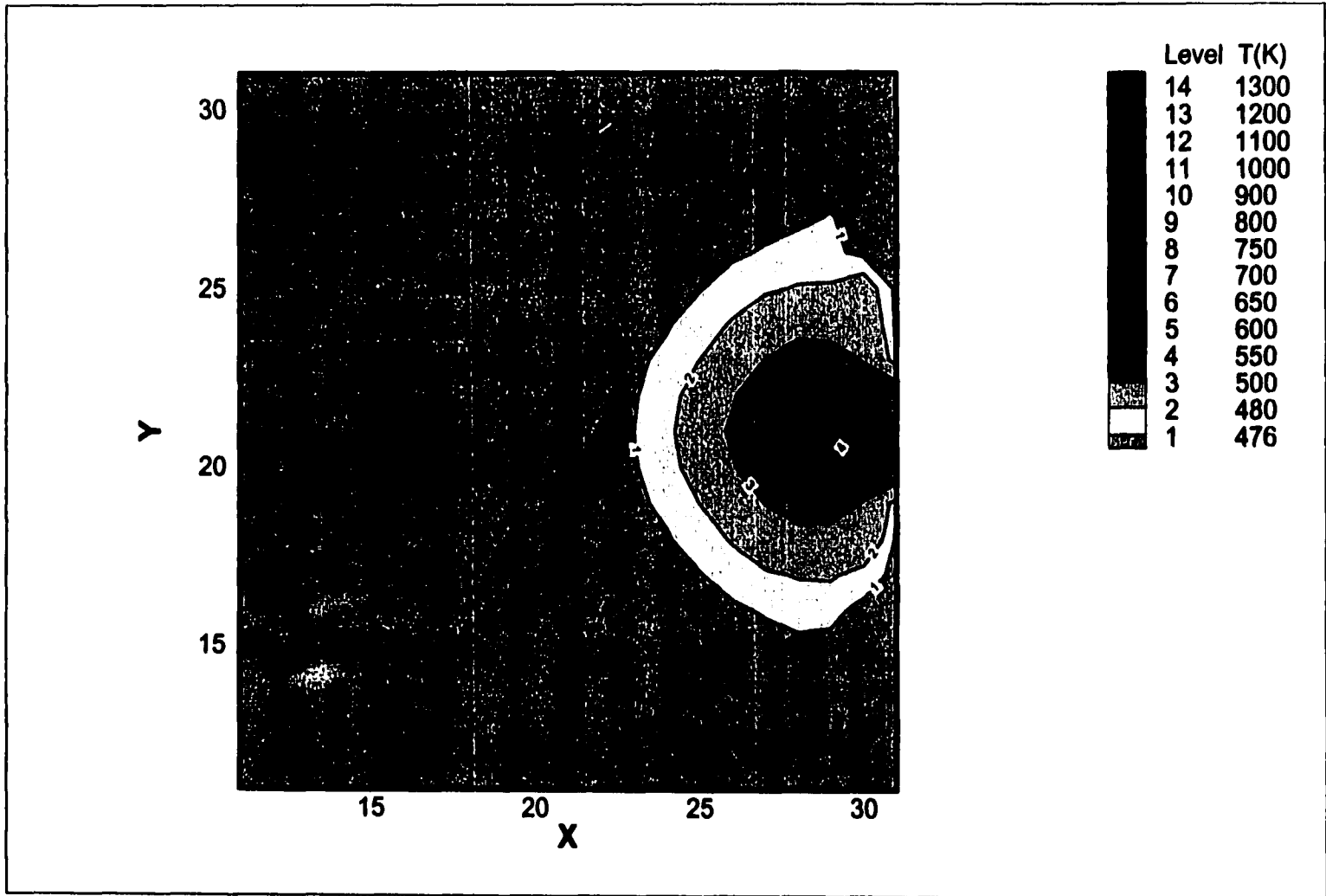


Figure 5.23 Temperature contour on the surface of the deposit ($P_0 = 0.08W$, Layer = 20, Position = E)

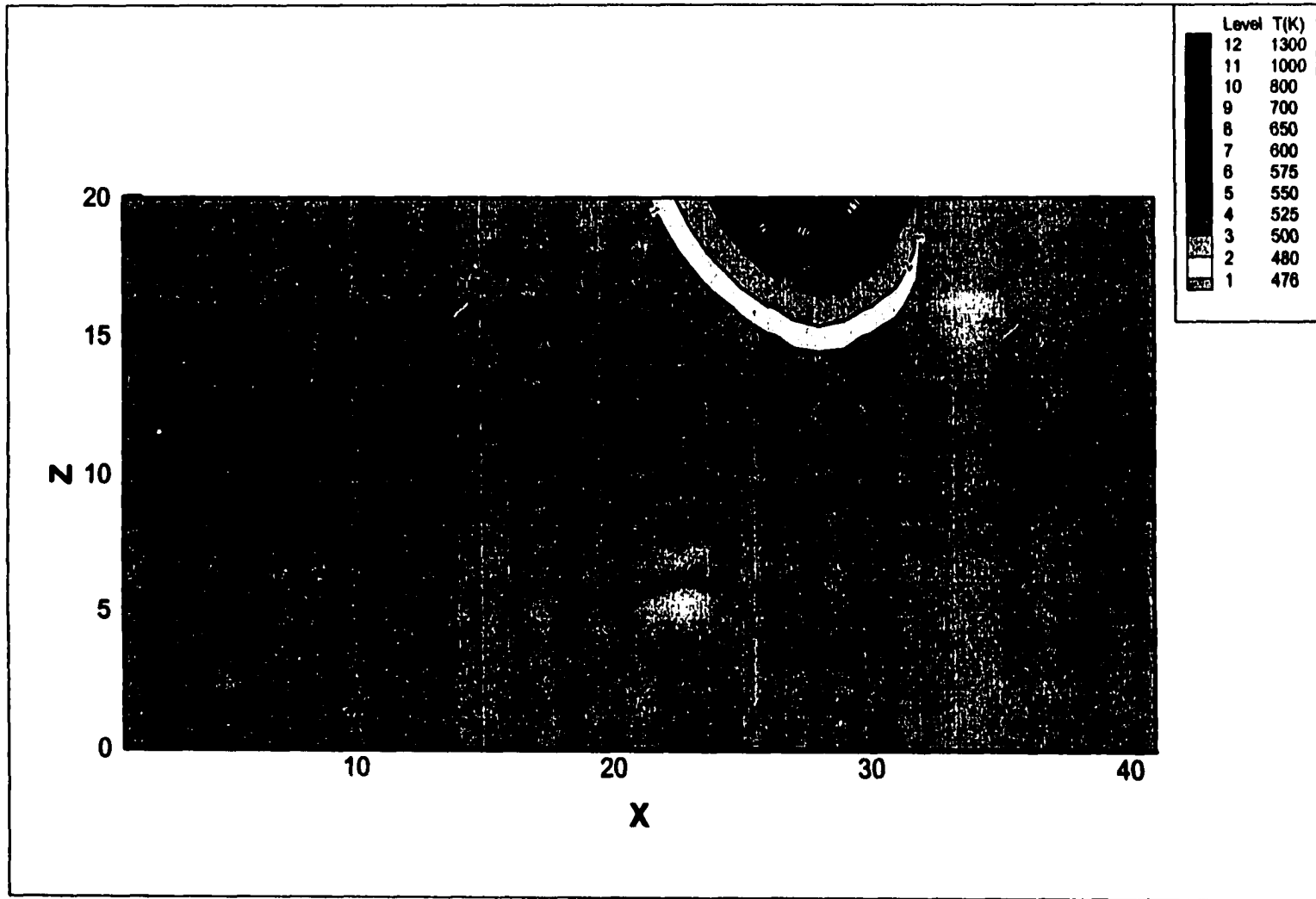


Figure 5.24 Temperature contour on the vertical cross-section of the substrate ($P_0 = 0.08W$, Layer = 0, Position = E)

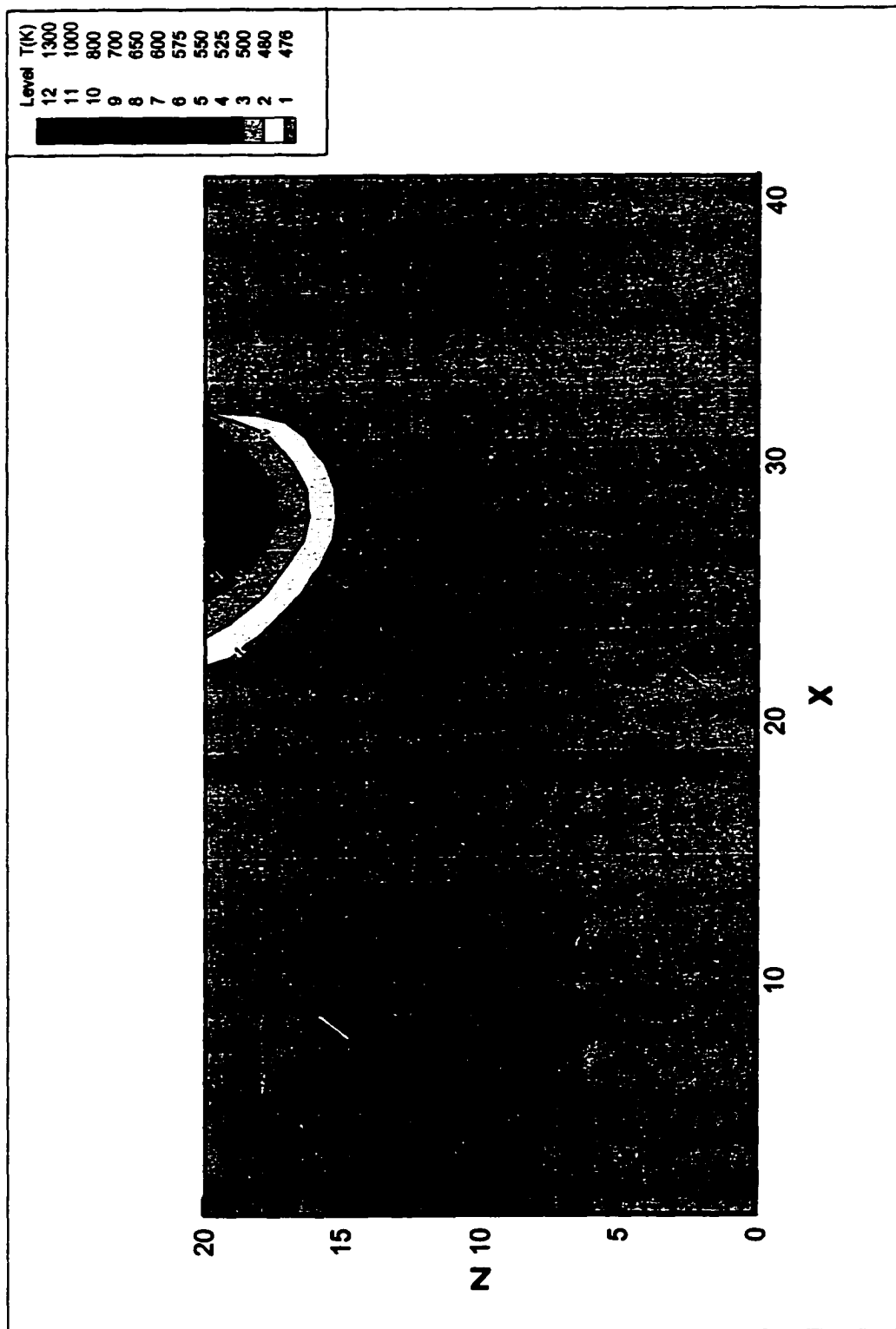


Figure 5.25 Temperature contour on the vertical cross-section of the substrate ($P_0 = 0.08W$, Layer = 5, Position = E)

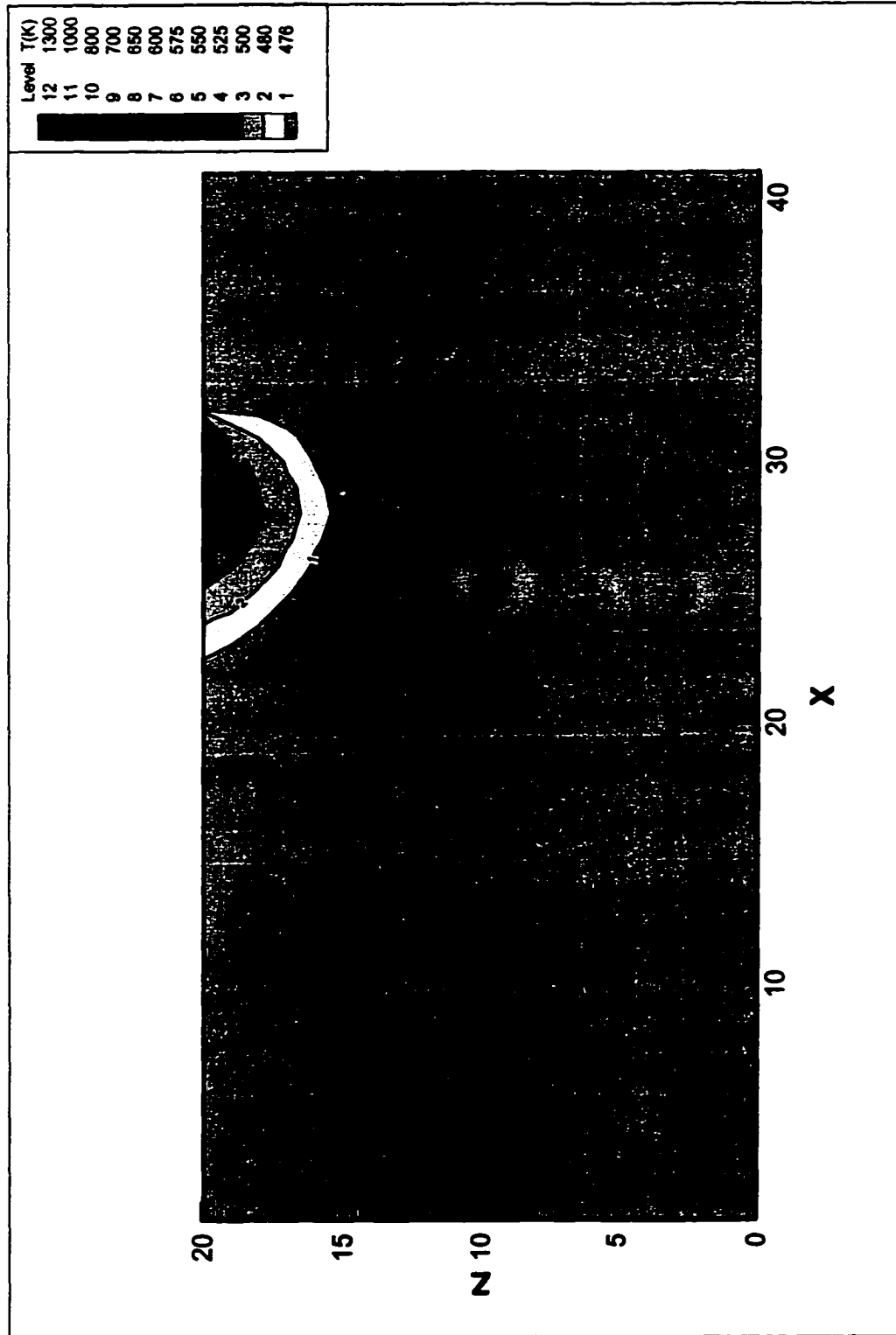


Figure 5.26 Temperature contour on the vertical cross-section of the substrate ($P_0 = 0.08W$, Layer = 10, Position = E)

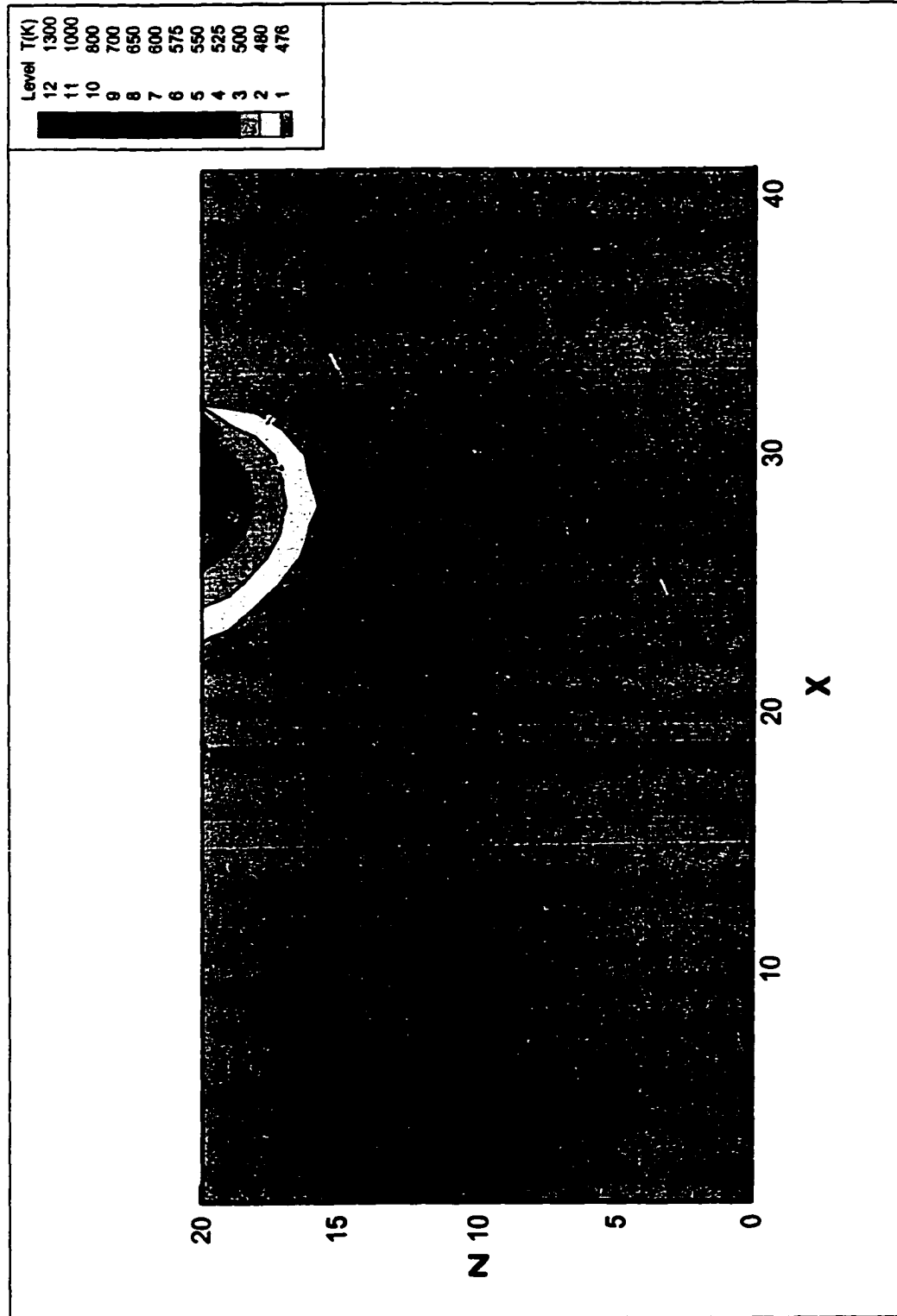


Figure 5.27 Temperature contour on the vertical cross-section of the substrate ($P_0 = 0.08W$, Layer = 15, Position = E)

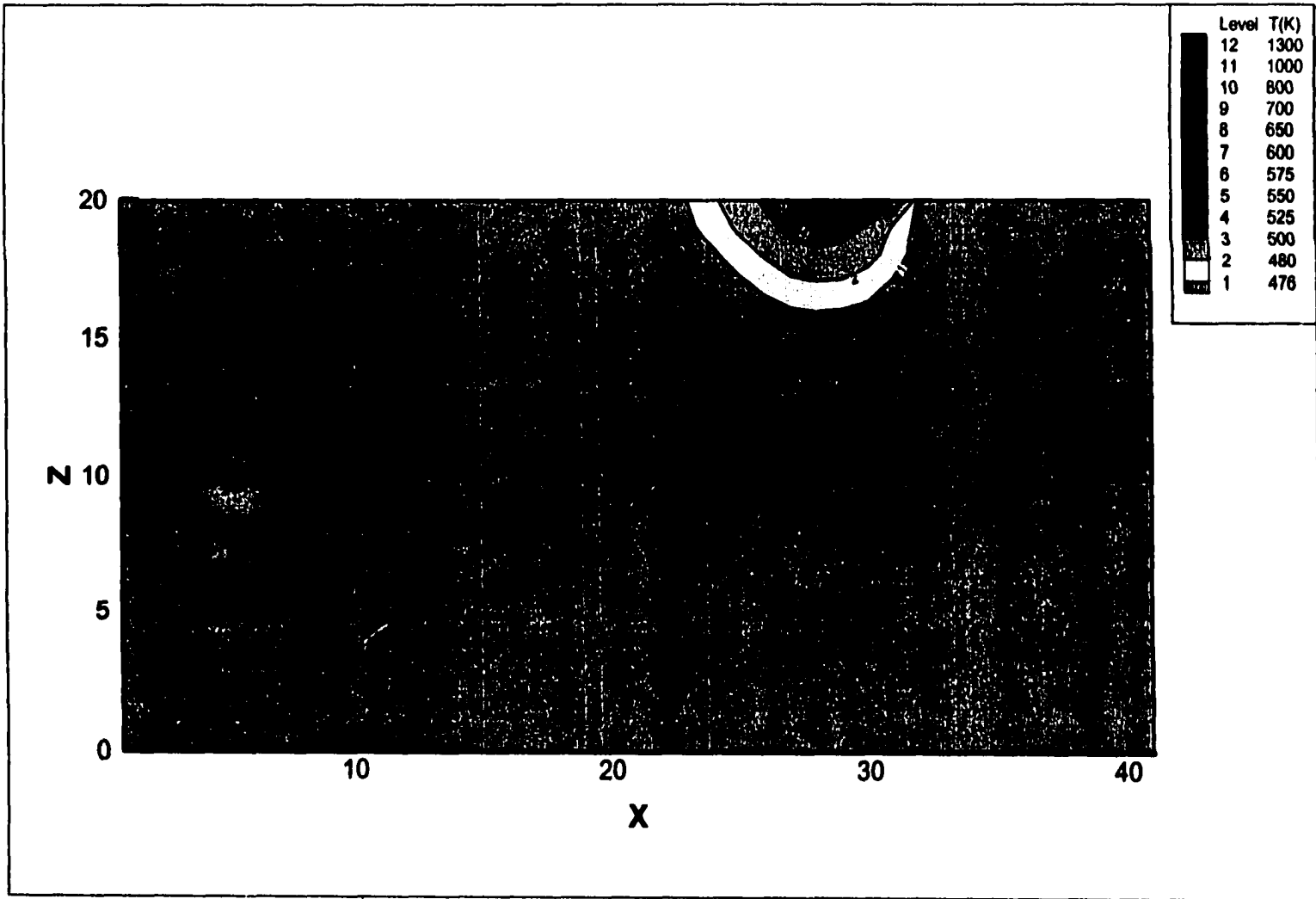


Figure 5.28 Temperature contour on the vertical cross-section of the substrate ($P_0 = 0.08W$, Layer = 20, Position = E)

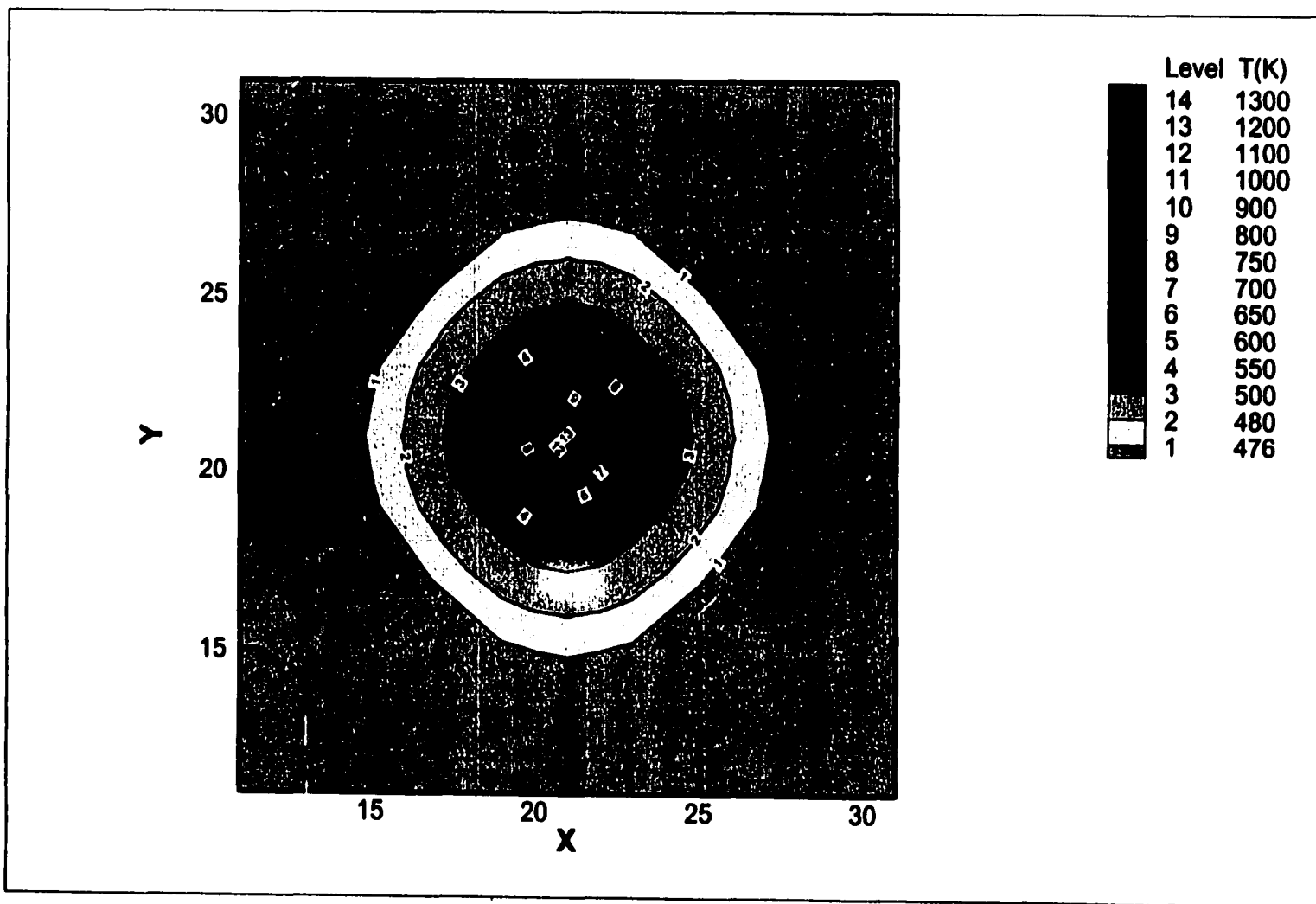


Figure 5.29 Temperature contour on the surface of the substrate ($P_0 = 0.05W$, Layer = 0, Position = A)

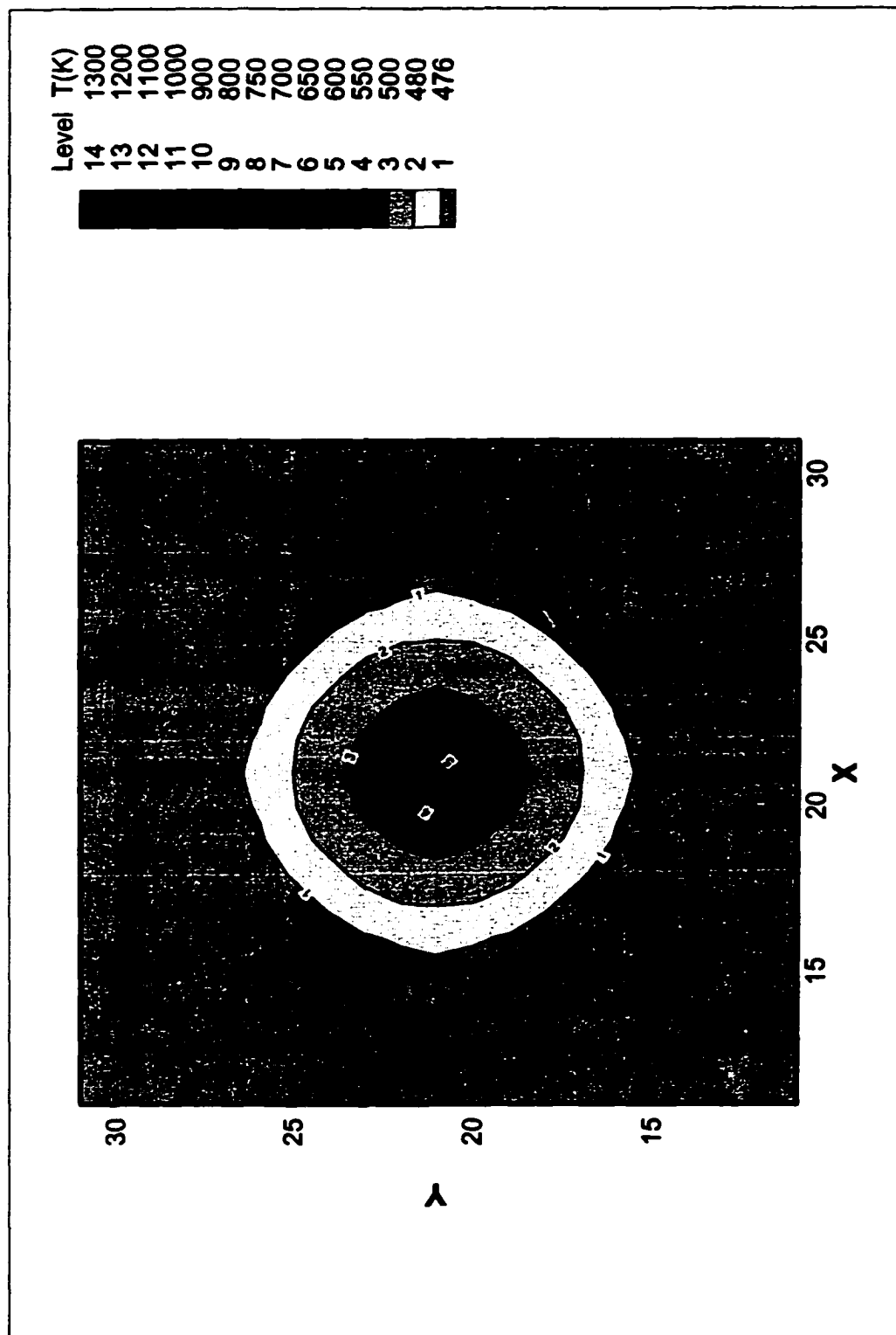


Figure 5.30 Temperature contour on the surface of the deposit ($P_0 = 0.05W$, Layer = 5, Position = A)

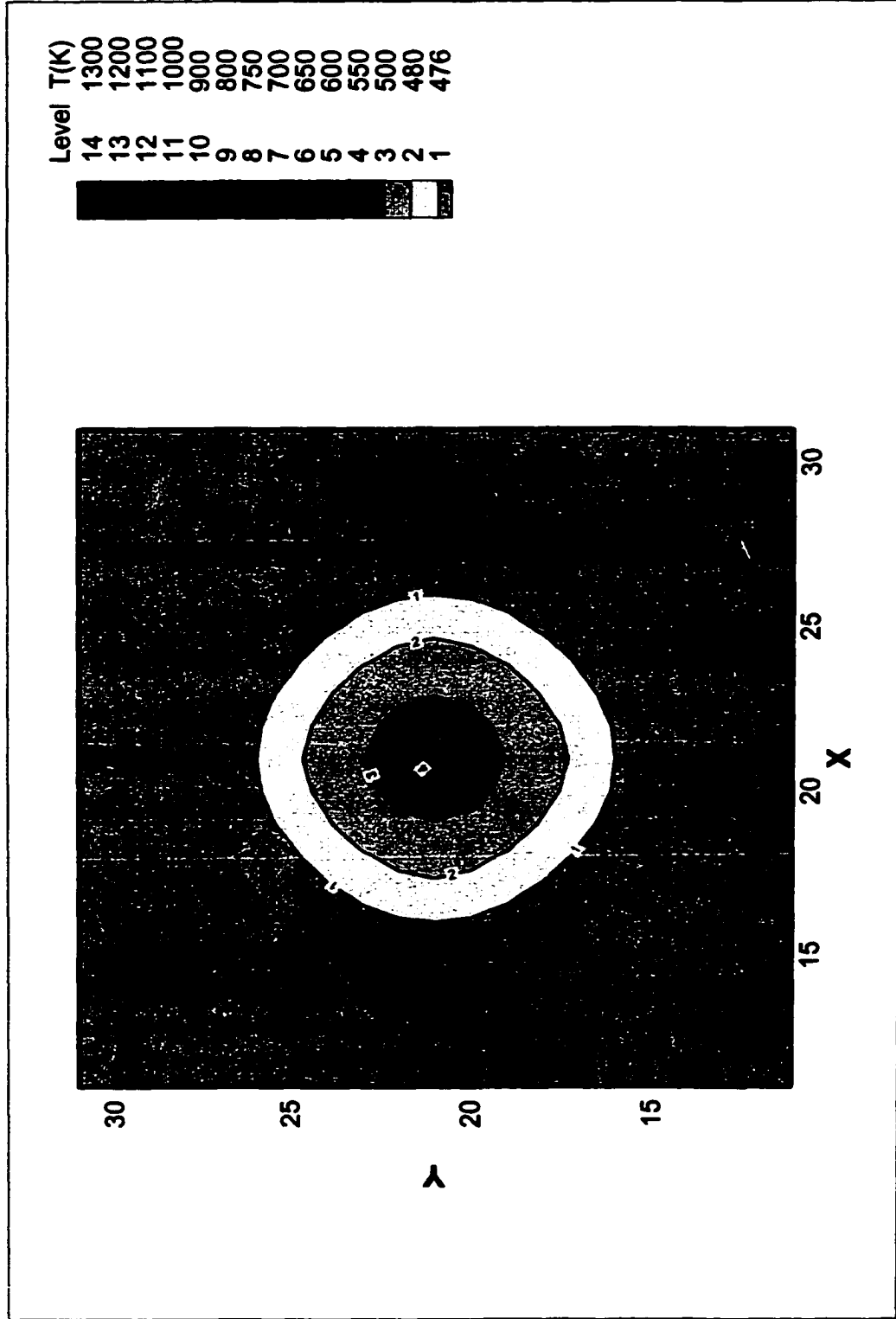


Figure 5.31 Temperature contour on the surface of the deposit ($P_0 = 0.05W$, Layer = 10, Position = A)

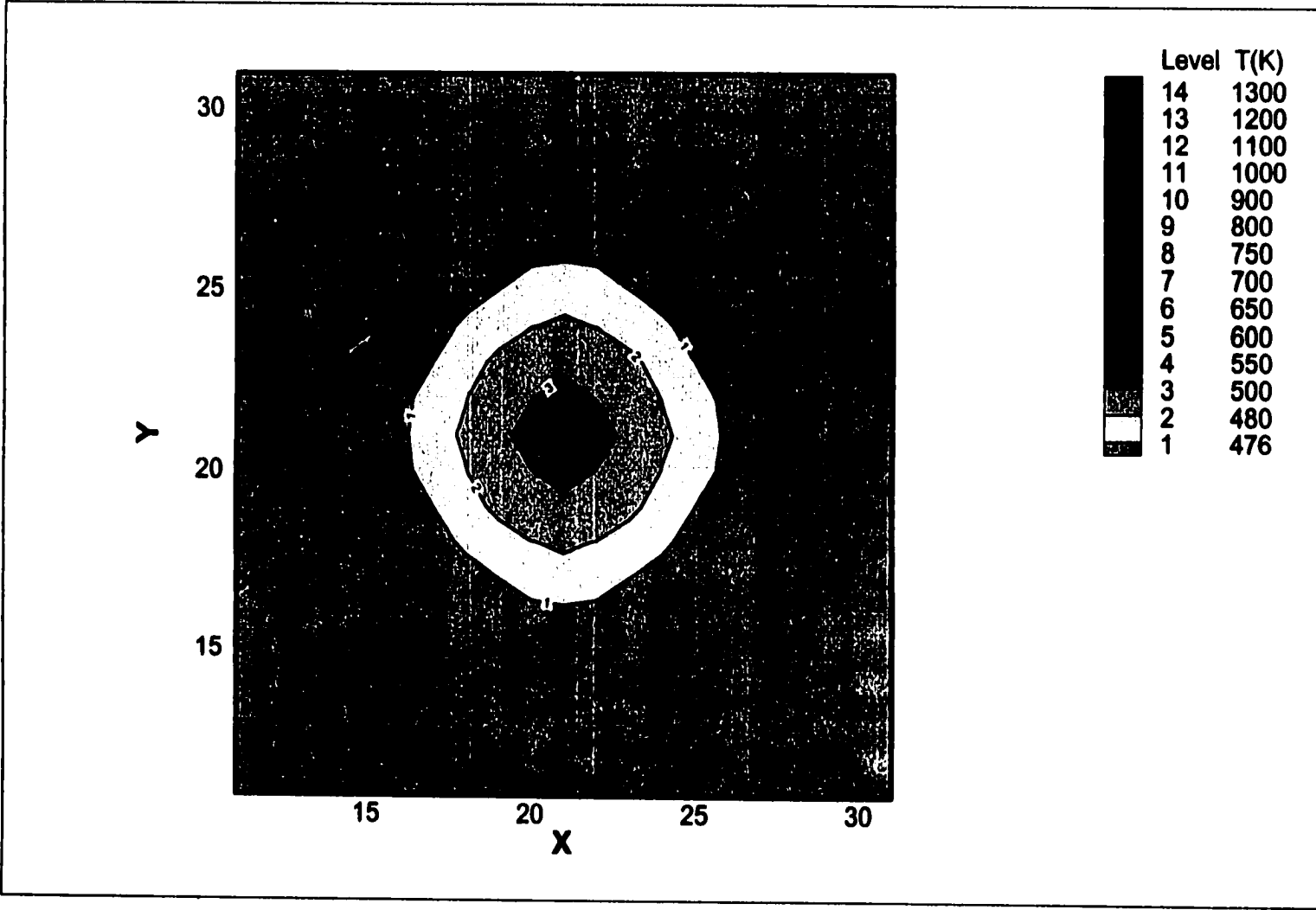


Figure 5.32 Temperature contour on the surface of the deposit ($P_0 = 0.05W$, Layer = 15, Position = A)

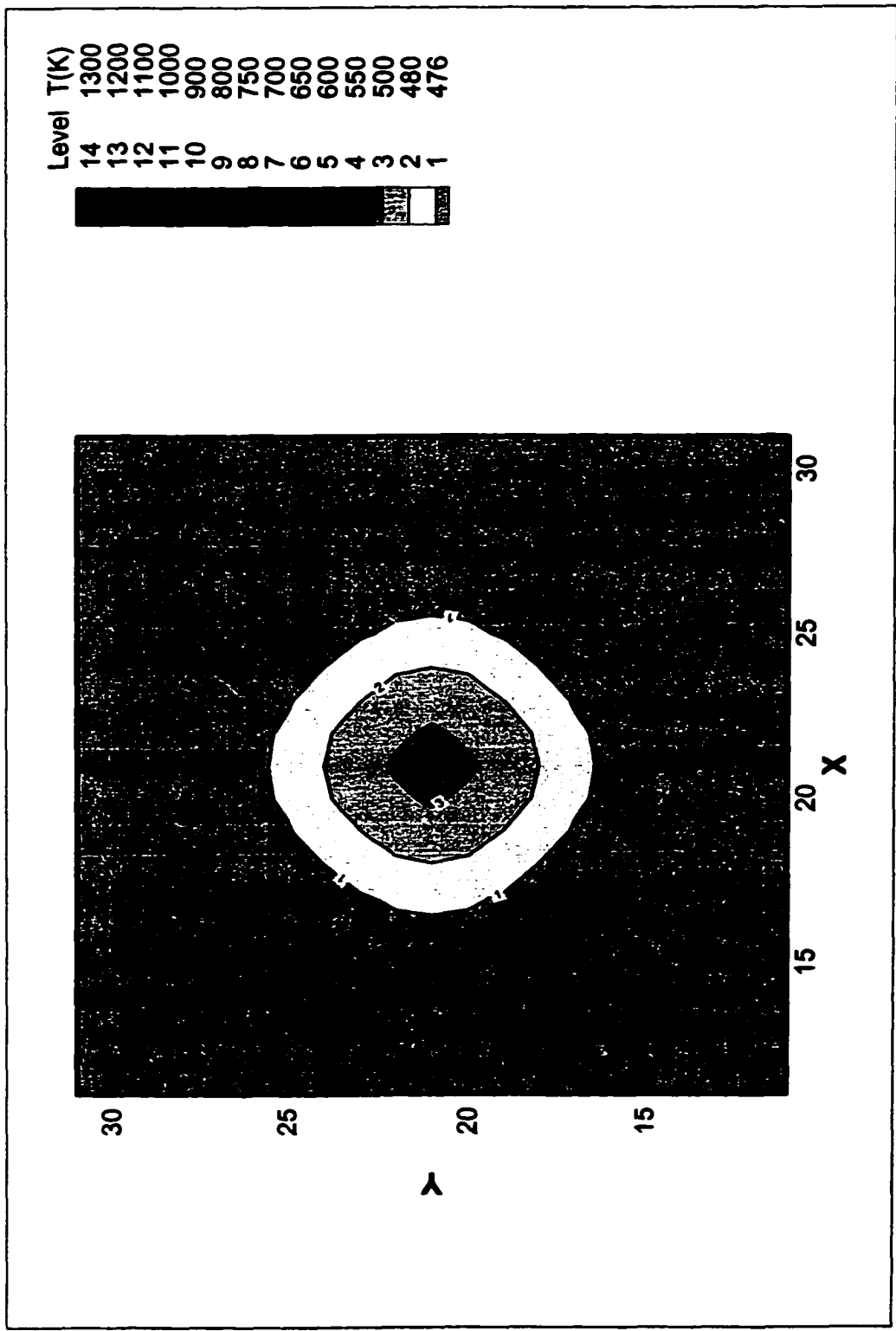


Figure 5.33 Temperature contour on the surface of the deposit ($P_0 = 0.05W$, Layer = 20, Position = A)

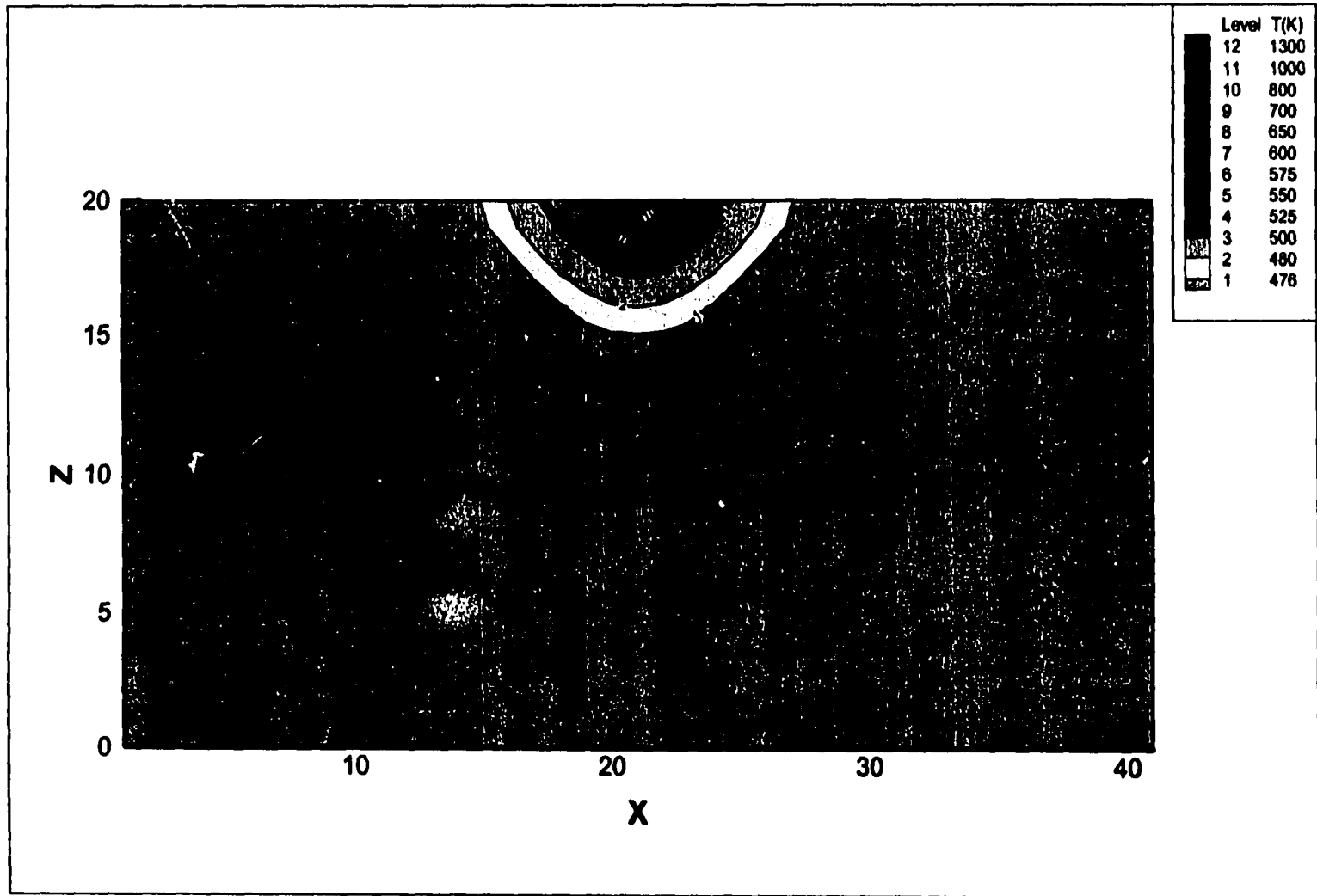


Figure 5.34 Temperature contour on the vertical cross-section of the substrate ($P_0 = 0.05W$, Layer = 0, Position = A)

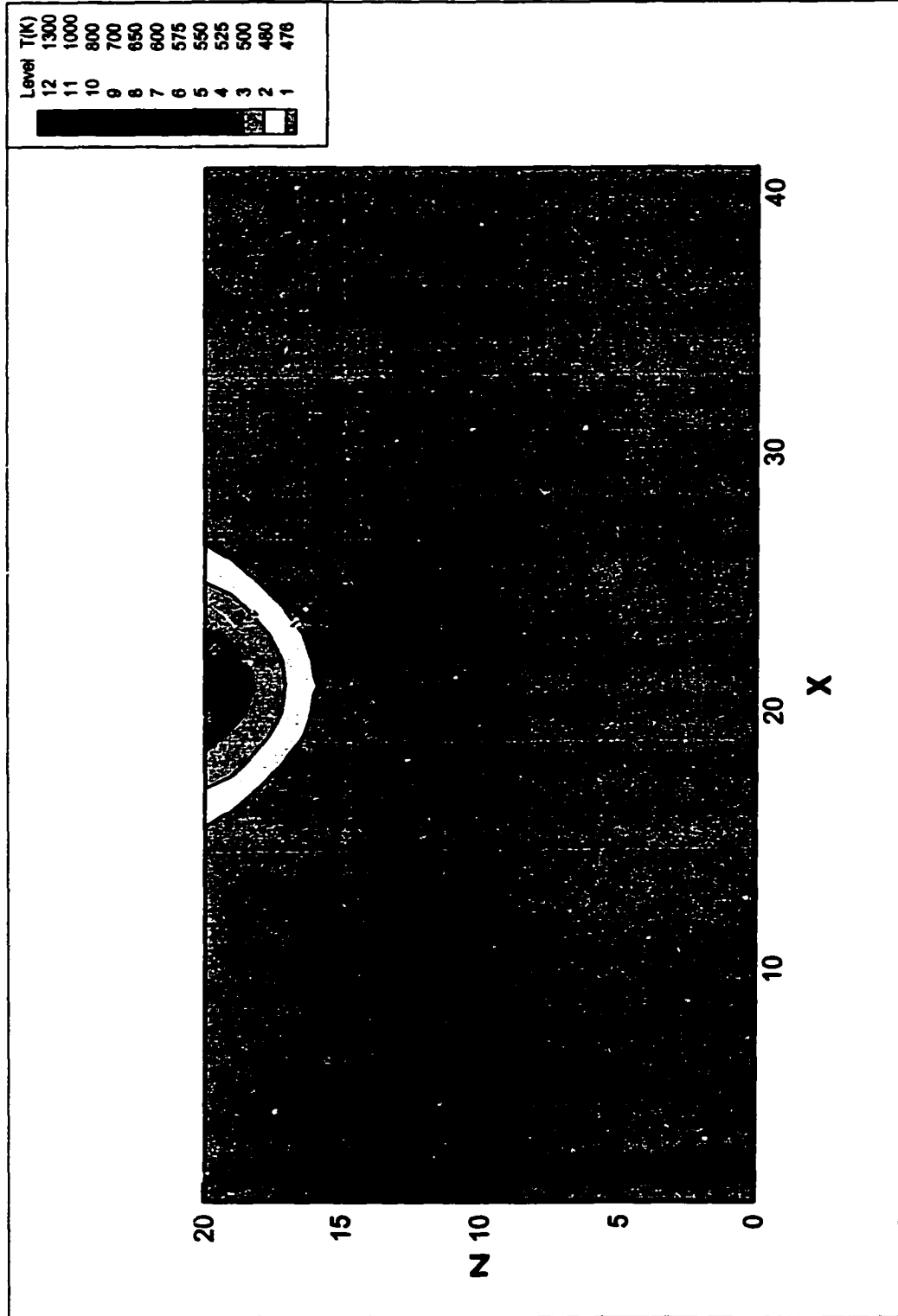


Figure 5.35 Temperature contour on the vertical cross-section of the substrate ($P_0 = 0.05W$, Layer = 5, Position = A)

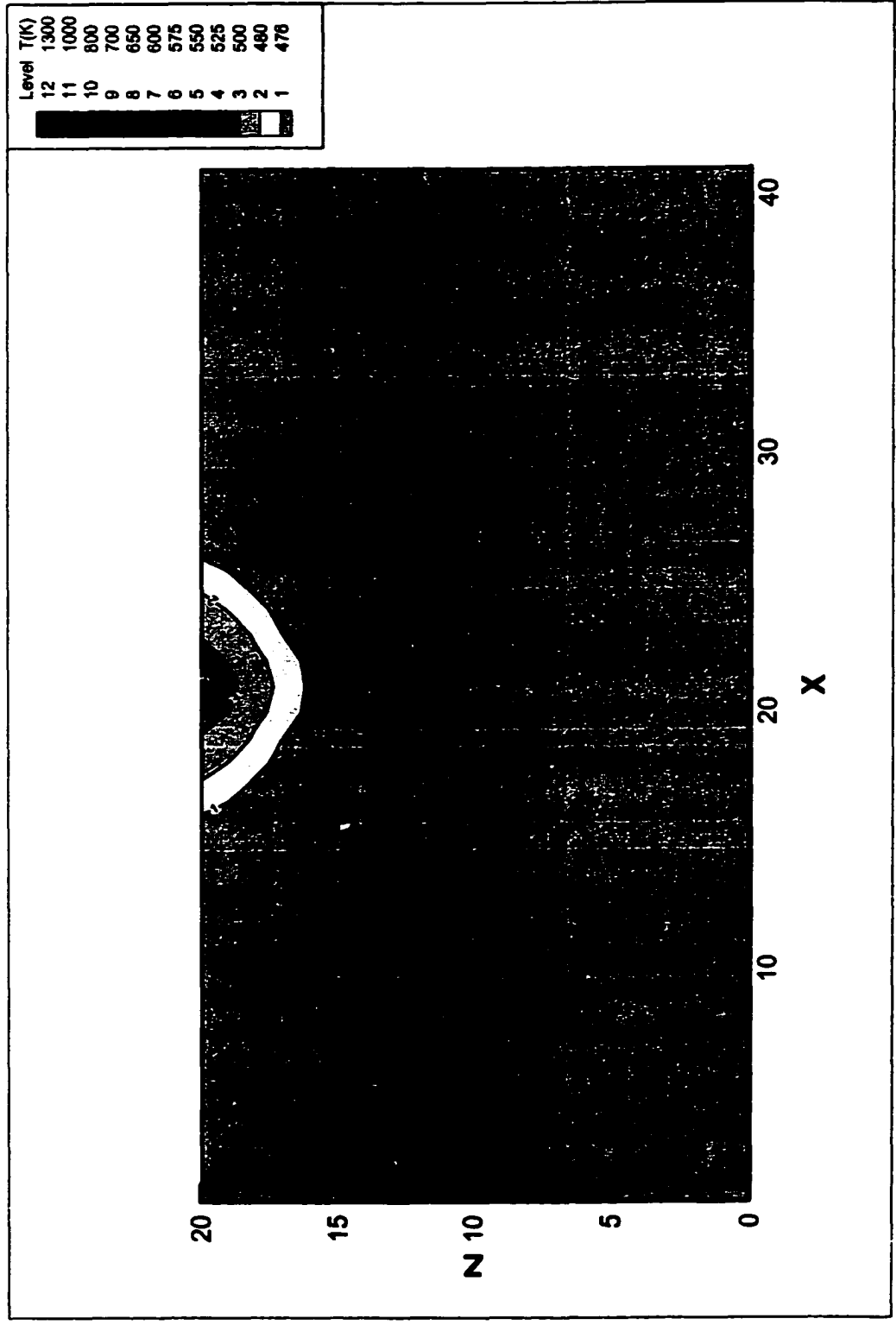


Figure 5.36 Temperature contour on the vertical cross-section of the substrate ($P_0 = 0.05W$, Layer = 10, Position = A)

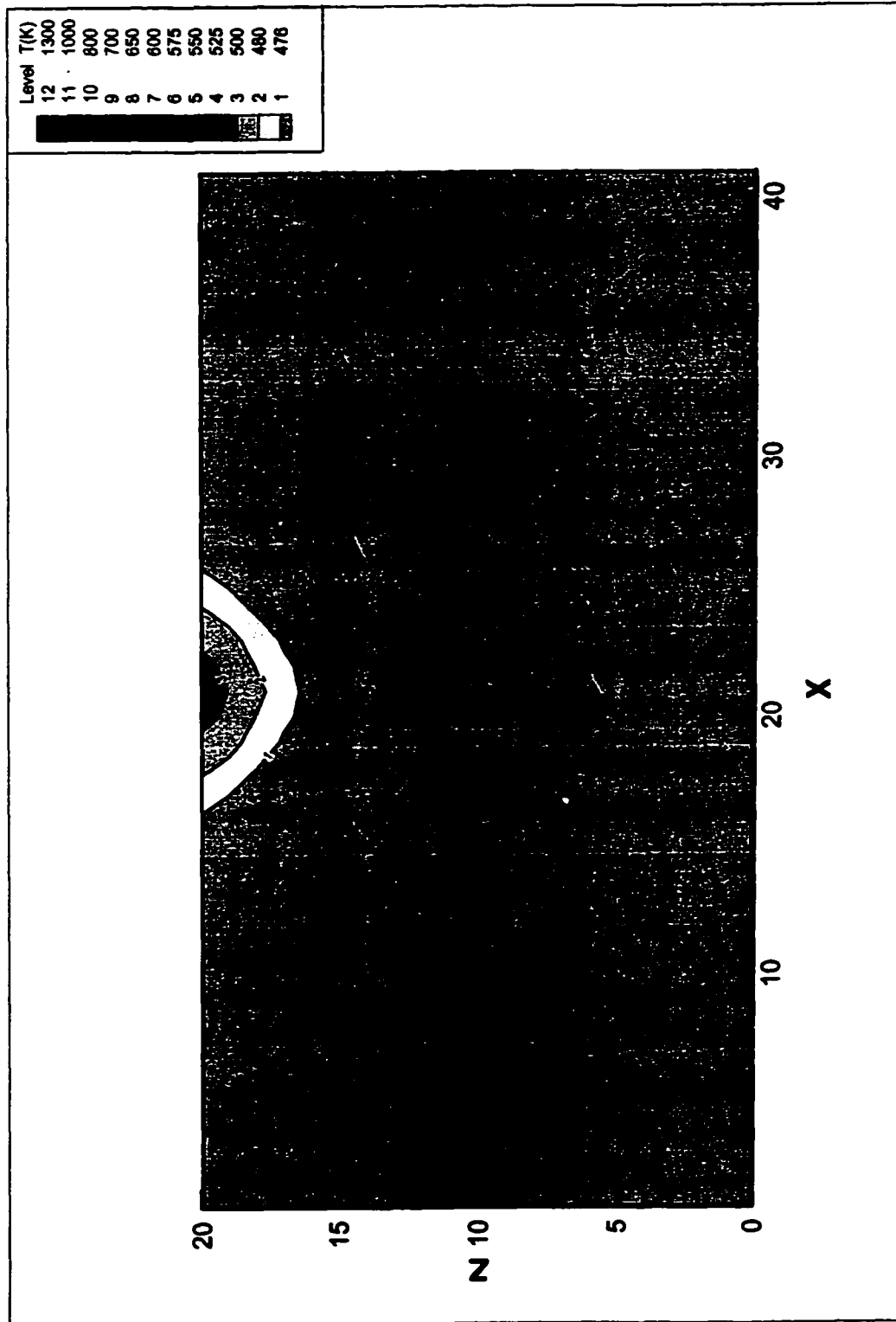


Figure S.37 Temperature contour on the vertical cross-section of the substrate ($P_0 = 0.05W$, Layer = 15, Position = A)

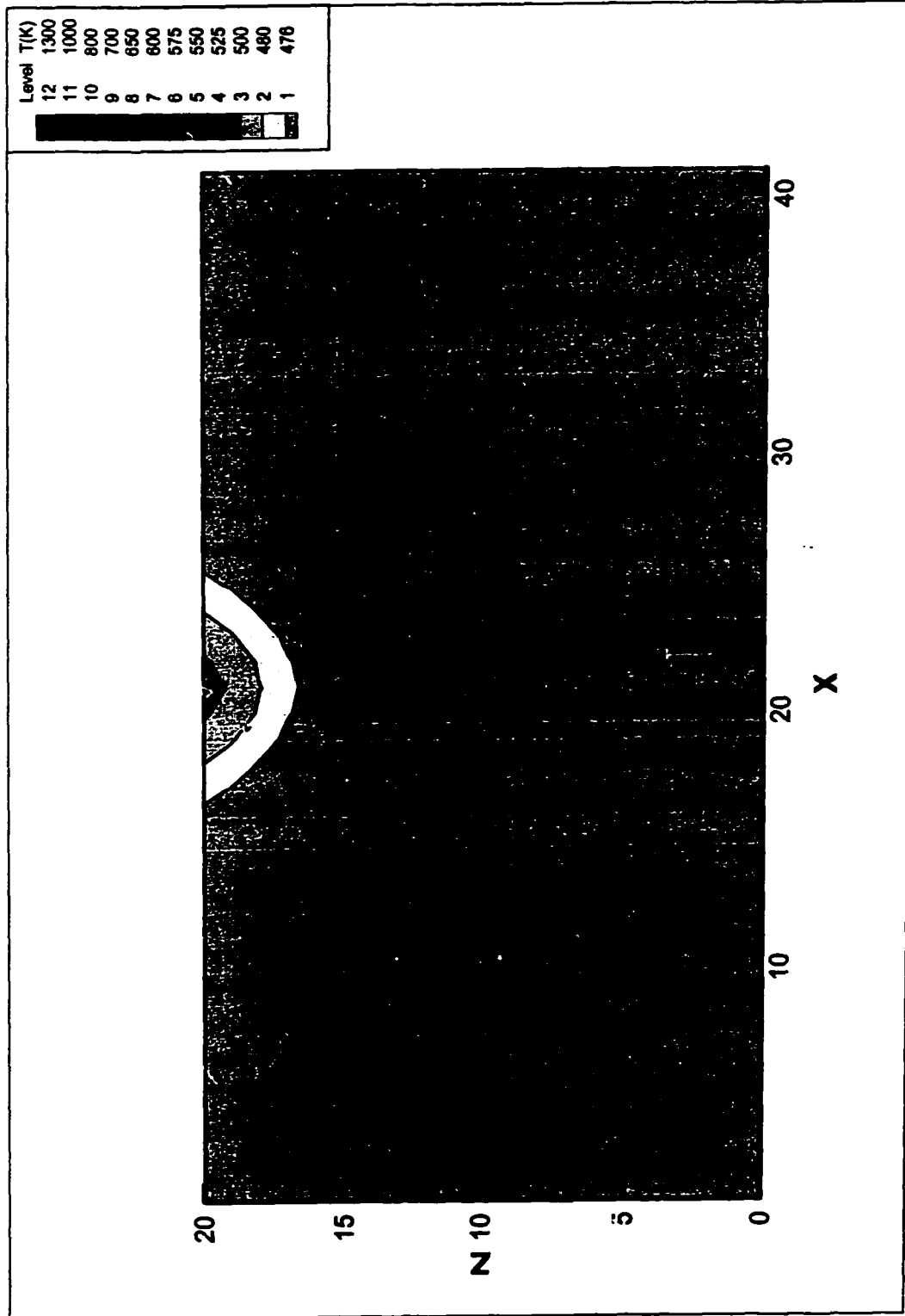


Figure 5.38 Temperature contour on the vertical cross-section of the substrate ($P_0 = 0.05W$, Layer = 20, Position = A)

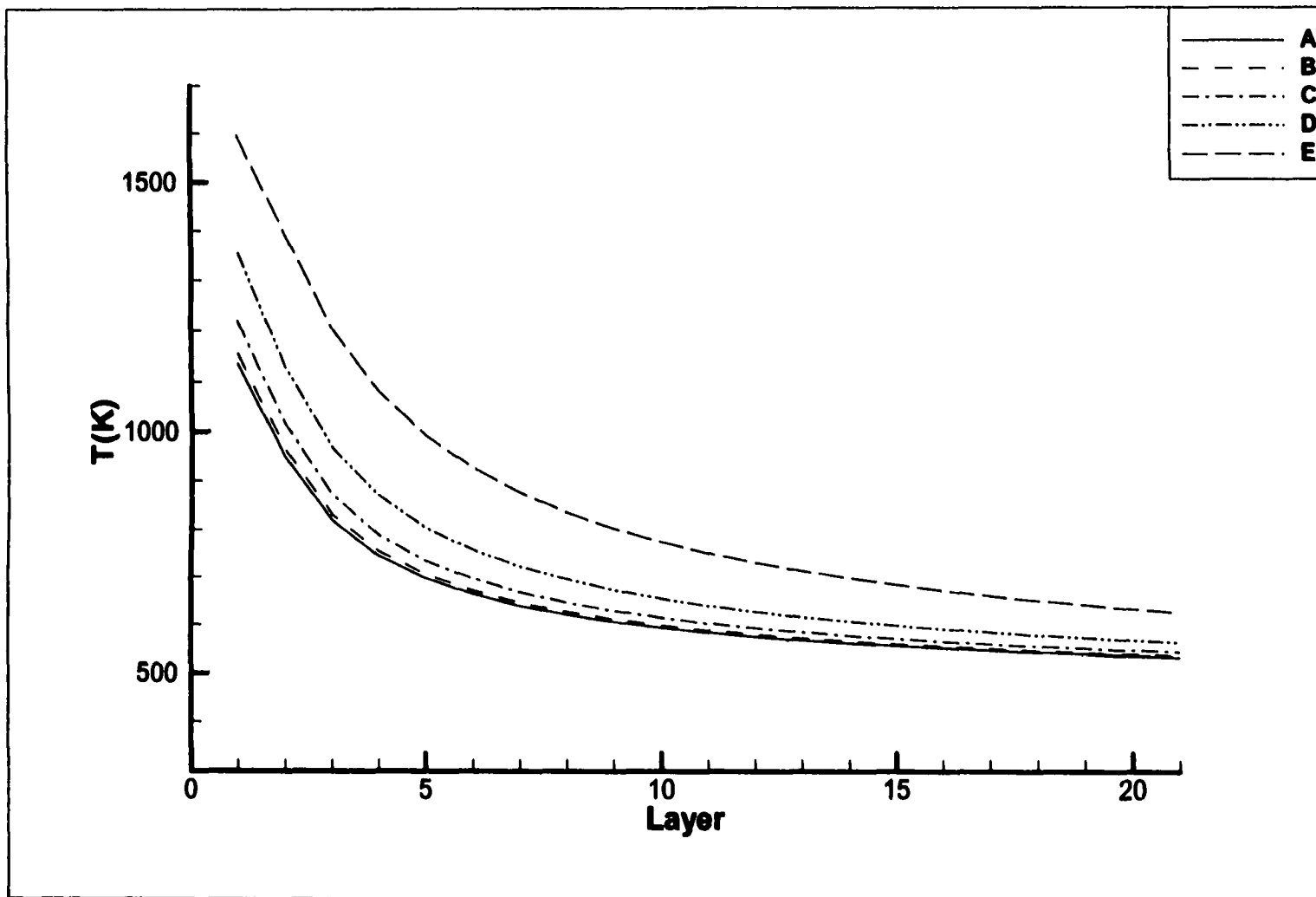


Figure 5.39 Highest temperature vs. layers of deposit on the surface of the microlens ($P_0 = 0.05W$, Position = A, B, C, D, E)

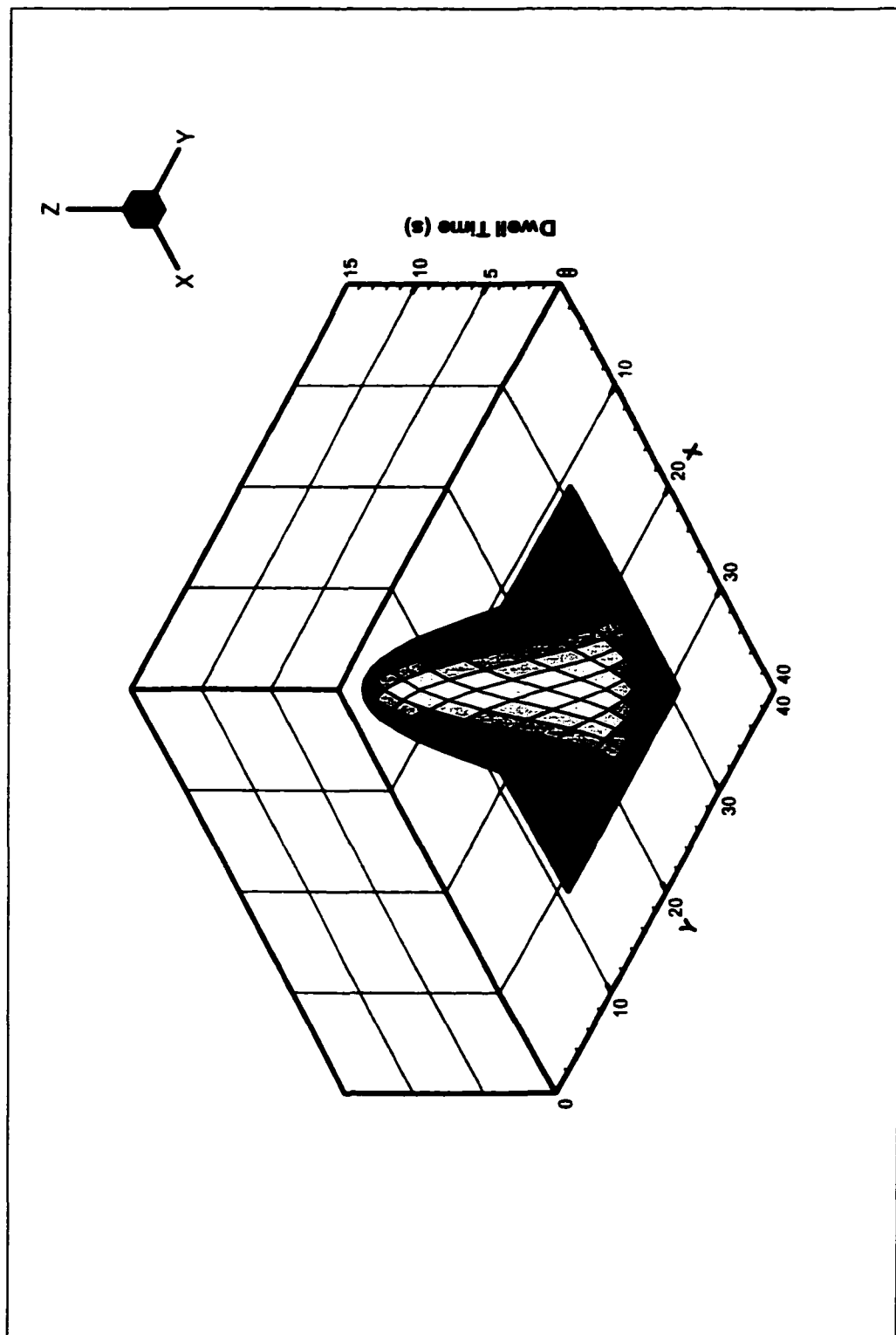


Figure 5.40 Sum of dwell times at each pixel for all layers 1-20 ($P_0 = 0.08W$)

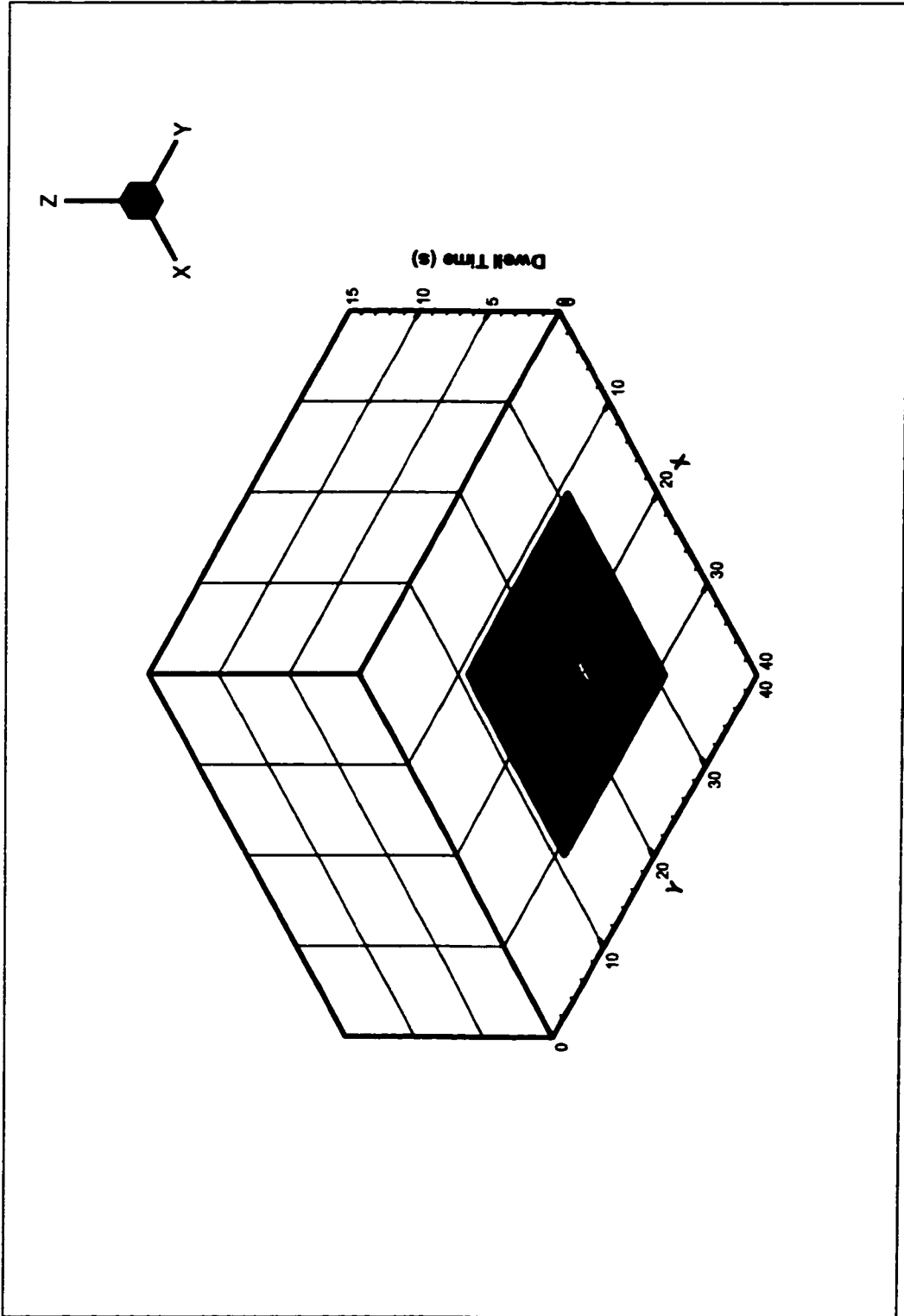


Figure 5.41 Sum of dwell times at each pixel for layers 6-10 ($P_0 = 0.08W$)

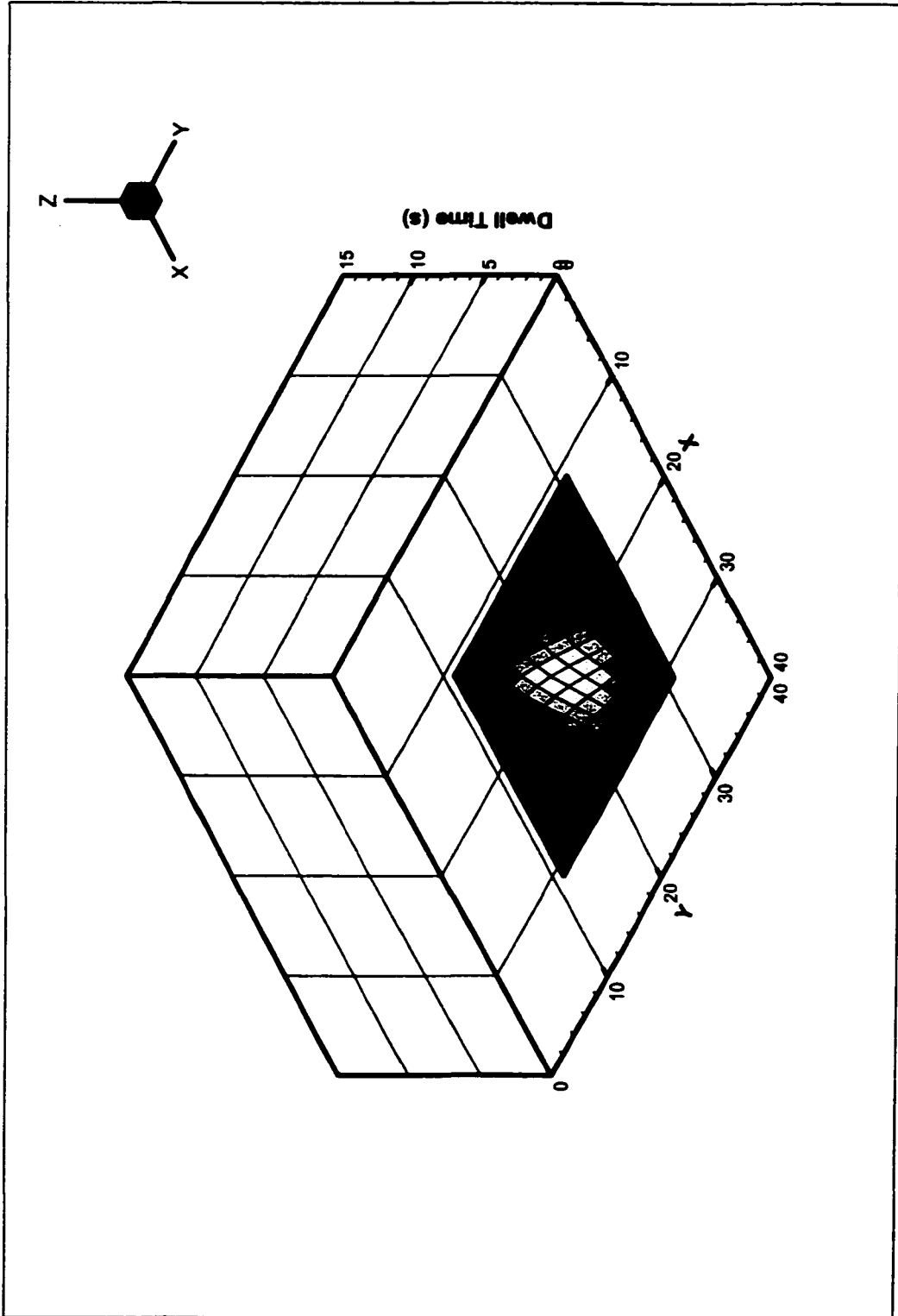


Figure 5.42 Sum of dwell times at each pixel for layers 11-16 ($P_0 = 0.08W$)

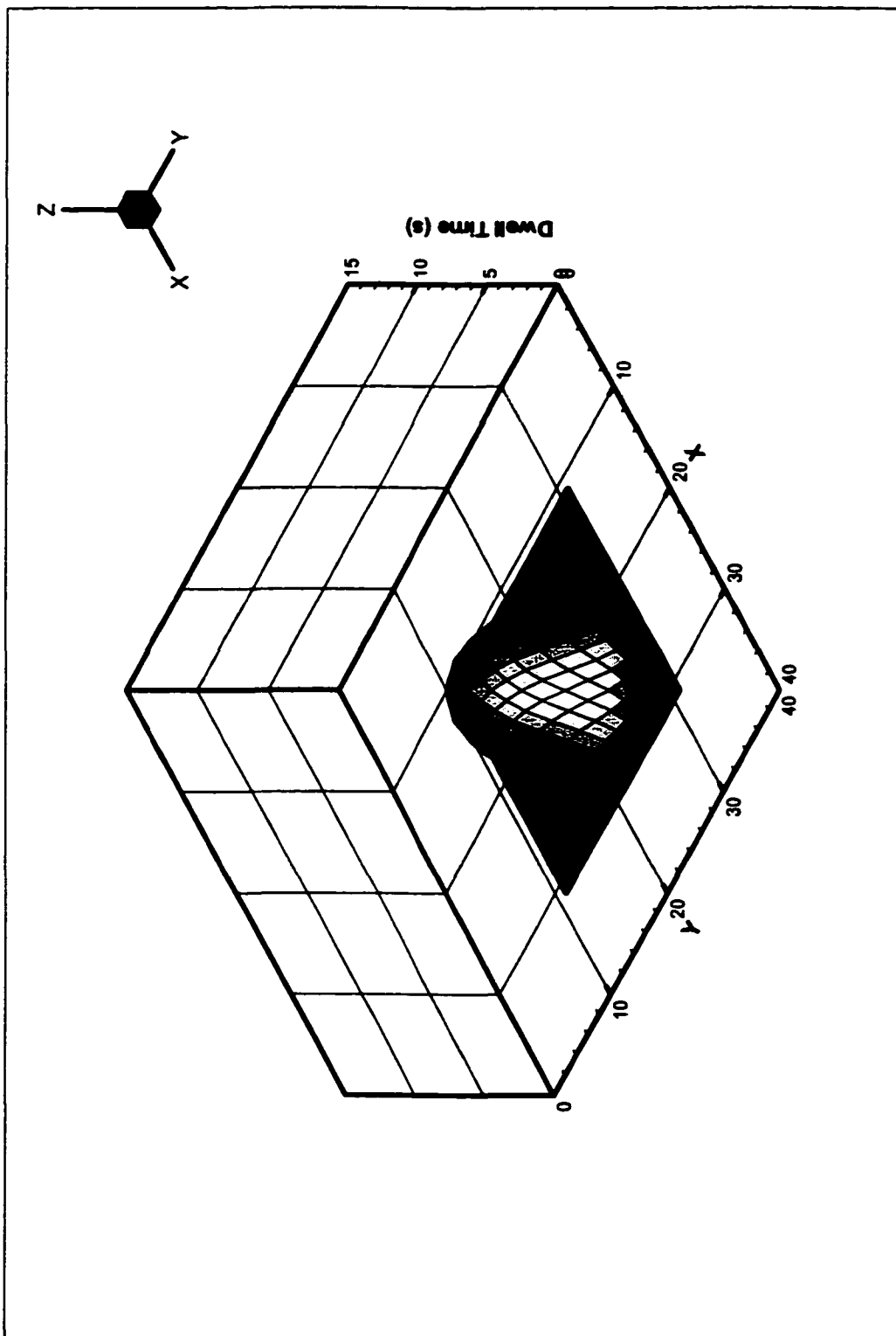


Figure 5.43 Sum of dwell times at each pixel for layers 16-20 ($P_0 = 0.08W$)

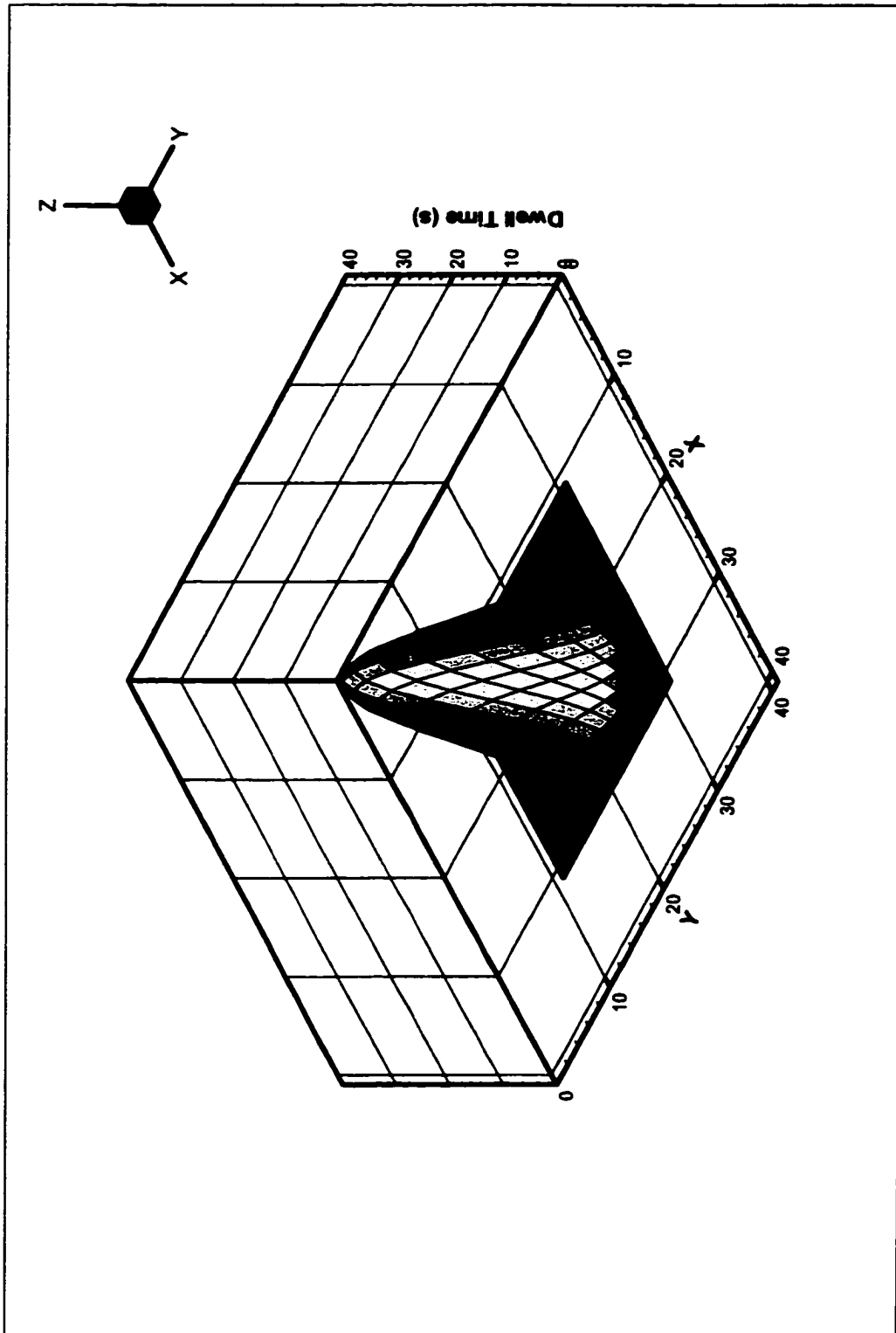


Figure 5.44 Sum of dwell times at each pixel for all layers 1-20 ($P_0 = 0.05W$)

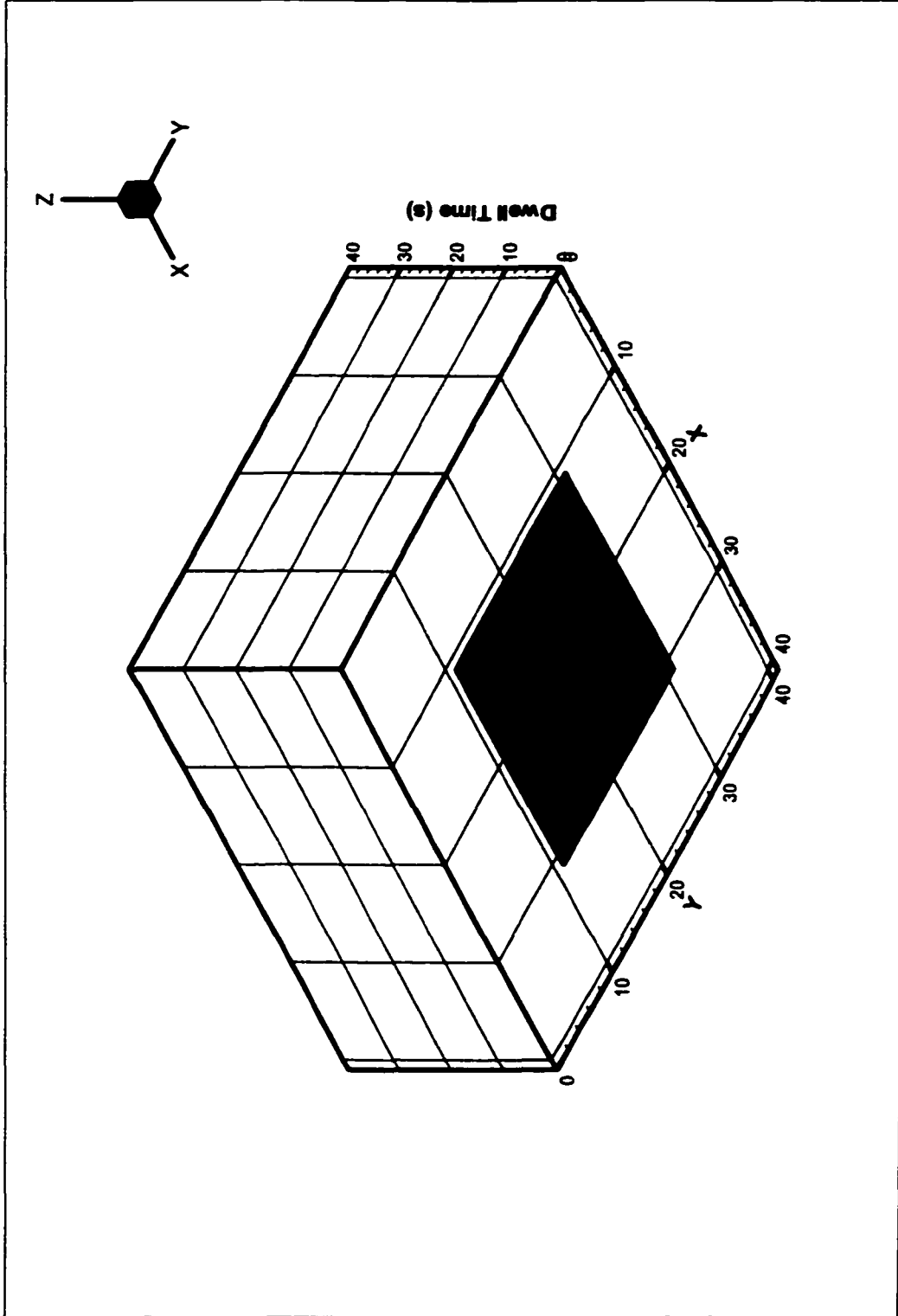


Figure 5.45 Sum of dwell times at each pixel for layers 6-10 ($P_0 = 0.05W$)

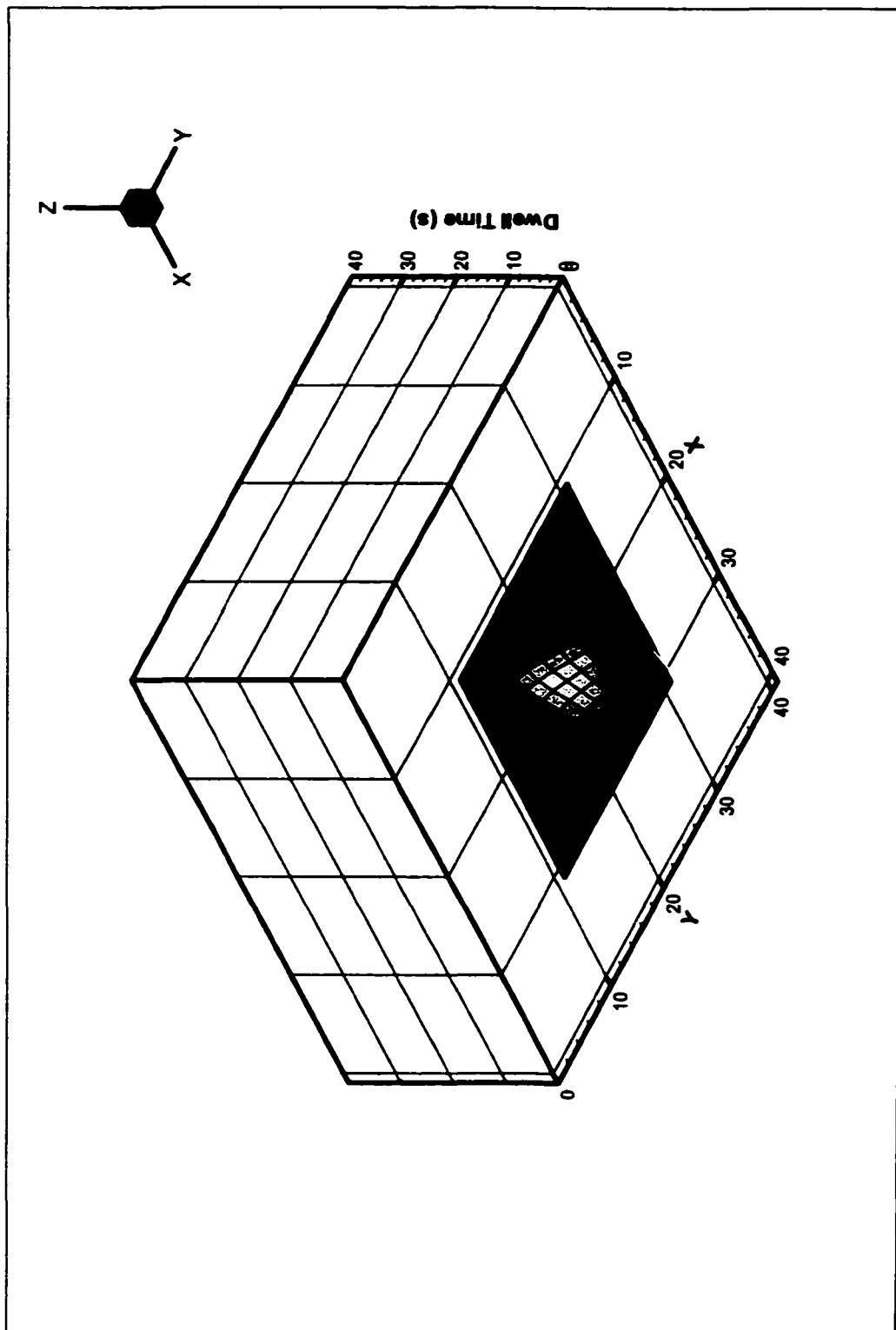


Figure 5.46 Sum of dwell times at each pixel for layers 11-15 ($P_0 = 0.05W$)

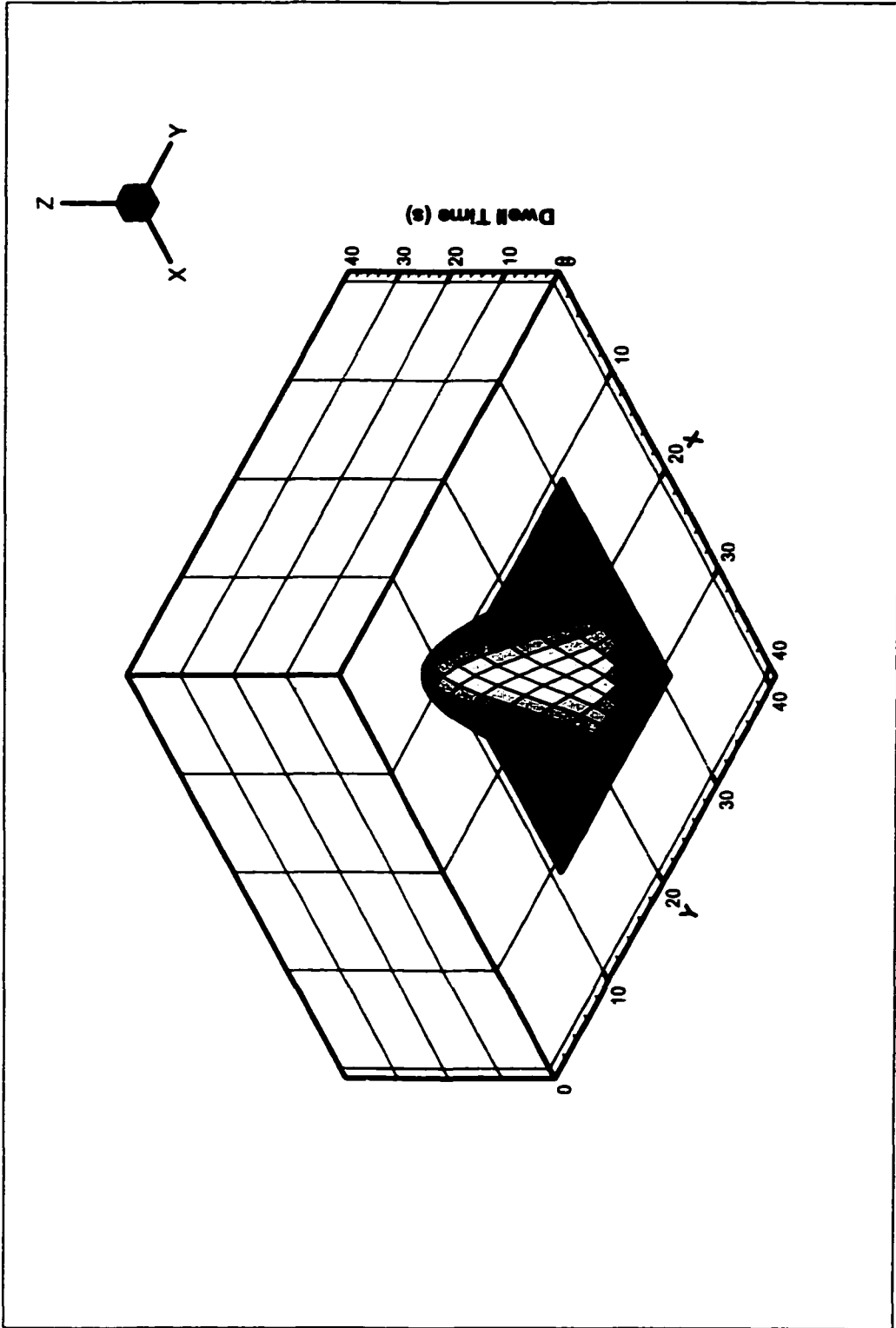


Figure 5.47 Sum of dwell times at each pixel for layers 16-20 ($P_0 = 0.05W$)

CHAPTER 6

SIMULATION OF A CONCAVE MICROLENS

In this chapter we use the mathematical model and the corresponding numerical method described in chapters 3 and 4 to simulate the process of fabrication of a concave microstructure. Again, we choose nickel as the deposit and graphite as the substrate. All the physical parameters are the same as in chapter 5, except for the geometry of the microlens which is concave instead of convex. The temperature distribution and the dwell times for each layer of the concave microlens are predicted.

6.1 Description of the Simulation

The geometry of the deposit is pre-specified, as shown in Figure 6.1. The mathematical description of the deposit has been given in Section 4.1. The diameter L is $20 \mu m$, maximum and minimum height H_1 and H_2 are $3 \mu m$ and $1 \mu m$, respectively. One can see that the height at the center of the microlens is $1 \mu m$ whereas the height at the edge is $3 \mu m$. The substrate is rectangular with dimensions $40 \times 40 \times 10 (\mu m^3)$. Assuming that the number of layers, n , is specified, H_1 and H_2 can be evenly divided into a number of subintervals, each with height h_1 and h_2 . Let $n = 20$, for each layer, $h_1 = 0.05 \mu m$ and $h_2 = 0.015 \mu m$.

The domain decomposition is similar to the case in Chapter 5. The deposit domain is a square instead of a circle. The size of each element (pixel) for deposit is $1\ \mu\text{m} \times 1\ \mu\text{m}$, as shown in Figure 6.2. The substrate is involved in the three-dimensional calculation, with each element having size of $1\ \mu\text{m} \times 1\ \mu\text{m} \times 0.5\ \mu\text{m}$. The concave microlens shapes resulting from 20 layers of deposit are given in Figure 6.3.

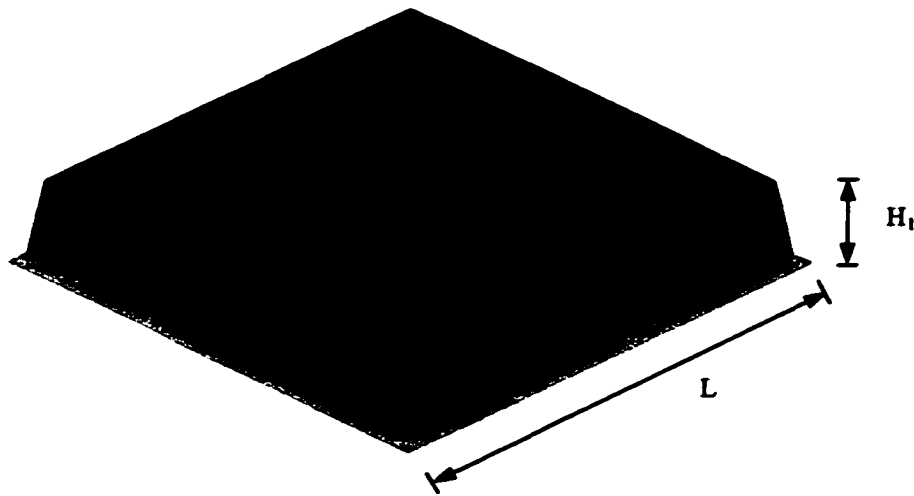


Figure 6.1 A concave microlens with a parabolic surface

From the analysis of the mathematical model in Chapter 3, we need to simulate the fabrication process of a concave microlens layer by layer. For each layer the laser beam moves from one pixel to the next neighboring pixel. The temperature distribution can be obtained when the laser beam is focused at each pixel. From this distribution, one may determine the pixel dwell time.

The computation includes the three algorithms described in Section 4.4. The tolerances are given in the computation as $\varepsilon_1 = 1.0 \times 10^{-2}$ and $\varepsilon_2 = 1.0 \times 10^{-4}$.

Equations (4.12) and (4.13) are used to calculate the growth ΔZ in each element for each layer, given a concave microlens with a pre-specified geometry. The ΔZ data form the right hand side of the linear system in Equation (4.27). Based on the calculated temperature distribution when laser beam is focused at each pixel, the left hand side of the linear system can be obtained from Equation (4.28). The linear system is then solved using Algorithm for predicting dwell time.

6.2 Physical Parameters

Several key parameters determine the outcome of the LCVD process. In this chapter, emphasis has been placed on the kinetics of growth, rather than diffusive transport of the precursor in the gas phase. Without considering convection, the primary mode of heat transfer is conduction to the substrate. The process parameter that most influences the growth is the laser power. The laser intensity and its distribution can be calculated from Equations (3.10) and (3.11).

Nickel was chosen as deposit material since nickel's thermoconductivity is representative of many transition and refractory metals. Nickel has a moderate thermoconductivity for a metal, $K_d = 65.6 W/m \cdot K$ at $600K$ and $E_a = 94000 J/mol$ [Maxwell 1996].

Graphite was chosen as substrate. The melting point of Graphite is $2273K$, much higher than Nickel ($1728K$). The conductivities of Nickel and Graphite are listed in Table 5.1. Other physical parameters are listed in Table 5.2.

We consider laser beam intensities of $0.08W$ and $0.05W$ in this chapter.

6.3 Temperature Distribution

The temperature distribution determines the growth rate and the dwell time at each. For the deposit with a pre-specified relatively flat shape, the area of the interface between the deposit and substrate is relatively large, so the primary mode of heat transfer is initially by conduction to the substrate. As the deposit begins to form, the temperature distribution become largely determined by conduction through the deposit and then to the substrate.

When the laser beam with intensity P_0 ($P_0 = 0.08\text{W}$) hits at the center of the deposition zone, the temperature contours on the surface of the substrate are given in Figures 6.4 to 6.8, for layer 0, 5, 10, 15 and 20. The temperature contours on the central vertical cross-section are given in Figures 6.9 to 6.13, corresponding to layer 0, 5, 10, 15 and 20. Here, the central vertical cross-section is the x-z plane that passes through A and E, and bisects the substrate. Layer 0 is the initial stage without deposit on the surface of the substrate.

When the laser beam is focused at one pixel, the corresponding temperature distribution can be obtained, in which the maximum temperature occurs at the same element where the laser beam is focused. As the number of layers increases, the height of deposit becomes larger and the maximum temperature drops down. The changes in trend of the maximum temperature with an increase in the number of layers are illustrated in Figure 6.14, in which the five lines correspond to the five pixels (A, B, C, D, E) where the laser beam is focused (see Figure 6.2). The maximum temperature drops fast and then slows down as the number of layers becomes large.

The maximum temperature is the largest when the laser beam hits the pixel near the center because the deposit height near the center is the smallest, and there is not enough cross-section area in deposit to transfer the heat to the surrounding area. This result can also be explained from Equation (3.37) that describes the heat flow in the deposit. The diffusion term in the Equation (3.37) contains the parameter h . Thus, when h is smaller the effect of diffusion is less significant and the peak temperature is higher.

6.4 Dwell Time vs. Deposit Growth

After the temperature distribution of the deposit has been predicted one can simulate the deposit growth and hence the geometry of the deposit at a certain time step, since the temperature determines the growth rate. In our case, the geometry of the deposit is pre-specified so we can predict the dwell time that the laser beam has to stay at each pixel for each layer to obtain the pre-specified deposit geometry.

Using the physical parameter values in Table 5.1, the dwell time at each pixel of each layer of the concave microlens can be predicted. For the first several layers, the height of the deposit is low, which limits the heat transport to the surrounding area. As a result, less time is needed to fabricate these layers. Figure 6.15 is the total dwell time at each pixel needed to fabricate the whole microlens with 20 layers. Figures 6.16 and 6.17 give the sum of the dwell times at each pixel for fabricating layers 11-15 and 16-20, respectively.

For ease of comparison, the dwell time contours are given in Figures 6.18 to 6.21, corresponding to the sum of the dwell times for fabricating layers 1-20, 6-10, 11-15 and 16-20, respectively.

From these results one can see that less time is needed to grow the deposit near the center than near the edge because the height near the center of deposit is smaller than that near the edge, it is relatively harder for heat at the center to flow to the surrounding area, and the temperature is thus higher when laser beam hits at the pixel near the center than near the edge (see Figure 6.14). As the height of the deposit becomes larger, the temperature of deposit drops down; hence more dwell time is needed per pixel to deposit another layer of the same height.

For a different laser intensity, the dwell time needed to fabricate the concave microlens with the same geometry (Figure 6.3) will be different. With $P_0 = 0.08W$, dwell time contours are given in Figures 6.22 to 6.25, corresponding to the sum of dwell times for fabricating layers 1-20, 6-10, 11-15 and 16-20, respectively.

Comparing Figure 6.22 with Figure 6.18, one can see that for lower laser intensity, the total dwell time at each pixel becomes larger since the temperature is lower at each pixel for each layer.

For different kinds of microstructures, the temperature distributions differ and the dwell times needed to fabricate the microstructure also differ. For a convex microlens the dwell time is larger near the central pixel (see Figure 5.40). However, for a concave microlens the dwell time is larger near the edge (see Figure 6.16). There are two reasons to account for the difference in dwell time distributions between Figure 5.40 and 6.16:

- (1) The height of the deposit at the central pixel is largest for a convex microlens and smallest for a concave microlens.

- (2) The maximum temperature reaches its minimum value at the central pixel for a convex microlens, whereas it reaches its maximum value at the central pixel for a concave microlens (see Figure 5.18 and 6.14).

The above results illuminate the interrelationship among the deposit growth (deposit geometry), temperature, and dwell time.

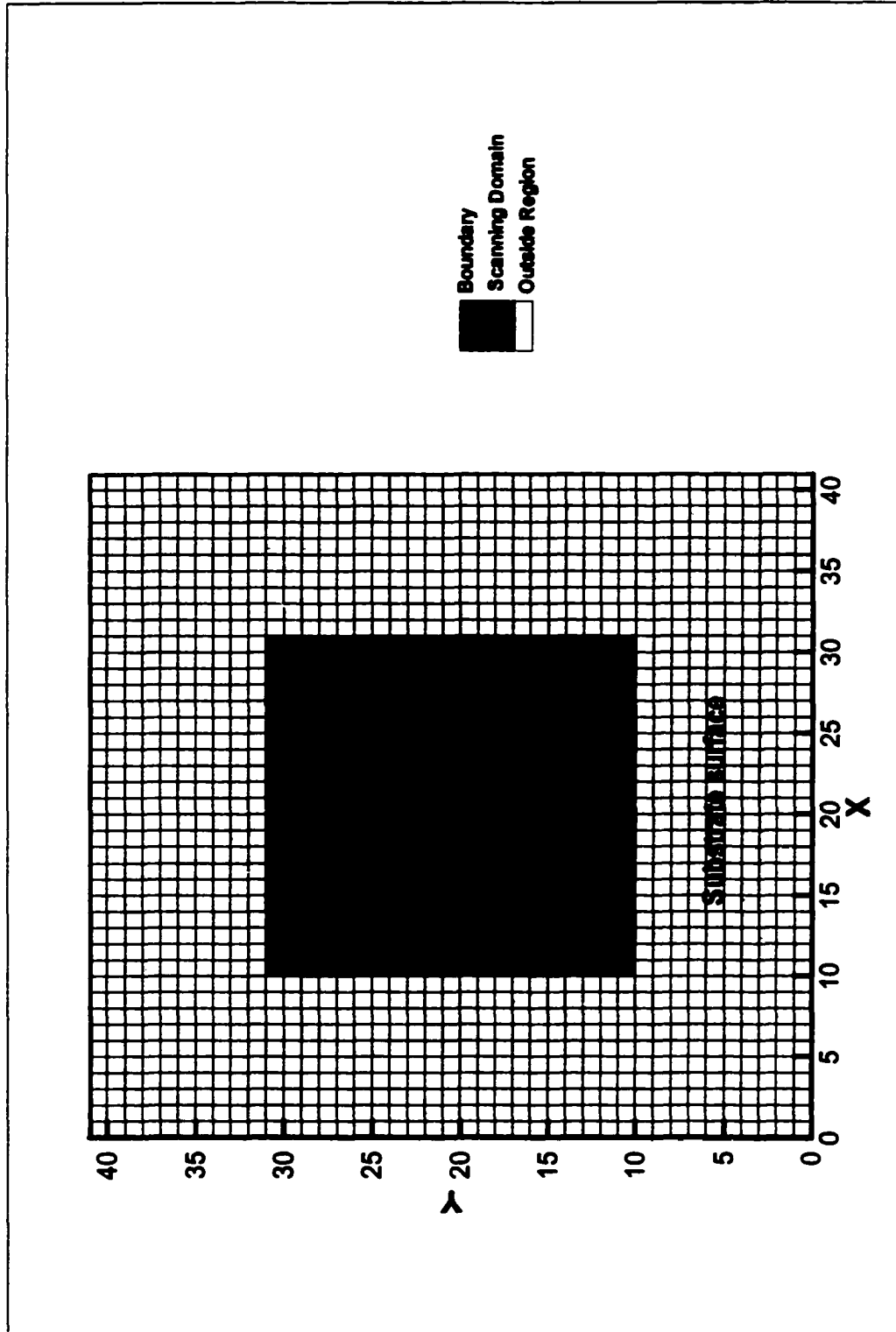


Figure 6.2 Mesh and deposit zone on the surface of the substrate

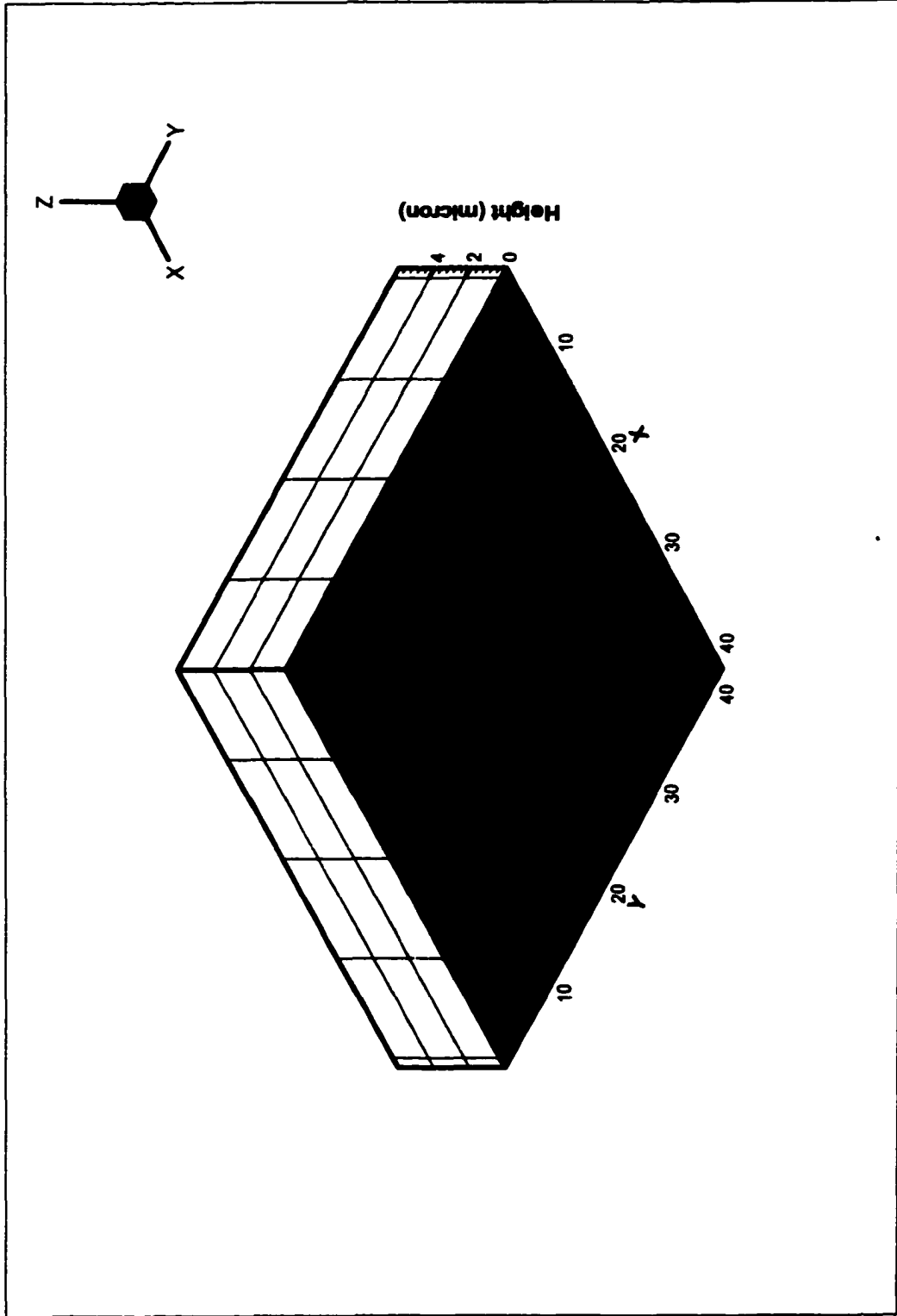
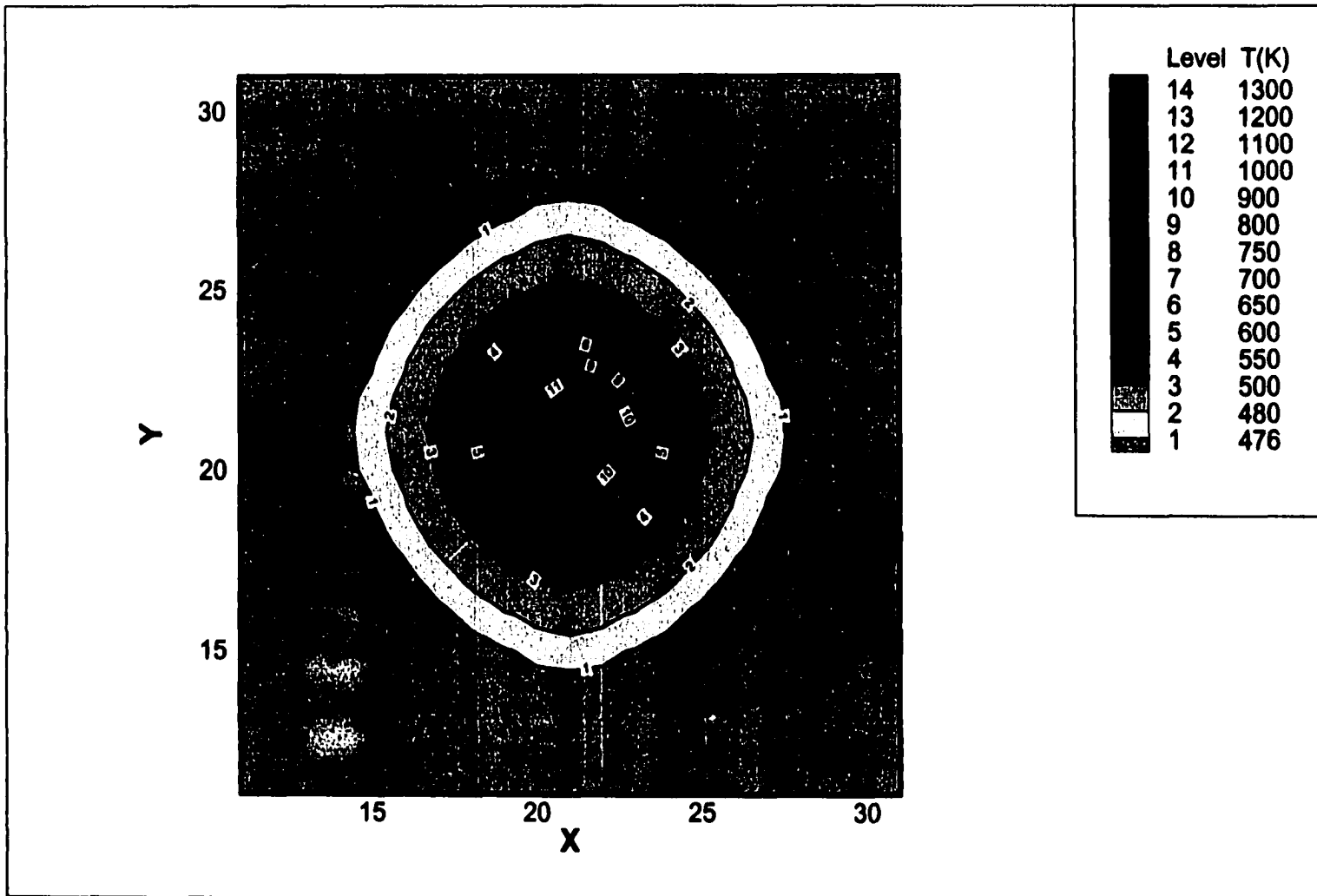
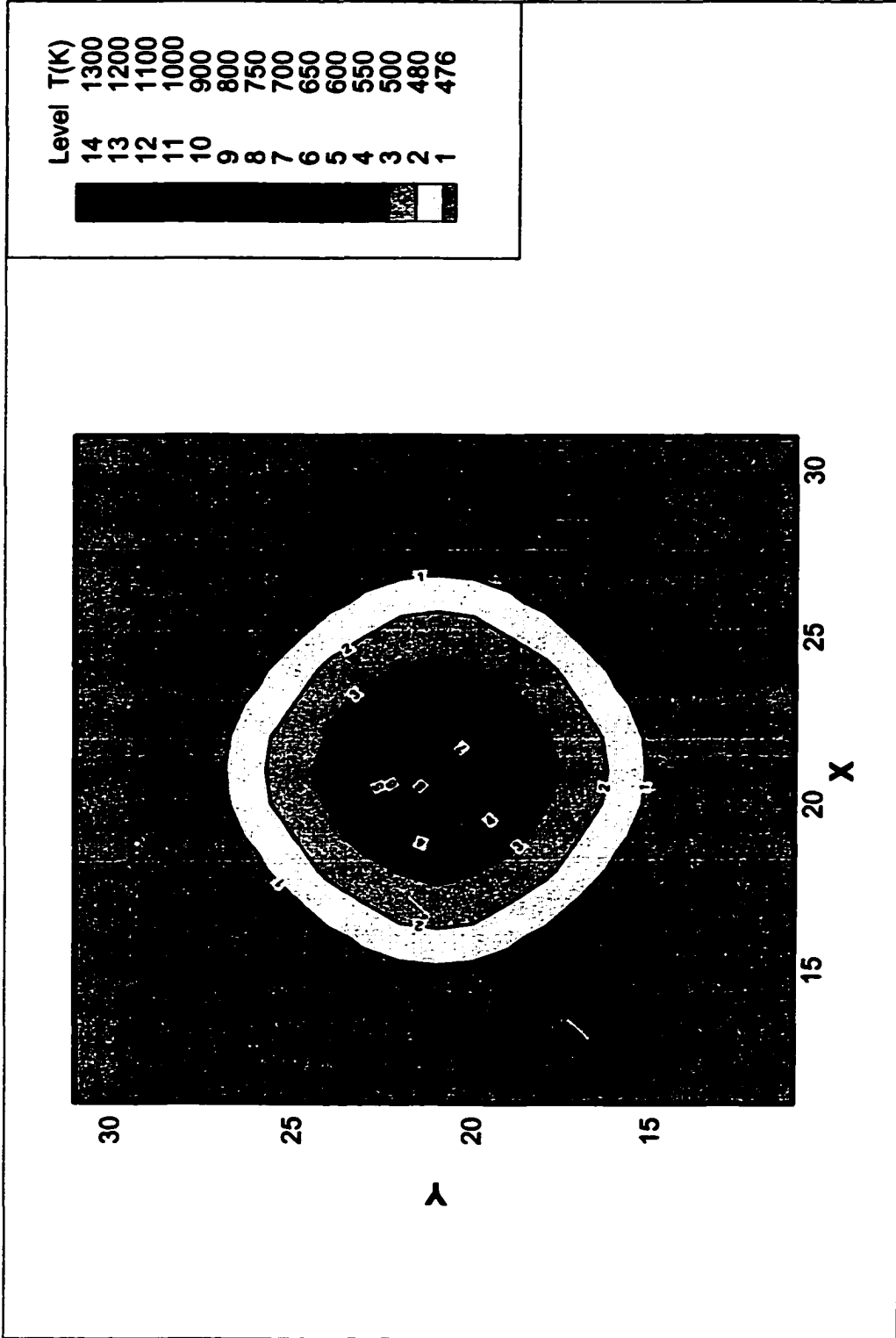


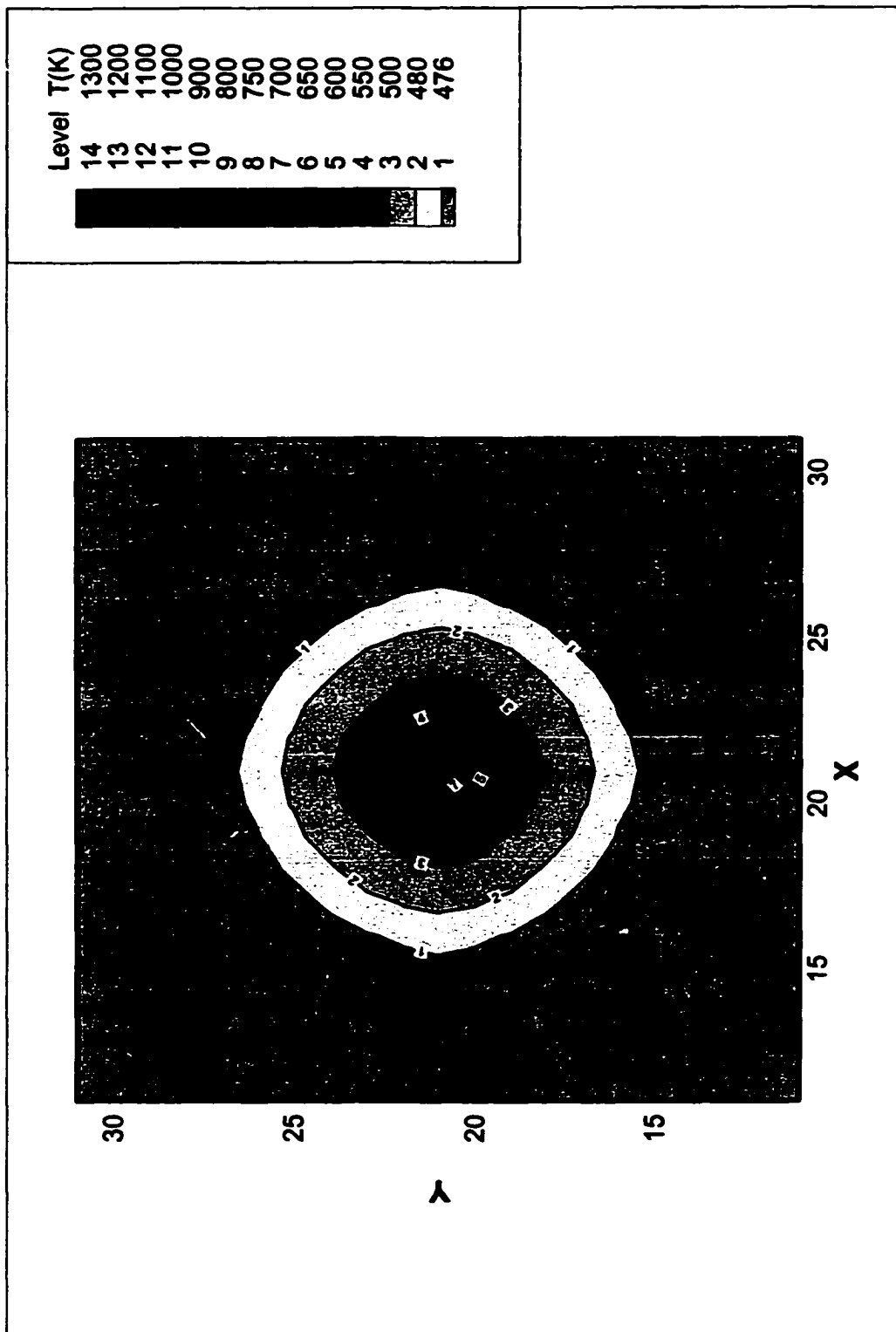
Figure 6.3 Concave Microlens resulting from 20 layers of deposit



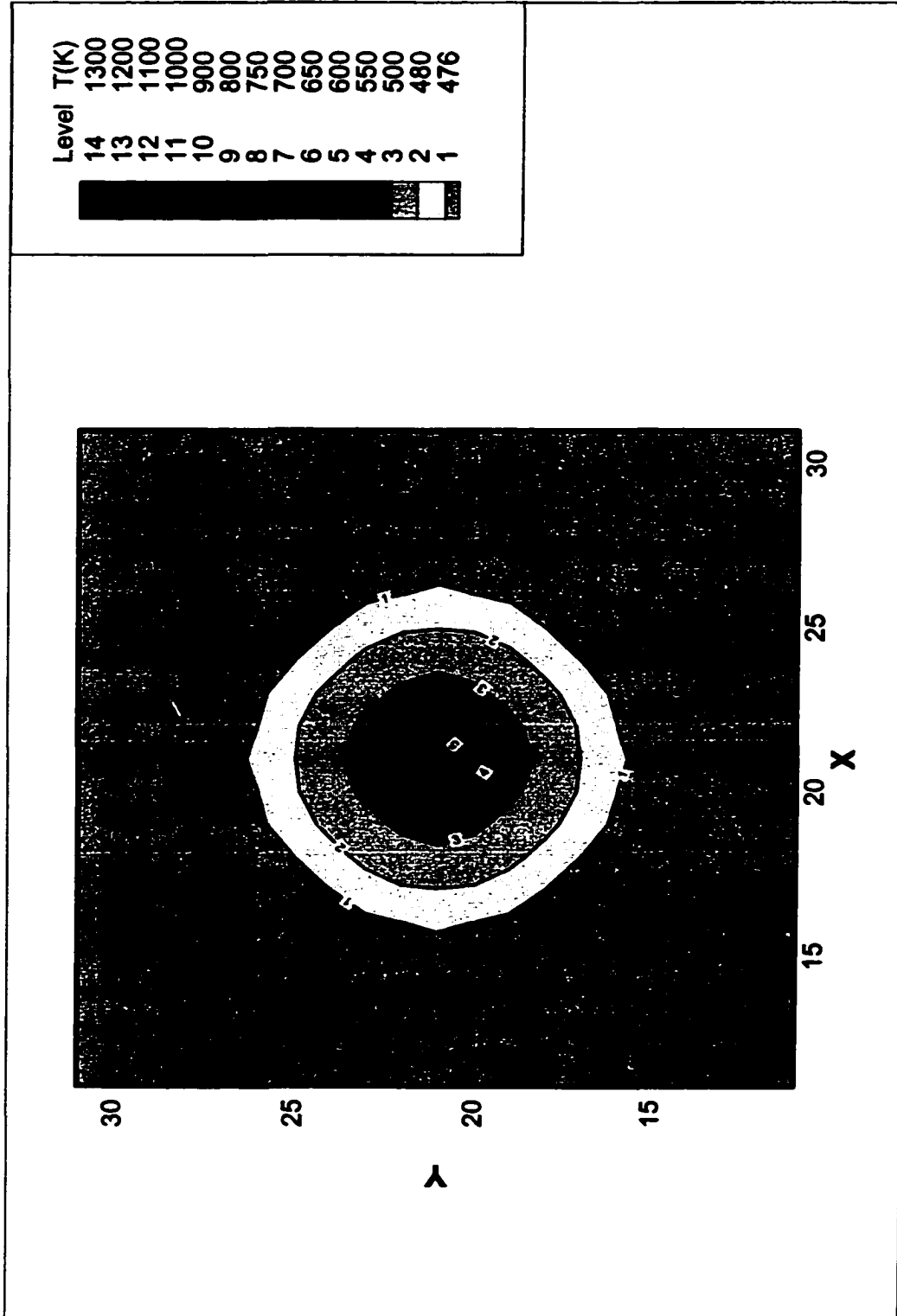
6.4 Temperature contour on the surface of the substrate ($P_0 = 0.08W$, Layer = 0, Position = A)



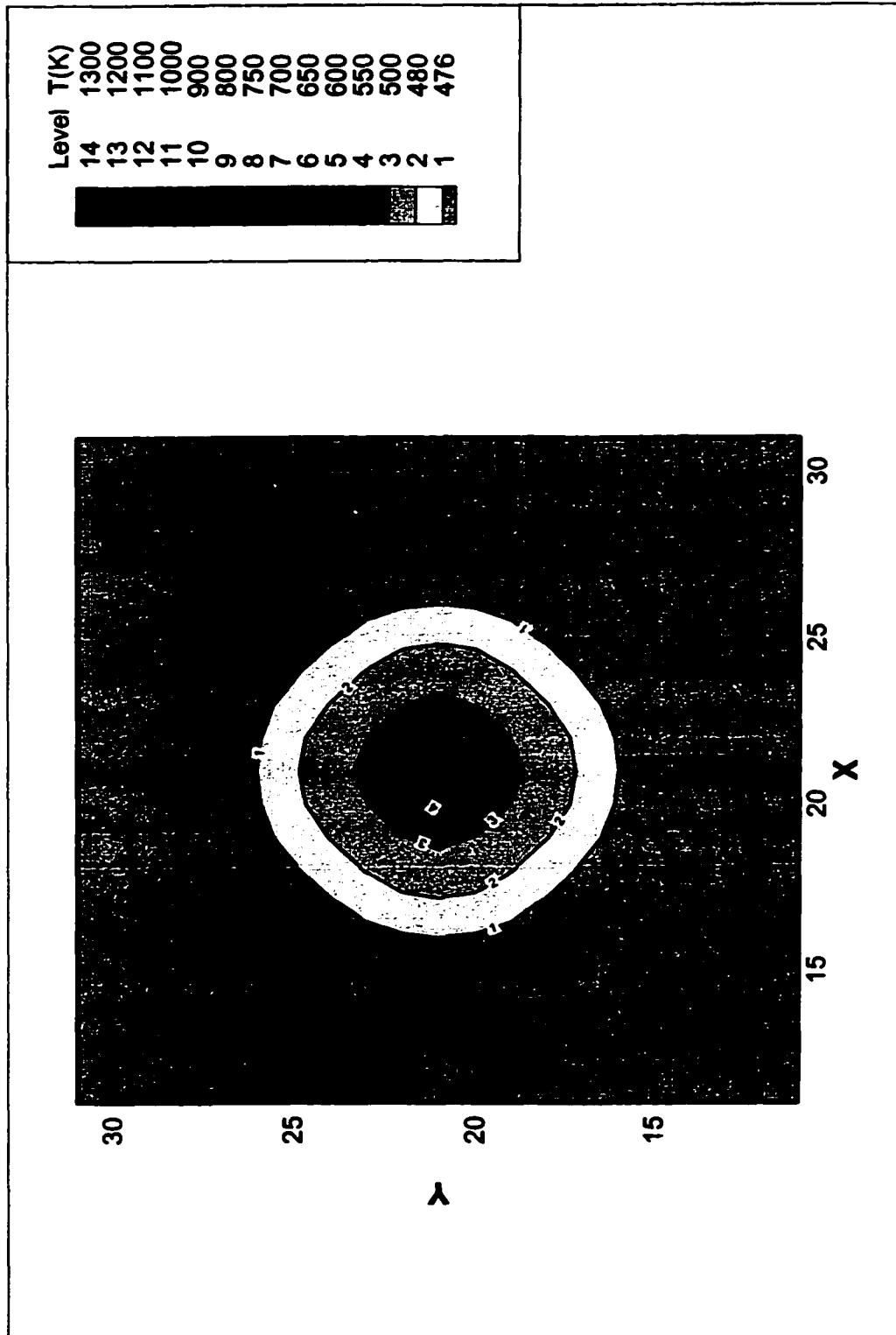
6.5 Temperature contour on the surface of the deposit ($P_0 = 0.08W$, Layer = 5, Position = A)



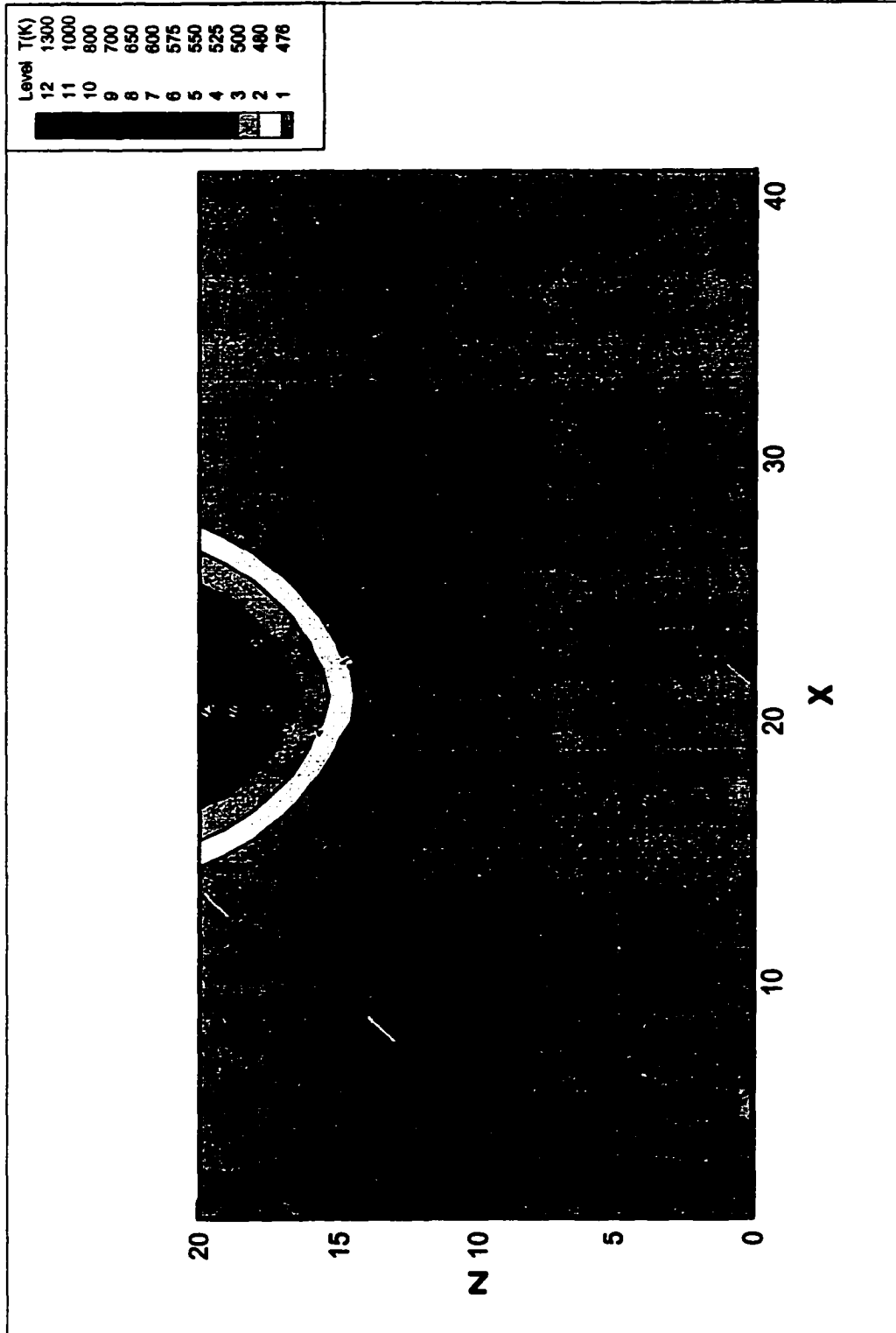
6.6 Temperature contour on the surface of the deposit ($P_0 = 0.08W$, Layer = 10, Position = A)



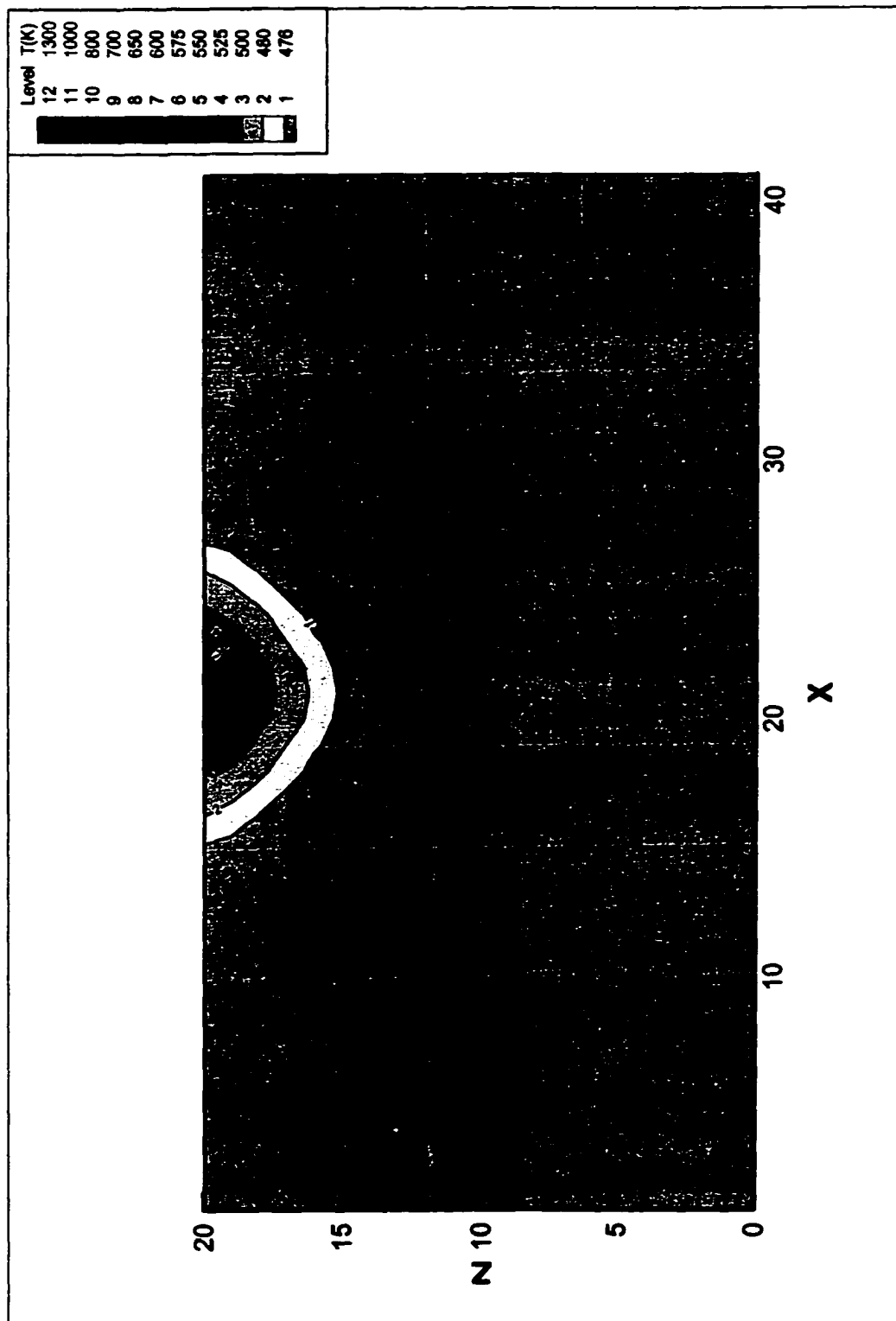
6.7 Temperature contour on the surface of the deposit ($P_0 = 0.08W$, Layer = 15, Position = A)



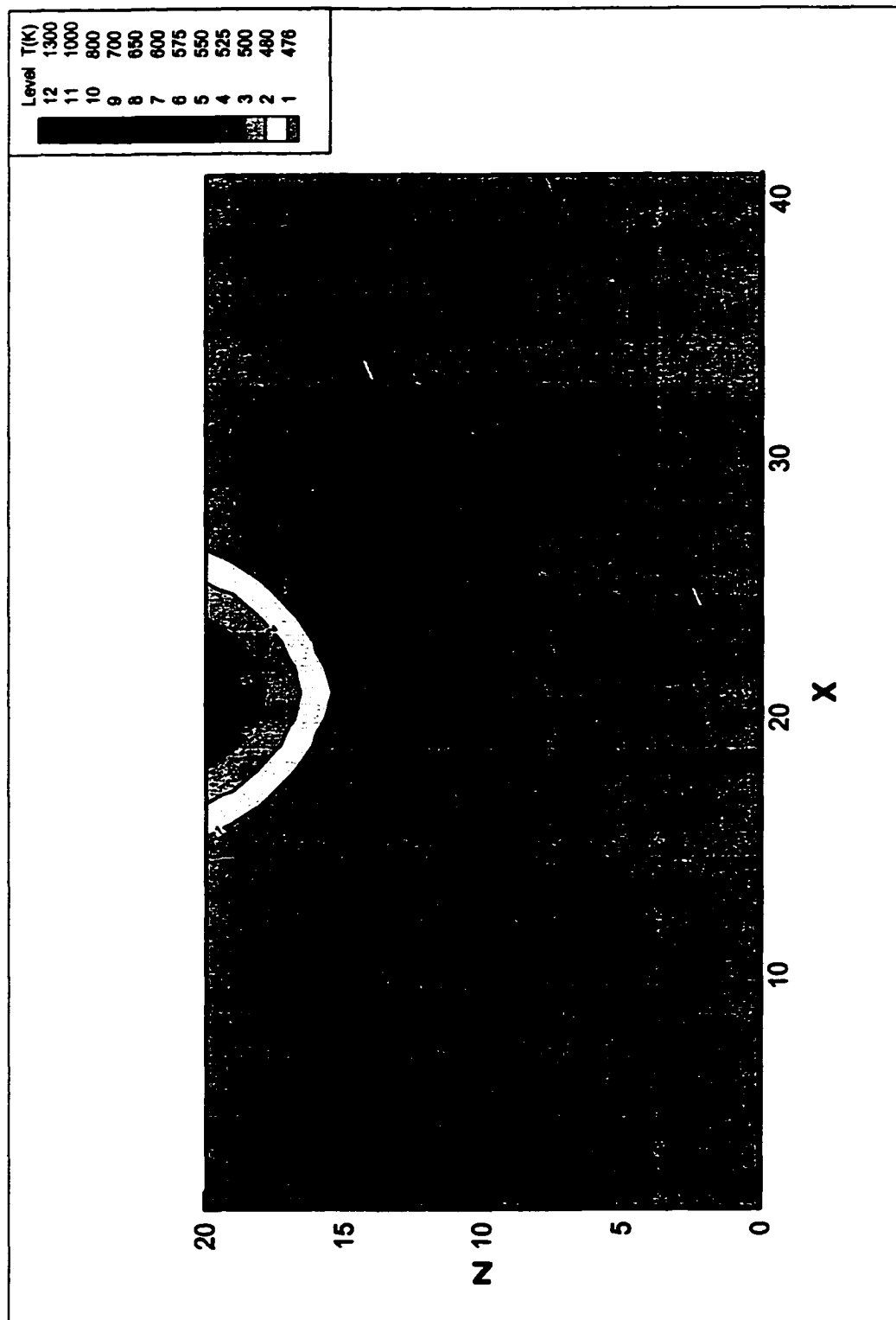
6.8 Temperature contour on the surface of the deposit ($P_0 = 0.08W$, Layer = 20, Position = A)



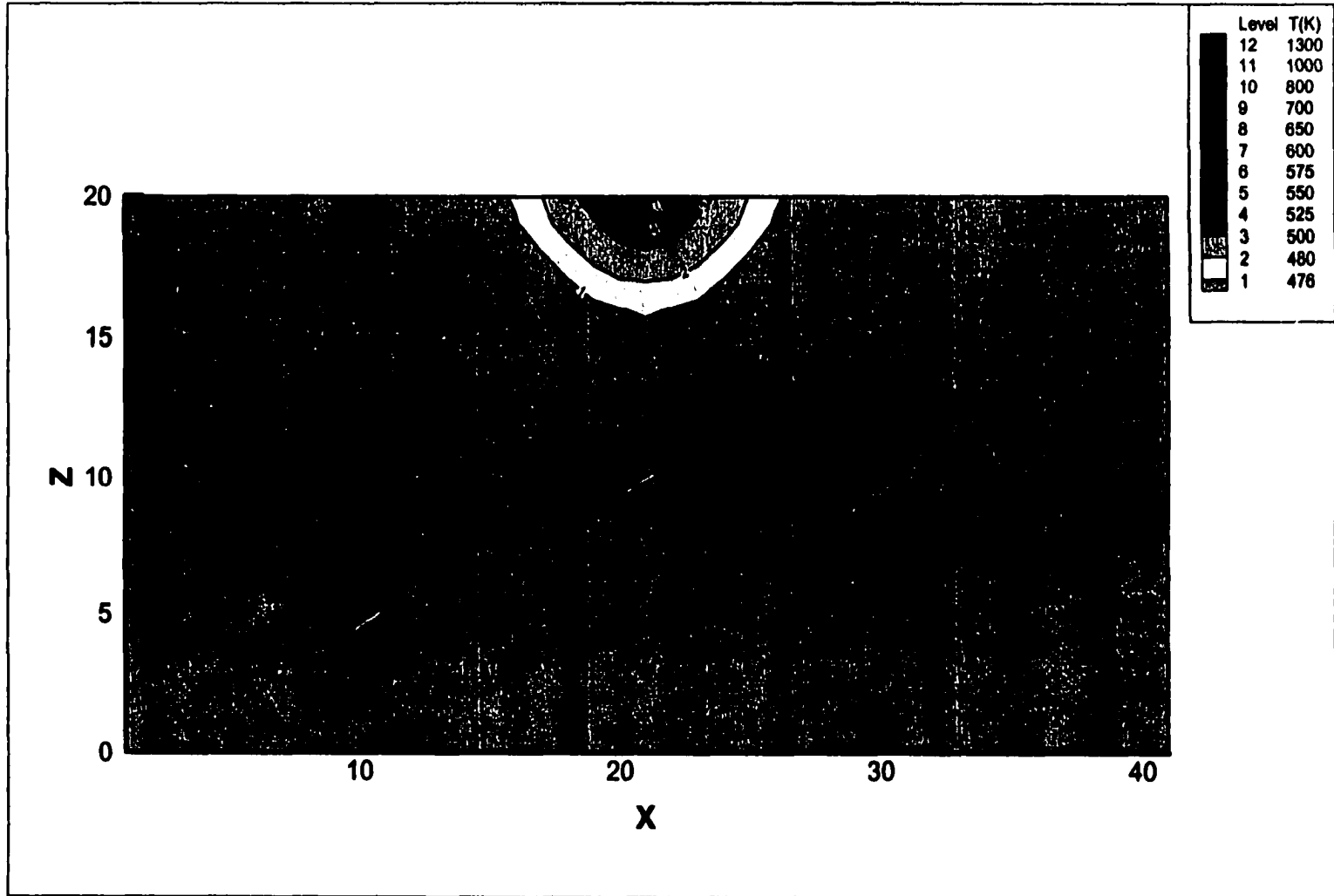
6.9 Temperature contour on the vertical cross-section of the substrate ($P_0 = 0.08W$, Layer = 0, Position = A)



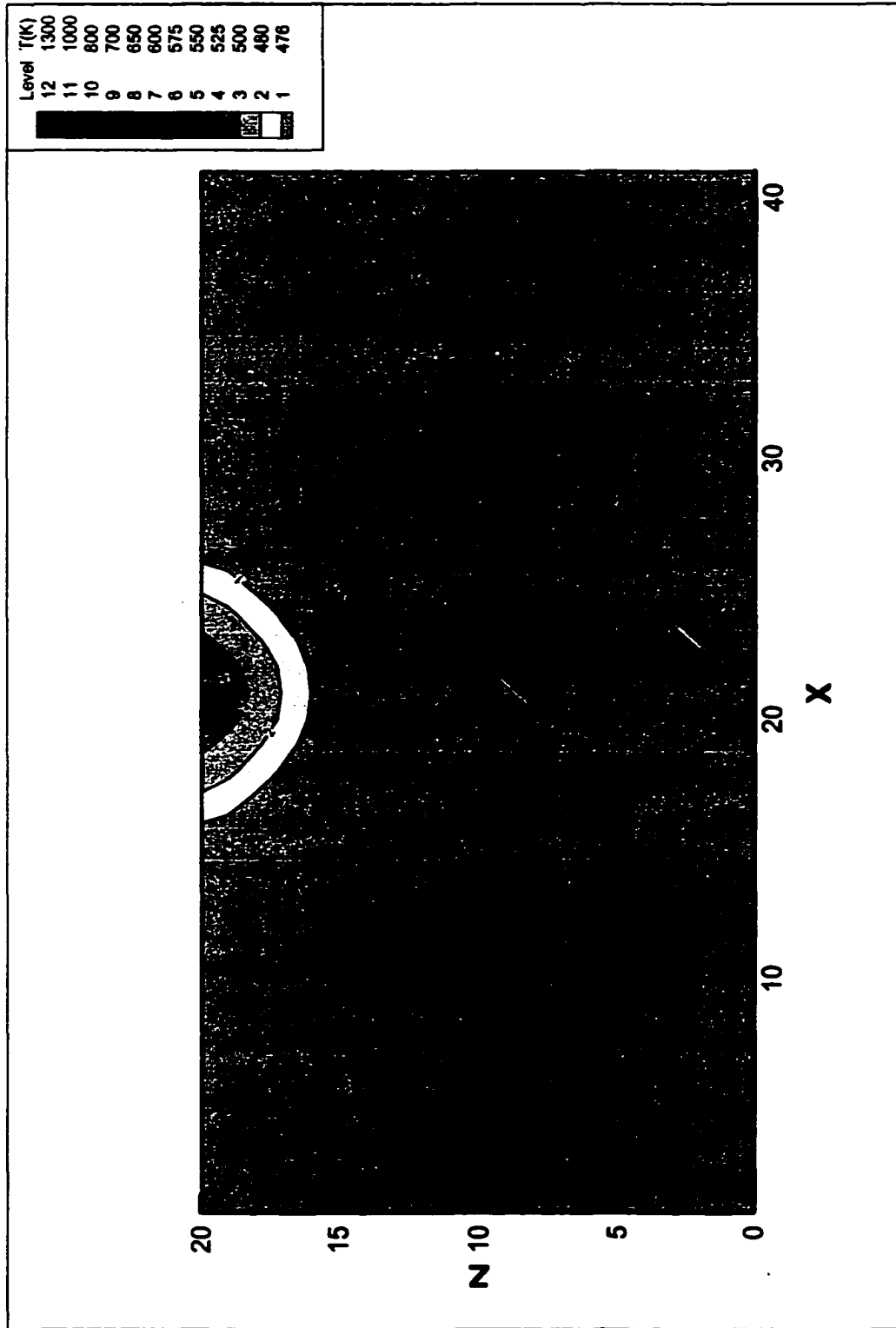
6.10 Temperature contour on the vertical cross-section of the substrate ($P_0 = 0.08W$, Layer = 5, Position = A)



6.11 Temperature contour on the vertical cross-section of the substrate ($P_0 = 0.08W$, Layer = 10, Position = A)



6.12 Temperature contour on the vertical cross-section of the substrate ($P_0 = 0.08W$, Layer = 15, Position = A)



6.13 Temperature contour on the vertical cross-section of the substrate ($P_0 = 0.08W$, Layer = 20, Position = A)

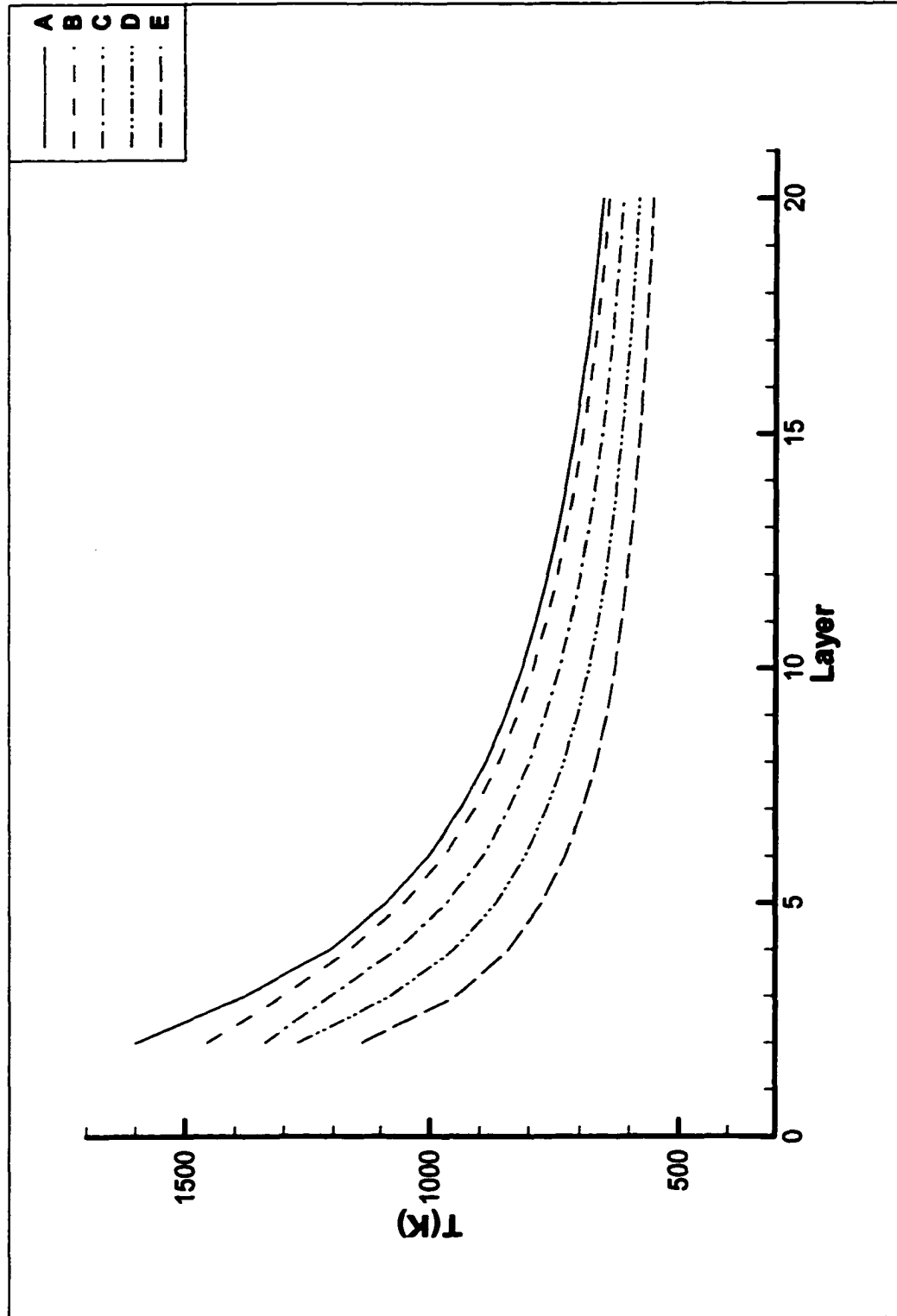


Figure 6.14 Highest temperature vs. layers of deposit on the surface of the concave microlens
($P_0 = 0.08W$, Position = A, B, C, D, E)

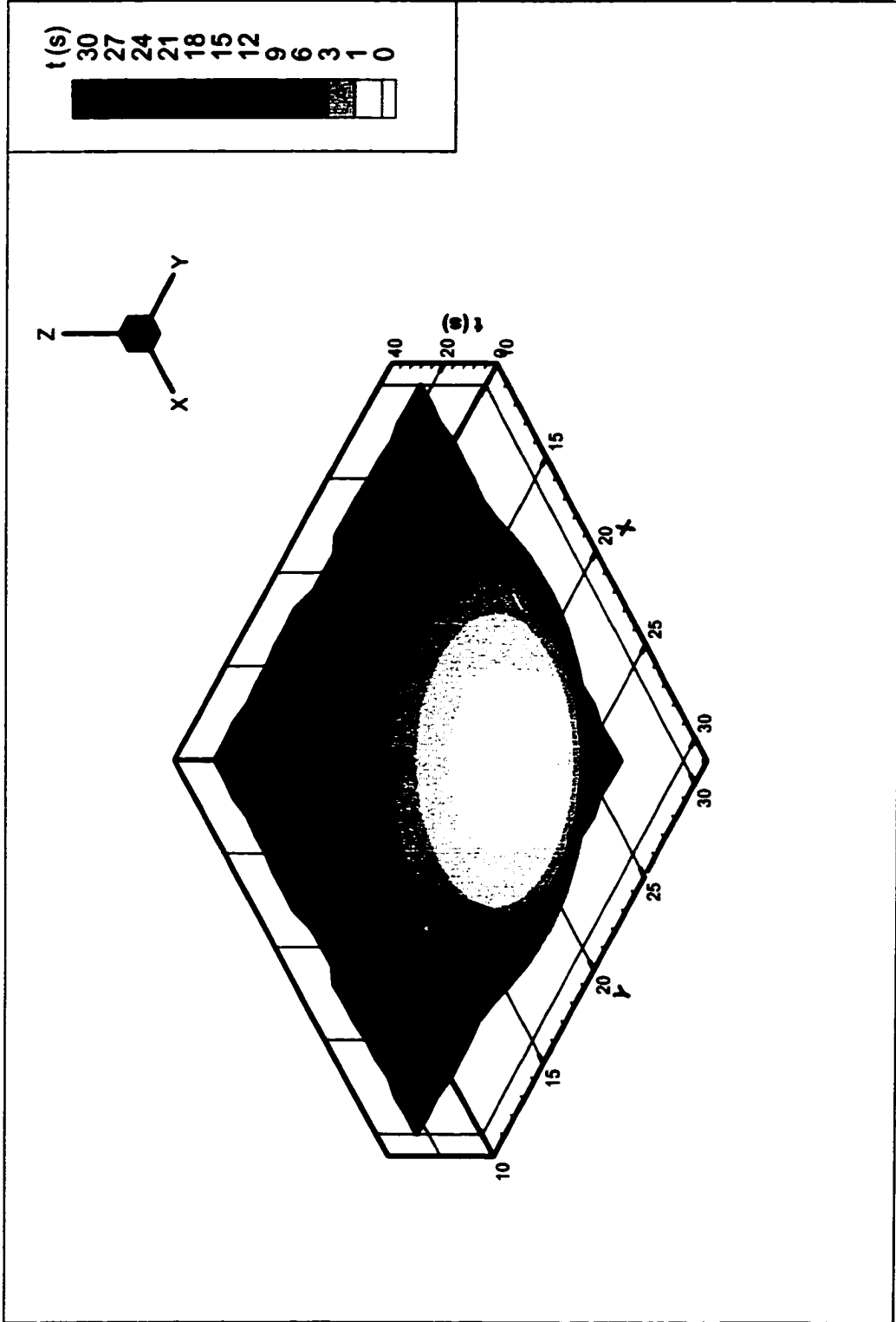


Figure 6.15 Sum of dwell times at each pixel for all layers 1-20 ($P_0 = 0.08W$)

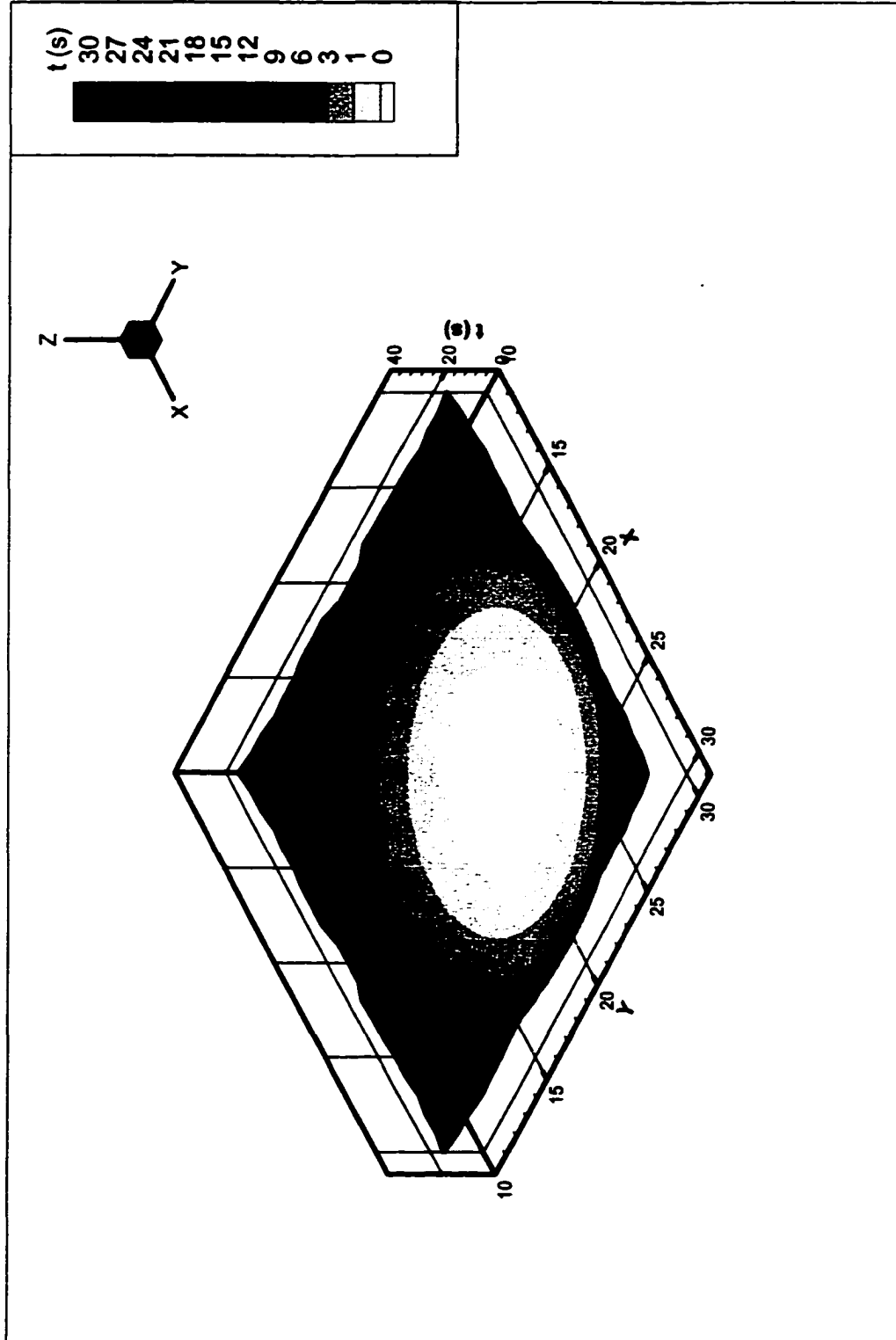


Figure 6.16 Sum of dwell times at each pixel for layers 16-20 ($P_0 = 0.08W$)

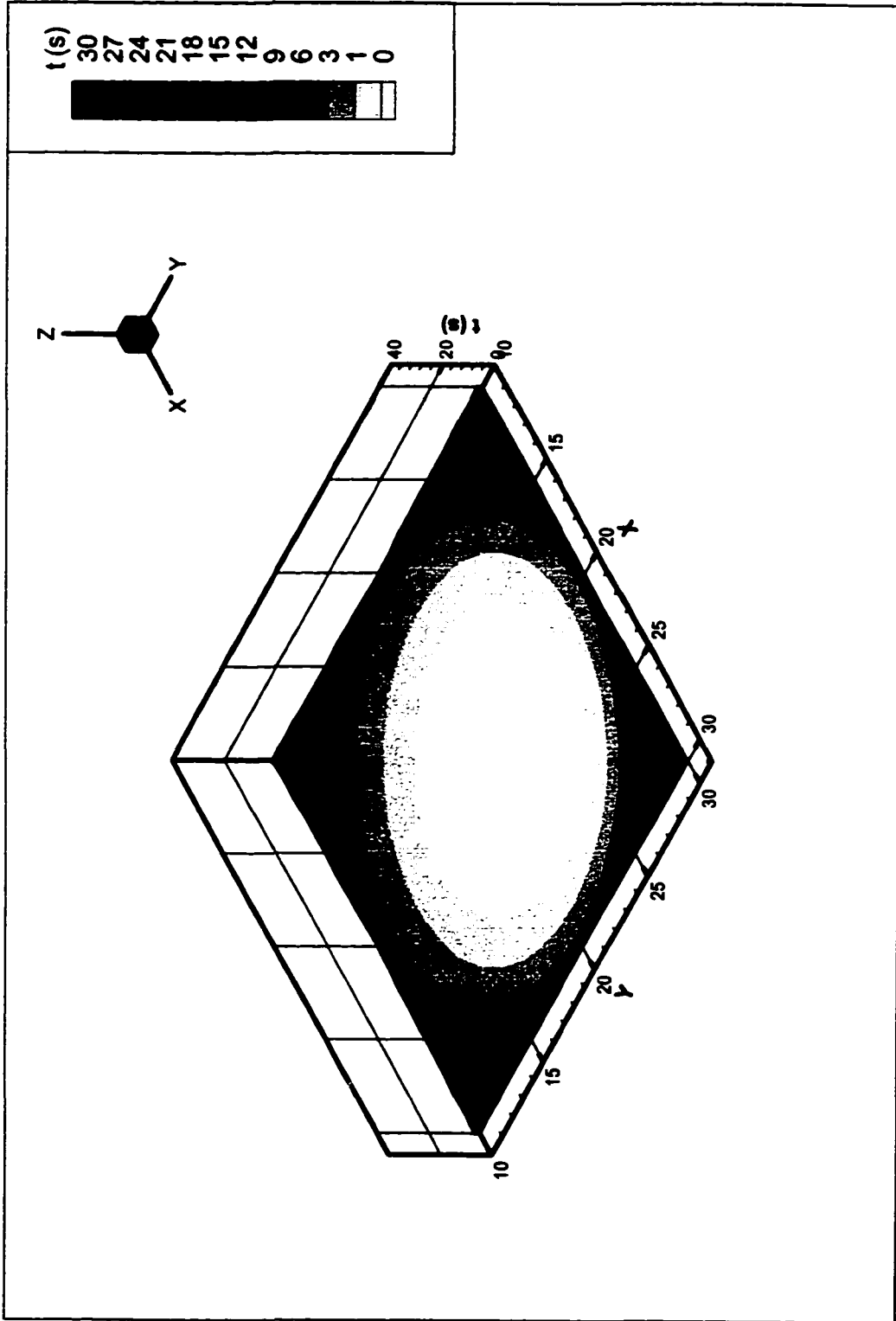


Figure 6.17 Sum of dwell times at each pixel for layers 11-15 ($P_0 = 0.08W$)

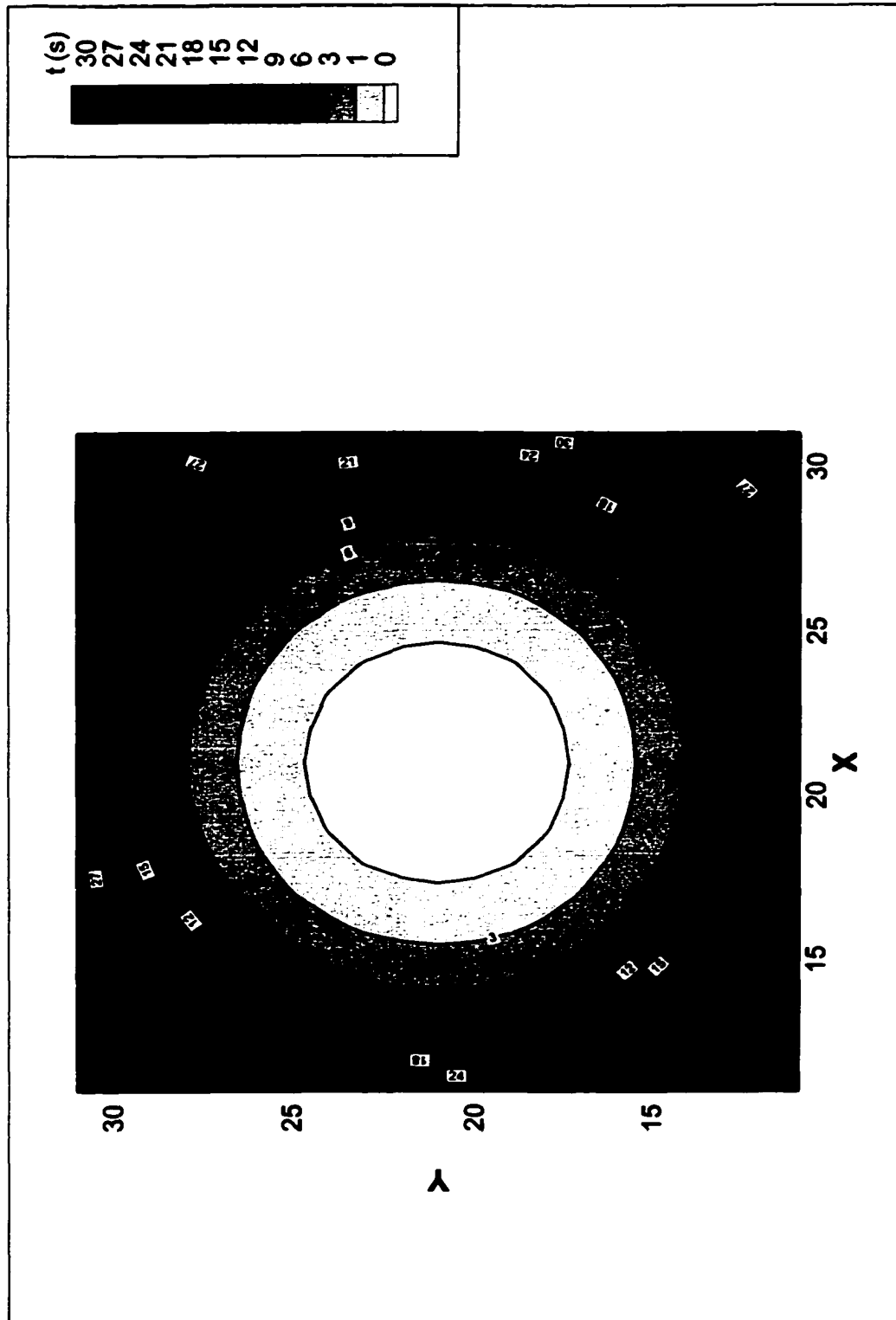


Figure 6.18 Contour of the sum of dwell times for all layers 1-20 ($P_0 = 0.08W$)

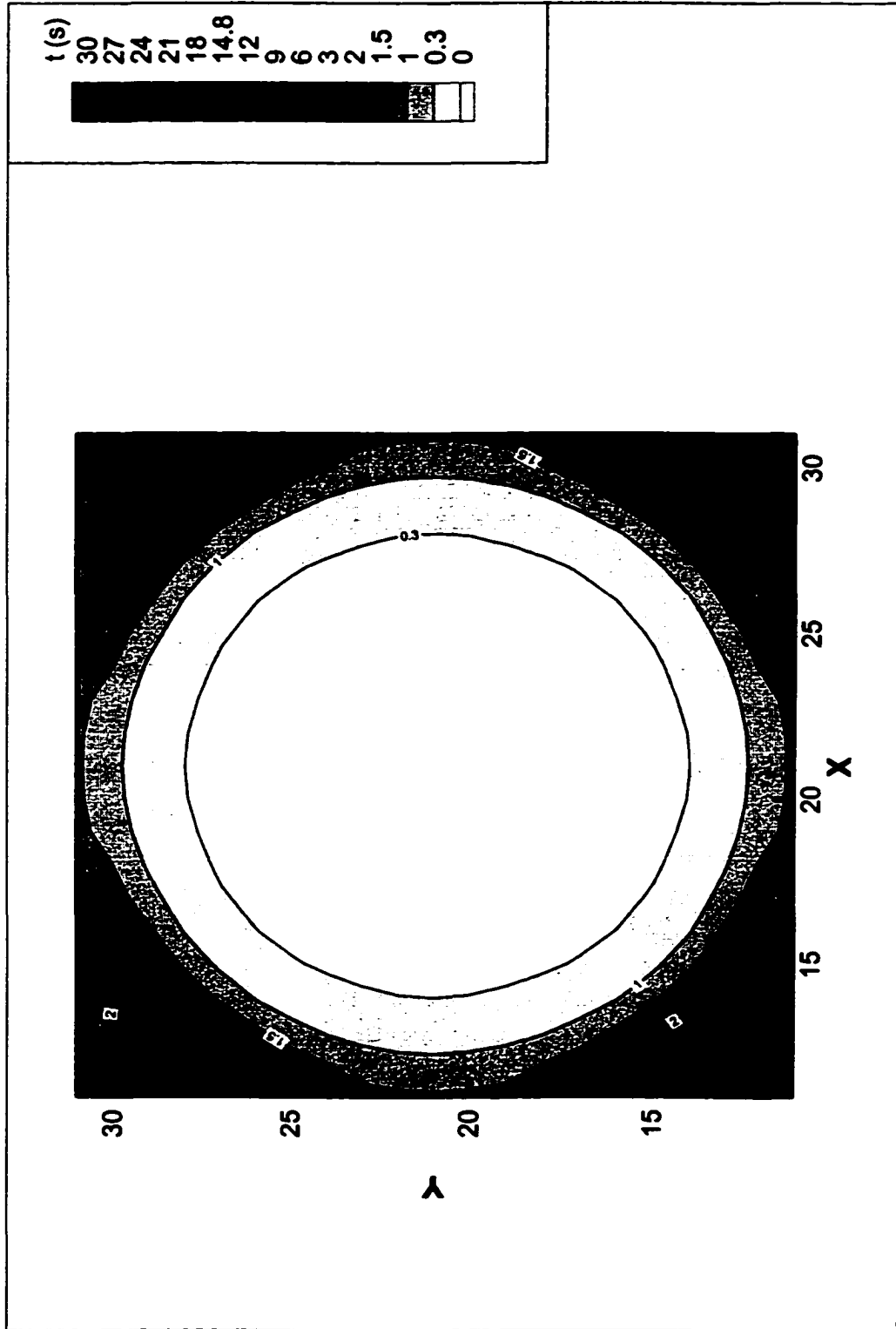


Figure 6.19 Contour of the sum of dwell times for layers 5-10 ($P_0 = 0.08W$)

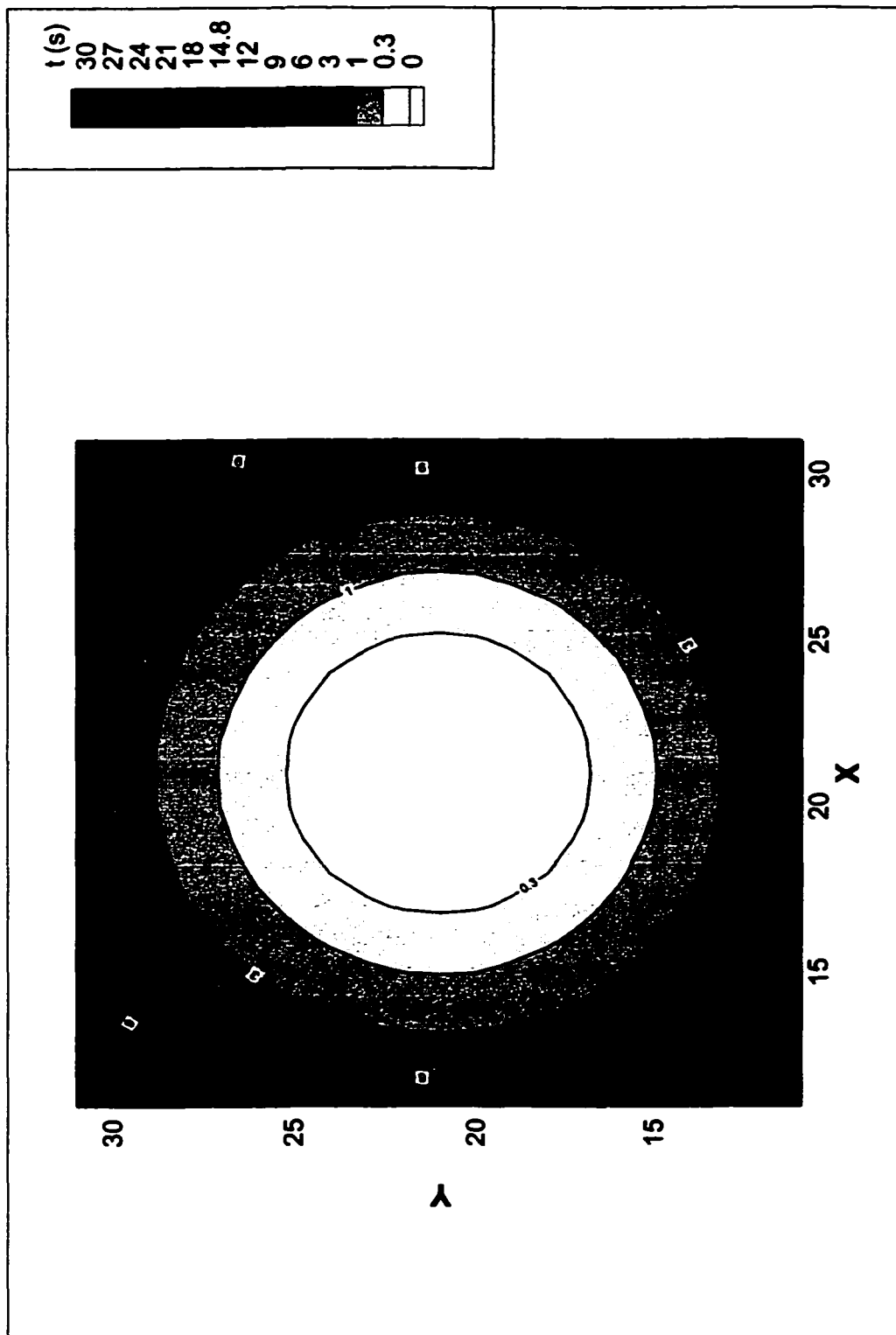


Figure 6.20 Contour of the sum of dwell times for layers 11-15 ($P_0 = 0.08W$)

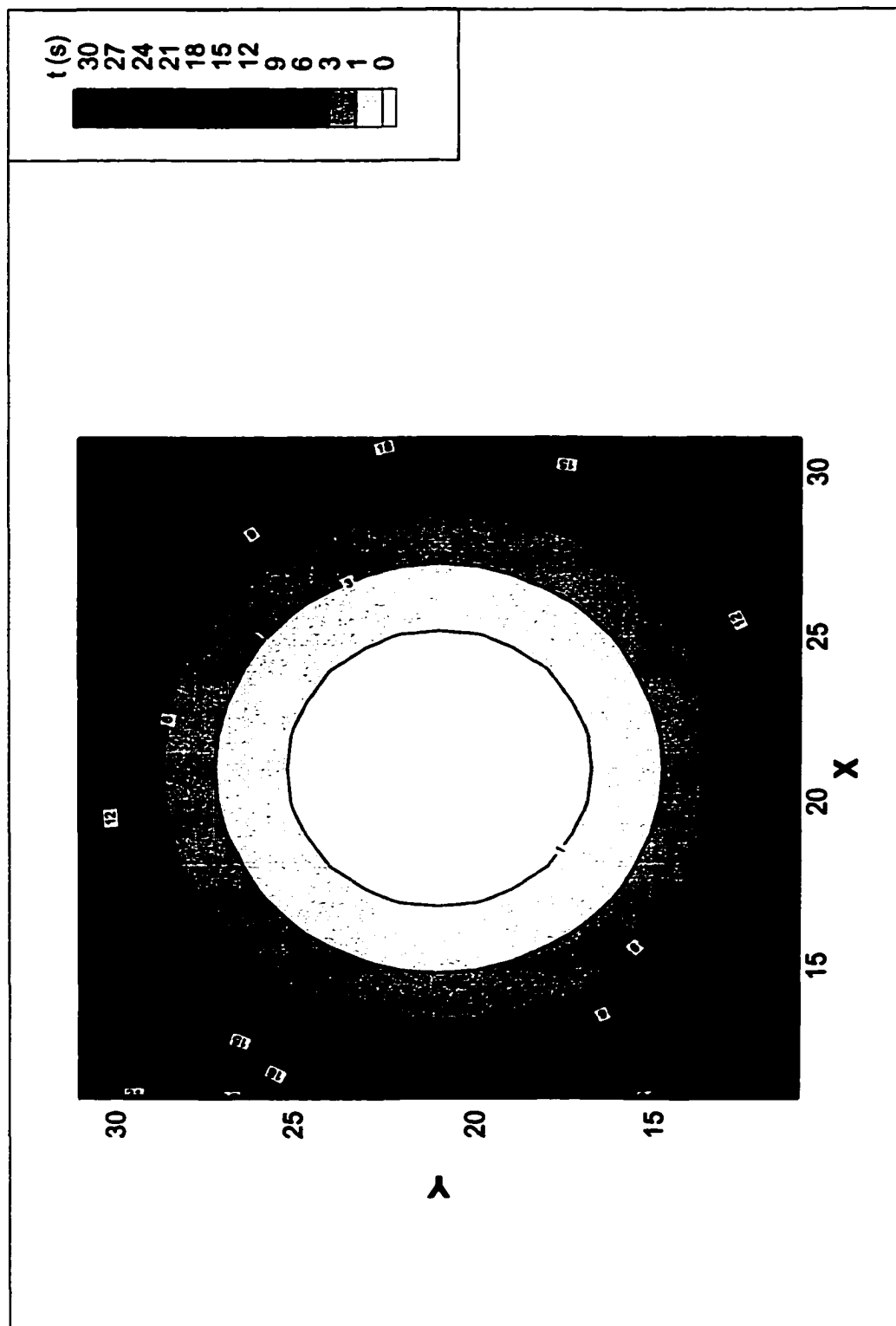


Figure 6.21 Contour of the sum of dwell times for layers 16-20 ($P_0 = 0.08W$)

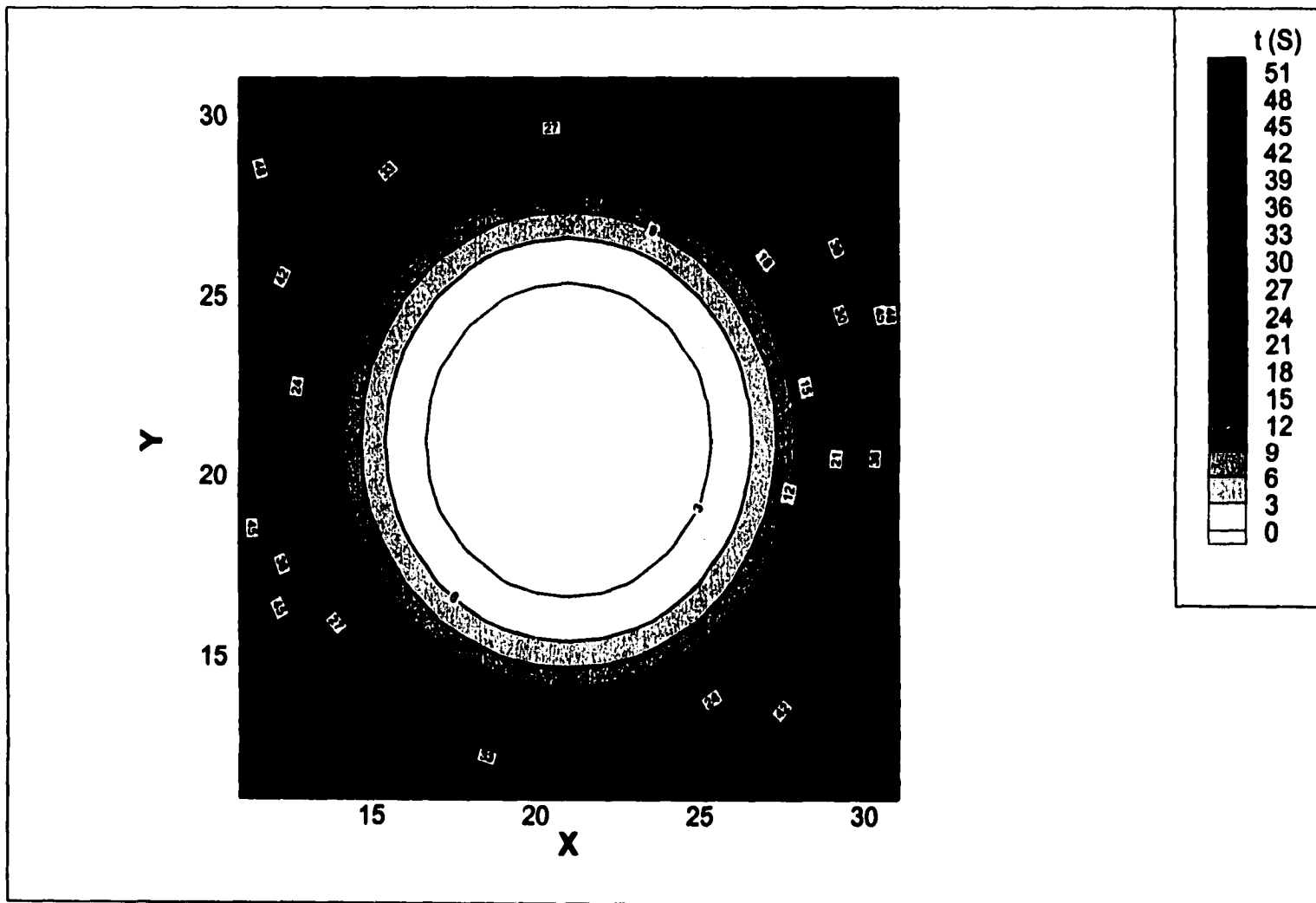


Figure 6.22 Contour of the sum of dwell times for all layers 1-20 ($P_0 = 0.05W$)

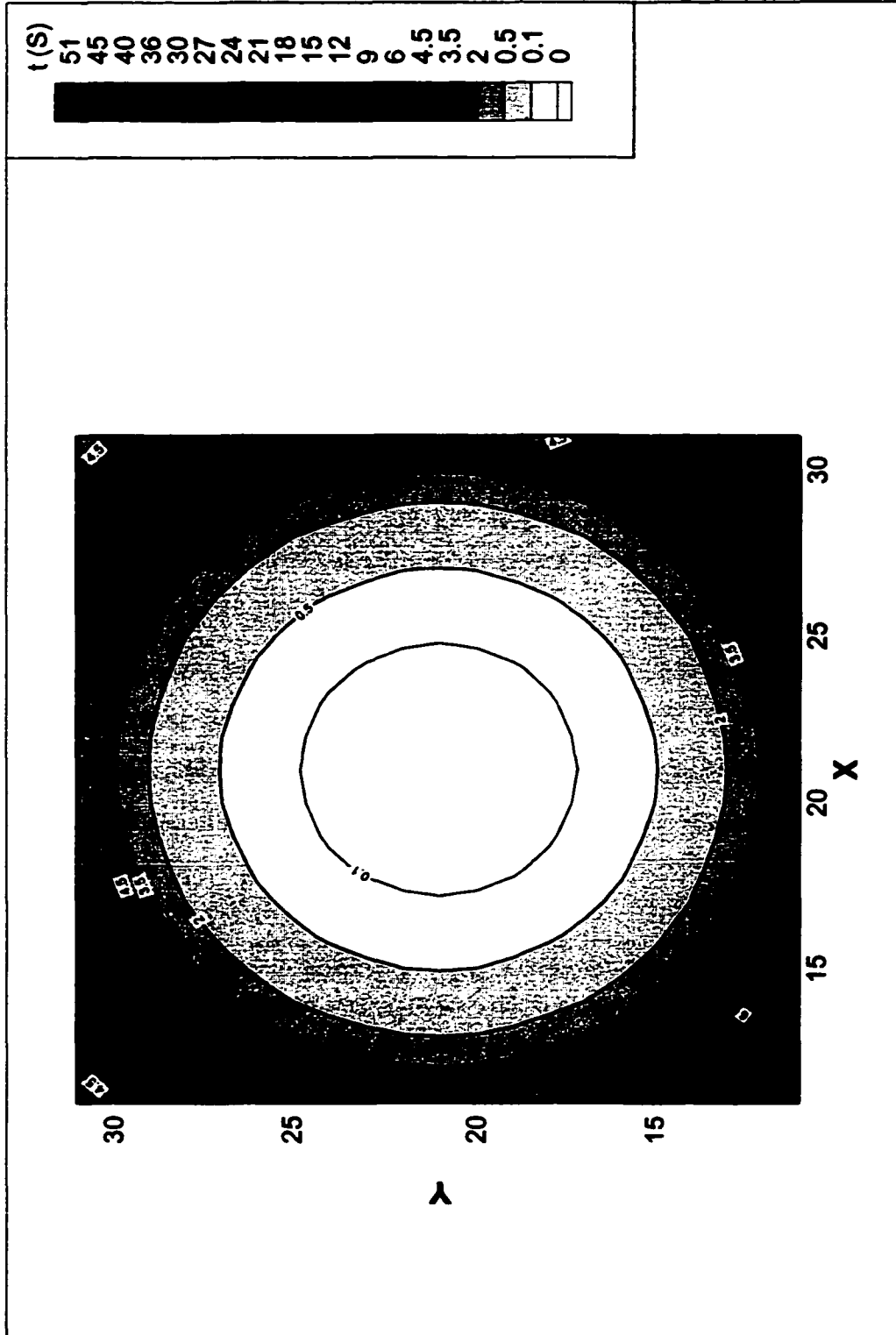


Figure 6.23 Contour of the sum of dwell times for layers 5-10 ($P_0 = 0.05W$)

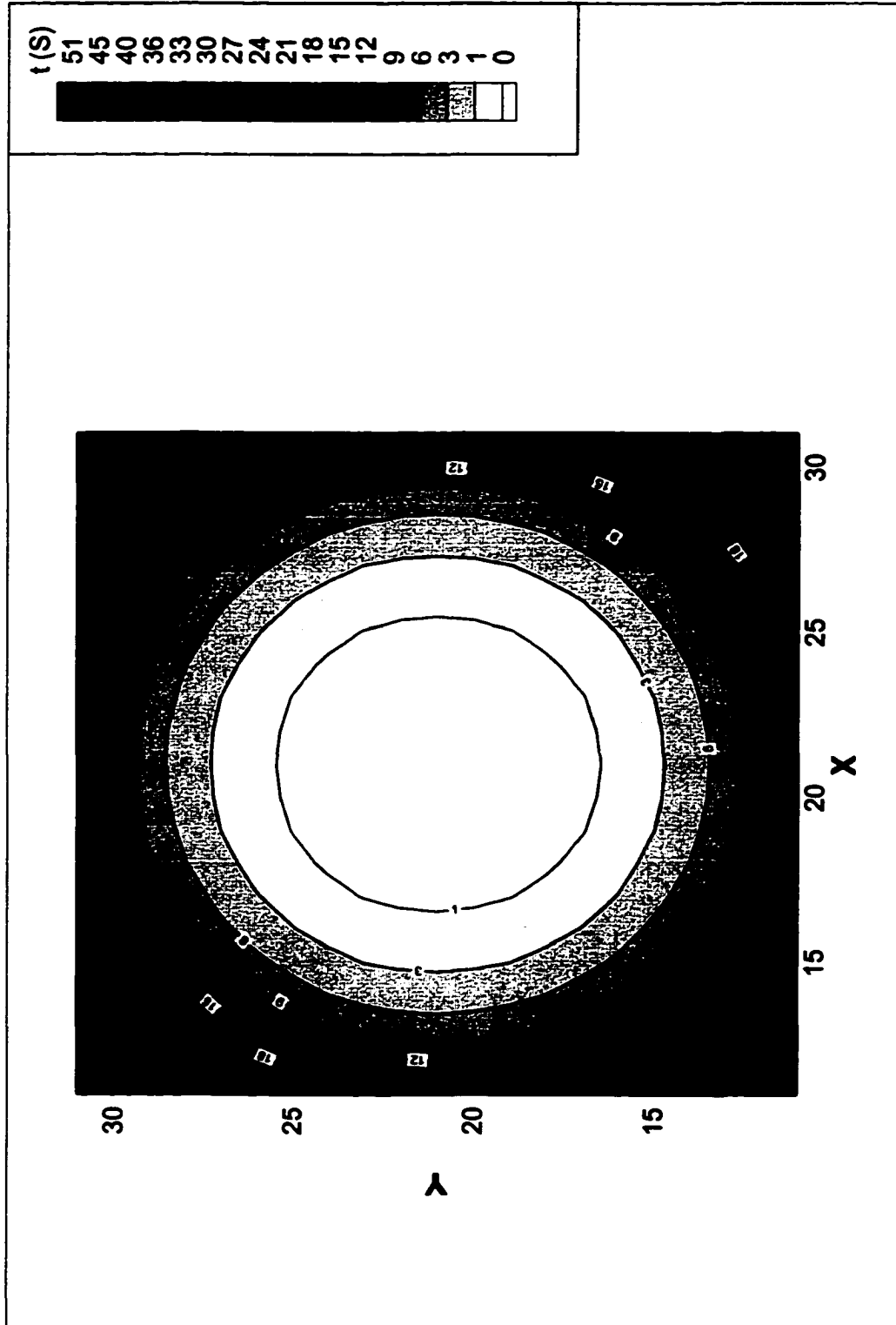


Figure 6.24 Contour of the sum of dwell times for layers 11-15 ($P_0 = 0.05W$)

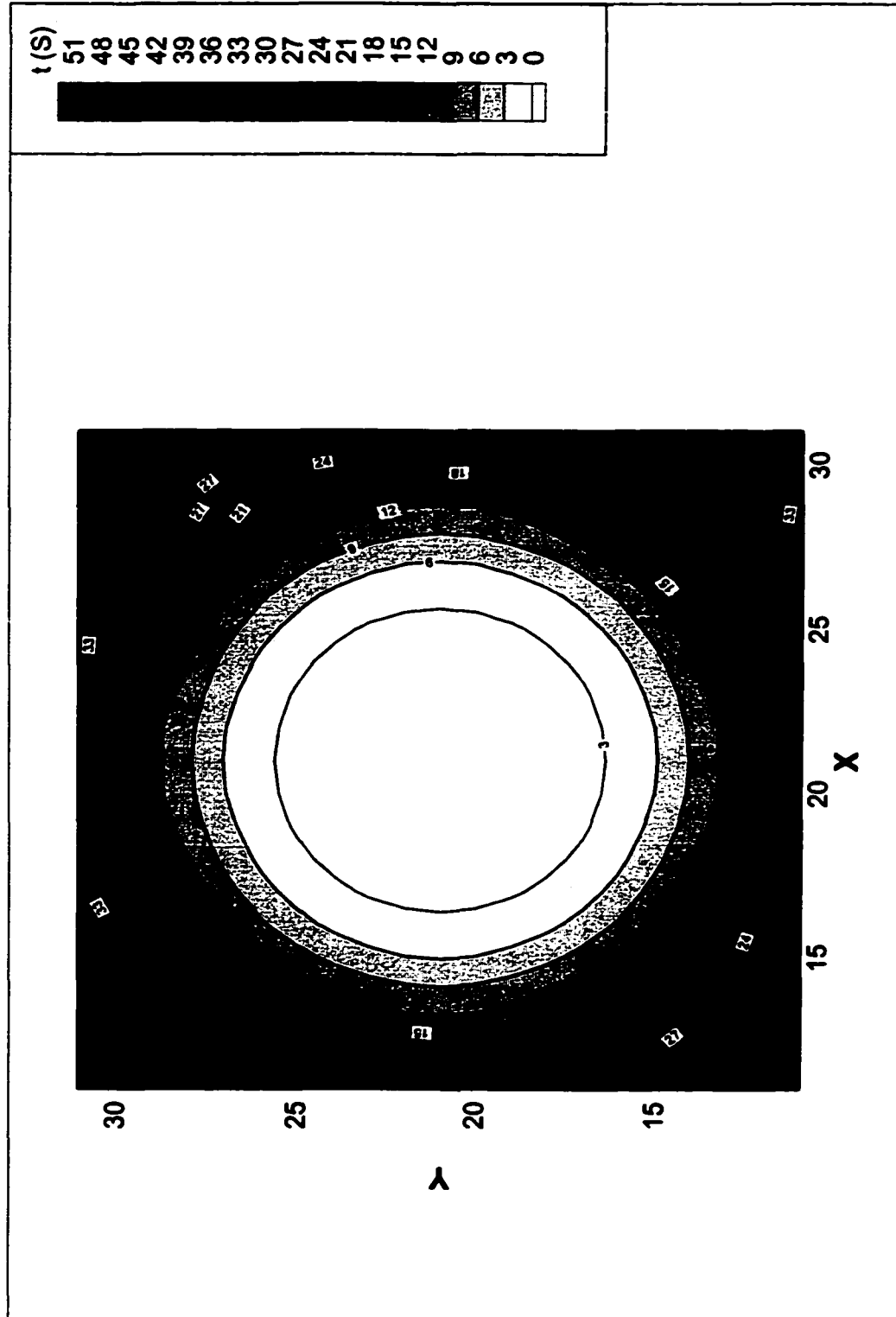


Figure 6.25 Contour of the sum of dwell times for layers 16-20 ($P_0 = 0.05W$)

CHAPTER 7

DISCUSSION AND CONCLUSION

The 3D-LCVD process is a viable mechanism for fabricating three-dimensional microstructures. Based on the investigation of pyrolytic LCVD, a new three-dimensional mathematical model has been developed to describe the heat transfer in the deposit and substrate and to predict the growth of deposit and the dwell time for fabricating a deposit with a pre-specified geometry.

The mathematical model describes the relationship among heat transfer, growth rate, and dwell time. The heat transfer equations describe the heat transfer not only in the deposit but also in the substrate. The general heat-transfer relation has been specified on the interface between the deposit and substrate. The conductivities of deposit and substrate may be different and may vary with temperature, which makes it possible to extend this model for simulating an LCVD process using different deposit and substrate materials. For a microstructure with a flat geometry, the temperature change along the vertical direction inside the deposit may be ignored since the heat conductivity of the deposit is much larger than that of the substrate, so it is simplified into a two-dimensional problem. However, a three-dimensional computation is used for predicting the temperature distribution inside the substrate.

A general parabolic equation is used to describe a deposit with a pre-specified geometry. For other kinds of shapes, it is possible to change this equation for calculating

the potential growth at each pixel for each layer. In the numerical examples, one only needs to specify the heights at the center and edge of the microlens for predicting the dwell times needed to fabricate a convex and a concave microlens. Therefore, the model can be easily applied to modeling the LCVD process with a variety of surface shapes as long as the ratio of height to length is relatively small.

The deposit growth is driven by a temperature above the threshold value, and the deposit grows along the normal direction on the surface of the deposit. The relation between the growth rate and the temperature is described by the Arrhenius equation. To simulate the process of LCVD, the temperature distribution should be first obtained. Given the deposit growth at each pixel, one cannot directly use the Arrhenius equation to predict the dwell time since temperatures affect the growth at a fixed pixel when the laser beam is focused at other neighboring pixels. In our model, the Gaussian laser beam is used, which covers several pixels even though it is focused at one fixed pixel at a time. At a fixed pixel, the sum of the deposits contributed for that pixel when the laser beam moves through all pixels is the actual deposit growth at that fixed pixel. Based on this analysis, a linear system has been obtained for predicting the dwell time at each pixel for each layer. This method is different from that used for modeling the LCVD process for a rod, in which the dwell time can be directly calculated from the Arrhenius equation, given the deposit growth and temperature.

Because of the complicated relationship among the temperature distribution of deposit and substrate, deposit growth, and dwell time, an iterative algorithm has been presented for solving the model. Jacobi and SOR methods are used to calculate the temperature and to solve the linear system. The properties of the linear system have been

examined. Several factors affect the properties of the linear system and hence affect the accuracy and convergence speed. An interesting relationship between the laser intensity distribution and the pixel size has been investigated. If the laser beam has a flatter distribution, it covers more pixels on the surface. Thus, the sum of the growths at a given pixel driven by the temperatures when the laser beam hits all other pixels (including the given pixel) may exceed the pre-specified growth at the fixed pixel, a result which can lead to unreasonable dwell time results. In our calculation, the SOR (or Gauss-Seidel) method gives the convergent solution for the linear system since its coefficient matrix is diagonally dominant.

Nickel and graphite are selected as materials for deposit and substrate, respectively. The temperature distribution is obtained when the laser beam hits each pixel in each layer. When the laser beam hits the central pixel, the temperature distribution is symmetric, whereas it is not symmetric when the laser beam hits a pixel near the edge because of the influence of the deposit boundary. For each temperature distribution, the maximum temperature occurs at the same pixel as which the laser beam hits. For each layer of a convex microlens, the temperature distribution becomes flatter when the laser beam hits the central pixel than when it hits the other pixels. Thus, the maximum temperature for each layer reaches its minimum value at the central pixel since the deposit height is larger near the central pixel and hence provides more room for heat transport to the surrounding area. For a fixed pixel the maximum temperature drops down with an increase in the number of layers. For the first several layers, the temperature drops fast and then slows down when the layer number becomes large. For different laser intensities, the corresponding temperature distributions are different. For a

given pixel on a layer, the maximum temperature for intensity $P_0 = 0.05W$ is lower than that for $P_0 = 0.08W$.

For each layer of a concave microlens, the maximum temperature reaches its highest value at the central pixel, where the deposit height is smallest, because there is less room for heat transport to the surrounding area. This result is different from that for a convex microlens. However, the relation between the maximum temperature and number of layers is similar to the result for a convex microlens. The maximum temperature at the first several layers drops fast and gradually slows down with an increase in layer number, and converge to a constant value.

The dwell time at each pixel of each layer has been obtained in order to control the scan process for fabricating a microlens with a pre-specified geometry. Near the central pixel of a convex microlens, more dwell time is needed to grow a deposit for a given height. This result can be explained as follows: (1) for each layer, the deposit growth along the normal direction on the surface of the deposit is larger at the central pixel than that at other pixels; (2) the maximum temperature is smallest at the central pixel. For each layer, the dwell time distribution also appears to have a convex parabolic shape. From these results one can see that for a given layer and pixel with the same deposit growth, the dwell time becomes larger when the laser intensity becomes smaller.

For a concave microlens, the pixel dwell time corresponding to each layer becomes larger when the number of layer increases, which is similar to the result for a convex microlens. However, the dwell time distribution for each layer is totally different from that of a convex microlens. For each layer of a concave microlens, the maximum temperature reaches its maximum value at the central pixel, which leads to the least dwell

time at the pixel. Thus the dwell time distribution appears to have a concave parabolic shape.

It is very difficult to develop a three-dimensional model that describes the relationship among the heat transfer of deposit and substrate, deposit growth and dwell time. In terms of the work, the current model may be extended to simulate the process of fabricating microstructures using other materials than nickel and graphite.

Experimental work is also strongly suggested to verify the model. After further verification of the model one may explore the possibility of fabricating a microstructure of a more complicated geometry or of arbitrary shape.

A further interest also is to develop a time-dependent 3D- LCVD model to simulate the whole process. Another challenging work is to include the precursor concentration calculation and consider the mass transport limitation in the current three-dimensional mathematical model.

APPENDIX

SOURCE CODE OF THE 3D-LCVD

MATHEMATICAL MODEL

Program: convex3d.f

```

c
c This program simulates the process for fabricating a microstructure
c with a pre-specified geometry using laser-induced chemical vapor
c deposition. It includes the following computations:
c
c 1) Three-dimensional temperature distribution of substrate
c 2) Two-dimensional temperature distribution of deposit
c 3) deposition growth along normal direction
c 4) dwell time at each pixel of each layer
c
c For the detailed information, please refer to the mathematical model
c
c Title: convex3d.f
c Author: Chaoyang Zhang
c Date: Jan., 2001
c Version: V4.0
c
c This version introduces the simulation of the process for fabricating
c a convex microlens into V3.0 which is for simulation of a concave
c microlens

```

```

parameter(mi=41,mj=41,mk=21,ml=51,mt=450)
parameter(imax=41,jmax=41,kmax=21,mmax=325,minner=293)
parameter(nx1=11,nx2=31,ny1=11,ny2=31)
parameter(conkd=0.0655,conks=0.0017,conv=0.0)
parameter(ea=94000.0,cr=8.314,ck=13700.0,t0=475)
parameter(dx=0.001,dy=0.001,dz=0.001,dh=0.0001)
parameter(dh1=0.0001,dh2=0.0)
parameter(m=3.95)
dimension h(mi,mj,ml),hgrowth(mi,mj,ml),hh(mi,mj)
dimension hhh(mi,mj)
dimension ts1(mi,mj,mk),ts2(mi,mj,mk)
dimension tsurf(mt,mt),a(mt,mt)
dimension tsurf1(mt,101),dwellt(mt,101)
dimension qin(mi,mj),qqin(mi,mj)
dimension X(mt),b(mt)
dimension kdomain(mi,mj),timeplot(mi,mj,ml),temp(mi,mj,ml)
dimension timetotal(mi,mj,ml),totalteachlayer(ml)
dimension angle(mi,mj,ml),coef(mi,mj,ml)
dimension Tdistr(mi,mj,ml)
dimension Tsub(mi,nj,ml)
dimension tempmin(ml),tempmax(ml)
dimension Tmax(mi,ml)

c*****
c Read the data
c*****
write(*,*)read the maximum iteration number'

```

```

read(*,*)maxiter
write(*,*)'read the over-relaxation factor'
read(*,*)wfactor
write(*,*)'read the given tolerance'
read(*,*)tol
write(*,*)'enter the layer number of deposit'
read(*,*)klay

c*****
c initialize array and variables
c*****
do i = 1,imax
do j = 1,jmax
  hhh(i,j)=0.0
  qin(i,j)=0.0
  qqin(i,j)=0.0
  hh(i,j)=0.0

do k = 1,kmax
  ts1(i,j,k)=t0
  ts2(i,j,k)=t0
  timetotal(i,j,k)=0.0
  Tdistr(i,j,k) = t0
  Tsub(i,j,k) = t0
end do
end do
end do

do k=1,klay
do i = 1,imax
  Tmax(i,k) = t0
end do
end do

do i=1,mmax
do j=1,mmax
  tsurf(i,j)=t0
  a(i,j)=0.0
end do
end do

do k=1,klay
  tempmax(k) = 0.0
  tempmin(k) = 5000.0
  totalteachlayer(k)=0.0
do i=nx1,nx2
do j=ny1,ny2
  anglecos=fy(i,j,k,nx1,nx2,ny1,ny2,dx,dy,dh1-dh2)
  angle(i,j,k)=anglecos
  coef(i,j,k)=fcoef(rn,anglecos)
end do
end do

```

```

    end do
    end do

c   calculate deposit growth
    call growth_ccave(nx1,nx2,ny1,ny2,klay,dx,dy,dh1,dh2,num,
+   kdomain, h, hgrowth)

    do i= 1,imax
    do j= 1,jmax
        if((i.ge.nx1.and.i.le.nx2).and.(j.ge.ny1.and.j.le.ny2))
+   then
            hhh(i,j) = h(i,j,20)
        else
            hhh(i,j) = 0.0
        end if
    end do
    end do

    write(*,*)"***** number= ", num, "   klayer=", klay
    write(*,*)"***** number= ", mmax, "   klayer=", klay

c*****
c   calculate the temperature
c*****
    do 100 k0=1,klay
        kcount=0
        do i=nx1,nx2
        do j=ny1,ny2
            hh(i,j)=h(i,j,k0)
        end do
        end do

        write(*,*)'The layer k0=',k0
        do jd=ny1,ny2
        do id=nx1,nx2
            if(kdomain(id,jd).eq.1) then
                kcount=kcount+1

                p0=0.05

c       calculate the temperature
            call tempsub(p0,k0,kdomain,angle,coef,hh,ts1,dt,id
+            jd,qin, ts2,maxiter, wfactor, tol)

            if(jd.eq.21) then
                Tmax(id,k0) = ts2(id, jd, 1)
            end if

            if(id.eq.21.and.jd.eq.21) then
                do j=ny1,ny2
                do i=nx1,nx2

```

```

      Tdistr(i,j,k0) = ts2(i,j,1)
    end do
  end do

  do i=nx1,nx2
    do k=1,mk
      Tsub(i,k,k0) = ts2(i,21,k)
    end do
  end do
end if

if(id.eq.21.and.jd.eq.21) then
  do j=ny1,ny2
    do i=nx1,nx2
      if(kdomain(i,j).ne.0) then
        qqin(i,j)=qin(i,j)
      end if
    end do
  end do
end if

kcell = 0
do ky=ny1,ny2
  do kx=nx1,nx2
    if(kdomain(kx,ky).eq.1) then
      kcell=kcell+1
      tsurf(kcount,kcell)=ts2(kx,ky,1)
      tsurf1(kcell,k0)=tsurf(210,kcell)
      a(kcount,kcell)=ck*exp(-ea/cr/tsurf(kcount,kcell))/
+ (1.0 +exp(t0-tsurf(kcount,kcell))/(0.01*t0))*1000.0
      if(tsurf(kcount,kcell).lt.(t0+1.0))
+ a(kcount,kcell)=0.0

    end if
  end do
end do

end if
end do
end do

c*****
c  calculate the dwell time
c*****
ii=0
do i=nx1,nx2
  do j=ny1,ny2
    if(kdomain(i,j).eq.1) then
      ii=ii+1
      b(ii)=hgrowth(i,j,k0)*1000.0
    end if
  end do
end do

```

```

end do
end do

call gs(a,b,X,minner)

do i=1,mmax
dwellt(i,k0)=X(i)
end do

kkk=0
do i=nx1,nx2
do j=ny1,ny2
timeplot(i,j,k0)=0.0
temp(i,j,k0)=300.0
if(kdomain(i,j).eq.1) then
kkk=kkk+1
timeplot(i,j,k0)=dwellt(kkk,k0)
totalteachlayer(k0)=totalteachlayer(k0)+timeplot(i,j,k0)
temp(i,j,k0)=tsurf(kkk, kkk)
if(k0 .eq. 1) then
timetotal(i,j,k0)=timeplot(i,j,k0)
else
timetotal(i,j,k0)=timetotal(i,j,k0-1)+timeplot(i,j,k0)
endif
end if
end do
end do

do i=nx1,nx2
do j=ny1,ny2
if(kdomain(i,j).eq.1) then
if(tempmax(k0) .lt. temp(i,j,k0)) tempmax(k0) = temp(i,j,k0)
if(tempmin(k0) .gt. temp(i,j,k0).and.kdomain(i,j).ne.0)
+ tempmin(k0) = temp(i,j,k0)
end if
end do
end do

write(*,112)tempmax(k0),tempmin(k0)
write(*,112)(timeplot(21,j,k0),j=ny1,ny2)
write(*,112)(Tdistr(21,j,k0),j=ny1,ny2)
write(*,112)(Tsub(j,2,k0),j=ny1,ny2)

100 continue
112 format(7f11.5)

c*****
c output simulated results
c*****
4 open(unit=06, file='d1.dat')

```

```

c  output the temperature change with layers at selected points
write(6,*)"
write(6,*)"**** Temperature change for selected points**** '
write(6,*)"VARIABLES="X", "T1", "T2", "T3", "T4", "T5"
WRITE(6,*)"ZONE I=21'
write(6,912)(k,(Tmax(i,k),i=21,29,2), k=1,klay)
912  format(i5, 2x,5f10.2)

write(6,*)'growth rate of several points in each layer '
write(6,301)(k,hgrowth(21,21,k)/totalteachlayer(k),
+ hgrowth(21,23,k)/totalteachlayer(k),hgrowth(21,25,k)/
+ totalteachlayer(k),hgrowth(21,27,k)/totalteachlayer(k),
+ hgrowth(21,29,k)/totalteachlayer(k),totalteachlayer(k),
+ k=1,klay)
301  format(i3,5f12.8,f15.6)

write(6,*)'Min temp in each layer '
write(6,312)(i, tempmax(i), tempmin(i),i=1,klay)
write(6,*)"**** the dwell time '

write(6,*)"
write(6,*)/Total Dwell time for layers of deposit. k=20'
write(6,*)"VARIABLES="I", "J", "DWELL TIME"
WRITE(6,*)"ZONE I=21, J=21, F=POINT'
write(6,3112)((i,j,timetotal(i,j,20),
+   j=ny1,ny2),i=nx1,nx2)

do k=1,klay-5,5
write(6,*)"
write(6,*)/Dwell time for the layers. klayer='k','K+5
write(6,*)"VARIABLES="I", "J", "DWELL TIME"
WRITE(6,*)"ZONE I=21, J=21, F=POINT'
write(6,3112)((i,j,timetotal(i,j,k+5)-timetotal(i,j,k),
+   j=ny1,ny2),i=nx1,nx2)
end do

198  format(2i5, i5)

c  output the laser intensity distribution
write(6,*)"
write(6,*)"**** Laser beam intensity distribution **** '
write(6,*)"VARIABLES="I", "J", "LASER INTENSITY"
WRITE(6,*)"ZONE I=21, J=21, F=POINT'
write(6,3112)((i,j,qqin(i,j),j=ny1,ny2),i=nx1,nx2)

c  output the temperature distribution at the surface of substrate
c  when laser beam focus on the center of the deposit
do k=1,klay,5
write(6,*)"
write(6,*)"** Temperature on surface**** , KK: ', k
write(6,*)"VARIABLES="I", "J", "TEMP DISTRIBUTION ON SUBSTRATE"

```



```

WRITE(6,*)'ZONE I=21, J=21, F=POINT'
write(6,3112)((i,j,Tdistr(i,j,k),j=ny1,ny2),i=nx1,nx2)
end do

c  output the temperature distribution on the vertical intersection
c  of substrate when laser beam focus on the center of the deposit
do k=1,klay,5
write(6,*)
write(6,*)** Vertical Temp **** KK : ', k
write(6,*)'VARIABLES="I", "J", "VERTICAL TEMP DISTRIBUTION"'
WRITE(6,*)'ZONE I=21, J=41, F=POINT'
write(6,3112)((i,k-1,Tsub(i,mk+1-k,kl),k=1,mk),i=1,imax)
end do

c  output the height of the deposit for selected layers
do k=5,klay,5
write(6,*)
write(6,*)***** HEIGHT *****
write(6,*)The layer of deposit. k=',k
write(6,*)'VARIABLES="I", "J", "HEIGHT"'
WRITE(6,*)'ZONE I=21, J=21, F=POINT'
write(6,3113)((i,j,1000.0*h(i,j,k),
+ j=ny1,ny2),i=nx1,nx2)
end do

do k=1,klay,1
write(6,3112)((i,j,timeplot(i,j,k),
+ j=ny1,ny2),i=nx1,nx2)
write(6,311)((i,j,k,1000.0*h(i,j,k),1000.0*hgrowth(i,j,k),
+ temp(i,j,k),
+ coef(i,j,k),angle(i,j,k),
+ j=ny1,ny2),i=nx1,nx2)
end do

312  format(i5, 2f14.2)
3112 format(2i5, f14.4)
3113 format(2i5, f14.6)
311  format(i3,i3,i3,2f15.8,f10.2, 2f12.8)

write(6,*)***** the dwell time '
do k=1,klay
write(6,*)The layer of deposit. k=',k
write(6,111)(dwellt(i,k),i=1,100)
write(6,211)(i,(1000.0*timeplot(i,j,k),j=ny1,ny2),i=nx1,nx2)
end do
write(6,*)***** the dwell time '
write(6,111)(X(i),i=1,mmax)
write(6,*)***** b(i) *****
write(6,111)(b(i),i=1,mmax)
111  format(5f14.10)
211  format(i2,7f10.5/2x,7f10.5/2x,7f10.5)

```

```

write(6,*)'*** temperature of the substrate ***'
do k=1,kmax
write(6,*)k=',k
write(6,20)(i,(ts2(i,j,k),j=1,40,2),i=1,40,2)
end do

write(6,*)"
write(6,*)'**** Heat distribution ***** =1 '
write(6,*)'id=',id, ' jd=', jd
do i =nx1,nx2
write(6,*) 'i=',i
write(6,21)(qqin(i,j),j=ny1,ny2)
end do

write(6,*)'*** temperature distribution on the surface '
write(6,*)' when laser beam focus on element i *** '
do i =100,num-150
write(6,*) 'i=',i
write(6,21)(tsurf(i,j),j=1,num)
end do

write(6,*)'matrix A and temperature distribution at element j'
do j =1,num
write(6,*) 'tsurface, j='j
write(6,21)(tsurf(i,j),i=1,num)
write(6,*) 'matrix A, j='j
write(6,23)(a(i,j),i=1,num)
write(6,*)'the b(i) '
write(6,23)(b(i),i=1,400,10)
end do

20  format(i4,10f7.1/4x,10f7.1)
21  format(10f8.1)
23  format(5f15.7)
close(6)
stop
end

c*****
c  function for angular of absorption
c*****
c alfa: the cos(angle)
function fcoef(rn,alfa)
  unx = alfa
  unr=sqrt(1.0-unx*unx)
  c1=sqrt(rn*rn-unr*unr)
  c2=unx-c1
  c3=unx+c1
  c4=rn*rn*unx-c1
  c5=rn*rn*unx+c1

```

```

c6=c2*c2/(c3*c3)+c4/c5
fcoef=1.0-0.5*c6
end

c***** subroutine for substrate temperature *****
  subroutine tempsub(p0,n,kdomain,angle,coef,hh,ts1,dt,id,jd,
c +   qin,ts2)
  +   qin,ts2,maxiter, w, tolerance)
  parameter(mi=41,mj=41,mk=21,ml=51)
  parameter(imax=41,jmax=41,kmax=21,mmax=325)
  parameter(nx1=11,nx2=31,ny1=11,ny2=31)
  parameter(dx=0.001,dy=0.001,dz=0.001,dh=0.0001)
  parameter(conkd=0.0655,conks=0.0017,conv=0.0)
  parameter(ea=94000.0,cr=8.314,ck=13700.0,t0=475)
  parameter(pi=3.1415926,delta=0.0005)
  dimension qin(mi,mj), hh(mi,mj), kdomain(mi,mj)
  dimension ts1(mi,mj,mk), ts2(mi,mj,mk)
  dimension angle(mi,mj,ml)
  dimension coef(mi,mj,ml)

  err=0.0

c   the initial condition
  do i=1,imax
  do j=1,jmax
  do k=1,kmax
    ts1(i,j,k)=t0
    ts2(i,j,k)=t0
  end do
  end do
  end do

c   boundary condition
  do j=1,jmax
  do k=1,kmax
    ts2(1,j,k)=t0
    ts2(imax,j,k)=t0
  end do
  end do

  do i=1,imax
  do k=1,kmax
    ts2(i,1,k)=t0
    ts2(i,jmax,k)=t0
  end do
  end do

  do i=1,imax
  do j=1,jmax
    ts2(i,j,kmax)=t0
  end do

```

```

end do

do i=nx1,nx2
do j=ny1,ny2
  qin(i,j) = p0/delta/sqrt(2.0*pi)/delta/sqrt(2.0*pi)
+   *exp(-((i-id)*(i-id)*dx*dx+(j-jd)*(j-jd)*dy*dy)
+   /2.0/delta/delta)
  qin(i,j)=qin(i,j)*angle(i,j,n)*coef(i,j,n)
end do
end do

iter = 0
1000   iter=iter+1

do i=nx1,nx2
do j=ny1,ny2
if(kdomain(i,j).eq.1) then
  cx1=(hh(i+1,j)+hh(i,j))/2.0*conkd/dx/dx
  cx2=(hh(i,j)+hh(i-1,j))/2.0*conkd/dx/dx
  cy1=(hh(i,j+1)+hh(i,j))/2.0*conkd/dy/dy
  cy2=(hh(i,j-1)+hh(i,j))/2.0*conkd/dy/dy
  cz=conks/dz
  cxyz=cz+cx1+cx2+cy1+cy2

  ts2(i,j,1)=(ts1(i,j,2)*cz+qin(i,j)
+   +cx1*ts1(i+1,j,1)+cx2*ts1(i-1,j,1)
+   +cy1*ts1(i,j+1,1)+cy2*ts1(i,j-1,1))/cxyz
  ts2(i,j,1)=ts1(i,j,1)+w*(ts2(i,j,1)-ts1(i,j,1))
else
  ts2(i,j,1)=t0
end if
end do
end do

do i=nx1,nx2
do j=ny1,ny2
  ts1(i,j,1) = ts2(i,j,1)
end do
end do

c   calculate the temperature on the boundary of the interface
c   between the deposit and the substrate
do i=nx1,nx2
do j=ny1,ny2
if(kdomain(i,j).eq.2) then
  numofl = 0
  sumofl = 0.0
  if(kdomain(i-1,j).eq.1) then
    sumofl = sumofl + ts2(i-1,j,1)
    numofl = numofl + 1
  end if
end if
end do
end do

```

```

    end if
    if(kdomain(i+1,j).eq.1) then
        sumof1 = sumof1 + ts2(i+1,j,1)
        numof1 = numof1 + 1
    end if
    if(kdomain(i,j-1).eq.1) then
        sumof1 = sumof1 + ts2(i,j-1,1)
        numof1 = numof1 + 1
    end if
    if(kdomain(i,j+1).eq.1) then
        sumof1 = sumof1 + ts2(i,j+1,1)
        numof1 = numof1 + 1
    end if
    ts2(i,j,1) = sumof1 / float(numof1)
end if
end do
end do

c   calculate the temperature of the substrate
do k=2,kmax-1
do i=2,imax-1
do j=2,jmax-1
    ts2(i,j,k)=(ts1(i-1,j,k)+ts1(i+1,j,k)+ts1(i,j-1,k)
+      +ts1(i,j+1,k)+ts1(i,j,k-1)+ts1(i,j,k+1))/6.0
    ts2(i,j,k)=ts1(i,j,k)+w*(ts2(i,j,k)-ts1(i,j,k))
end do
end do
end do

do i=1,imax
do j=1,jmax
do k=2,kmax
    if((ts2(i,j,k)-ts1(i,j,k))/ts1(i,j,k).gt.err)
+      err=(ts2(i,j,k)-ts1(i,j,k))/ts1(i,j,k)
    ts1(i,j,k)=ts2(i,j,k)
end do
end do
end do

if(err.gt.tolerance.and.iter.lt.maxiter) goto 1000

if(id.eq.21.and.jd.eq.21) then
    write(*,*) 'err= ', err, ' iter=', iter
end if

return
end

c*****
c  subroutine for obtain temperature
c*****

```

```

subroutine dta(ea,cr,ck,tsurf,a)
dimension tsurf(100,100), a(100,100)
do i=1,100
do j=1,100
a(i,j)=ck*exp(-ea/cr/tsurf(i,j))
end do
end do
return
end

c*****
c calculating the angle between the z and normal direction
c*****
function fy(i,j,n,nx1,nx2,ny1,ny2,dx,dy,dh)
radius=dx*(nx2-nx1)/2.0
ix0=(nx1+nx2)/2
jy0=(ny1+ny2)/2
x=dx*(i-ix0)
y=dy*(j-jy0)
fy = (sqrt(radius*radius*radius*radius +
+ 4.0*n*n*dh*dh*(x*x+y*y)))/(radius*radius)
fy=1.0/fy
end

c*****
c calculate the growth of deposit at each point along the normal
c direction
c*****
c h00 is the basic height of the the microstructure
subroutine growth_ccave(nx1,nx2,ny1,ny2,klayer,dx,dy,
+ dh1,dh2,
+ n_point,kdomain, h, hgrowth)
real h01, h02, hd0, radius
parameter(imax=41,jmax=41,ml=51,mmax=325)
dimension kdomain(imax,jmax), h(imax,jmax,ml),
+ hgrowth(imax,jmax,ml)
h00 = 0.00005

do k=1,ml
do i=1,imax
do j=1,jmax
kdomain(i,j)=0
h(i,j,k)=0.0
hgrowth(i,j,k)=0.0
end do
end do
end do

do k=1,ml
n_point = 0

```

```

do i=nx1,nx2
do j=ny1,ny2
  xk=dx*(i-21)
  yk=dy*(j-21)
  rk=dx*10
  h(i,j,k)=dh1*k+(dh2-dh1)*k*(xk*xk+yk*yk)/rk/rk+h00
  if(sqrt(xk*xk+yk*yk).le.(dx*(10.0+0.1))) then
    kdomain(i,j)=1
    if(sqrt(xk*xk+yk*yk).ge.(dx*(9.5+0.0)))kdomain(i,j) =2
    n_point=n_point+1
    if(h(i,j,k) .lt. 0.0) h(i,j,k) = 0.0
    if((k.ne.1).and.(dh2.gt.dh1).and.(h(i,j,k).gt.(dh2*k)))
+     h(i,j,k) =dh2*k
    else
      kdomain(i,j) = 0
      h(i,j,k)=0.0
    end if
  end do
end do
end do

h01=dh1
h02=dh2
hd0=h02-h01
ix0=imax/2+1
jy0=jmax/2+1
write(*,*)"h0,ix0,jy0", h0,ix0,jy0

do n=1,ml
do i=nx1,nx2
do j=ny1,ny2
  x=dx*(i-ix0)
  y=dy*(j-jy0)
  radius=dx*(nx2-nx1)/2.0
  if(kdomain(i,j).ne.0) then
    if( n.eq.1) then
      hgrowth(i,j,n)=h(i,j,n)
    else
      if(x.eq.0.0.and.y.eq.0.0) then
        hgrowth(i,j,n)=h01
      else
        a = -4.0*n*n*(n+1)*hd0*hd0*hd0*(x*x+y*y)
        b = radius*radius*radius*radius*radius*radius+
+       4.0*n*(n+1)*hd0*hd0*radius*radius*(x*x+y*y)
        c = -h01*radius*radius*radius*radius*radius*radius -
+       hd0*radius*radius*radius*radius*(x*x+y*y)
        rou = 2.0*c/(-b-sqrt(b*b-4.0*a*c))
        fi = (sqrt(radius*radius*radius*radius +
+       4.0*n*n*hd0*hd0*(x*x+y*y)))/(radius*radius)

```

```

      hgrowth(i,j,n)=rou*fi
89   format(i3,2f8.4,7e18.10)
      end if
      end if
      if(hgrowth(i,j,n).lt.0.0) hgrowth(i,j,n) = 0.0
      end if
      end do
      end do
      end do
      return
      end

c*****
c Gauss_Siediel Iteration Method to solve linear system
c*****
      subroutine gs(as,b,x1,n)
      parameter(mt=450,mmax=325)
      dimension as(mt,mmax),a(mt,mmax+1),b(mmax),x1(mmax)

c   transfer array as(n,n) to a(n,n+1)
      do i = 1,n
        do j = 1,n
          a(i,j)= as(i,j)
        end do
        a(i,n+1) = b(i)
        x1(i) = 0.0
      end do

c   the tolerance
      tol = 0.00001

c   maximum number of iterations.'
      nn = 1000

      k = 1
100  if (k.gt.nn) goto 200

c   infinity-norm
      err = 0.0
c   step 3
      do 10 i=1,n
        s = 0.0
c   do-loop computed the summation
        do 20 j=1,n
20    s = s-a(i,j)*x1(j)
          s = (s+a(i,n+1))/a(i,i)
          if(abs(s).gt.err) err=abs(s)
          x1(i) = x1(i)+s
10  continue
      if(err.le.tol) then

```



```
        goto 400
    end if
c    step 5
    k = k+1
    goto 100
200 continue
400 continue

return
end
```

REFERENCES

- [Abraham 1987] E. Abraham and J. M. Halley, "Some Calculations of Temperature Profiles in Thin Films with Laser Heating," *J. Appl. Phys. A*, Vol. 42, (1987), pp. 279-285.
- [Abtahi 1986] A. Abtahi, P. F. Braunlich and P. Kelly, "Theory of Transient Temperature Response of a Two-Layer System Heated with a Localized Laser Beam," *J. Appl. Phys.* Vol. 60, No. 10, (1986), pp. 3417-3421.
- [Allen 1985] S. D. Allen, R. Y. Jan, S. M. Mazuk, and S. D. Vernon, "Real Time Measurement of Deposition Initiation and Rate in Laser Chemical Vapor Deposition," *J. Appl. Phys.* 58, No. 1, (1985), pp. 327-331.
- [Allen 1986] S. D. Allen, J. A. Goldstone, J. P. Stone, and R. Y. Jan, "Transient Nonlinear Laser Heating and Deposition: A Comparison of Theory and Experiment," *J. Appl. Phys.* Vol. 59, No. 5, (1986), pp. 1653-1657.
- [Arnold 1993.1] N. Arnold, R. Kullmer and D. Bäuerle, "Simulation of Growth in Pyrolytic Laser-CVD of Microstructure I. One-Dimensional Approach," *Microelectronic Engineering*, Vol. 20, (1993), pp. 31-41.
- [Arnold 1993.2] N. Arnold and D. Bäuerle, "Simulation of Growth in Pyrolytic Laser-CVD of Microstructure II. Two-Dimensional Approach," *Microelectronic Engineering*, Vol. 20, (1993), pp. 43-54.
- [Bartholomeusz 1988] B. J. Bartholomeusz, "Thermal Response of a Laser-Irradiated Metal Slab," *J. Appl. Phys.*, Vol. 64. No. 8, (1988), pp. 3815-3819.
- [Bäuerle 1990] D. Bäuerle, B. Luk'yanchuk, and K. Piglmayer, "On the Reaction Kinetics in Laser-Induced Pyrolytic Chemical Processing," *J. Appl. Phys. A*, Vol. 50, (1990), pp. 385-396.
- [Bäuerle 1986] D. Bäuerle, *Laser Processing and Chemistry*, Springer-Verlag, New York, (1986).
- [Baum 1989] T. H. Baum, C. E. Larson, and R. L. Jackson, "Laser-Induced Chemical Vapor Deposition of Aluminum," *J. Appl. Phys. Lett.*, Vol. 55, No. 12, (1989), pp. 1264-1266.

[Bloembergen 1978] N. Bloembergen, "Foundations of Laser-Solid Interactions, Laser-Solid Interactions and Laser Processing," *AIP Conf. Proc.*, No. 50, (1978), pp. 1-9.

[Boman 1995] M. Boman and D. Bäuerle, "Laser-Assisted Chemical Vapor Deposition of Boron," *J. of Chinese Chemical Society*, Vol. 42, (1995), pp. 405-411.

[Boyd 1984] I. W. Boya, T. D. Binnie, J. I. B. Wilson and M. J. Colles, "Absorption of Infrared Radiation in Silicon," *J. Appl. Phys.*, Vol. 55, No. 8, (1984), pp. 3061-3063.

[Brugger 1972] K. Brugger, "Exact Solution for the Temperature Rise in a Laser-Heated Slab," *J. Appl. Phys.*, Vol. 43, No. 2, (1972), pp. 577-583.

[Burden 1997] R. L. Burden and J. D. Faires, *Numerical Analysis*, Sixth Edition, Brooks, (1997).

[Burgener 1982] M. L. Burgener and R. E. Reedy, "Temperature Distributions Produced in a Two-layer Structure by a Scanning CW Laser or Electron Beam," *J. Appl. Phys.*, Vol. 53, No. 6, (1982), pp. 4357-4363.

[Calder 1982] I. D. Calder and R. Sue, "Modeling of CW Laser Annealing of Multilayer Structure," *J. Appl. Phys.* Vol. 53, No. 11, (1982), pp. 7545-7550.

[Chang 1996] H. Chang, L. Lee, R. Huang, et al., "Physical and Chemical Properties of the Cylindrical Rods SiC_x ($x=0.3-1.2$) Growth from $\text{Si}(\text{CH}_3)\text{Cl}_2$ by Laser Pyrolysis," *Material Chemistry and Physics*, Vol. 44, (1996), pp. 59-66.

[Cheburaeva 1986] P. F. Cheburaeva and I. N. Chaporova, "Role of Tantalum in the TiC-WC-TaC-Co Hard Metals. I. Effect of Tantalum Concentration on the Composition and Properties of the Carbide and Cobalt Phase in the TiC-WC-TaC-Co Hard Metals," Translated from *Poroshkovaya Metallurgiya*, No. 4, (1986), pp. 75-79.

[Chou 1989] W. B. Chou, M. N. Azer, and J. Mazunder, "Laser Chemical Vapor Deposition of Ti from TiBr_4 ," *J. Appl. Phys.*, Vol. 66, No. 1, (1989), pp. 191-195.

[Dai 1999] W. Dai, R. Nassar, C. Zhang, S. Shabanian, and J. Maxiwell, "A Numerical Model for Simulating Axisymmetric Rod Growth in Three-Dimensional Laser Chemical Vapor Deposition," *J. Numerical Heat Transfer*, Vol. 36, (1999), pp. 251-262.

[David 1988] D. E. Kotecki and I. P. Herman, "A Real Time Monte Carlo Simulation of Thin Film Nucleation in Localized-Laser Chemical Vapor Deposition," *J. Appl. Phys.* Vol. 64, No. 10, (1988), pp. 4920-4942.

[Doppelbauer 1984] J. Doppelbauer, G. Leyendecker, and D. Bäuerle, "Raman Diagnostics of Heterogeneous Chemical Processes, Determination of Local Concentrations," *J. Appl. Phys. B*, Vol. 33, (1984), pp. 141-147.

[Doppelbauer 1987] J. Doppelbauer and D. Bäuerle, "Kinetics of Laser-Induced Pyrolytic Chemical Processes and the Problem of Temperature Measurements, in Interfaces under Laser Irradiation," ed. by L. D. Laude, D. Bäuerle and M. Wautelet, NATO ASI Series (Nijhoff, Dordrecht 1987) p.277.

[El-Adawi 1986] M. K. El-Adawi and E. F. Elshehaway, "Heating a Slab Induced by a Time-Dependent Laser Irradiance – an Exact Solution," *J. Appl. Phys.*, Vol. 60, No. 7, (1986), pp. 2250-2255.

[Falk 1997] F. Falk, J. Meinschien, G. Mollekopf, K. Schuster, and H. Stafast, "CN_x Thin Films Prepared by Laser Chemical Vapor Deposition," *Material Science and Engineering B*, Vol. 46, (1997), pp. 89-91.

[Garrido 1991] C. Garrido, B. Leon and M. Perez-Amor, "A Model to Calculate the Temperature Induced by a Laser," *J. Appl. Phys.*, Vol. 69, No. 3, (1991), pp. 1133-1140.

[Ghez 1975] R. A. Ghez and R. A. Laff, "Laser Heating and Melting of Thin Films on Low-Conductivity Substrate," *J. Appl. Phys.*, Vol. 46, No. 5, (1975), pp. 2103-2110.

[Harrach 1977] R. J. Harrach, "Analytical Solution for Laser Heating and Burnthrough of Opaque Solid Slabs," *J. Appl. Phys.*, Vol. 48, No. 6, (1977), pp. 2370-2383.

[Imen 1989] K. Imen, J. Y. Lin, and S. D. Allen, "Steady-State Temperature Profile in Thermally Thin Substrate induced by Arbitrary Shaped Laser Beams," *J. Appl. Phys.* Vol. 66, No. 2, (1989), pp. 488-491.

[Incropera 1985] Frank P. Incropera and David P. DeWitt, *Fundamentals of Heat and Mass Transfer*, Second Edition, John Wiley & Sons, (1985).

[Jang 1998] T. Jang, W. Moon, et al, "Effect of Temperature and Substrate on the Growth Behaviors of Chemical Vapor Deposited a Films with Dimethylethylamine Alane Source," *Thin Solid Films*, Vol. 333, (1989), pp.137-141.

[Jellison 1983] G. E. Jellison and F. A. Modine, "Optical Functions of Silicon between 1.7 and 4.7 eV at Elevated Temperatures," *Physical Review B*, Vol. 27, No. 12, (1983), pp. 7466-7472.

[Kar 1989] A. Kar and J. Mazumder, "Three-Dimensional Transient Thermal Analysis for Laser Chemical Vapor Deposition on Uniformly Moving Finite Slab," *J. Appl. Phys.* Vol. 65, No. 8, (1989).

[Kar 1991] A. Kar, M. N. Azer and J. Mazumder, "Three-Dimensional Transient Mass Transfer Model for Laser Chemical Vapor Deposition of Titanium Finite Slab," *J. Appl. Phys.* Vol. 69, No. 2, (1991), pp. 757-765.

[Kirichenko 1990] N. Kirichenko, K. Piglmayer, and D. Bäuerle, "On the Kinetics of Non-Equimolecular Reactions in Laser Chemical Processing," *J. Appl. Phys. A*, Vol. 51, (1990), pp. 498-507.

[Lehmann 1994] O. Lehmann and M. Stucke, "Three-Dimensional Laser Direct Writing of Electrically Conducting and Isolating Microstructures," *Materials Letter*, Vol. 21, (1994), pp. 131-136.

[Levoska 1989] J. Levoska, T. T. Rantala and J. Lenkkeri, "Numerical Simulation of Temperature Distribution in Layered Structures During Laser Processing," *Applied Surface Science*, Vol. 36, (1989) pp. 12-22.

[Leyendecker 1983] G. Leyendecker, J. Doppelbauer, and D. Bäuerle, "Raman Diagnostics of CVD System: Determination of Local Temperature," *J. Appl. Phys. A*, Vol. 30, (1983), pp. 237-243.

[Liau 1994] Z. L. Liau, D. W. Nam, and R. G. Waarts, "Tolerances in Microlens Fabrication by Multilevel Etching and Mass-Transport Smoothing," *Applied Optics*, Vol. 33, No. 31, (1994), pp. 7371-7376.

[Maxwell 1996] J. Maxwell, *Three-Dimensional Laser-Induced Pyrolytic Modeling, Growth Rate Control, and Application to Micro-Scale Prototyping*, Ph.D. Thesis, Rensselaer Polytechnic Institute, Troy, New York, (1996).

[Mizunami 1995] T. Mizunami, N. Toyama, and T. Sakaguchi, "Laser-Energy Dependence of Optical Emission from Radical and Atoms in Laser-Induced Chemical-Vapor Deposition of SiC," *J. Appl. Phys.* Vol. 78, (1995), pp. 3525-3527.

[Mansuripur 1982] M. Mansuripur, et al., "Laser-Induced Local Heating of Multilayers," *Applied Optics*, Vol. 21, No. 6, (1982), pp. 1106-1114.

[Nassar 2000] R. Nassar, W. Dai, C. Zhang, H. Lan and J. Maxwell, "A Mathematical Model for Process Control in Laser Chemical Vapor Deposition," *Proceeding of the Third International Conference on Modeling and Simulation of Microsystems*, San Diego, California, (2000), pp. 517-519.

[Oh 1985] J. E. Oh, N. J. Ianno and A. U. Ahamed, "Temperature Profiles Induced by a Stationary CW Laser Beam in a Multi-Layer Structure: Applications to Solar Cell Interconnect Welding," *Applied Physics Communications*, Vol. 5, No. 3, (1985), pp. 113-138.

[Paek 1973] U. C. Paek and A. Kestenbaum, "Thermal Analysis of Thin-Film Micromachining with Lasers," *J. Appl. Phys.*, Vol. 44, No. 55, (1973), pp. 2260-2268.

- [Perecherla 1988] A. Perecherla and W. S. Williams, "Room-Temperature Thermal Conductivity of Cemented Transition-Metal Carbides," *J. Am. Ceram. Soc.*, Vol. 71, No. 12, (1988), pp.1130-33.
- [Peterson 1989] G. P. Peterson and L. S. Fletcher, "On the Thermal Conductivity of Dispersed Veramics," *J. of Heat Transfer*, Vol. 111, (1989), pp. 824-829.
- [Piglmayer 1984] K. Piglmayer, J. Doppelbauer, and D. Bäuerle, "Temperature Distribution in CW Laser Induced Pyrolytic Deposition," *Mat. Res. Soc. Symp. Proc.* Vol. 29, (1984), pp. 47-54.
- [Scholl 1982] M. S. Scholl, "Target Temperature Distribution Generated and Maintained by a Scanned Laser Beam," *Applied Optics*, Vol. 21, No. 12, (1982), pp. 2147-2152.
- [Seigel 1992] Seigel, R., Howell, J. R., *Thermal Radiation Heat Transfer, 3rd Ed.*, Hemisphere Publishing Corp., Boston, (1992), p.113.
- [Shappur 1987] F. Shappur and S. D. Allen, "Experimental Determination of Laser Heated Surface Temperature Distribution," *Appl. Phys. Lett.* Vol. 50, No. 12, (1987), pp. 723-724.
- [Suh 1984] S. Y. Suh and D. L. Anderson, "Latent Heat Effect of Pulsed Laser Beam Induced Temperature Profiles in Optical Recording Thin Films," *Applied Optics*. Vol. 23, No. 22, (1984).
- [Tamir 1995] S. Tamir, Y. Komem, M. Eizenberg and J. Zahavi, "Growth Mechanism of Silicon Films Produced by Laser-Induced Chemical Vapor Deposition," *Thin Solid Films*, Vol. 261, (1995), pp. 251-255.
- [Wang 1996] Q. Wang, Y. Zhang and D. Gao, "Theoretical Study on the Fabrication of a Microlens Using the Excimer Laser Chemical Vapor Deposition Technique," *Thin Solid Films*, Vol. 287, (1996), pp.243-246.